Progress in quantum error correction and simulation, a many-body physics approach

Asmae Benhemou

A dissertation submitted in partial fulfillment of the requirements for the degree of

Doctor of Philosophy

 ${\bf University} \ {\bf College} \ {\bf London}.$

Department of Physics and Astronomy
University College London

Primary supervisors: Prof. Jiannis K. Pachos, Prof. Dan E. Browne Secondary supervisor: Prof. Alessio Serafini

Declaration

I, Asmae Benhemou, confirm that the work presented in this thesis is my own. Where information has been derived from other sources, I confirm that this has been indicated in the work.

Asmae Benhemou London, United Kingdom May 21, 2025

Abstract

Quantum computers can perform computational tasks in an exponentially large state space, provided the system maintains high fidelity. However, quantum systems are highly susceptible to errors arising from environmental coupling and intrinsic quantum processes. Building and operating a quantum processor therefore requires a robust strategy to protect the encoded information from errors. This challenge gave rise to the field of quantum error correction, which employs redundancy to encode quantum information using sophisticated protocols. In parallel, topological phases of matter have emerged as exciting platforms for achieving faulttolerant and scalable quantum computation. These states exhibit intrinsic error resistance due to their topological nature, making them ideal candidates for encoding and manipulating quantum information. A symbiotic relationship has developed between these research areas, inspiring the study of topological quantum error-correcting codes. This thesis explores four themes: candidate logical encodings for topological quantum computing systems using the braiding and interaction of quasi-particle defects, including the surface code and a chain of parafermions; improved decoding for topological quantum codes; and proposals for quantum simulation leveraging the power of neutral atoms for braiding qudit topological states, and simulating quantum effects in black holes.

Impact Statement

Quantum computers are expected to perform tasks in exponentially large computational spaces, provided a high enough operational fidelity. Accessing such operations can provide an advantage in specific problems that remain intractable for state-of-the-art supercomputers, including modelling atoms in a molecule [Llo96], cryptography [Sho97] and optimisation [FGG14; Jor+24].

Building and operating large-scale quantum processors requires strategies to protect quantum information from errors that arise due to interactions with the environment and processes intrinsic to quantum systems. A prominent technique for addressing this challenge is quantum error correction, which redundantly encodes quantum states into a larger number of physical qubits. Another promising approach is topological quantum computing, where information is encoded in the topological properties of quantum states that emerge in two-dimensional systems.

In Part I, this thesis presents contributions to both quantum error correction and topological quantum computing. While these paradigms differ in their physical realisations, they are connected through their reliance on encoding quantum information in fault-tolerant structures. We demonstrate this by exploring non-Abelian anyonic behaviour in toric code defects, where punctures with peculiar boundaries reproduce exotic fusion rules and logical operations via braiding. Additionally, our insights from quasiparticles in the colour code lead to a decoding algorithm for the surface code, providing exponential improvements in logical error rates under depolarising noise. We also investigate another non-Abelian anyon species, \mathbb{Z}_3

parafermions, and show how their interactions enable the generation of non-Clifford gates, advancing the toolkit for topological qudit-based quantum computing. Collectively, these results strengthen the connection between topological quantum computing and error correction, contributing to both the theoretical and practical feasibility of robust quantum technologies. We emphasise that defect-based computation, and the decoding of topological quantum codes, are critical areas of research for the development of practical fault-tolerant quantum computation. Moreover, the discovery and implementation of non-Clifford gates are essential for achieving universal quantum computation.

In Part II, we explore a third paradigm: analogue quantum simulation. Unlike gate-based quantum computation, which processes information through discrete sequences of quantum gates, analogue quantum simulation mimics the dynamics of complex quantum systems by directly mapping them onto controllable physical platforms. This method allows the study of phenomena that are otherwise difficult to explore in natural systems.

We propose a scheme for simulating aspects of black hole physics using ultracold atoms in locally Floquet-driven optical lattices. By creating a position-dependent tunnelling profile, the system encodes the curved spacetime geometry of (1+1)-dimensional black holes, enabling the study of effects like Hawking radiation. We develop a simple method for measuring the Hawking temperature, relying on onsite atom population measurements. We extend our simulation to (2+1)-dimensional black holes using 2D optical lattices, incorporating atomatom interactions to probe quantum properties such as information scrambling. This work demonstrates the potential of analogue quantum simulation to advance our understanding of quantum gravity and explore complex quantum phenomena.

Acknowledgements

I begin by expressing my gratitude to my PhD supervisors. I thank Prof. Jiannis K. Pachos for his guidance and original, intuitive explanations of the physics we explored together, and Prof. Dan E. Browne for his support, patience, and for fostering a welcoming and collaborative environment in his group.

I am deeply grateful to my parents, Fatima and Mourad, for their love, relentless support and words of wisdom—I owe all of my passions in and for life to them. I specifically thank my mom for reading me *Les atomes de l'Univers* by Étienne Klein [Kle03] when I was little. I am also grateful for my siblings, Anas and Lina, for their unconditional love and witty sense of humour, and of course everyone else in our family, with a special thought for my grandparents Khadija and Ahmed.

During my PhD I was lucky to have the support of wonderful friends, Ruxandra Bob, Anne Suffel, Tiffany Loera, Jeanne Magnan, Marija Radulovic, Tisha Dasgupta, Arthur Pesah, George Umbrarescu, Timo Hillman, Shraddha Singh, Jonathan Conrad, Hasan Sayginel and many more. A special mention goes to Basudha Srivastava and Oscar Higgott, and thanks to Armanda Quintavalle for the many laughs. I also cherish many joyful moments with Cohort 6 of the UCL Quantum CDT, and the IBM Quantum summer school. I'd also like to thank new friends who have made the office and conferences so fun and memorable.

I would also like to thank my peers and collaborators: Toonyawat Angkhanawin, Prof. Charles S. Adams, Kaavya Sahay, Lingling Lao, Benjamin J. Brown, Georgia Nixon, Aydin Deger, Prof. Ulrich Schneider, Juliette Soule, and Dominic J. Williamson. Finally, I extend my thanks to Aleksander Kubica and Sam Roberts for their mentorship during my internships at the AWS Center for Quantum Computing and PsiQuantum, which were consequential in shaping my understanding of state-of-the-art quantum computing.

This thesis is based on work contained in the following publications:

- Asmae Benhemou, Jiannis K Pachos, and Dan E Browne. "Non-Abelian statistics with mixed-boundary punctures on the toric code". In: *Physical Review A* 105.4 (2022), p. 042417. DOI: https://doi.org/10.1103/PhysRevA.105.042417
- Asmae Benhemou et al. "Universality of Z₃ parafermions via edge-mode interaction and quantum simulation of topological space evolution with Rydberg atoms". In: *Physical Review Research* 5.2 (2023), p. 023076. DOI: https://doi.org/10.1103/PhysRevResearch.5.023076
- Asmae Benhemou et al. "Minimising surface-code failures using a color-code decoder".
 In: arXiv preprint arXiv:2306.16476 (2023). DOI: https://doi.org/10.48550/arXiv.2306.16476
- Asmae Benhemou et al. "Probing quantum properties of black holes with a Floquet-driven optical lattice simulator". In: arXiv preprint arXiv:2312.14058 (2023). DOI: https://doi.org/10.48550/arXiv.2312.14058

Contents

1	Intr	oducti	ion	1
Ι	De	fects,	logic and decoding on topological quantum codes	4
2	Pre	limina	ries	5
	2.1	Basics	of quantum information	5
	2.2	Eleme	nts of quantum computing	11
		2.2.1	Qubits and qudits	11
		2.2.2	Quantum gates	12
	2.3	Quant	rum error correction	15
		2.3.1	Correcting classical information	15
		2.3.2	Correcting quantum information	19
		2.3.3	Stabilizer codes	20
			2.3.3.1 Noise models	22
		2.3.4	Fault-tolerance	24
		2.3.5	Topological quantum codes	26
			2.3.5.1 The surface code	26
			2.3.5.2 The colour code	28
			2.3.5.3 Relationship between toric and colour codes	30
		2.3.6	Decoding quantum codes	32

CONTENTS						
			2.3.6.1	The quantum decoding problem		32
			2.3.6.2	Minimum-weight perfect matching		34
		2.3.7	Fault-to	lerant logic and code deformations		37
			2.3.7.1	Fault-tolerant gates		37
			2.3.7.2	Code deformations		38
	2.4	Topolo	ogical pha	ases and quantum computing		40
		2.4.1	Topologi	ical order		41
		2.4.2	Algebrai	ic properties of anyons		42
			2.4.2.1	The toric code anyon model		45
			2.4.2.2	The Ising anyon model		46
		2.4.3	Topologi	ical quantum computing		49
		2.4.4	The Kits	aev models		50
		2.4.5	The Ma	jorana chain and zero-energy edge modes		57
		2.4.6	Twist de	efects in topological codes		59
3	Nor	n-Abel	ian stati	stics of mixed-boundary punctures		62
	3.1	Introd	uction			62
	3.2	Defect	s on the s	surface code		64
	3.3	Fusion	and excl	hange of mixed-boundary punctures		66
		3.3.1	The syst	tem		66
		3.3.2	Logical	encoding		67
		3.3.3	Fusion a	action		68
		3.3.4	Braiding	g action		69
	3.4	Discus	ssion			72
4	Uni	versali	ty of \mathbb{Z}_3	parafermions via edge mode interaction		74
	4.1	Intro	duction .			74
	4.2	Parafe	ermion ed	ge-modes and computation		77
		4.2.1	The para	afermion chain		77

CONTENTS	ix
----------	----

		4.2.2	Parafermion edge modes
		4.2.3	Computing with parafermions
	4.3	A dyn	amical gate from parafermion interaction
		4.3.1	Decimation of the highest-energy term
		4.3.2	Effective Hamiltonian from PEM interaction
		4.3.3	Asymmetric \mathbb{Z}_3 parafermion chain
	4.4	A No	n-Clifford gate $\mathcal U$ from parafermion edge-mode interaction 89
		4.4.1	Dynamical gate
		4.4.2	${\cal U}$ in the Clifford hierarchy
		4.4.3	Universality with \mathcal{U}
		4.4.4	Contextual qutrit states using \mathcal{U}
	4.5	Discu	ssion
5	Cor	related	d matching on the surface code 99
	5.1	Introd	uction
	5.2	Mater	ialised symmetries and decoding
		5.2.1	Symmetries of the colour code
		5.2.2	Matching decoders code symmetries
	5.3	Mapp	sing surface code errors to colour code errors
	5.4	Surfa	ce code performance under depolarising noise
		5.4.1	Correcting Pauli- Y errors on the surface code
		5.4.2	Path-counting of failure mechanisms
		5.4.3	Low error-rate performance
		5.4.4	Thresholds
	5.5	Colou	ur code performance under bit-flip noise
		5.5.1	Path-counting
		5.5.2	Low error-rate performance
		5.5.3	Thresholds

CONTENTS	X

	5.6	Discussion
II	Sin	mulation of black hole properties using a quantum system 127
6	Pre	liminaries 128
	6.1	Black hole phenomena and quantum systems in curved spacetime
		6.1.1 Black holes and thermodynamics
		6.1.2 Hawking radiation and black hole evaporation
	6.2	Introduction to relevant quantum many-body systems
		6.2.1 The XY model
		6.2.2 The Bose-Hubbard model
		6.2.3 Optical lattices and Floquet driving
7	Blac	ck hole simulation using optical lattices 140
	7.1	Introduction
	7.2	The tight-binding model and the Dirac Equation $\dots \dots \dots$
	7.3	An optical lattice simulator of Dirac fermions in a black hole background $$ 144
	7.4	Hawking temperature from radiation population
	7.5	Resilience to errors
	7.6	2D Implementation of the black hole simulator $\dots \dots \dots$
	7.7	Chaotic behaviour
	7.8	Discussion
8	Con	aclusion 160
\mathbf{A}	App	pendices 163
	A1	Simulating parafermions with Rydberg atoms
	A2	Pseudocode for unified decoding on the surface code $\dots \dots \dots$
	A3	Thresholds for the even-distance surface code using varied weights 170

CONTENTS	xi

A4	A note on other derivations of Hawking radiation
A5	Diagonalising the XY model
A6	Floquet Engineering

List of Figures

2.1	The Bloch sphere representing the state of a single qubit. \dots	10
2.2	Tanner Graph of the 7-bit Hamming Code	18
2.3	The distance-7 unrotated and rotated toric and surface codes	27
2.4	The colour code	28
2.5	Unfolding the colour code	31
2.6	A schematic of the minimum-weight perfect matching decoder	34
2.7	Topological F -move and R -move	45
2.8	Schematic of a topological quantum computation	48
2.9	Non-contractible loop of the torus	52
2.10	Logical \overline{X} operators of the toric code	54
2.11	The Kitaev honeycomb model	55
2.12	Schematic action of twist defects	61
3.1	Different types of puncture defects on the toric code	64
3.2	Twists on the toric code	65
3.3	A mixed-boundary puncture	66
3.4	A state of a pair of mixed-boundary punctures	67
3.5	Logical encoding of four mixed-boundary punctures	68
3.6	Braiding operation shown for state $ e_1e_2\rangle m_3m_4\rangle \dots \dots$	70
3.7	Logical gate by braiding operation in the four-puncture system	71

TIOT OF FIGURES	•••
LIST OF FIGURES	X111

3.8	A logical \overline{Z} operator for the four mixed-boundary punctures
4.1	Schematic of localised and delocalised edge modes in a parafermion chain 79
4.2	Schematic of single qutrit gates on a logical qutrit encoded in four parafermions. 80
4.3	Schematic of a 3-site parafermion chain with weak onsite and strong nearest-
	neighbour couplings
4.4	The three lowest energy eigenvalues for H_2 with $J_i=1 \ \forall i$ and varying f 87
4.5	Magnitude (a) and phase (b) plots for 5000 sampled states computed by creat-
	ing random words of length 50 using $\mathcal U$ and Clifford operations, and applying
	them on the initial state $ \psi\rangle= 0\rangle$
4.6	Magnitude (a) and phase (b) plots of a dense set of 10000 sampled qutrit states
	using random words of length 50 composed of the $\mathcal U$ and Clifford operations.
	The colour plot indicates the values of \mathcal{M}
4.7	Magnitude (a) and phase (b) plots of states close to the strange states $ S_a\rangle$,
	$ S_b\rangle$ and $ S_c\rangle$, within a trace distance of 0.2
5.1	Manifold which preserves the global symmetry of the 4.8.8 colour code 102
5.2	Schematic of the unified lattice for the 4.8.8. colour code
5.3	Weight-4 error on a $d=8$ colour code lattice, which can be interpreted as a
	weight-2 error on the $d=4$ surface code
5.4	The mapping of surface code Pauli errors errors to colour code bit-flips 109
5.5	The $d=4$ surface code, with depolarising errors
5.6	The logical failure rate data for the surface code under low physical error rates
	computed using the splitting method [BV13] to test the restricted and unified
	decoders for even surface code distances
5.7	The logical failure rate $P_{\rm fail}$ (in logarithmic scale) as a function of physical error
	rate p for the restricted and unified surface codes of even distance d , under an
	i.i.d depolarising noise channel

LIST OF FIGURES xiv

5.8	The logical failure rates at low physical error rates computed using the splitting
	method [BV13] for the restricted and unified decoders on the colour code under
	i.i.d bit-flip noise
5.9	The logical failure rate $P_{\rm fail}$ as a function of physical error rate p for codes of
	different distance d , under an i.i.d bit-flip noise model
6.1	Finkelstein diagram
7.1	Schematic of the black hole simulator
7.2	A black hole simulator implemented using local Floquet driving of a 1D optical
	lattice
7.3	Extracting the Hawking temperature from the density evolution of a single
	particle initialised inside the horizon
7.4	Error-resilience to random onsite potentials, additive random nearest-neighbour
	and random next-nearest neighbour tunnelling
7.5	Analogue quantum simulation of a 2D black hole using a Floquet-driven square
	optical lattice
7.6	An 8×8 lattice with 90° rotational symmetry can be simulated using 16 sites.
	The black and yellow dots show the full 8×8 lattice, only the yellow dots in the
	shaded region are needed for the 16 site simulation described in Sec. 7.7. Black
	lines indicate tunnelling between neighbouring sites common to both the full
	system and the 16 site simulation. To the simulation, we add three additional
	tunnelling terms indicated by blue curves, connecting sites $1 \rightarrow 16, 5 \rightarrow 15,$
	$9 \rightarrow 14. \dots \dots$

LIST OF FIGURES xv

7.7	Comparing level statistics between finite 2D square lattices encoding flat (or-
	ange) and curved (blue) space-time backgrounds. The mean gap ratio $\langle r \rangle$ is
	computed using Eq. 7.19 for varying particle number $N.$ For the blue data,
	$\alpha = 0.46, \ J_0 = 1$ and we add a perturbation of strength $\epsilon = 0.01$ (dashed
	lines) or $\epsilon=0.0625$ (solid lines) to lift degeneracies. For the flat system, ho-
	mogeneous tunnelling is set to $\kappa J_0 = 0.28$. The expected mean gap ratios
	$\langle r_{\rm GOE} \rangle = 0.5295 \pm 0.0006$ and $\langle r_{ m Poiss} \rangle \approx 0.386$ [OH07] for a GOE and Pois-
	sonian ensemble in the thermodynamic limit are indicated by red-dotted and
	black-dotted lines. The curved spacetime encoded in the blue data gives rise to
	higher values of $\langle r \rangle$ and hence does not break the ergodicity expected for the
	flat system
A -1	
A.1	Four-level Rydberg atom system coupled by four monochromatic classical mi-
	crowave fields
A.2	The logical failure rate P_{fail} as a function of physical error rate p for surface
	codes of different even distance d , under i.i.d depolarising noise

List of Tables

4.1	Trace distances \mathcal{D} and non-contextuality inequality \mathcal{M} of the three sampled	
	states in Fig. 4.7 closest to $ S_a\rangle$, $ S_b\rangle$ and $ S_c\rangle$	96

Chapter 1

Introduction

There exist certain classes of problems that are intractable to solve using classical computers, whereas quantum computers are expected to surpass this limitation. These are processors which exploit quantum theory to encode information using quantum systems that can exist in states of superposition, entanglement, and experience interference [NC10]. Such problems are found in the fields of simulation of materials, such as individual atoms in a molecule [Llo96], cryptographic protocols [Sho97], and optimisation [FGG14; Jor+24]. We envisage that operating quantum computers will lead to the development of new technologies, and understanding of complex physics from sub-atomic to supergalactic scales. To this effect, various hardware platforms are currently investigated, including superconducting chips [Han+24; Ach+24], neutral atom arrays [Blu+23], trapped ions [Mos+23], photonic and bosonic architectures [Bou+21; Mar+23; Bar+23], silicon-based qubits [Cir+21], topological quantum states [Bon+10] and more.

The road to building a quantum computer is a noisy one. Indeed, carrying out even a small quantum computation with sufficiently low failure rates requires high fidelity of qubits and operations. These correspond to components in a physical quantum circuit, that each undergo errors. These errors occur due to the delicate nature of quantum systems, as these experience decoherence through interactions with their environment. Moreover, hardware

limitations (e.g. miscalibrated pulses, faulty control signals), imperfect readout devices and leakage out of the computational space can all affect the quality of quantum circuit execution. For instance, it is estimated that factoring 2048-bit RSA integers in 8 hours requires 20 million noisy qubits with a characteristic physical gate error rate of 10^{-3} [GE21].

Along with improved hardware, quantum errors are addressed by using redundancy to encode logical information in a protected subspace. This is in many ways analogous to techniques in classical coding theory, which are ubiquitous in our communication systems and cryptographic protocols. Classical computers manipulate bits of information according to deterministic algorithms, where each bit is in a specific state at any given time, and vulnerable to being "flipped". In contrast, quantum systems are subject to a continuum of errors, generally modelled using Pauli error channels. Quantum error-correction (QEC) consists of techniques to detect and correct these errors, by encoding information into entangled states of larger numbers of physical quantum bits [Sho95]. QEC has successfully been demonstrated in a recent experiment [Ach+24].

A separate approach to achieving fault-tolerant quantum computation consists of encoding quantum information in the decoherence-free ground subspace of a topologically ordered quantum state [Pac12]. The computational space consists of the fusion pathways of a collection of emergent quasiparticles, anyons, and quantum gates are carried out by adiabatically winding anyons around each other. The topological nature of the system is the key to the protection against errors that quantum systems typically incur.

Quantum simulation is a third method for manipulating quantum information [Dal23]. This technique consists of utilising an accessible and highly controlled quantum system to infer knowledge of another quantum system, that is not directly accessible. Analogue quantum simulation is distinguished from digital computational models in that it often involves continuous interactions that naturally replicate the behaviour of a target system, instead of discrete operations on qubits. Note that errors in analogue evolution do tend to accumulate, unlike active quantum error-correction in the digital case. A prominent platform for quantum simulation is trapped ultracold atoms near absolute zero temperature in a grid-like potential,

referred to as optical lattices [Blo05; GB17b; Sch+20b; NUS23]. These systems are effectively described by a Bose-Hubbard model, and offer versatile ways of tuning its Hamiltonian to simulate diverse complex models. The ability to independently tune all Hamiltonian parameters, i.e. the local potentials, hopping and coupling, and achieve next-to-nearest-neighbour interactions as well as different periodicities, offers an exciting platform to simulate quantum many-body phenomena. Combined with the high-resolution probing of cold atoms in the lattice, this allows us to learn properties of physical systems that remain intractable via alternative computational models.

This thesis is divided in two Parts. In Part I, we present a collection of works showcasing results in various aspects of topological quantum computing and QEC. We start with the relevant background theory in Chapter 2. In Chapter 3, we explored how exotic defects, namely mixed-boundary punctures, can emulate Majorana anyon behaviour by combining their Abelian statistics with a nonlocal encoding. In Chapter 4, we extended the work in [BK05] to the more general parafermions with fractional non-Abelian statistics, by analysing the \mathbb{Z}_3 parafermion edge mode interaction to obtain a tunable non-Clifford gate, thereby contributing to universal quantum computing by accessing resourceful non-contextual states. In Chapter 5, we designed a decoder by mapping the surface code onto the colour code, improving resilience of the former to depolarising noise. This resulted in an exponential reduction in logical error rates for minimum-weight errors, inspiring further investigations into hybrid decoding approaches and fault-tolerant schemes. In Part II of this thesis, we present an experimental proposal to simulate the emergent curved spacetime at the event horizon of a Schwarzschild black hole. In Chapter 6, we introduce background theory and context behind this system, as well as the many-body quantum Hamiltonians describing our simulator. Our work in Chapter 7 describes this mapping, and introduces a scheme to measure Hawking temperatures in the laboratory by leveraging the controllable interactions in optical lattices, combined with precise single-site measurements. We conclude with general remarks and future directions in Chapter 8.

Part I

Defects, logic and decoding on topological quantum codes

Chapter 2

Preliminaries

In this chapter, we review the foundational concepts, key topics, and relevant literature in the fields of fault-tolerant quantum computing and quantum error correction. We start with necessary concepts in quantum theory and establish some notation. Next, we delve into the field of error correction, examining both classical and quantum error-correcting codes. We then introduce topological order, a central theme in this work, that is pivotal in the development of fault-tolerant quantum computation. This chapter provides a comprehensive overview of the theoretical tools and systems addressed in this thesis.

2.1 Basics of quantum information

We begin by introducing the notions and notation that will be used throughout this thesis to describe the states and dynamics of quantum systems [Pre15]. Quantum theory is a complete mathematical framework for physical phenomena which specifies how to represent states, observables, measurements, evolutions and interactions. In quantum mechanics, states of physical systems are represented by elements $|\psi\rangle$ in a Hilbert space \mathcal{H} , that is a vector space over the complex field \mathbb{C} . This space is equipped with an inner product $\langle . \rangle$ which respects

positivity, linearity, and skew-symmetry such that for two quantum states $|\psi\rangle, |\phi\rangle \in \mathcal{H}$,

$$\langle \psi | \psi \rangle > 0 \text{ for } | \psi \rangle \neq 0$$
 (2.1)

$$\langle \phi | (a | \psi_1 \rangle + b | \psi_2 \rangle) = a \langle \phi | \psi_1 \rangle + b \langle \phi | \psi_2 \rangle \tag{2.2}$$

$$\langle \phi | \psi \rangle = \langle \psi | \phi \rangle^* \tag{2.3}$$

with the space complete in the norm $||\psi|| = \sqrt{\langle \psi | \psi \rangle}$. States in \mathcal{H} are represented by normalised vectors, which are physically invariant under overall phases, such that $|\psi\rangle \equiv e^{i\alpha} |\psi\rangle$ where $|e^{i\alpha}| = 1$. Linear superpositions of quantum states can exist, such that the overall state can be written as a sum of orthogonal basis states, with relative phases between these states.

Operators acting on quantum systems are linear maps of the form $\hat{O}: |\psi\rangle \to \hat{O} |\psi\rangle$, where the adjoint operator O^{\dagger} is defined by

$$\langle \phi | O\psi \rangle = \langle O^{\dagger} \phi | \psi \rangle \tag{2.4}$$

for all states $|\psi\rangle$, $|\phi\rangle$, where $|\hat{O}\psi\rangle = \hat{O}|\psi\rangle$. Observables in quantum mechanics refer to measurable features of a physical system, and are described by self-adjoint (Hermitian) operators, i.e. operators respecting

$$\langle \phi | \hat{O} | \psi \rangle = \langle \psi | \hat{O} | \phi \rangle^* \qquad \forall | \psi \rangle, | \phi \rangle.$$
 (2.5)

Eigenstates of self-adjoint operators $\hat{O} \in \mathcal{H}$ form a complete orthonormal basis in \mathcal{H} , s.t. one can write

$$\hat{O} = \sum_{i} o_i |i\rangle\langle i| \tag{2.6}$$

where each $|i\rangle\langle i|$ is the orthogonal projection onto the space of eigenvectors with eigenvalue o_i , and $\{|i\rangle\}$ the orthonormal basis of eigenstates of \hat{O} . Information in a quantum state can be retrieved through the process of measurement. Consider a quantum system in a state $|\psi\rangle$. Measurement corresponds to the interaction between the system and a measurement operator

 \hat{O} , which has eigenstates $\{|o_j\rangle\}$ with eigenvalues $\{o_j\}$. When a measurement is performed, the quantum state collapses into one of the eigenstates $|o_j\rangle$, and the outcome o_j is observed. The probability of this outcome is given by the Born rule:

$$p(o_j) = |\langle o_j | \psi \rangle|^2. \tag{2.7}$$

Repeating the same measurement will yield the same outcome o_j with probability 1, as the system is now in the eigenstate $|o_j\rangle$.

In quantum mechanics, the Schrödinger equation describes how the state of a system evolves in time. If the system is closed, this time evolution is described by a unitary operator U. Specifically, given an initial quantum state $|\psi(t_1)\rangle$, the final state at time t_2 is obtained under the transformation

$$|\psi(t_2)\rangle = U(t_2, t_1) |\psi(t_1)\rangle \tag{2.8}$$

where this time evolution obeys

$$\frac{d}{dt}|\psi(t)\rangle = -i\hat{H}(t)|\psi(t)\rangle. \tag{2.9}$$

The operator \hat{H} , referred to as the *Hamiltonian* of the system, is Hermitian, and has the dimensions of energy. If \hat{H} is a time-independent operator, the evolution takes the simpler form

$$\hat{U}(t_2, t_1) = e^{-i(t_2 - t_1)\hat{H}}. (2.10)$$

An important feature of quantum mechanics lies in the way composite systems behave. A two-composite system consisting of subsystems \mathcal{A} and \mathcal{B} , respectively prepared in states $|\psi\rangle_{\mathcal{A}}$ and $|\psi\rangle_{\mathcal{B}}$, lives in a Hilbert space defined by the tensor product of the individual subsystem Hilbert spaces, $\mathcal{H}_{\mathcal{A}\mathcal{B}} = \mathcal{H}_{\mathcal{A}} \otimes \mathcal{H}_{\mathcal{B}}$, and is denoted by the tensor product $|\psi\rangle_{\mathcal{A}} \otimes |\psi\rangle_{\mathcal{B}}$. The joint Hilbert space is spanned by basis states of the form $\{e_{\mathcal{A}}, e_{\mathcal{B}}\}$ where $|e_{\mathcal{A}}, e_{\mathcal{B}}\rangle \equiv |e_{\mathcal{A}}\rangle \otimes |e_{\mathcal{B}}\rangle$ which respectively designate the basis states spanning $\mathcal{H}_{\mathcal{A}}$ and $\mathcal{H}_{\mathcal{B}}$. Operators acting on the

first or second system independently take the form

$$O_{\mathcal{A}} \otimes \mathbb{1}_{\mathcal{B}} , \mathbb{1}_{\mathcal{A}} \otimes O_{\mathcal{B}}.$$
 (2.11)

where the identity operator $\mathbb{1}_{i\in\{\mathcal{A},\mathcal{B}\}}$ indicates the trivial action on a subsystem.

Since a quantum processor can operate on multiple subsystems as both input and output, we can characterise the nature of these states from an information-theoretic perspective. A quantum bit, or qubit, is a unit of quantum information, analogous to the classical bit which takes a value in $\{0,1\}$. A qubit is described by a state in the smallest non-trivial Hilbert space, the two-dimensional vector space $\mathcal{H} = \mathbb{C}^{\otimes 2}$, spanned by $\{|0\rangle, |1\rangle\}$. This is known as the computational basis, where $|0\rangle = (1 \ 0)^T$ and $|1\rangle = (0 \ 1)^T$. A general qubit state can be written as a linear superposition of the these states:

$$|\psi\rangle = \alpha |0\rangle + \beta |1\rangle \tag{2.12}$$

where $\alpha, \beta \in \mathbb{C}$ and $|\alpha|^2 + |\beta|^2 = 1$. A measurement on a qubit in the computational basis returns the outcome $|0\rangle$ with probability $|\alpha|^2$, and $|1\rangle$ with probability $|\beta|^2$. A qubit can be described using a geometrical interpretation of the state in Eq. 2.12. Indeed, a qubit in an arbitrary state can be written as

$$|\psi\rangle = \cos\frac{\theta}{2}|0\rangle + \sin\frac{\theta}{2}e^{i\phi}|1\rangle$$
 (2.13)

using the polar representation of the complex amplitudes α and β , as the quantum state does not change if we multiply it with any number of unit norm. The angles $\theta, \phi \in \mathbb{R}$ define a point on the three-dimensional unit sphere, known as the *Bloch sphere*, such that $0 \le \theta < \pi$, and $0 \le \phi < 2\pi$, as shown in Fig. 2.1. This formally follows from a 2-to-1 homomorphism of SU(2) on SO(3). The state of a qubit can be represented by a *density operator*

$$\rho = \frac{1}{2}(I + \mathbf{r} \cdot \boldsymbol{\sigma}) \tag{2.14}$$

where \mathbf{r} is the *Bloch vector* $\mathbf{r} = (\sin \theta \cos \phi, \sin \theta \sin \phi, \cos \theta)$, and $\boldsymbol{\sigma}$ is the three-component vector of Pauli matrices, i.e.

$$\sigma^x = \begin{pmatrix} 0 & 1 \\ 1 & 0 \end{pmatrix}, \quad \sigma^y = \begin{pmatrix} 0 & i \\ -i & 0 \end{pmatrix}, \quad \sigma^z = \begin{pmatrix} 1 & 0 \\ 0 & -1 \end{pmatrix}$$
 (2.15)

with the 2×2 identity matrix 1 sometimes included. The Pauli matrices form an orthogonal basis for the complex vector space for all 2×2 matrices, and satisfy the following commutation and anti-commutation relations:

$$[\sigma^i, \sigma^j] = 2i\epsilon_{ijk}\sigma^k, \qquad \{\sigma^i, \sigma^j\} = 2\delta_{ij}I \tag{2.16}$$

where $i, j, k \in \{x, y, z\}$, ϵ_{ijk} is the Levi-Civita symbol, and the Kronecker delta δ_{ij} . An isolated quantum state, as described in Eq. 2.13, is known as a pure state. Pure states are characterised by having a trace $\text{Tr}(\rho^2) = 1$, and are represented by points on the surface of the Bloch sphere. A qubit can also be described by a classical mixture of pure states described by density matrices of the form

$$\rho = \sum_{i} p_i |\psi_i\rangle\langle\psi_i|, \qquad (2.17)$$

with $\text{Tr}(\rho^2) < 1$ and probabilities $p_i \in [0, 1]$. Mixed states can arise due to interactions with the environment or lack of full knowledge of the system. In the Bloch sphere representation, they occupy points inside the sphere. A single-qubit quantum gate is a unitary linear operation which can be visualised as a rotation on the Bloch sphere, and written as

$$U = e^{i\alpha} R_{\hat{n}}(\theta) \tag{2.18}$$

for $\alpha, \theta \in \mathbb{R}$, and \hat{n} a three-dimensional unit vector on the Bloch sphere. The operator $R_{\hat{n}}(\theta) \equiv \exp\left(-i\frac{\theta}{2}\,\hat{n}\cdot\boldsymbol{\sigma}\right)$ rotates the state vector on the Bloch sphere by an angle θ about the \hat{n} axis.

As described earlier, consider a bipartite composite system to which we assign orthonormal

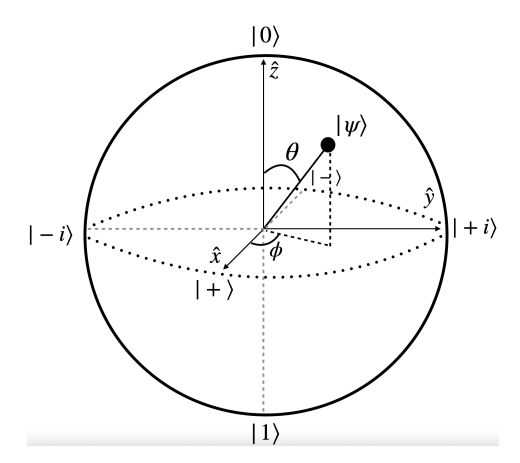


Figure 2.1: The Bloch sphere representing the state of a single qubit.

bases $\{|0\rangle_{\mathcal{A}}, |1\rangle_{\mathcal{A}}\}$ and $\{|0\rangle_{\mathcal{B}}, |1\rangle_{\mathcal{B}}\}$. Quantum mechanics allows for states of the joint system which describe quantum correlations between \mathcal{A} and \mathcal{B} , such that an arbitrary state of the system is given by

$$|\psi\rangle_{\mathcal{AB}} = \sum_{e_{\mathcal{A}}, e_{\mathcal{B}}} a_{e_{\mathcal{A}}, e_{\mathcal{B}}} |e_{\mathcal{A}}\rangle \otimes |e_{\mathcal{B}}\rangle, \text{ where } \sum_{e_{\mathcal{A}}, e_{\mathcal{B}}} |a_{e_{\mathcal{A}}, e_{\mathcal{B}}}|^2 = 1.$$
 (2.19)

The density operators of systems \mathcal{A} and \mathcal{B} are obtained by performing partial traces over the respective other subsystem, as follows:

$$\rho_{\mathcal{A}} = \operatorname{Tr}_{\mathcal{B}}(|\psi\rangle\langle\psi|_{\mathcal{A}\mathcal{B}}), \ \rho_{\mathcal{B}} = \operatorname{Tr}_{\mathcal{A}}(|\psi\rangle\langle\psi|_{\mathcal{A}\mathcal{B}}),$$
(2.20)

where $\rho_{\mathcal{A}}$ and $\rho_{\mathcal{B}}$ are self-adjoint, positive semidefinite, and have unit trace. Entanglement is a fundamental concept in quantum mechanics that describes a type of correlation between quantum systems. When two or more quantum systems become entangled, their states are interdependent, meaning the state of one system cannot be described independently of the

others. For example, the following states are known as the Bell states,

$$|\Phi^{\pm}\rangle = \frac{1}{\sqrt{2}} \left(|00\rangle \pm |11\rangle \right), \tag{2.21}$$

$$|\Psi^{\pm}\rangle = \frac{1}{\sqrt{2}} \left(|01\rangle \pm |10\rangle \right), \tag{2.22}$$

which are referred to as maximally entangled since the reduced density matrices $\rho_{\mathcal{A}} = \rho_{\mathcal{B}} = 1/2$ indicate that neither qubit has coherence or a definite state on its own, i.e. $\mathbf{r}_A = \mathbf{r}_B = 0$. Hence, the state of each qubit is completely mixed when traced over the other subsystem. In this notation, we abbreviated a state $|a\rangle \otimes |b\rangle$ as $|ab\rangle$. The earlier definitions naturally extend to larger multipartite composite systems, but cannot be visualised as simply as the single-qubit case due to the higher dimensionality and the complex nature of entanglement. In this thesis, we focus on examples of many-body quantum systems that exhibit strong entanglement, which is leveraged for applications in quantum computing.

2.2 Elements of quantum computing

Quantum computing harnesses properties of quantum systems as processing units, and quantum operations which are not accessible by classical systems, to enable speed-ups over classical algorithms for certain families of problems [DJ92; BV93; Kit95; Gro96]. In this section, we will define fundamental concepts of quantum computing which will be relevant to our work.

2.2.1 Qubits and qudits

In classical information theory, the information characterising a message is encoded in strings of bits of the form $x_1x_2...x_n$, where $x_i \in \mathbb{F}_2$. Each bit can take one of two values: 0 or 1, and the information is processed using logic gates such as AND, OR, and NOT, and information is processed deterministically using classical algorithms. In Sec. 2.1 we defined the qubit as a two-level system living in the vector space \mathbb{C}^2 . A collection of n such qubits constitutes a register with 2^n basis states written as $|q_1\rangle \otimes |q_2\rangle ... \otimes ... |q_n\rangle$ where $q_i \in \mathbb{F}_2$. Qudits are higher-

dimensional quantum systems, generalising the binary quantum bit in Eq. 2.12 to d-ary digits where d > 2 is the dimension of the system, and are an alternative to qubits as quantum information units [BB02]. A qudit state can be described as a vector

$$|\psi\rangle = \sum_{i=0}^{d-1} \alpha_i |e_i\rangle, \qquad (2.23)$$

where $\alpha_i \in \mathbb{C}^d$ and $\sum_i |\alpha_i|^2 = 1$. Like qubits, qudits can be used to encode information, and computation is performed by applying qudit gates on the encoded states. Since qudits inhabit a larger Hilbert space compared to qubits, they can store more quantum information and enable the simultaneous execution of multiple control operations. These advantages offer the potential to reduce circuit complexity, and improve the efficiency of quantum algorithms and scalability [NC10; Wan+20].

2.2.2 Quantum gates

After initialising a set of quantum registers, quantum computation proceeds with a sequence of unitary operations that evolve the quantum state, known as quantum gates. These operations are prescribed by a quantum algorithm, and projective measurements on the system are performed to read out the outcomes [NC10]. The Pauli matrices in Eq. 2.15 are examples of single-qubit unitary and Hermitian gates with eigenvalues ± 1 . We can also consider n-fold tensor products of Pauli matrices, e.g. the three-qubit gate $X \otimes I \otimes Z$. Henceforth, we refer to the Pauli matrices σ^x , σ^y , and σ^z as X, Y, and Z, respectively, in the context of QEC. Every n-qubit quantum gate can be written as a unique linear combination of n-qubit Pauli gates (of which there are 4^n). The Pauli matrices act on the computational basis in the following way

$$X |0\rangle = |1\rangle, \qquad X |1\rangle = |0\rangle,$$

 $Z |0\rangle = |0\rangle, \qquad Z |1\rangle = -|1\rangle,$
 $Y |0\rangle = -i |1\rangle, \qquad Y |1\rangle = i |0\rangle.$ (2.24)

Other important gates include the phase gate R_{ϕ} and Hadamard gate, which respectively apply a specific ϕ -phase shift on the quantum state, and create a superposition:

$$R_{\phi} |0\rangle = |0\rangle, \qquad R_{\phi} |1\rangle = e^{i\phi} |1\rangle,$$

$$H |0\rangle = |+\rangle, \qquad H |1\rangle = |-\rangle,$$
(2.25)

where

$$R_{\phi} = \begin{pmatrix} 1 & 0 \\ 0 & e^{i\phi} \end{pmatrix}, \qquad H = \frac{1}{\sqrt{2}} \begin{pmatrix} 1 & 1 \\ 1 & -1 \end{pmatrix},$$
 (2.26)

and the states $|\pm\rangle = (|0\rangle \pm |1\rangle)/\sqrt{2}$ represent the equal superpositions shown in Fig. 2.1. An example gate which generates entanglement between two qubits is the controlled-NOT (CNOT) gate which negates the second qubit if the first qubit is in state $|1\rangle$, i.e.

CNOT
$$|0\rangle |\psi\rangle = |0\rangle |\psi\rangle$$
,
CNOT $|1\rangle |\psi\rangle = |1\rangle X |\psi\rangle$. (2.27)

The theory behind quantum computation relies upon access to gates from different levels of the *Clifford hierarchy*, defined by Gottesman and Chuang in Ref. [GC99] as

$$\mathcal{C}^{(k+1)} := \{ U | UPU^{\dagger} \in \mathcal{C}^{(k)}, \forall P \in \mathcal{P}_n \}$$
(2.28)

where $\mathcal{P}_n := \mathcal{P}^{\otimes n}$ is the *n*-qubit Pauli group defined at k=1. This definition classifies quantum gates based on their ability to map Pauli operators to other operators through conjugation. The second level in the hierarchy is known as the *Clifford* group, and includes the Pauli group, H and CNOT gates. In fact, the full single-qubit Clifford group is given by $\mathcal{C}^{(2)} = \langle H, S, \omega \rangle$, where $S = \sqrt{Z}$, and is promoted to the *n*-qubit Clifford group by addition of the CNOT in the generating set. The Clifford group is significant in fault-tolerant quantum computing, as it is composed of gates that map Pauli operators to Pauli operators, hence preserving the structure of the Pauli group under conjugation.

A set of quantum gates is called universal if any unitary transformation on an arbitrary number of qubits can be realised to an arbitrary precision by composing gates from this set. This can be, for example, the set of operations accessible using a quantum processor. It is known that complementing the single-qubit Clifford group with a gate in $\mathcal{C}^{(3)}$ such as the T gate,

$$T = \sqrt{S} = \begin{pmatrix} 1 & 0 \\ 0 & e^{i\pi/4} \end{pmatrix},\tag{2.29}$$

generates a group that is dense in SU(2), thereby providing a universal gate-set according to the Solovay-Kitaev theorem [Kit97; BK05]. Hence, any single-qubit unitary operator can be expressed in the form $O = C_n T C_{n-1} T ... C_1 T C_0$ where $C_i \in \mathcal{C}^{(2)} \ \forall i$, which can be optimised such as to minimise the number of T gates, also known as the T-count, using a reduction procedure [MA08; KMM12; Boy+00].

Universality of computation extends naturally to logic in qudit systems. For prime d, it is known that Clifford unitaries together with an arbitrary non-Clifford gate are sufficient for universal quantum computing [CAB12]. In the general case, earlier results proved that a set of single-qudit unitaries dense in SU(d), supplemented with a two-qudit gate that acts non-trivially on the full $d \times d$ Hilbert space, i.e. does not map separable states to separable states, is sufficient to approximate any unitary on n qubits [Vla02; Sch19; SK17]. The Clifford hierarchy in Eq. 2.28 also extends to qudit systems. The first level is the qudit Pauli group, generated by qudit analogues of the X and Z Pauli matrices known as the cyclic shift and clock operators, which act on the d-dimensional Hilbert space defining a qudit such that

$$\sigma |k\rangle = |(k+1) \bmod d\rangle, \qquad \tau |k\rangle = \omega^k |k\rangle,$$
 (2.30)

where $\omega = e^{2\pi i/d}$ is the primitive d-th root of unity. The gate σ effectively cycles through the d computational states, while τ generalises the phase application of the Pauli-Z operator. With this definition, we can identify the Clifford group as $\mathcal{C}^{(2)}$. Higher levels are of interest for any d-dimensional qudit system in order to achieve universality, and in particular, any gate from

the third level $\mathcal{C}^{(3)}$ supplementing the Clifford group generates a universal gate set. While in general for $k \geq 3$ the gate sets in the Clifford hierarchy do not form a group, the subset of diagonal operators $\mathcal{C}_d^{(k)} \subset \mathcal{C}^{(k)}$ does, making investigations for a T-gate qudit analogue tractable as shown in Refs. [HV12; CAB12; CGK17]. In particular, Cui et al. showed that a diagonal gate U in any level of the Clifford hierarchy for qudits of dimension d can be written as

$$U = \sum_{j \in \mathbb{Z}_d} \exp\left(2\pi i \sum_m \delta_m(j)/d^m\right) |j\rangle\langle j|, \qquad (2.31)$$

where $\delta_m(j)$ is a polynomial over \mathbb{Z}_d^m , and the level of the Clifford hierarchy containing U is given by the degree of $\delta_m(j)$ with the largest m [CGK17]. In Chapter 4, this definition will be useful to characterise a unitary operator acting on a qutrit subspace.

2.3 Quantum error correction

2.3.1 Correcting classical information

In any given system, transferring information from one party to another can incur errors on the message if the transfer medium, or communication channel, is subject to noise. The most general error is a single bit-flip, which enacts the operation

$$0 \leftrightarrow 1$$
.

One of the simplest noise channels, the binary symmetric channel, describes a scenario in which a bit-flip occurs independently on each bit of a string with a probability $p \in [0, 1]$ at each time step. Hence, the expected time for a bit to be corrupted is approximately $\mathcal{O}(1/p)$ time steps, with higher p leading to a greater likelihood of error in the transmission or storage process. To protect the information against such noise, it can be encoded redundantly using an error-detecting, or error-correcting code. For instance, one bit of information can be encoded

in two copies under the mapping

$$0 \leftrightarrow 00$$
, $1 \leftrightarrow 11$. (2.32)

The parity of a bit string $x_1x_2...x_n$ is defined as $P = \bigoplus_{i=1}^n x_i$, where \oplus is the XOR operation. An even and odd parity respectively refers to the values $P = 0 \mod 2$ and $P = 1 \mod 2$. Hence, 00 and 11 have even parity, but if an error occurs on one of the two copies, the pairs detected by the receiver will be either 01 or 10, which have odd parity and are therefore outside the *codespace* defined by Eq. 2.32.

An error is therefore detectable on this message. Beyond detection, an error-correction mechanism is required to ensure the recovery of the message. This is achieved by increasing the redundancy of the encoding. Error-correcting codes, such as the Hamming codes or Reed-Solomon codes, are widely used to improve reliability in digital communication systems and quantum information processing [Sha48; MS77; CS96].

An [n, k] error-correcting code C of length n over the binary field is a subset of \mathbb{F}_2^n that encodes k bits' worth of logical information into n physical bits, where n > k in order to introduce redundancy to protect the message from errors. Its codewords are elements $c_i \in C$ where the block length n refers to the size of a bit string. The code C is the image of an encoding map which maps a set of messages to the codewords of C. A code has two crucial properties. First, the encoding rate refers to the redundancy parameter given by the minimum number of bits necessary to convey the protected information, that is

$$R = k/n. (2.33)$$

This rate measures the efficiency of the code as its capacity to stock information. Secondly, its (minimum) distance d is defined as the minimum Hamming distance between two distinct codewords, where the Hamming distance between two binary strings c_1, c_2 of equal length is

the number of locations in the strings where their binary entries differ:

$$d = \min_{\substack{c_1, c_2 \in C \\ c_1 \neq c_2}} d(c_1, c_2), \qquad d(c_1, c_2) = |\{i | c_{1,i} \neq c_{2,i}\}|.$$
(2.34)

For example, the [3,1] repetition code encodes a single logical bit using the map

$$0 \to 000 , 1 \to 111.$$
 (2.35)

When a received word is outside of the codespace $\{000, 111\}$, one or more errors must have occurred. A decoder uses knowledge of the noise model, the structure of the code, and the received word, to predict which codeword was sent. In this case, the decoder can use a majority vote strategy, whereby the bit-string 010 (110) would be corrected to 000 (111). Given a prior error rate p, this reduces the overall logical error rate p_L to

$$p_L = p^3 + 3p^2(1-p). (2.36)$$

For higher n, p_L follows a binomial expression which is suppressed to zero as $n \to \infty$ for p below a threshold value.

A linear [n, k, d] code is typically defined as the row space of a generator matrix, allowing any codeword to be expressed as a linear combination of the rows of G. The code can also be defined by the kernel of a parity-check matrix H, which itself is the generator matrix for the code C^{\perp} dual to C, which consists of all vectors in \mathbb{F}_2^n orthogonal to the vectors in C. The following relations ensue:

$$GH^T = 0$$
, rank $G = k$, rank $H = n - k$. (2.37)

This formalism can also be generalised to alphabets larger than \mathbb{F}_2 , such as \mathbb{F}_q , but we exclusively consider binary codes in this thesis. Error-detection in a classical code is achieved by evaluating one or more parity checks. Each parity check corresponds to the sum over \mathbb{F}_2 of

the values of sets of physical bits. These checks are mathematically represented by the matrix H in Eq. 2.37, in which each row corresponds to a parity check on a subset of the n bits. A valid codeword satisfies the linear constraints imposed by these parity checks, i.e.

$$H\mathbf{c}^{\top} = \boldsymbol{\sigma} = \mathbf{0},\tag{2.38}$$

where σ is the *syndrome* vector. The syndrome indicates which parity checks are violated. Indeed, a bitstring **x** lying outside the codespace satisfies

$$H\mathbf{x}^{\top} = \boldsymbol{\sigma} \neq \mathbf{0},\tag{2.39}$$

which indicates that errors have corrupted the information. After detection, we must correct the errors to restore the original message. This task can be formulated as solving a linear system defined by Eq. 2.39. This problem, known as the decoding problem, is central to error correction. While Gaussian elimination provides an exact solution for many cases, practical decoding algorithms often aims to approximate optimal solutions efficiently. These may incorporate heuristics or probabilistic techniques to handle complexities arising from practical considerations [Gal63; MS77; FL97].

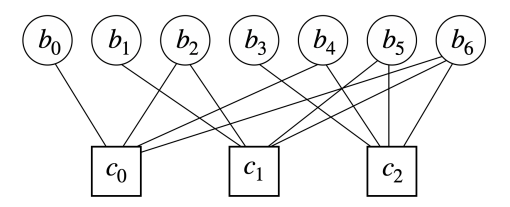


Figure 2.2: Tanner Graph of the 7-bit Hamming Code, where c and b respectively represent check and bit nodes. An edge is drawn between b_i and c_j if $H_{j,i} = 1$ in Eq. 2.40.

Among the simplest classes of error-correcting codes are the Hamming codes [Ham50]. These are are linear block codes with parameters $[n, k] = [2^m - 1, 2^m - 1 - m]$, where m = n - k is the number of parity-check constraints imposed on each codeword. The simplest case is the

[7,4] Hamming code, defined by the generator and parity check matrices:

$$G = \begin{bmatrix} 1 & 0 & 0 & 0 & 1 & 1 & 0 \\ 0 & 1 & 0 & 0 & 1 & 0 & 1 \\ 0 & 0 & 1 & 0 & 0 & 1 & 1 \\ 0 & 0 & 0 & 1 & 1 & 1 & 1 \end{bmatrix}, H = \begin{bmatrix} 1 & 0 & 1 & 0 & 1 & 0 & 1 \\ 0 & 1 & 1 & 0 & 0 & 1 & 1 \\ 0 & 0 & 0 & 1 & 1 & 1 & 1 \end{bmatrix}.$$
(2.40)

The *Tanner graph* is a graphical representation of a code consisting of a bipartite graph connecting bit nodes to check nodes, representing the parity check constraints, as shown in Fig. 2.2 [Tan81].

While classically one of the simplest ways to handle errors is through repetition, this strategy cannot be applied on quantum information due to the *no-cloning theorem*, which prohibits the exact duplication of an arbitrary unknown quantum state [NC10]. Hence, a more complex formalism is necessary to address quantum errors, as we discuss below.

2.3.2 Correcting quantum information

Quantum information is subject to decoherence, a phenomenon that corrupts quantum states and thereby undermines the reliability of quantum computation. To mitigate and control this effect, several strategies have been developed including quantum error mitigation [Cai+23], dynamical decoupling [VKL99] and quantum error correction (QEC). In this thesis, we focus on QEC, a method aimed at protecting logical quantum information by encoding it redundantly, in a computational subspace of a larger physical Hilbert space. A quantum error-correcting code involves the encoding of k logical qubits into a larger number of physical qubits n, and is defined as an isometry between two Hilbert spaces:

$$Q: \mathbb{C}^{2^k} \to \mathbb{C}^{2^n}$$
.

A QEC code is characterised by its parameters [n, k, d], where the code distance d is the minimum weight of an error configuration that can trigger a logical error, that is the smallest

number of qubits that must be affected to cause a logical error. The theoretical feasibility of QEC codes was established in seminal work by Shor and Steane [Sho95; Ste96b], and Gottesman's mathematical framework for *stabilizer codes* which greatly simplified the understanding and construction of quantum error-correcting codes [Got96].

2.3.3 Stabilizer codes

Stabilizer codes encompass a broad class of QEC codes and offer a structured framework for designing and analysing quantum codes with desirable properties. Consider an Abelian subgroup $S \subset \mathcal{P}_n$ of the *n*-qubit Pauli group $\mathcal{P}_n = \{\pm \mathbb{1}, \pm i\mathbb{1}, X, Y, Z\}^{\otimes n}$, generated by a set of elements $g_1, g_2, ... g_m \in \mathcal{P}_n$ known as the *stabilizer generators*, and satisfying $-\mathbb{1} \notin S$. A stabilizer code is defined as the subspace of states in \mathcal{Q} , where

$$Q = \{ |\psi\rangle \in \mathbb{C}^{2^n} \mid s |\psi\rangle = |\psi\rangle \ \forall s \in \mathcal{S} \}, \tag{2.41}$$

meaning that the states in the code space \mathcal{Q} are eigenstates of the elements $s \in S$ with a +1 eigenvalue. A stabilizer code defined on n qubits with m stabilizer generators encodes

$$k = n - m \tag{2.42}$$

logical qubits. The logical operators of a stabilizer code are elements of \mathcal{P}_n that commute with every stabilizer $s \in \mathcal{S}$ but that are not themselves in \mathcal{S} , i.e. elements of the normaliser

$$\mathcal{N}(\mathcal{S}) = \{ P \in \mathcal{P}_n \mid Ps = sP, \ \forall s \in \mathcal{S} \}$$
 (2.43)

which satisfy $\mathcal{N}(\mathcal{S}) \setminus \mathcal{S}$. These operators act non-trivially on the codespace while preserving its structure (i.e., they map codewords to other codewords). The distance of the code is

$$d = \min_{\mathcal{L} \in \mathcal{N}(\mathcal{S}) \setminus \mathcal{S}} |\mathcal{L}|, \tag{2.44}$$

where the weight | . | of an operator is the number of qubits on which it acts non-trivially.

The stabilizer generators of a quantum code are measured during information processing, and by design the measurement outcome of a stabilizer $s \in \mathcal{S}$ on a code state $|\psi\rangle$ must return the outcome +1. Errors on the physical qubits are modelled as elements of \mathcal{P}_n . An error $E \in \mathcal{P}_n$ is detectable if it anticommutes with at least one $s \in \mathcal{S}$ such that

$$s(E|\psi\rangle) = -E|\psi\rangle$$
,

in which case measuring s yields a -1 outcome, indicating the presence of the error. These observed values form a syndrome, where the term is borrowed from classical coding theory as defined in Sec. 2.3.1. The syndrome is then used to recover the encoded information by identifying the most likely error pattern, using a decoder.

A notable category of stabilizer codes is the Calderbank-Shor-Steane (CSS) codes [CS96; Ste96a]. A CSS code \mathcal{Q} is defined as the direct sum of two classical linear codes C_X and C_Z that work together to correct both phase-flip and bit-flip errors, i.e.

$$Q := C_X + C_Z. \tag{2.45}$$

The stabilizers of a CSS code are products of Pauli-X and Pauli-Z operators. A key condition for CSS codes is that the dual of C_Z satisfies $C_Z^{\perp} \subseteq C_X$, which ensures commutativity of the stabilizer generators and proper encoding of the logical qubits. Each of the classical codes is defined by a parity check matrix, H_X and H_Z respectively. This orthogonality condition then becomes

$$H_X H_Z^T = \mathbf{0}. (2.46)$$

A CSS code using n physical qubits encodes

$$k = \dim(C_X) - \dim(C_Z^{\perp})$$

$$= n - \operatorname{rank}(H_X) - \operatorname{rank}(H_Z)$$
(2.47)

logical qubits, and protects information up to the code distance $\min(d_X, d_Z)$, where

$$d_X := \min\{|\mathcal{L}_X| : \mathcal{L}_X \in C_X \setminus C_Z^{\perp}\},$$

$$d_Z := \min\{|\mathcal{L}_Z| : \mathcal{L}_Z \in C_Z \setminus C_X^{\perp}\}.$$
(2.48)

One of the simplest CSS codes is the Steane code with parameters [7,1,3] [Ste96b]. The Steane code is constructed by using two copies of the [7,3,4] Hamming code in Eq. 2.40, where each copy respectively defines the codes C_X and C_Z . This code can be represented using the graph in Fig. 2.4(1), where each stabilizer (face) represents a stabilizer generator supported on four qubits of the code. The Steane code encodes one logical qubit, and can correct up to $\lfloor (d-1)/2 \rfloor = 1$ bit-flip or phase-flip errors on any of the seven qubits.

In QEC, the syndrome information—whether an error occurred and its type—is extracted without directly measuring the data qubits. This preserves the encoded logical state, enabling error correction without collapsing the quantum state. This syndrome extraction is achieved by entangling the data qubits associated with a stabilizer generator to ancillary qubits, through a carefully designed *syndrome extraction circuit* [Den+02]. While this thesis does not explicitly utilise such circuits, it is implied that some of the codes and operations discussed are implemented in this way.

2.3.3.1 Noise models

The time evolution of a closed quantum system is described by unitary quantum operations. However, it is natural for quantum systems to interact with their environment, which leads to correlations building up between the two, regardless of whether the principal system and environment started in a product state or with initial correlations.

There exists a set of noise channels of relevance to quantum error correction, namely the bit-flip, phase-flip and depolarising channels. We start with a description of the latter, since we can obtain the remaining channels in its limits. The depolarising noise channel provides a simple yet generic description of the system-environment interaction. Since it simplifies noise

modelling, it is used as a benchmark for engineered quantum systems such as QEC codes. This is due to the fact that it describes how likely a quantum state is to evolve toward the maximally mixed state, and therefore directly relates to the decoherence process, i.e. how the state degrades over time. More complex noise channels, such as amplitude and phase damping, can then be considered as extensions or generalisations of the depolarising channel, incorporating additional phenomena. Given a multi-qubit quantum state described by a density operator ρ , the depolarising channel assumes that errors occur independently on each qubit, meaning that each qubit interacts with a different environment, and acts according to

$$\mathcal{E}(\rho) = (1 - p_x - p_y - p_z)\rho + p_x X \rho X + p_y Y \rho Y + p_z Z \rho Z. \tag{2.49}$$

This expression simplifies further when the error rates for each Pauli operator are equal, i.e. $p = p_x = p_y = p_z$, yielding the *uniform* depolarising noise channel

$$\mathcal{E}(\rho) = (1-p)\rho + \frac{p}{3}X\rho X + \frac{p}{3}Y\rho Y + \frac{p}{3}Z\rho Z. \tag{2.50}$$

Additionally, for this and any noise channel, if each qubit experiences the same error probabilities $p_{i \in \{x,y,z\}}$, the errors are said to be identically distributed. The bit-flip channel is found by setting the error probabilities in Eq. 2.49 to $p_y = p_z = 0$ and $p = p_x$ followed by renormalisation, i.e.

$$\mathcal{E}_{flip}(\rho) = (1 - p)\rho + pX\rho X, \qquad (2.51)$$

which describes the action of the bit-flip error. Similarly the phase-flip channel is derived by setting $p_x = p_y = 0$, $p = p_z$, and is related to the bit-flip channel through conjugation with the Hadamard operator in Eq. 2.26.

These noise models provide an appropriate error modelling framework to test the properties of a quantum error-correcting code, but they do not capture the full picture. However, it is known that correcting all weight $\leq t$ Pauli errors is sufficient to correct any arbitrary weight- $\leq t$ quantum error, as general noise processes can be expressed as linear combinations

of Pauli errors [Got97; NC10]. In practice, executing a code involves running a quantum circuit composed of quantum state preparation, single and multi-qubit operations, and measurements. A more comprehensive noise model to evaluate code performance is one in which errors occur randomly at each gate, including during measurement errors during the syndrome extraction. This model reveals how entangling gates can induce correlated failure mechanisms, causing errors to propagate in the circuit. This *circuit-level* noise model is commonly used as a benchmark for QEC codes and decoding algorithms [Fow+12a]. When relaxed to consider only Pauli errors, it is referred to as the *code capacity* error model, and *phenomenological* model when accounting for additional measurement errors [WHP03; Den+02]. Both variations are valuable for studying the impact of error patterns on the code performance.

2.3.4 Fault-tolerance

The QEC formalism offers a framework to transmit quantum information reliably. However, it is not sufficient to realise robust quantum computation for several reasons. First, quantum information encoded in a collection of qubits is vulnerable to errors even in an idle state due to environmental interactions. Additionally, QEC codes depend on single- and multi-qubit operations for error detection, recovery, and logical gates, which are inherently imperfect in practice. Another critical requirement of QEC is the preparation of fixed initial states and reliable quantum state measurement, both of which are prone to errors from imperfect protocols and faulty measurement apparatus. These challenges are taken into account within the broader theory of fault-tolerant quantum computation [KL97; KLZ98b; Den+02].

In this framework, quantum information is encoded using a QEC code, and the error correction procedure is applied frequently in order to prevent the accumulation of errors, thereby maintaining a low probability of code failure. Achieving this requires designing gates, state preparation protocols, and measurement circuits that minimize uncorrectable errors. A cornerstone of the theory of fault-tolerance is the *threshold theorem*, which informs us that arbitrarily long quantum computation is possible under realistic assumptions of the noise model undergone by the quantum computer. This theorem can be formulated in various ways

[AB97; KLZ98a; AGP05], and states that:

Theorem 2.1. A ideal quantum circuit consisting of N operations (including state preparation, unitary gates, measurements, and storage steps) can be simulated with a probability of error less than ϵ using a noisy quantum circuit. The noisy circuit will require $O(N \log^m(N/\epsilon))$ operations, where each operation introduces errors with probability p, provided that p is below a fixed threshold value p_{th} , and where m is a constant.

This theorem asserts that in order to simulate the ideal circuit with a low probability of error, the number of operations in the noisy circuit must increase, and importantly that if the error probability of quantum gates throughout a circuit remains below a critical threshold value p_{th} , errors can be corrected effectively, enabling successful and efficient quantum computation with arbitrarily high fidelity. This highlights the role of QEC in achieving fault-tolerance. This result also highlights the major need to reduce the physical error rates at the level of quantum computing hardware, design efficient QEC codes, and accurate classical post-processing algorithms for error correction to achieve fault tolerance. The value of p_{th} depends on the specific error correction or fault-tolerant method being used. Different QEC codes have different thresholds for noise tolerance, based on how effectively they can detect and correct errors. For instance, surface codes and colour codes are known to have high thresholds, as discussed in Sec. 2.3.6.2, meaning they can tolerate higher error rates.

Fault-tolerant protocols are typically discussed as a family since, as circuit size increases or the target logical error rate decreases, controlling error propagation requires a resource overhead that must scale efficiently. The threshold theorem guarantees that for a fault-tolerant family, this overhead grows polynomially with $\log{(N/\epsilon)}$. This theorem has been proven using various approaches including code concatenation [KLZ96; AGP05], statistical mechanics models of topological codes (discussed in Sec. 2.3.5), and quantum Low-Density Parity Check (qLDPC) codes with constant encoding rate [Got13].

2.3.5 Topological quantum codes

A prominent approach to designing QEC codes leverages the properties of topological manifolds, as first demonstrated by Kitaev in Ref [Kit01]. Topological quantum codes (TQCs) represent families of codes that integrate geometric locality, a crucial feature for addressing the locality constraints in various quantum computing architectures, using stabilizer operators that act through local interactions between qubits arranged on a lattice, while information is encoded in the system's global degrees of freedom. Formally, a TQC is defined as a local and translationally invariant stabilizer code. These characteristics can be described as follows.

Consider a set of qubits arranged in a D-dimensional array, with a stabilizer group S generated by local and translationally invariant operators (excluding boundaries and defects). In this setting, locality means that each stabilizer generator acts only on qubits that are nearby in the lattice. More precisely, there exists a constant w, independent of system size, such that

$$|s| < w \quad \forall s \in \mathcal{S}, \tag{2.52}$$

where |s| denotes the size of the smallest ball that contains all the qubits acted on by s, generally in terms of graph connectivity, or in this case specifically the geometric support of the operator s on the lattice. This notion of locality is used to define a *family* of stabilizer codes with members of arbitrary large distance. This property plays a central role in the construction and scalability of topological quantum codes. Moreover, the condition that $\mathcal{Z}(\mathcal{S}) \propto \mathcal{S}$ ensures that undetectable errors do not affect the encoded states, and $\mathcal{Z}(\mathcal{S})$ is the centraliser of \mathcal{S} [Bom13]. Here we review two examples of TQCs which will be relevant to our work.

2.3.5.1 The surface code

The toric code is a CSS stabilizer code originally defined on a two-dimensional lattice with periodic boundary conditions, as shown in Fig. 2.3(1) [Kit03a; Den+02]. Each edge e of the lattice hosts a single physical qubit. The stabilizer group of the code is generated by two type

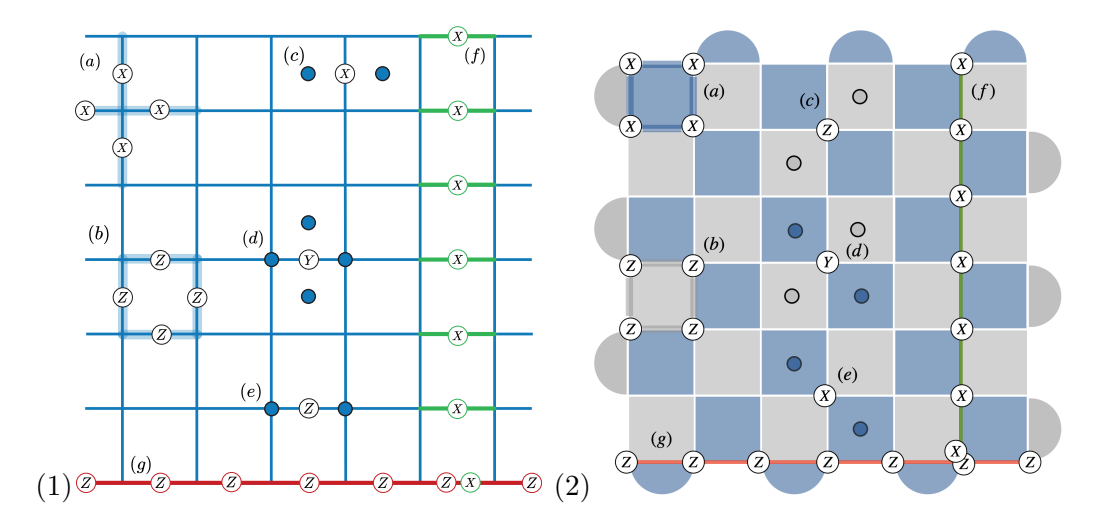


Figure 2.3: (1) The distance-7 unrotated surface code with qubits on the edges. (a) An X-type (star) parity check operator. (b) A Z-type (face) parity check operator. (c,d,e) Single-qubit X, Y and Z errors and their syndromes. (f) A vertical \overline{X} logical operator. (g) A horizontal \overline{Z} logical operator. (2) The rotated surface code. Both codes in (1) and (2) become toric when considering periodic boundary conditions.

of operators: vertex operators A_v and face operators B_f . The vertex operator is defined at each site v of the lattice, acting on the qubits located on the incident edges ∂v , and the face operator is defined for each face f such that the set ∂f of edges is adjacent to the face f, i.e.

$$A_v = \prod_{e \in \partial v} X_e, \qquad B_f = \prod_{e \in \partial f} Z_e. \tag{2.53}$$

The toric code encodes two logical qubits, one of which is defined by the logical operators \overline{X} and \overline{Z} in Fig. 2.3(1)(f) and Fig. 2.3(1)(g). We review this code in detail in Sec. 2.4.4.

The planar variant of the toric code, knows as the *surface code*, is defined on an open lattice with boundaries as shown in Fig. 2.3(1), when ignoring periodicity. In this code, the product of Z stabilizer operators gives rise to *smooth* boundaries at the top and bottom of the lattice, while the product of the X stabilizers creates *rough* left and right boundaries on the lattice. Since these boundary conditions emerge from essentially slicing the torus, only one logical qubit is encoded, with the logical Z and X operators respectively generated by

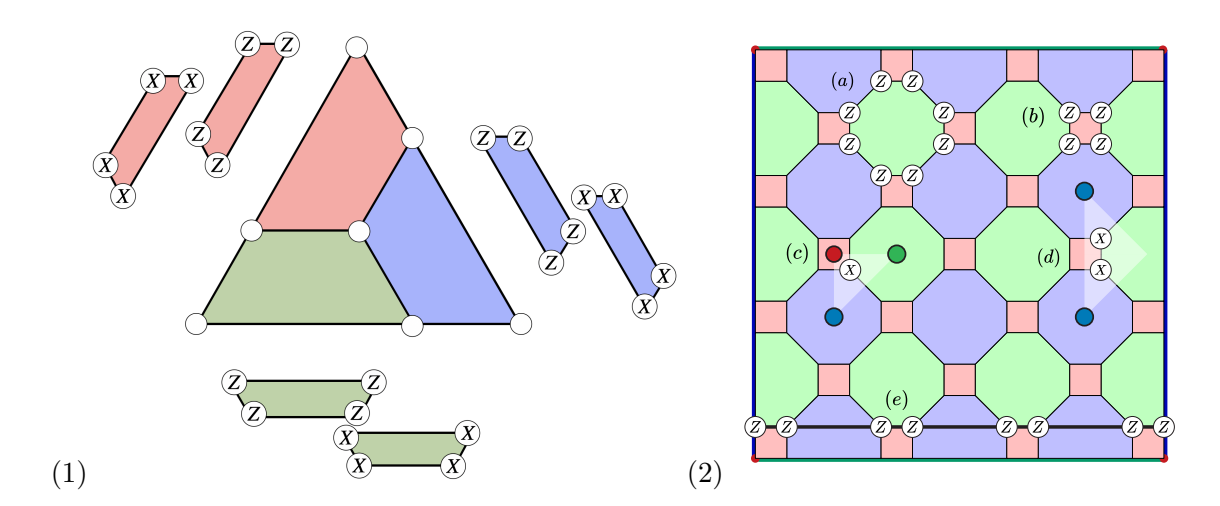


Figure 2.4: (1) The distance-3 colour code on a hexagonal lattice. (2) The distance-8 square-octagonal colour code with square boundaries. (a) An octagonal stabilizer generator. (b) A square stabilizer generator. (c) a single-qubit X-error. (d) A two-qubit X-error. (e) A horizontal logical operator.

strings of Pauli operators terminating at the rough boundaries and smooth boundaries, as shown in Fig. 2.3(1) [BK98; Den+02]. A Pauli error on a single qubit is detected by adjacent stabilizers as indicated in Fig. 2.3. In this thesis we also encounter the rotated surface code, a variant of the surface code where the lattice is rotated by $\pi/4$, as depicted in Fig. 2.3(2). The rotated surface code has parameters $[[n, 1, \sqrt{n}]]$, or k = 2 when toric boundary condition are considered [Wen03; NO09; Bev+19]. The qubits of the code are positioned on the vertices, and the stabilizers correspond to X and Z face operators, forming the characteristic chequerboard pattern visible in the figure.

2.3.5.2 The colour code

The colour code is a CSS topological quantum code introduced in Ref. [BM06]. In its twodimensional form, the physical qubits v occupy the vertices of a three-colourable lattice, with stabilizers associated with the faces on the lattice. The colour code was first introduced on a hexagonal lattice, as illustrated in Fig. 2.4(1) on a 7-qubit lattice. Note that this example also corresponds to the Steane code, which is the smallest instance in the family of quantum Hamming codes [Ste96a]. In fact, the H_X and H_Z parity check matrices of the 7-qubit colour code are both exactly that of the [7, 4, 3] Hamming code defined in Eq. 2.40. We also show the colour code defined on the regular square-octagonal lattice with square boundaries in Fig. 2.4(2). Each face f on the colour code supports two stabilizer operators

$$S_f^X = \prod_{v \in \partial f} X_v , S_f^Z = \prod_{v \in \partial f} Z_v$$
 (2.54)

where ∂f denotes the qubits on the boundaries of face f. A set of colour labels red, green and blue in the set $C = \{r, g, b\}$ can be chosen to label the objects on this code. For instance, each face is assigned a label $\mathbf{u} \in \mathcal{C}$ such that no two faces of same colour touch. The square-octagonal lattice in Fig. 2.4(2) features boundaries and corners highlighted with distinct colours. A colour label is attributed to a boundary such that the qubits lying on the boundary of colour $\mathbf{u} \in \mathcal{C}$ do not support a face of colour \mathbf{u} , meaning that there is no stabilizer operator of colour **u** that acts on the qubits of this boundary. A region of the lattice containing a single qubit, that is part of stabilizer operators of colour **u** only, is referred to as a corner of colour **u**. These two definitions imply that we find a **u**-coloured corner at a vertex (i.e qubit) where two boundaries of colours \mathbf{v} and \mathbf{w} overlap, where $\mathbf{u} \neq \mathbf{v} \neq \mathbf{w} \neq \mathbf{u}$, as illustrated by the four red-coloured corner vertices, and blue (resp. green) vertical (resp. horizontal) boundaries of the square-octagonal (4.8.8) colour code shown in Fig. 2.4(2). We note that a corner of colour **u** is also a member of its two adjacent boundaries, which must necessarily have colours v and w. The colour code in Fig. 2.4 encodes two logical qubits with an even code distance d, using $n = 2(d-1)^2 + 2$ physical qubits. We define representatives of the logical operators of the code as follows:

$$\overline{X}_{\mathbf{u}} = \prod_{v \in \delta \mathbf{u}} X_v, \qquad \overline{Z}_{\mathbf{u}} = \prod_{v \in \delta \mathbf{u}} Z_v$$
 (2.55)

where the product is taken over qubits lying on a boundary $\delta \mathbf{u}$ of colour $\mathbf{u} \in \{\mathbf{g}, \mathbf{b}\}$, and obey the commutation relation $\overline{X}_{\mathbf{u}}\overline{Z}_{\mathbf{v}} = -\overline{Z}_{\mathbf{v}}\overline{X}_{\mathbf{u}}$ if and only if $\mathbf{u} \neq \mathbf{v}$. Otherwise, the logical

operators commute. These represent strings terminating at opposite boundaries of the same colour, of which we show an example in Fig. 2.4(e). Pauli errors on the qubits of the code give rise to a syndrome, also referred to as a syndrome defect, as shown in Fig. 2.4(c) for a bit-flip error which is detected by the three adjacent Z stabilizers. A defect is attributed the colour from \mathcal{C} of the violated stabilizer it lies on. Unlike the surface code, a single error in the colour code generates three syndrome defects instead of two. This reflects the richness of the colour code Tanner graph, resulting in more sophisticated decoding requirements.

2.3.5.3 Relationship between toric and colour codes

A special relationship exists between the toric and colour code. Indeed, Yoshida and Bombin established that 2D stabilizer Hamiltonians with local interactions that obey certain symmetries—particularly translational symmetry—are equivalent to the toric code [Yos11; BDP12]. This equivalence implies that the ground states of the Hamiltonians reside in the same quantum phase. The latter is defined as a state of matter that arises from quantum mechanical effects, typically at near or absolute-zero temperature, and cannot be captured by classical order parameters [Sac23]. Typically, quantum phases exhibit nonlocal correlations, often characterised by entanglement, where the state of one part of the system depends on the state of another, regardless of distance.

It was shown in Ref. [CGW10] that two gapped ground states belong to the same quantum phase if and only if they are related by a local unitary evolution. From this follows the possibility to map one to the other using local unitary operations, up to the addition and removal of ancillary qubits. This equivalence was specifically derived in Ref. [KYP15] between the toric code and colour code, which we briefly describe in 2D here.

Consider the colour code defined on a lattice $\mathcal{L}_{c,c}$ using the set of stabilizer generators $C_{c,c,c}$, without boundaries, as shown in Fig 2.5(a). There exists a local Clifford unitary operator \mathcal{U} that decouples the colour code into two lattices \mathcal{L}_{c_1} and \mathcal{L}_{c_2} where $c_1, c_2 \in \{\mathbf{r}, \mathbf{g}, \mathbf{b}\}$ such that

$$U[C_{c.c.}(\mathcal{L}_{c.c.})]U^{\dagger} = C_{t.c.}(\mathcal{L}_{c_1}) \otimes C_{t.c.}(\mathcal{L}_{c_2})$$
 (2.56)

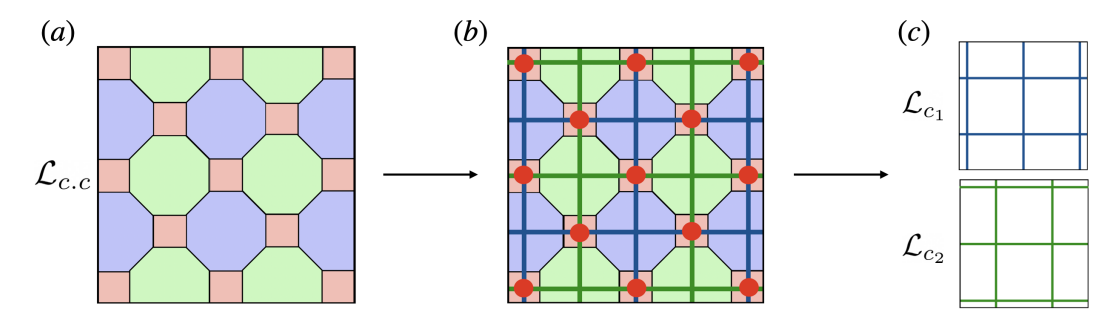


Figure 2.5: Schematic of the mapping from the colour code in (a) to two copies of the toric code in (c), where the coupling between the lattices in shown in (b).

where we can choose the product operator

$$U = \bigotimes_{f \in \mathcal{F}} U_f, \tag{2.57}$$

where \mathcal{F} is the set of all faces in $\mathcal{L}_{c.c}$ of colour $c_3 \in \{\mathbf{r}, \mathbf{g}, \mathbf{b}\}$, such that $c_1 \neq c_2 \neq c_3$, and U_f is a Clifford unitary acting on the qubits in \mathcal{F} . Performing this tensor product of local unitaries can be interpreted as shrinking the faces of colour c_3 on $\mathcal{L}_{c.c.}$, for $c_3 = \mathbf{r}$ w.l.o.g., that transforms the stabilizer generators of $C_{c.c.}$ such that every Z or X operator is mapped onto a stabilizer supported either on a face of colour c_1 or c_2 , specifically **g** or **b** in Fig. 2.5(b). Two lattices emerge from this local deformation of the colour code, \mathcal{L}_{c_1} and \mathcal{L}_{c_2} , that define two disentangled toric codes as depicted in Fig. 2.5(c). The number of logical qubits encoded in the colour code on a torus is the difference between the number of physical qubits and the number of linearly-independent stabilizer constraints. This is exactly k = 4, consistent with the topology and the tri-valent structure of the lattice [CT16]. A local unitary as described above maps the four qubits of each r stabilizer onto two qubits of the toric codes defined on \mathcal{L}_{c_1} and \mathcal{L}_{c_2} respectively. For instance, On an $L \times L$ torus, the 4.8.8 colour code contains $8L^2$ qubits and $8L^2 - 4$ linearly independent stabilizers, resulting in the parameters [[8L², 4, L]]. The lattice includes $2L^2$ red faces supported on the $8L^2$ qubits, with both X- and Z-type check defined on each face. The local unitary mapping the four qubits at the vertices of a red face onto two qubits, respectively belonging to \mathcal{L}_{c_1} and \mathcal{L}_{c_2} , creating two toric code layers, each using $2L^2$ physical qubits. This means that the logical qubits from the colour code split into two pairs of logical qubits respectively defined on each $[[2L^2, 2, L]]$ toric code. This mapping between the stabilizer groups is rigorously described in Ref. [KYP15], and generalises to other geometries, the higher-dimensional toric and colour codes, with and without boundaries. We exploit this structural connection in the context of decoding in Chapter 5.

2.3.6 Decoding quantum codes

Quantum error-correcting codes protect information by encoding it into logical degrees of freedom resilient to noise. For this purpose, they rely on a recovery process that involves solving a decoding problem.

2.3.6.1 The quantum decoding problem

During computation, noise generates errors, which are identified by measuring the stabilizer generators of the code. This produces syndrome data represented by a binary vector $\sigma \in \mathbb{F}_2^m$, where each bit corresponds to the eigenvalue $o \in \{-1, +1\}$ of a stabilizer measurement (+1 is mapped to bit 0 and -1 to bit 1). Consider an error E on the n physical qubits of the code, which triggers the syndrome $\sigma(E)$. Analogously to the classical case (cf. Sec. 2.3.1), a decoder is a classical algorithm that takes as input $\sigma(E)$, and prior knowledge of the noise model, to determine which physical errors occurred. The decoder outputs a recovery operator $C \in \{1, X, Y, Z\}^{\otimes n}$ such that the syndrome of the correction satisfies $\sigma(C) = \sigma(E)$. Applying this operator restores the state to the code space, and if successful, ensures $CE |\psi\rangle = |\psi\rangle$, thereby recovering the original quantum state. If the error and correction operators differ by an element of the stabilizer group, i.e. C' = sE for $s \in \mathcal{S}$, then

$$C'(E|\psi\rangle) = s|\psi\rangle = |\psi\rangle$$
 (2.58)

for a code state $|\psi\rangle$. This property follows from $\sigma(E) = \sigma(C) = \sigma(C')$, and defines an equivalence of Pauli error (and correction) operators. Hence, the decoder only needs to

output a correction which is in the same equivalence class as the error E affecting the code state.

The decoding problem can be optimally solved using a Maximum likelihood Decoder (MLD). In classical coding theory, the MLD finds the codeword that maximises the likelihood of the observed outcome, given an underlying noise model. MLD works similarly in QEC, in that it attempts to find the encoded code state that maximises the probability of successful recovery, conditioned on the syndrome, and under a given noise model (usually a stochastic Pauli noise channel) [Den+02; BSV14]. An exact implementation of MLD comes with high computational complexity, due to the need to evaluate the sum of probabilities of all error configurations, for each logical equivalence class. Moreover, this computation scales exponentially in the number of logical qubits, and must be repeated for each syndrome. Hence, this problem is generally approximated to balance accuracy and speed. Approximate polynomial-time algorithms, including renormalisation group decoders [DP10] and neural network-based decoders [TM17; CR18; Bai+19; Bau+23b], are commonly used. Moreover, practical decoders must be capable of handling more complex noise models, including measurement and gate errors, to maintaining the advantage of QEC codes in a fault-tolerant setting.

Decoders must also be efficient in real-time decoding during quantum computation, where syndrome data accumulates and needs decoding at each round of error-correction. Efficient and practical decoding strategies have been developed by tailoring decoding methods to specific types of codes, such as the minimum-weight perfect matching (MWPM) decoder [Den+02] for the surface code, and approximations like the Union-Find decoder [DN21]. Rather than finding the most probable error configuration, these aim to minimise the total sum of error probabilities of the corrections needed to match the syndrome. For more general QEC codes, belief-propagation (with ordered statistics decoding) is used—a probabilistic iterative algorithm that estimates marginal probabilities of different error configurations based on the syndrome data [Rof+20; PK21].

At sufficiently low error rates and with an appropriate error model, the probability of a decoder finding a successful correction rapidly approaches 1 as the code distance increases.

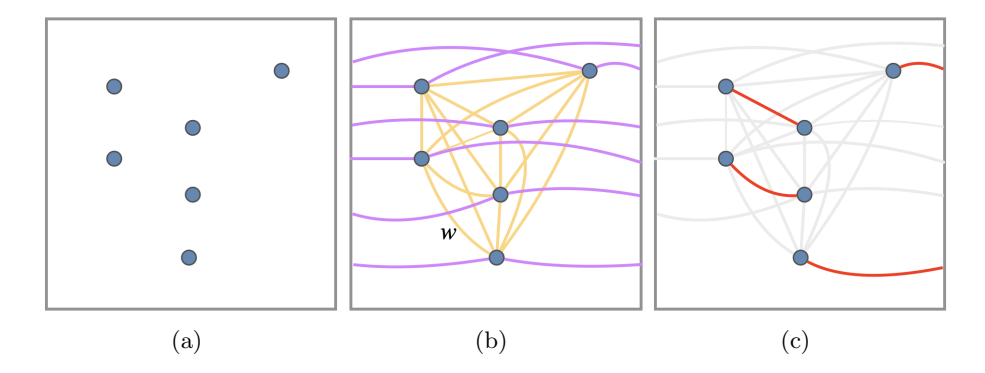


Figure 2.6: A schematic of the minimum-weight perfect matching decoder. (a) The MWPM decoder sees a graph where nodes are -1 syndrome measurement outcome locations (b) A simple implementation of the MWPM decoder builds a complete graph weighted by length of the (weighted) shortest path between two nodes on the graph. The purple edges are matched to a virtual node when the code has open boundaries. (c) The result after finding the minimum-weight subset of edges is shown in red, and the remaining edges are shaded.

The threshold and sub-threshold scaling of the success rate both depend on the noise model incurred. MLD can be mapped onto sampling from the partition function of a disordered classical statistical-mechanics model (e.g. percolation theory or random-bond Ising models), where the behaviour of errors on the code resembles that of spin configurations leading to frustrated terms in a classical Hamiltonian [Den+02]. The decoder thus seeks to find the ground state of a system with noise or disorder, and a phase transition occurs at the threshold (cf. Theorem 1 in Sec. 2.3.4). Below this error rate, the system is "ordered", and error-correction succeeds with high probability. Above the threshold, the system becomes disordered, increasing the likelihood of logical errors. Increasing code distance (akin to increasing system size) enhances error suppression, much like how an ordered phase stabilises below the critical temperature in a thermodynamic system [CF21].

2.3.6.2 Minimum-weight perfect matching

The minimum-weight perfect matching (MWPM) decoder is one of the most well-studied decoding algorithms, and the most successful decoder implemented on the surface code

[Den+02]. It employs a combinatorial optimisation algorithm to find the most likely set of errors given some syndrome data. A perfect matching in a graph G = (V, E) is a subset $M \subseteq E$ where every vertex $v \in V$ is incident to exactly one edge in M. In other words, every vertex is paired with exactly one other vertex, and no vertex is left unmatched. A graph that has a perfect matching must have an even number of vertices, as each edge in the matching covers exactly two vertices. The Tanner graph of the surface code satisfies this condition, and in general, it is this fundamental structure—namely, a parity conservation law in the syndromes—that makes this decoding problem suitable for matching-based decoding [Bro22].

Consider an error E supported on |E| qubits on the surface code, and assumed to be Pauli, which gives rise to the syndrome σ upon measurement. The MWPM decoder is designed to find the lowest-weight error configuration that generates σ , and returns a correction operator based on this identification. The measured syndrome discloses information on the boundary of the error strings, as shown in Fig 2.6(a). Assuming errors are independently and identically distributed, the probability of an error string E occurring is determined by the probabilities of individual errors in the operator, i.e.

$$p(E) = (1-p)^{n-|E|} p^{|E|}$$
(2.59)

$$= (1-p)^n \left(\frac{p}{1-p}\right)^{|E|} \tag{2.60}$$

where p is the underlying physical error rate, assumed constant for all qubits, and for all error types. The most probable error is one that maximises the likelihood p(E), and equivalently minimises |E|. Consider a fully connected graph with vertices given by the locations of the syndromes, as shown in Fig. .2.6(b). Each edge is assigned a weight given by the Manhattan distance between the vertices it connects. Note that when the lattice has open boundaries, matching a syndrome to the boundary is represented by an edge connecting the syndrome to a virtual node located at the boundary, as indicated in Fig. 2.6(c). The weight of the error E can be expressed as the sum of the weights of edges along the path connecting the

corresponding syndromes. We can re-express Eq. 2.60 as

$$p(E) = (1-p)^n \prod_{e \in \text{edges}(E)} \left(\frac{p}{1-p}\right)^{|e|}.$$
 (2.61)

A solution is obtained by maximising any function proportional to p(E). Indeed, since maximising p(E) is equivalent to maximising $\log p(E)$, and the logarithm is a monotonic function, we can instead minimise the negative log-likelihood, i.e. given by

$$\log p(E) \propto -\sum_{e \in \text{edges}(E)} |e| \log \left(\frac{1-p}{p}\right)$$
 (2.62)

which translates into minimising the total path weight. Thus, maximising p(E) corresponds to finding a set of edges that connects the syndromes in pairs with minimal weight, i.e. a minimum-weight perfect matching. This problem was first introduced by Edmonds in 1965 then solved by the Blossom algorithm [Edm65; Kol09], with a worst-case runtime of $\mathcal{O}(n^4)$. For the surface code under bit-flip (or phase-flip) noise, MWPM achieves the high threshold of 10.3% [Wan+09], just below the estimated $\sim 10.9\%$ from the phase transition of the spin model associated with the toric code and its decoder threshold [MC02; HPP01]. The colour code is also known to admit comparatively high thresholds [KBM09; Kat+10; SB22; GJ23].

State-of-the-art implementations of MWPM achieve an expected runtime that is linear in the number of graph nodes below threshold and under stochastic noise [HG23]. In general, MWPM tolerates a large rate of errors, particularly when errors are identically and independently distributed. It also performs well in the presence of measurement errors and circuit-level noise, with thresholds around 3% and $\sim 1\%$ respectively for the surface code [WHP03; Wan+09; Fow+12a]. It is important to note that the MWPM decoder operates by separately matching the syndromes from X and Z stabilizer measurements on decoupled matching graphs, treating the errors as uncorrelated. Additional strategies must then be adopted to address Y-type correlations which simultaneously affect X and Z stabilizers (since Y = iXZ) as shown in Fig. 2.3(1)-(d). These include two-stage decoding, where the X

graph is decoded first, and the solution is used to re-weigh the edges of the graph before decoding the Z syndrome graph [Wan+09], or belief-matching which employs the BP algorithm to weigh the edges before calling MWPM [CA18; Hig+23]. The MWPM decoder has been applied to the colour code, surface codes on hyperbolic geometry, fracton codes and more [DT14; Bre+17; BW20]. It has also been conjectured that MWPM could be generalised to decode arbitrary topological and qLDPC codes[BW20; Bro22].

2.3.7 Fault-tolerant logic and code deformations

2.3.7.1 Fault-tolerant gates

In Sec. 2.2.2 we reviewed the universal quantum computational model, then introduced QEC codes as a means to achieve fault-tolerant computation. Logical gates act on logical qubits to process quantum information. To ensure fault-tolerance beyond the state encoding, physical errors must propagate throughout the computation in a controlled and harmless fashion. In principle, fault-tolerance requires that a logical gate U be implemented by a constant-depth quantum circuit to prevent excessive error spread throughout the system [Got13]. Additionally, geometric locality in the circuit simplifies its physical implementation and control of the error propagation [PY15].

Given two quantum codes C_1 and C_2 , respectively defined by the stabilizer groups S_1 and S_2 , using the same number of qubits n and encoding the same number of logical qubits k, the set of Clifford operators that transform these codes such that $US_1U^{\dagger} = S_2$ defines operations on the code specified by the description of U. For instance, when $C_1 = C_2$, and $U = u^{\otimes n}$ is a tensor product of local single-qubit unitaries, U is referred to as a transversal operation on the code [Sho96]. Transversal operations are the simplest fault-tolerant operations, as local errors on a physical qubit do not propagate to other qubits, making them significant in the context of error correction. However, there are two important caveats: transversal operations are not guaranteed to preserve the codespace or implement a valid logical operation, and the Eastin-Knill theorem [EK09] shows that no quantum code can have both transversal and

universal gate sets.

A promising technique for achieving universal fault-tolerant quantum computation is magic state distillation (MSD) [BK05]. This method leverages resource states and stabilizer operations to enable the execution of non-Clifford gates, which are crucial for universal quantum computation. The input states, known as magic states, can be produced via MSD and subsequently injected (i.e. teleported) into the quantum code for processing.

However, the production of these resource states and Clifford operations incurs significant costs. MSD typically involves a trade-off between fidelity and resource consumption, as higher-quality magic states require greater numbers of noisy initial states and distillation rounds. Each round amplifies the fidelity of the magic states at the expense of increased operational overhead. Furthermore, these processes are highly sensitive to errors, as imperfections in the input magic states or the operations can propagate and degrade the overall performance of the protocol. The cost is exacerbated by the non-zero failure rates of the Clifford operations used in the distillation process, particularly due to two-qubit gate errors. Efficient MSD protocols and alternative techniques are being developed to mitigate these costs [CC19; WHY24; GSJ24; Rod+24].

2.3.7.2 Code deformations

Code deformation is an alternative method for operating on a quantum code fault-tolerantly. This method consists of a sequence of operations that modifies a quantum code by changing some or all of the stabilizer generators of its stabilizer group. This can be used to initialise, transform and measure the logical qubits of the code, and typically proceeds by incremental changes to the codespace [BM09b; Vui+19].

Here, we focus on code deformations via unitary transformations, under which the stabilizer group S_1 defining a code C_1 changes as follows

$$US_1U^{\dagger} = S_2, \tag{2.63}$$

where generally only a small subset of generators of S_1 are acted on non-trivially. If a unitary U transforms a code such that $C_1 = C_2$, the logical operators transformed by U reveal the unitary transformation applied to the encoded logical qubits, up to a phase. This evolution is given by:

$$UX_{i}U^{\dagger} \sim_{\mathcal{S}} \prod_{j} X_{j}^{a_{ij}} Z_{j}^{b_{ij}}$$

$$UZ_{i}U^{\dagger} \sim_{\mathcal{S}} \prod_{i} X_{j}^{c_{ij}} Z_{j}^{d_{ij}}$$

$$(2.64)$$

$$UZ_iU^{\dagger} \sim_{\mathcal{S}} \prod_j X_j^{c_{ij}} Z_j^{d_{ij}} \tag{2.65}$$

where $a_{ij}, b_{ij}, c_{ij}, d_{ij} \in \mathbb{Z}_2$ and $\sim_{\mathcal{S}}$ indicates equivalence up to a stabilizer $s \in \mathcal{S}$. Applying a code deformation involves a sequence of unitaries $U = U_l...U_1$ which map the code onto itself. Such a sequence can give rise to logical Clifford gates acting on the encoded qubits. More generally, since a code can always be expanded by adding ancillary initialised qubits, code deformation extends to cases where the initial and final number of qubits differ. The number of encoded qubits can also vary between the original and transformed codes, in which case, the condition in Eq. 2.63 cannot be enforced, as it corresponds to deformations that change the topology of the code.

Let C_1 encode k qubits, and C_2 encode k+1 qubits. It follows from Eq. 2.47 that $|S_2|$ = $|\mathcal{S}_1|-1$. The Clifford operators U which transform encoded states to encoded states satisfy $S_2 \subsetneq US_1U^{\dagger}$. Upon transformation, US_1U^{\dagger} is a subset of the normaliser of S_2 , generated by

$$\{S_i\}_{i=1}^{n-k} \cup \{L\}$$

where $L \in \mathcal{N}(S_2) \setminus \mathcal{S}_2$ is a logical Pauli operator initialised with eigenvalue +1 after U is applied, meaning that the code deformation introduces a logical degree of freedom initialised in a specific state. In Chapter 3, we make use of several logical qubits introduced in this way. Additionally, degrees of freedom can be removed via code deformation by considering the reverse scenario, where C_1 encodes k qubits and C_2 encodes k-1 qubits. In this case, a logical Pauli operator of C_1 is mapped onto a stabilizer $s \in \mathcal{S}_2$ by the action of U, and is effectively measured, which reduces the number of logical qubits in C_1 by one. The degrees of freedom of this qubit map to the syndrome measurement outcomes of a stabilizer $s \in S_2$.

Code deformations on the surface code have been extensively studied, first introduced in Ref. [Den+02] as a means to enlarge the code, and extended to apply fault-tolerant logic on the code. These deformations modify the stabilizer group that defines the surface code in a way that reshapes its lattice geometry. Indeed, given a surface code defined on a fixed underlying lattice, code deformations can alter the boundaries of the code, introduce non-trivial cycles by puncturing the lattice, and add defect lines that drastically reconfigure the stabilizer generators [BM09b]. Code deformations can also move these defects on the lattice to apply operations on the codespace fault-tolerantly [Bro+17], which we explore in Chapter 3.

Undesired measurement outcomes can be corrected by direct application of a suitable unitary operator, or by applying many rounds of QEC to infer and correct the errors that occurred when measuring the logical qubits. Therefore, in practice, code deformations can be interleaved with QEC, provided the error-correction procedure succeeds with high probability, as is the case with the surface code.

2.4 Topological phases and quantum computing

Topology is pervasive in the description of certain quantum states. As we briefly touched upon in Sec. 2.3.5, a topological phase of matter (TPM) is an umbrella term encompassing many-body quantum states that fundamentally differ from classical matter. Indeed, these quantum states are not described by the Landau theory of phase transitions, i.e. by spontaneous symmetry breaking [Lan+37], but rather by topological invariants. This means that they are not simply described by local order parameters, such as magnetisation, but rather global characteristics [Tho+82]. For example, consider a collection of bosons or fermions confined to a (2+1)-dimensional manifold. At zero-temperature, this system is in a (2+1)-dimensional topological phase of matter, if it is described by a (2+1)-dimensional unitary spin topological quantum field theory (TQFT) [Wit88; Pac12]. In the following, we will consider states which

behave according to the laws of TQFTs in the low energy limit, and review how these systems provide a natural way to encode, manipulate, and transmit quantum information.

2.4.1 Topological order

Topological order (TO) refers to a type of quantum order in many-body systems that cannot be characterised by local order parameters or spontaneous symmetry breaking. A system is said to exhibit topological order when it possesses a degenerate ground state manifold that is robust against local perturbations and when its low-energy excitations obey non-trivial braiding statistics. These features typically emerge in systems with a finite energy gap Δ separating the ground state from excited states. That is, there exists a non-zero minimum energy required to excite the system, even in the thermodynamic limit. This energy gap provides topological protection, meaning that local perturbations to the system do not lift the groundstate degeneracy nor cause transitions between the ground and excited states. Physically, this implies that certain global properties of the system—such as ground state degeneracy depending on the topology of the underlying manifold—remain invariant under smooth, continuous deformations. This is analogous to how continuous deformations preserve the topological properties of a surface. For example, in the case of topological insulators, variations in pressure or electric fields leave the topological properties of the state unchanged [HK10]. In practice, the protection becomes more effective as system size increases, often scaling such that the energy splitting between degenerate ground states decays exponentially with system size L, i.e. $\delta E \propto \exp^{-L/\xi}$ where ξ is a length characterising the spatial decay of correlations in the system. The size L is the characteristic length scale of the system, such as the lattice constant, or the length of a topological nanowire [LSD10]. Importantly, this is not the bulk energy gap Δ , but rather the finite-size splitting between the ground states.

Another defining feature of TO is the presence of emergent localised quasi-particles known as anyons [Kit06]. In classical mechanics, exchanging two identical particles does not alter the state of the system. However, in quantum mechanics, particle exchanges lead to far richer behaviour. In three-dimensional quantum systems described by a wavefunction $|\psi\rangle$, such an

exchange results in a sign change, i.e.

$$U|\psi\rangle = e^{i\theta}|\psi\rangle, \qquad (2.66)$$

and $\theta=0$ or $\theta=\pi$ correspond to the exchange statistics of bosons and fermions, respectively. In contrast, anyons emerge in topologically ordered phases and can exhibit any exchange statistics. This generalisation allows for a continuous spectrum of exchange behaviours beyond the binary classification of bosons and fermions, and even extends to unitary matrices instead of simple phases in Eq. 2.66. Importantly, while TO in a material implies it is a TPM, the converse is not always true. TO specifically relates to the existence of anyons within the system. Moreover, two gapped states of matter belong to the same topological phase if and only if their Hamiltonians can be continuously deformed into each other without closing the excitation gap. This invariance under gap-preserving transformations is fundamental to the classification of topological phases. The classification and study of topologically ordered systems remain active areas of research due to the complexity and richness of their structures [Yos11; Wen13; ABK21].

2.4.2 Algebraic properties of anyons

Anyonic models are mathematical structures that describe the quasiparticle excitations in topologically ordered systems. Formally, they are described by a unitary braided fusion category C, whose simple objects $a, b, c... \in C$ label the distinct anyon types, each associated with a topological charge [Kit06]. The set includes a unique trivial (or vacuum) object $\mathbf{1} \in C$ which acts as the identity under fusion. Anyons obey rules given by a unitary braided tensor category [Wan10]. Specifically, the charges of anyons obey an associative fusion algebra, described by the fusion rule:

$$a \times b = \sum_{c \in C} N_{ab}^c c \tag{2.67}$$

where the $N_{ab}^c \in \mathbb{Z}_{\geq 0}$ are the fusion multiplicities. These integers indicate the number of different ways anyons of type a and b can combine to form an anyon of type c. The fusion process must be finite ensuring that for any fixed a and b, the sum $\sum_c N_{ab}^c$ is a finite integer. Furthermore, the associativity of the fusion algebra imposes the condition

$$\sum_{e} N_{ab}^{e} N_{ec}^{d} = \sum_{f} N_{af}^{d} N_{bc}^{f}.$$
(2.68)

This associativity ensures the consistency of combining anyons in different orders. To each fusion product, we associate an N_{ab}^c -dimensional vector space V_{ab}^c and, in the time-reversed picture, a splitting space V_c^{ab} defining its dual. The vacuum charge 1 fuses trivially, meaning $N_{a1}^c = N_{1a}^c = \delta_{ac}$. For every $a \in C$, there exists a conjugate particle $\bar{a} \in C$ such that a and \bar{a} fuse trivially, i.e. $a + \bar{a} = 1$. The quantum dimension d_i of an anyon $i \in C$ is the dimension of the Hilbert space associated with its fusion, and need not be an integer, which is a hallmark of non-Abelian anyons, characterising a fusion space that grows non-trivially with the number of anyons. In fact, anyons are classified as Abelian if their fusion space is one-dimensional $(d_i = 1)$, meaning the fusion outcome is deterministic, and independent of prior operations. In contrast, non-Abelian anyons have fusion outcomes that are not uniquely determined, as their fusion can result in a superposition of different anyon species. This multiplicity $(d_i > 1)$ reflects intrinsic degrees of freedom associated with the possible fusion outcomes. Moreover, the relation

$$d_a d_b = \sum_c N_{ab}^c d_c \tag{2.69}$$

ensures that the quantum dimensions form a one-dimensional representation of the fusion algebra [Wan10]. The total quantum dimension of an anyon model is given by $\mathcal{D} = \sqrt{\sum_i d_i^2}$ where $i \in C$, and governs, for instance, the topological entanglement entropy and the scaling of the Hilbert space dimension in the thermodynamic limit. An important result is that the dimension M_n of the Hilbert space \mathcal{H}_n , obtained by the fusion of n anyons of species i, corresponds to the number of possible fusion outcomes. In the limit of large n, this scales

exponentially as $M_n = \dim(\mathcal{H}_n) \sim d_i^n$. This scaling is an approximation. The exact dimension depends on the detailed structure of the fusion algebra and interactions between the anyons. Consider a fixed collection of n anyons that undergo successive fusions, ultimately resulting in either a single final state or multiple states spanning a higher-dimensional Hilbert space \mathcal{H}_n . If the same final state can be achieved through a different sequence of fusions, then these two fusion paths are related by a change of basis in \mathcal{H}_n known as an F move, as illustrated in Fig. 2.7(a) [Pac12]. This relationship can be expressed as:

$$|(a \times b) \to d; (d \times c) \to f\rangle = \sum_{e} (F_{abc}^f)_e^d |(b \times c) \to e; (a \times e) \to f\rangle. \tag{2.70}$$

Anyon models are also characterised by their exchange statistics, which determine a set of braiding rules. For a fixed fusion channel $|a, b \to c\rangle$, the exchange of anyons a and b is described by the evolution R_{ab}^c , known as an R-move, or a half-twist of anyon c as shown in Fig. 2.7(b). This exchange introduces a global phase factor

$$R_{ab} | a \times b \to c \rangle = e^{i\theta_{ab}} | a \times b \to c \rangle.$$
 (2.71)

A matrix R can be constructed with diagonal entries given by the phases obtained from all possible fusion outcomes of $a \times b$. If the result of $a \times b$ is a superposition of multiple fusion outcomes, then the exchange is affected by F-moves and is described by a braiding operator. This is a unitary operator B corresponding to a representation of the braid group B_n on n strands representing the anyons in (1+1)D. A braid interlaces these strands, as shown in Fig. 2.8, and can be expressed as a product of elements in the generating set of B_N . Since this braiding is dependent on F moves, the B matrix is generally non-diagonal. For example, consider the fusion of anyons a, b and c as depicted in Fig. 2.7(a) with f as the total fusion outcome. The braiding of the anyons a and b is given

$$B_{ab} = F_{acb}^{f^{-1}} R_{ab} F_{acb}^f (2.72)$$

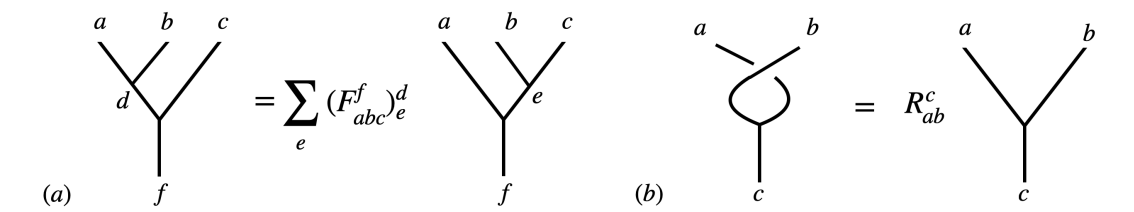


Figure 2.7: (a) An F move is a unitary operator which transforms between two fusion basis states representing different orders of fusions of anyons a, b and c to obtain outcome f, where time flows downwards and d and e are intermediate anyons. The index e on the right hand side runs over all possible outcomes of the fusion $b \times c$. (b) An R move represents the clockwise exchange of anyons a and b leading to fusion outcome c. This exchange is equivalent to a half-twist of anyon c, and generates an overall phase R_{ab}^c .

where the F-matrices depend on the intermediary fusion states and final fusion outcome. This equation can be interpreted as a change of basis in which a and b are fused first, followed by an R-move, and finally a return to the original basis. The braiding operation alters the phase or mixes fusion outcomes in a manner that preserves the topological properties of the anyons.

These relations are summarised by the *pentagon* and *hexagon* equations:

$$\sum_{n} (F_{efc}^{k})_{a}^{d} (F_{agh}^{k})_{b}^{c} = \sum_{i} (F_{fgh}^{d})_{i}^{c} (F_{eih}^{k})_{b}^{d} (F_{efg}^{b})_{i}^{a}$$
(2.73)

$$\sum_{b} (F_{fge}^{h})_{b}^{c} R_{eb}^{h} (F_{efg}^{h})_{a}^{b} = R_{eg}^{c} (F_{feg}^{h})_{a}^{c} R_{ef}^{a}$$
(2.74)

named after the geometric configuration they inherit from their representation as commutative diagrams (cf. Figs. 4.6&4.7 in Ref. [Pac12]). These equations become trivial for Abelian anyons, since the fusion space is one-dimensional, and exchange operators are simply scalars. The physics of these systems is described using a category-theoretic formalism in the mathematical literature [Wan10; Bar+19].

2.4.2.1 The toric code anyon model

The toric code is a quantum double of \mathbb{Z}_2 , characterised by Abelian anyons comprising a vacuum charge 1, excitations e and m, and their composite e. These anyons obey specific

fusion rules: each anyon fuses with another of the same type to yield the vacuum, and $e \times m = \epsilon$. The self and mutual statistics of these anyons are captured by R-matrices, which describe the evolution of the system under the exchange of anyons:

$$R_{ee} = R_{mm} = 1,$$

$$R_{\epsilon\epsilon} = -1,$$

$$R_{em}R_{me} = R_{e\epsilon}R_{\epsilon e} = -1.$$

$$(2.75)$$

The braiding relations in Eq. 2.75 indicate that e and m are both bosons, while ϵ is a fermion. The anyons e and m are mutual semions, meaning that braiding an e around an m introduces a phase of -1. Similarly, e and ϵ , as well as m and ϵ , exhibit semionic behaviour. On the toric code, defined on a lattice of qubits, these anyons manifest at the ends of operator strings: e anyons at the ends of Pauli-Z operators, and m anyons at the ends of strings of Pauli-X operators.

2.4.2.2 The Ising anyon model

Ising anyons belong to the non-Abelian Ising model, characterised by the anyon charges 1, σ and ψ [Kit06], with the following fusion rules:

$$\psi \times \psi = \mathbf{1}, \qquad \psi \times \sigma = \sigma, \qquad \sigma \times \sigma = \mathbf{1} + \psi,$$
 (2.76)

where ψ is a fermion. Two Ising anyons σ can fuse to either the vacuum charge **1** or one ψ . Consequently, a pair of σ -anyons spans a two-dimensional Hilbert space, with basis states labelled by their fusion channels:

$$|\sigma\sigma \to \mathbf{1}\rangle$$
, $|\sigma\sigma \to \psi\rangle$. (2.77)

To access this two-dimensional space for computation, a qubit can be encoded in the global state of a composite system of four σ -anyons, subject to the constraint of total fermion parity

conservation. The basis in this space can be spanned by the states

$$|(\sigma\sigma)(\sigma\sigma) \to \mathbf{1}; \mathbf{1}\rangle, \qquad |(\sigma\sigma)(\sigma\sigma) \to \psi; \psi\rangle.$$
 (2.78)

Here, the notation $(\sigma\sigma)$ refers to grouping pairs of σ -anyons for fusion. Consider a set of four Ising anyons labelled 1, 2, 3 and 4. Changing the fusion order from (12)(34) to (13)(24) represents a basis transformation in this Hilbert space, given by the fusion matrix

$$F_{\text{Ising}} = \frac{1}{\sqrt{2}} \begin{pmatrix} 1 & 1 \\ 1 & -1 \end{pmatrix},$$
 (2.79)

while all other F-matrices in the model contribute phase factors only [Pac12]. The braiding properties of Ising anyons are described by R-matrices:

$$R_{\psi\psi} = -1,$$

$$R_{\sigma\sigma} = e^{-i\frac{\pi}{8}} \begin{pmatrix} 1 & 0 \\ 0 & i \end{pmatrix}$$

$$R_{\psi\sigma}R_{\sigma\psi} = -1.$$
(2.80)

Using the F and R operators above, the braiding operator for Ising anyons is expressed as

$$B = FR^2F^{-1} = e^{-i\frac{\pi}{4}} \begin{pmatrix} 0 & 1\\ 1 & 0 \end{pmatrix}. \tag{2.81}$$

This operation implements a non-trivial unitary gate, specifically the Pauli-X logical operation (up to a global phase factor). By combining such operations, one can generate the Clifford group through braiding anyons from two σ -pairs encoding a qubit. [Iva01; LO18].

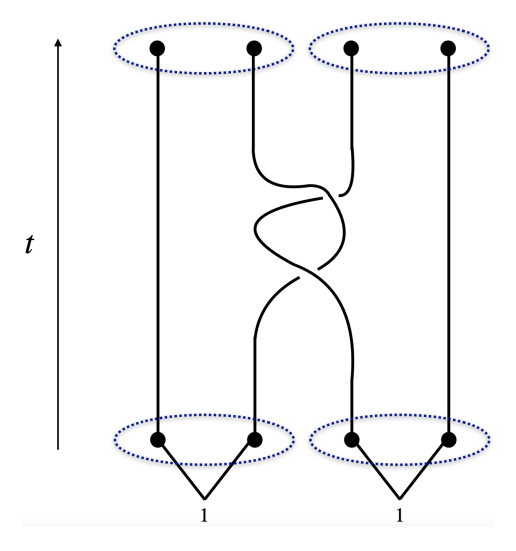


Figure 2.8: Schematic of a topological quantum computation. Four anyons are created at the start of the computation from the vacuum. A set of braiding operations is performed, here a double exchange of the second and third anyons, and the pairs of anyons are fused again at the end. The dotted loops indicate two qubits 1 and 2, each encoded in a fixed state corresponding to the fusion outcome of the enclosed anyons, for instance here the vacuum state $|0\rangle_1 |0\rangle_2$. The result of the computation is encoded in the amplitudes of the state of the system after the braiding, i.e. the worldlines of the anyons, and is revealed by the probabilistic fusion outcomes of the measurement encoded by the final dotted loops. For instance, if the particles here were four Fibonacci anyons, the final state would be $|0\rangle_1 |0\rangle_2$ [FS18] with probability $\approx 15\%$, and $|1\rangle_1 |1\rangle_2$ with $\approx 85\%$. If no braid had been performed, each of the two pairs would deterministically fuse to vacuum. Note that in (3+1)D the path configurations of N worldlines are elements of the permutation group S_N , and the power of topological quantum computation is lost.

2.4.3 Topological quantum computing

Systems that support anyons can be used to encode a degenerate subspace that is decoherencefree, hence providing a quantum memory inherently robust against control errors and local perturbations. The braiding of such quasi-particles can implement quantum gates on the encoded system. Topological quantum computation (TQC) originally referred to a model of quantum computation that uses the braiding and fusion of non-Abelian anyons to approximate any unitary transformation in the Hilbert space associated with the anyonic degrees of freedom [Fre+03; Pac12]. This model arose from the observation that the computation of certain knot invariants [Kau90] is classically hard, yet becomes tractable using particles whose dynamics are characterised by such invariants. This is closely tied to the definition of anyons, which naturally encode representations of the braid group. Indeed, the evolution of anyonic systems is governed by operations in a topological quantum field theory (TQFT), allowing for the computation of knot invariants like the Kauffman polynomial [KB93], to encode and extract information about the state of the system. Because evaluating certain Kauffman invariants (e.g., the Jones polynomial at appropriate roots of unity) is BQP-complete, a topological quantum computer that can realise these evaluations through braiding operations is theoretically capable of universal quantum computation.

Specific anyon models were shown in [Fre+03] to support universal quantum computation, the simplest being the Fibonacci model. This model supports a single non-trivial anyon, τ , with the fusion rule $\tau = 1 + \tau$ [RR99]. In contrast, the Ising model (cf. Sec. 2.4.2.2) is not universal through braiding alone, as it requires additional resources like magic state distillation to achieve universal quantum computation.

Schematically, TQC involves initialising a system of n non-Abelian anyons located at positions z_i for $i \in [1, n]$. This many-body system defines an M-dimensional protected computational subspace \mathcal{H} , as described in Sec. 2.4.2. An arbitrary wavefunction in this subspace can be expressed as:

$$|\psi(z)\rangle = \sum_{m=1}^{M} a_m |m; z\rangle$$
 (2.82)

where $z = (z_1, z_2, ..., z_n)$, and $a_m \in \mathbb{C}$ are amplitude coefficients. A non-trivial operation on this state is performed by a braid $b \in B_n$, representing a controlled unitary operation realised by adiabatically exchanging the positions of the anyons along paths defined by z, as illustrated in Fig. 2.8. This process exploits the Aharonov-Bohm effect, where the system acquires a statistical phase directly related to the exchange statistics of the anyons and the topology of the braiding paths.

After the computation, the state of the system is determined by fusing anyons in pairs and measuring the outcomes. Each fusion result corresponds to a unique basis state of the computational subspace, and their amplitudes determine the probability of each set of fusion outcomes. As illustrated in Fig. 2.8 for two qubits encoded using four Fibonacci anyons, the outcome of the computation is obtained by repeated measurements to construct a probability distribution reflecting the state of the quantum system. Implementing a specific quantum algorithm in this framework involves designing an appropriate sequence of braids, a process known as topological quantum compiling, which is analogous to how classical compilers convert high-level code into machine instructions [Hor+07].

Two significant remarks about TQC are warranted. First, the experimental realisation of anyons, particularly non-Abelian anyons, remains a substantial challenge [SFN15a]. Secondly, the topological protection can still be compromised. Potential errors include anyon leakage into non-computational states [XW08], interaction-induced splitting of the ground state degeneracy or phase transitions [Fei+07], and temperature-induced closing of the topological gap.

2.4.4 The Kitaev models

To illustrate the concepts introduced in this section, we review two influential and analytically solvable models of topological order proposed by A. Yu. Kitaev [Kit03a]: the toric code [Kit03a], and the Kitaev honeycomb model [Kit06].

The toric code is defined on a two-dimensional lattice of size $L \times L$ with periodic boundary conditions, i.e. a tessellated torus. It features a degenerate, topologically protected ground

state, making it suitable for use as a quantum memory, as detailed in Sec. 2.3. This is the ground state of the Hamiltonian

$$H_{\text{tcm}} = -\sum_{v} A_v - \sum_{p} B_p,$$
 (2.83)

where the terms consist of the following four-body interactions

$$A_v \equiv \prod_{j \in \partial v} \sigma_j^x, \qquad B_p \equiv \prod_{j \in \partial p} \sigma_j^z, \qquad \prod_v A_v = \prod_p B_p = +1$$
 (2.84)

which are precisely the stabilizer generators in Eq. 2.53 defining a quantum code. These terms each have eigenvalues ± 1 , and respect the relations

$$[A_v, A_{v'}] = [B_p, B_{p'}] = [A_v, B_p] = 0 (2.85)$$

for any v, v', p, p'. The ground state is a common eigenstate of all A_v and B_p terms with eigenvalue +1, with energy $E_0 = -4L^2$. Since the system contains $n = 2L^2$ sites, and there are $2L^2 - 2$ independent terms in the Hamiltonian, the ground state is 4-fold degenerate. This ground state takes the form

$$|\Psi\rangle \propto \prod_{v} \frac{1}{2} \left(\mathbb{1} + A_v\right) |0\rangle^{\otimes n},$$
 (2.86)

which follows from the fact that $\sigma^z |0\rangle = |0\rangle$ for all spins on the lattice, and indicates the absence of excitations. It can be interpreted as the superposition of all trivial loops on the lattice. These excitations can be created by applying a Pauli operator on a spin, which violates (flips the eigenvalue of) a term of the Hamiltonian. An operator σ_j^z flips two neighbouring star operators, and thereby creates two quasiparticles, the *e*-anyons of the toric code model, c.f. Sec. 2.4.2.1. Similarly, a σ_j^x operator flips two neighbouring plaquette operators, and thereby creates two *m*-anyons at these locations. These operations, and their combination,

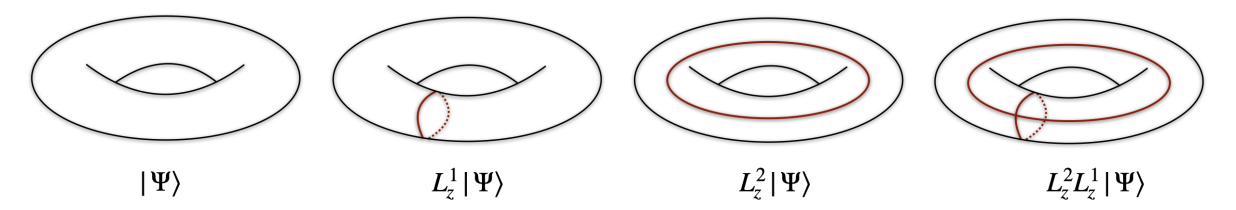


Figure 2.9: A genus-1 torus representing a lattice on which the toric code Hamiltonian is defined. The ground state of the code is four-fold degenerate as represented by the states shown in the figure from left to right. These respectively indicate the vacuum state $|\Psi\rangle$, the state $L^1_z |\Psi\rangle$ obtained by creating a pair of e anyons and wrapping them around one nontrivial loop on the torus – as represented by the red string –, the state $L^2_z |\Psi\rangle$ obtained by creating a pair of e anyons and wrapping them around the second non-trivial loop, and the state $L^2_z L^1_z |\Psi\rangle$ obtained by combining both non-contractible loops.

create the following excited states

$$\sigma_{i}^{z} |\Psi\rangle = |e, e\rangle, \qquad \sigma_{i}^{x} |\Psi\rangle = |m, m\rangle, \qquad \sigma_{i}^{y} |\Psi\rangle = |\epsilon, \epsilon\rangle$$
 (2.87)

where the latter is the fermion in the toric code anyon model. Since any two terms share overlap on an even number of sites, the minimum excitation energy is $E_{\min} = 4$. Measuring the interaction terms of the Hamiltonian reveals the presence of anyons, which is analogous to measuring the stabilizer generators to obtain a syndrome in QEC. Anyons can also be fused by application of Pauli rotations to return to vacuum, which is exactly the decoding problem solved by a MWPM algorithm in Sec. 2.3.6.2.

Encoding information using this quantum phase can be done by considering how to transition between the four degenerate ground states. This can be achieved using the ability to create a string of anyons, extend it by applying a series of Pauli rotation on the sites supported on the string, and fusing the end points of the string such as to annihilate the two boundary anyons. In doing so, the final state is excitation-free and therefore a ground state. Since the torus has non-trivial genus, consider creating such a string using a series of σ^z rotations along each non-contractible loop of the lattice. This final configuration, while being a ground state, is different from the original $|\Psi\rangle$. The four states, namely $|\Psi\rangle$, $L_z^1|\Psi\rangle$, $L_z^2|\Psi\rangle$ and $L_z^2L_z^1|\Psi\rangle$ are invariant under continuous deformations, linearly independent since they are topologically

inequivalent, and form the four-fold degeneracy derived above, as shown in Fig. 2.9. Consider the loop defined by the operator L_z^1 , which has eigenvalue ± 1 based on whether there is a non-trivial topological excitation around a loop encircling the torus in the vertical direction. Similarly, the operation L_z^2 encircles the torus in the opposite direction, and has eigenvalue ± 1 depending on the presence of a topological excitation around the torus in the horizontal direction. It is obvious that $[L_z^1, L_z^2] = 0$, and the four combinations of their eigenvalues encode a two-qubit Hilbert space which can be used to define two logical qubits. Consider next the action of an operator L_x^1 defining a non-contractible loop composed of a series of σ^x rotations, as shown in Eq. 2.10. This operator does not affect L_z^1 , since it can be smoothly displaced to avoid overlap with this σ^z -loop, and similarly for the L_x^2 and L_x^2 , summarised as

$$[L_x^1, L_z^1] = [L_x^2, L_z^2] = 0. (2.88)$$

In the case where a loop of σ^x and σ^z operators wrap around the torus in opposite directions, they unavoidably overlap at an odd number of sites, meaning that

$$\{L_x^1, L_z^2\} = \{L_x^2, L_z^1\} = 0.$$
 (2.89)

The relations in Eq. 2.88 and Eq. 2.89 show that the L_z and L_x operators define the Pauli \overline{Z} and \overline{X} operators of the two logical qubits encoded in the ground state of the toric code.

These logical basis states encoding a qubit in the ground state manifold are topologically distinct, and provide robustness against local perturbations, which is the hallmark of TQC. Indeed, consider the excitation gap in the toric code Hamiltonian

$$H = H_{tcm} + \lambda V \tag{2.90}$$

where V is an arbitrary Hamiltonian with local terms only, and λ small. The energy splitting

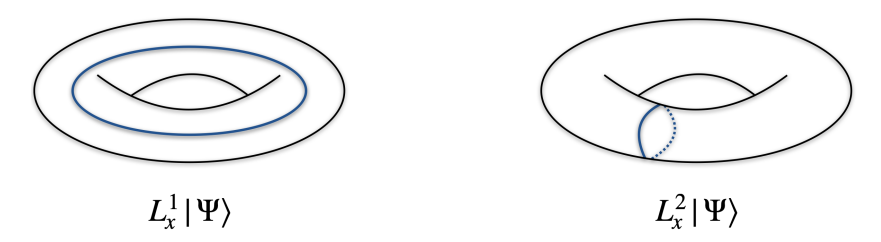


Figure 2.10: A genus-1 torus representing a lattice on which the toric code Hamiltonian is defined. The operators L_x^1 and L_x^2 respectively represent two strings of σ^x rotations which wrap around the torus in the horizontal (left) and vertical (right) directions. This process describes the creation, transport and annihilation of two m anyons around the toric code lattice.

induced by the perturbation V, which attempts to couple two ground states, is given by

$$\Delta E = \langle \Psi_i | V | \Psi_j \rangle \sim e^{-\beta \Delta L}, \tag{2.91}$$

where β is the inverse temperature. Any splitting or mixing of the four ground state sectors is exponentially suppressed with the system size L, due to V being local. This means that V cannot effectively couple states with different global properties unless anyons are created that traverse the torus completely. Hence, the information stored in these states is inherently protected for sufficiently large system sizes.

The anyon excitations that arise in the toric code are all Abelian (cf. 2.4.2.1) and therefore not directly useful as a resource for topological quantum computing. However, their computational power can be increased by introducing local defects that behave like the Ising anyon (cf. 2.4.2.2). The latter is a non-Abelian quasiparticle excitation which natively emerges in other models, such as the Kitaev honeycomb model (KHM). To understand the motivations of Chapter 3, it will be useful to highlight the relationship between this model and the toric code phase.

The KHM describes a nearest-neighbour two-spin interaction on a planar honeycomb

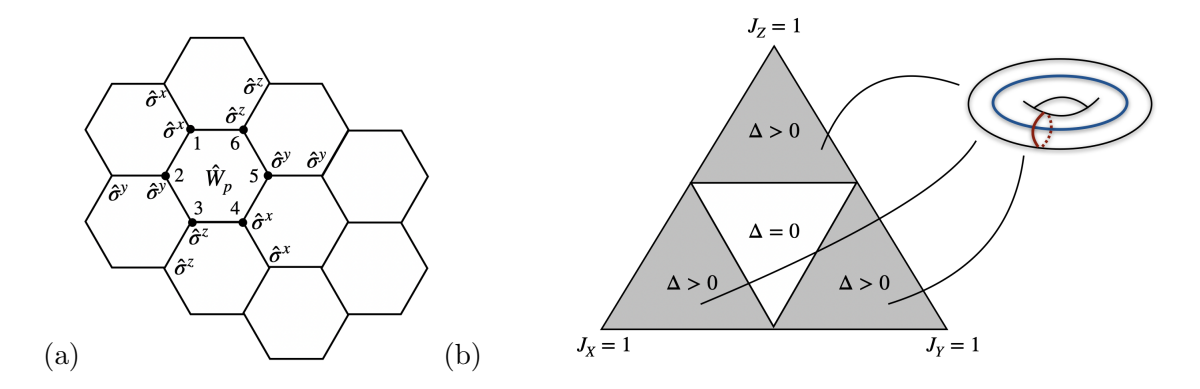


Figure 2.11: (a) Schematic of the bulk of the Kitaev honeycomb model with two-body Pauli terms on links of different directions of a hexagon on the lattice, and the emergent plaquette operator \hat{W}_p . (b) The phase diagram of the honeycomb model, indicating the gapless $\Delta=0$ and gapped $\Delta>0$ regions referring to the non-Abelian and toric code phases respectively, dependent of the coupling constants J_x, J_y and J_z .

lattice given by the Hamiltonian

$$H_{\text{hcm}} = -J_x \sum_{x \text{ links}} \sigma_i^x \sigma_j^x - J_y \sum_{y \text{ links}} \sigma_i^y \sigma_j^y - J_z \sum_{z \text{ links}} \sigma_i^z \sigma_j^z$$
 (2.92)

where $J_x, J_y, J_z \in \mathbb{R}$ are coupling constants. As shown in Fig. 2.11(a), the interactions couple quantum spins depending on their direction on the lattice. From this model, we can extract hexagonal plaquette operators of the form

$$W_p \equiv \sigma_1^x \sigma_2^y \sigma_3^z \sigma_4^x \sigma_5^y \sigma_6^z, \tag{2.93}$$

which commute with all the terms of Eq. 2.92(a) that do not involve the plaquette spins, since each spin operator in Eq. 2.93 acts on a vertex which is part of the same spin-type link, as well as terms involving the boundary links of W_p using the fact that $[\sigma_i^{\alpha}\sigma_j^{\beta}, \sigma_i^{\gamma}\sigma_j^{\gamma}] = 0$. Moreover, any two plaquettes commute since their support overlaps on zero or two sites. Hence, each plaquette term W_p can be simultaneously diagonalised, with eigenvalues $w_p = \pm 1$. Moreover, it can be shown that the plaquette operators form a maximal set of independent commuting conserved quantities, whose eigenvalues label distinct sectors of the full Hilbert space. In

particular, in the regime $J_x, J_y, J_z > 0$, the ground state of the honeycomb model is described by the $w_p = +1$ sector for all p [Kit06]. Moreover, since $\prod W_p = 1$, excitations living on such plaquettes, known as vortices and corresponding to an eigenvalue of -1 of the plaquette operator, always appear in pairs. In fact, this model has been solved exactly by Kitaev [Kit03b] by representing the spin operators in an extended Hilbert space of two Majorana fermions located at each lattice site. Alternatively, it can be mapped to a 2D p-wave Fermi superfluid [CN08].

In the limit where one coupling J_{α} for $\alpha \in \{x, y, z\}$ is larger than the sum of the remaining two, there is a non-zero gap between the ground state manifold and any state hosting an excitation $W_p = -1$. The low-energy effective Hamiltonian of the system with periodic boundary conditions, at the lowest non-trivial perturbation order, is equivalent to the toric code phase. The excitations living on the plaquettes are known as *vortices*, and behave precisely as the toric code anyons, as indicated in Fig. 2.11(b) [Kit03b; SDV08]. In contrast, the central region of Fig. 2.11(b) is a highly frustrated phase under any of the following conditions:

$$|J_x| \le |J_y| + |J_z|,$$
 (2.94)

$$|J_y| \le |J_z| + |J_x|,\tag{2.95}$$

$$|J_z| \le |J_x| + |J_y|,\tag{2.96}$$

which is gapless unless a magnetic field term is introduced to Eq. 2.92. Under this condition, vortices in this phase behave like the non-Abelian Ising anyons, c.f. Sec. 2.4.2.2. Consider the case where only two vortices live in the system, separated by a distance δ . In the Abelian phase, the gap in the fermionic spectrum is practically oblivious to δ and to the presence of a magnetic field. In contrast, the gap in the non-Abelian phase decreases exponentially with δ . For sufficient distance, the presence of two vortices located at sites i and i+1 carries a nonlocal massless Majorana mode, and the fusion outcome of the vortices reveals the occupation of this mode. An unoccupied mode corresponds to the vacuum 1 fusion outcome, while an

occupied mode is the fusion yielding a fermion ψ , as prescribed by the Ising anyon model. The occupation of these modes does not alter the energy of the system, from which the name Majorana zero-mode arises. The presence of n zero-modes in the spectrum is associated with a 2^n -fold ground state degeneracy, which can be lifted when the vortices are brought closer, such that the fusion outcome is revealed (which removes the protection needed in topological quantum computing) [Pac07; Lah+08]. The Kitaev honeycomb model is a rich and attractive platform for the study of materials supporting exotic quasiparticles, particularly since it is experimentally tractable [Ban+16; CJK10], in contrast with the four-body interactions of the toric code Hamiltonian.

2.4.5 The Majorana chain and zero-energy edge modes

In this thesis, we will consider logical encodings using non-Abelian anyons which behave like Majorana modes at the edge of a domain wall, and a generalisation of the Ising chain supporting similar objects. For this purpose, let us review how edge modes emerge in the Majorana chain. The Ising model is a fundamental system of interest in various fields, most notably statistical mechanics. Tremendous effort has gone into computing properties of this model in one and two dimensions, which was made easier by its mapping from spins to free fermions [SML64]. In [Kit01], Kitaev introduced a different perspective by considering the fermions as degrees of freedom of a "quantum wire", and showed the emergence of topological order in the ordered phase of the Ising chain, where the magnetisation used as the spin local order parameter becomes nonlocal.

In 1D, the Ising model is given by the Hamiltonian

$$H_{Ising} = -f \sum_{j=1}^{L} \sigma_j^x - J \sum_{j=1}^{L-1} \sigma_j^z \sigma_{j+1}^z$$
 (2.97)

where $f, J \in \mathbb{R}_{\geq 0}$, and the system exhibits a \mathbb{Z}_2 symmetry upon flipping all the spins. This chain has two phases with a critical point at f = J, such that the phase is ordered at f < J, with a two-fold ground state degeneracy that is lost in the disordered phase when f > J.

The Hamiltonian in Eq. 2.97 can be mapped to a model of nonlocal free fermions using the Jordan-Wigner transformation [JW28],

$$a_j = \left(\prod_{k=1}^{j-1} \sigma_k^x\right) \sigma_j^z, \qquad b_j = i \left(\prod_{k=1}^{j-1} \sigma_k^x\right) \sigma_j^z \sigma_j^x \tag{2.98}$$

which describes a chain with two fermions at each site i. The nonlocal strings in these expressions lead to the following commutation relations for all i, j:

$$\{a_j, b_k\} = 2\delta_{jk}, \qquad \{b_j, b_k\} = 2\delta_{jk}, \qquad \{a_j, b_k\} = 0$$
 (2.99)

where $a_j^2 = b_j^2 = 1$, and the Hermitian operators a_j and b_j are referred to as Majorana operators, similarly to those encountered in Sec. 2.4.4. Under this transformation, Eq. 2.97 becomes

$$H_M = if \sum_{j=1}^{L} a_j b_j + iJ \sum_{j=1}^{L-1} b_j a_{j+1}.$$
 (2.100)

This chain can be rewritten in terms of complex fermions $c^{\dagger} = a + ib$ which obey the ubiquitous anti-commutation relations, and admits a symmetry operator $(-1)^F = \prod_{j=1}^L (-ia_j b_j)$ which measures the fermion parity in the system where $F = \sum_j c_j^{\dagger} c_j$.

A fermionic zero mode Ψ is a fermion operator which respects $[H, \Psi]$, $\{(-1)^F, H\} = 0$ and $\lim_{L\to\infty} \Psi^{\dagger}\Psi = 1$. Moreover, when localised near the edge of the system, this becomes a zero-energy edge mode, such that the dependence of the fermion operator in the bulk of the chain drops exponentially with the distance. The previous conditions ensure that the spectrum is the same in the even and odd fermion parity sectors, and the operator Ψ maps between these two sectors. In the case where f=0 in Eq. 2.97 only the hopping term remains, in which case the fermions a_1 and b_L vanish in Eq. 2.99, resulting in

$$[H_M, a_1]_{f=0} = [H_M, b_L]_{f=0} = 0.$$
 (2.101)

This indicates that a_1 and b_L are two edge zero-modes since they anticommute with the

fermion parity operator. Since the model is free, these modes can be found exactly for f < J, even with spatially-varying couplings, and their support exponentially decays with chain length. Note that the Kitaev honeycomb model in 2D, as presented in Sec. 2.4.4, arises from coupling three Ising spin chains, and is equivalent to a free-fermion model in a background \mathbb{Z}_2 gauge field, on which Majorana zero-modes also emerge as paired vortices. In fact, various proposals exist to realise and detect Majorana fermions [Ali12].

The Ising-Majorana chain can be generalised to richer systems with n-spin states and \mathbb{Z}_n symmetry, also shown to support topologically ordered phases [Fen12]. In Chapter 4, we study how zero-energy edge modes in the \mathbb{Z}_3 case can be exploited in the context of quantum computation.

2.4.6 Twist defects in topological codes

In this section we review the definition of *twist defects*, namely defects associated with an anyon symmetry. Consider a mapping of the form

$$\mathcal{K}: C_1 \to C_2 \tag{2.102}$$

where C_1 and C_2 are two anyon models characterising two topologically ordered phases. This mapping \mathcal{K} is said to be an anyonic symmetry if it implements automorphisms on an anyon model C, thereby permuting the labels of anyons in C. The anyons of the model get mapped under the action of the symmetry, such that

$$a \to \mathcal{K}a$$
 (2.103)

for any $a \in C$. Twist defects are semiclassical defects which behave like immobile fluxes, and are associated with the action defined by the element of the anyon symmetry group, which is enacted by adiabatically winding an anyon around the location of the twist defect, as shown in Fig. 2.12. Twist defects are not dynamical excitations of a Hamiltonian, but can them-

selves trap non-Abelian zero-modes at their location. Since these non-Abelian excitations are not deconfined, only their projective non-Abelian statistics are accessible [BJQ13a; TRC14; KTH14]. Despite this characteristic, their confinement to twist defects offers a potential platform for trapping non-Abelian excitations. This is particularly promising for robust TQC and nonlocal storage of quantum information. An extensive study of the theory and realisation of twists is presented in Ref. [Teo16].

Given that a twist defect acts on a charge label as per Eq. 2.103, it is natural to wonder how the defect itself changes from this quasi-particle exchange. The physical consistency comes from considering the internal structure of the twists. Indeed, we can consider the fusion of two defects with conjugate symmetries \mathcal{K} and \mathcal{K}^{-1} attached by a branch cut. The fusion outcome of this pair of defects must be trivial, as an anyon winding around the pair experiences a trivial action. However, if an anyon encircles a defect, the fusion outcome is affected. This can be seen as an absorption process by the twist when a charge is exchanged, which allows the twist to mediate interactions between multiple anyonic sectors, effectively generating fusion channels that combine characteristics of the anyons involved. Hence, the action of a twist defect can be framed as a multi-channel fusion as described in Sec. 2.4.2. To reveal topological the properties of twist defects, it is useful to consider the Wilson loop algebra of pairs of twist defects [TRC14; BJQ13b], which we implicitly consider for defects on the toric code in Chapter 3.

It has been shown that twists can be realised using lattice dislocations which break translational or rotational symmetries in topologically ordered lattice models [Bom10; TRC14; BQ12; YW12]. These "domain walls" act as a map from one phase of matter to another, such that anyons traversing this defect line are acted on by a symmetry, as per Eq. 2.103. At each end of this line are located point-like boundary defects, i.e. twists, as shown in Fig. 2.12.

To illustrate this point, we consider the implementation of twist defects in the toric code anyon model. A twist defect on the toric code, as discussed in Sec. 2.3.5.1 and Sec. 2.4.4, can be realised by modifying the stabilizer pattern on the lattice to enact a \mathbb{Z}_2 symmetry on the anyon model, i.e. $e \leftrightarrow m$, as shown in Fig. 2.12. This can be achieved by dislocating the chequerboard

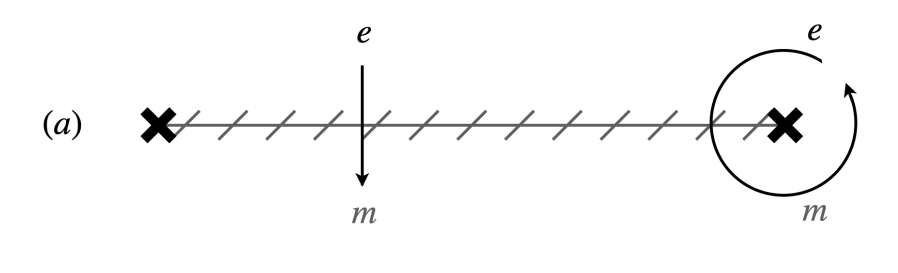




Figure 2.12: Schematic of the action of twists using the toric code anyon model. (a) An anyon e passing through a domain wall is mapped to the an anyon e in the middle on the domain wall or at the edge around a twist (indicated as a cross). (b) An anyon e exchanges type twice under a 360° rotation around a twist, and goes back to the identity under the \mathbb{Z}_2 symmetry of the model.

stabilizers depicted in Fig. 2.3(b), or performing a series of Pauli-Y measurements along a string of qubits on the lattice [Bom10; Bro+17]. Both methods disrupt the regular stabilizer structure to create defects known to exhibit the non-Abelian properties of Ising anyons, cf. Appendix B of Ref [Bom10]. Importantly, these twists enable novel mechanisms for topological quantum computation. For instance, Ref. [Bro+17] demonstrated how the braiding and fusion of twist defects in the toric code can be used to perform fault-tolerant Clifford gates.

Chapter 3

Non-Abelian statistics with mixed-boundary punctures on the toric code

3.1 Introduction

Lattice models consisting of a qubit ensemble arranged on a two-dimensional surface are a practical tool to study certain topological systems. These models, such as stabilizer codes [Got97; Fow+12a], allow for computational schemes that encode quantum information in nonlocal degrees of freedom. In Sec. 2.3.5.1 and Sec. 2.4.4, we reviewed the canonical example of the toric code, which encodes logical qubits in the degenerate ground states of a square spin lattice defined on a torus, and outlined how it emerges in the Abelian phase of the Kitaev honeycomb model [Kit03b; Kit06; KSV09]. The toric code admits local, point-like defects and nonlocal, line-like defects. Punctures are local defects corresponding to holes on the lattice. They were introduced as candidates for quantum memory and computation through their braiding [Den+02; DIP16; RHG07], while twists are the endpoints of nonlocal domain walls that enforce a symmetry on the toric code anyons as described in Sec. 2.4.6 [BJQ13a; Teo16].

Twists are computationally interesting since they were shown to behave like Majorana zero modes under fusion and exchange [Bom10; ZDJ15; YW12]. A novel hybrid of these two defect types was even introduced in Ref. [KP20], also capable of encoding logical qubits.

This chapter presents the results published in Ref. [BPB22], in which we investigate the topological properties of yet another defect on the toric code, namely mixed-boundaries punctures. Following the adiabatic equivalence between vortices and twists demonstrated in the non-Abelian phase of Kitaev's honeycomb lattice model [HFP20], we studied all possible deformations of twists that could be adiabatically deformed to punctures. We find that no deformation of these defects provides point-like defects that could support the desired statistics. Thus, we resorted to the mixed-boundary punctures as the optimal tool for an encoding of Majoranas that takes advantage of the Abelian statistics of anyons on the toric code, and the nonlocal encoding of gates. Moreover, our choice is congruent with the insight in Ref. [Woo+08] that the quantum dimensions of the Ising model and of the toric code are equal. This lays the basis for utilising toric code anyon statistics in order to realise more complex Ising anyon properties. In particular, we demonstrate non-Abelian fusion and braiding properties reminiscent of Majorana exchange. To achieve this, we employ local lattice defects of the toric code with mixed boundaries, in conjunction with a nonlocal logical encoding between them. Our approach enriches the class of defects capable of reproducing the behaviour of Majorana anyons, helping bridge the gap between their exotic statistics and physical realisation, and expanding directions for their simulation on a quantum processor [Bau+23a; KML23; Xu+23; 23; Xu+24; Igb+24].

This chapter is organised as follows. The defects on the surface code relevant to the following investigation are introduced in Sec. 3.2. In Sec. 3.3, we introduce defects which generalise punctures to instances with hybrid boundaries in order to encode non-Abelian fusion channels, and demonstrate their Ising-like fusion and braiding statistics after defining a logical encoding based on a superposition of their population states. We discuss our results in Sec. 3.4.

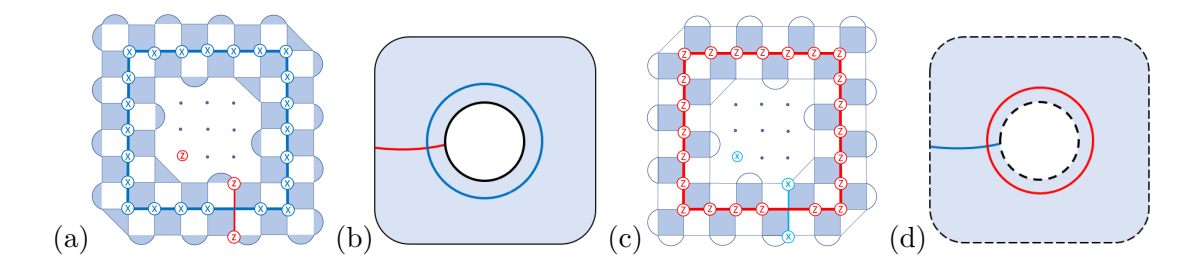


Figure 3.1: Different types of puncture defects on the toric code. The puncture and code boundary in (a) are rough while the puncture and code boundary in (c) are smooth. The measured stabilizers creating the punctures, and non-contractible loops stabilising them, are also shown for each puncture type in (a) and (c). Panels (b) and (d) show their respective diagrammatic representations as introduced in Ref. [Bro+17].

3.2 Defects on the surface code

A useful way to encode information on the toric code with open boundary conditions, i.e. the surface code, is to introduce defects on the lattice. One such defect is the puncture, which corresponds to a region of the code where certain stabilizer generators are no longer enforced. This effectively removes those parity-check constraints, creating a hole in the lattice. The qubits in this region are disentangled from the code by ceasing to measure the associated stabilizers, which modifies the code space and introduces logical degrees of freedom localised at the boundary of the puncture [DIP16; Fow+12a], see Sec. 2.3.7.

The type of boundary of a puncture depends on which type of stabilizer was measured in its creation, namely rough (smooth) boundary for Pauli Z(X)-type as shown in Fig. 3.1. When the code and puncture boundaries are of the same type, a logical qubit is encoded by defining a logical operator \overline{X} as a sequence of Pauli-X operations supported on qubits along a loop enclosing the puncture, and \overline{Z} as a string of Pauli-Z applied on qubits between code and puncture boundaries, satisfying the necessary anti-commutation as described in Fig. 3.1 (a) and (b), and equivalently for a smooth puncture in Fig. 3.1 (c) and (d). From the topological anyon picture, the two-level system is designed by encoding the parity of the puncture's anyon population, where each anyon has been passed from the code boundary to the puncture. These are e anyons if the boundaries are rough, and m if smooth. Another type of extrinsic defects

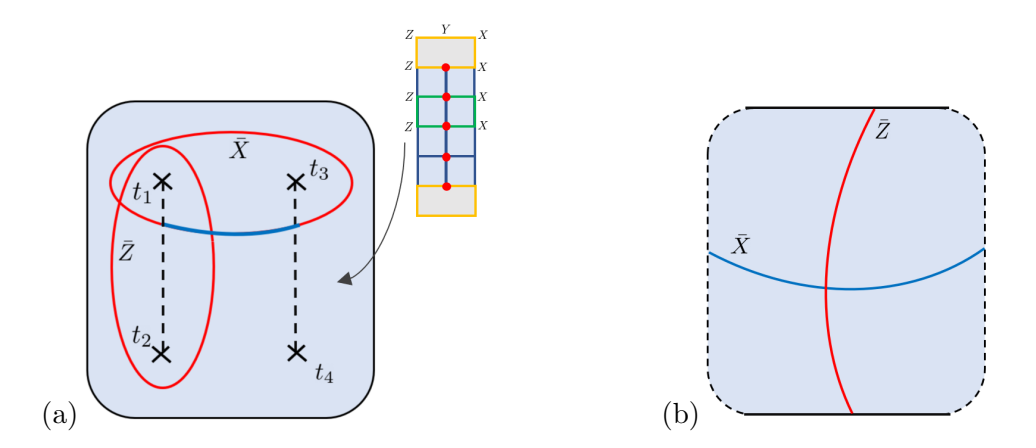


Figure 3.2: Twists on the toric code. Panel (a) shows a qubit encoded using two pairs of twists, with logical operators \overline{X} and \overline{Z} . Panel (b) shows twist defect lines moved to the corners of the code boundary [Bro+17].

on the planar code is the twist defect, which is created in a pair by introducing a translation [Bom10] or a series of measurements on the lattice [Bro+17] modifying its stabilizers. Locally, the lattice is modified in such a way that X and Z stabilizers are interchanged. One way to realise a twist is by deforming the code such that two neighbouring plaquette operators $Z_aZ_bZ_cZ_d$ and $X_cX_dX_eX_f$ (i.e. adjacent white and blue faces on the rotated surface code shown in Fig. 3.1(a)), are deformed through measurement or dislocation to a stabilizer operator of the form $Z_aZ_bX_eX_f$. This is shown in Fig. 3.2(a), where several such stabilizers are combined on a vertical line, resulting in weight-5 operators of the form XXYZZ located at the end points, which support the twist defect locations. As with MZMs, twists were shown to behave like Ising anyons. Two pairs of twists can encode a logical qubit as shown in Fig. 3.2, and logical Pauli operations are achieved by braiding twists. In Ref. [Bro+17] Brown et al. showed that the planar code with mixed boundaries supports corner defects which can be deformed into twists on the lattice. Hence, there is an equivalence between the right and left panels in Fig. 3.2.

The graphical notation here is consistent with the language introduced in Ref. [Bro+17]. The blue background represents the planar code bulk; a dashed line is a smooth boundary condensing m anyons, while a continuous one is rough and condenses e anyons.

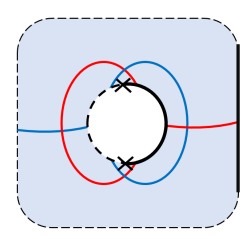


Figure 3.3: A mixed-boundary puncture. Both blue (X-type) and red (Z-type) strings can terminate at its boundaries. The red and blue loops stabilise this defect, and the crosses indicate the meeting point of rough and smooth boundaries, i.e. twists. Note that we need a hybrid code boundary for the attached strings.

3.3 Fusion and exchange of mixed-boundary punctures

3.3.1 The system

In Fig. 3.2(b) corners of the surface code correspond to points at which smooth and rough boundaries are juxtaposed. Given their relationship with twists, we ask whether punctures with mixed boundaries can exhibit Ising-like behaviour. Indeed, by this definition, one can see that a puncture with mixed boundaries, shown in Fig. 3.3, carries two twists, located at the meeting point of the different boundaries. A mixed-boundary puncture is created by measuring both X and Z-type stabilizers [BM09a; DIP16]. The strings allowed at its boundaries, and the loop operators that stabilise it in Fig. 3.3 indicate that a mixed-boundary puncture condenses both e and m anyons. Since one can encode a qubit using four MZMs or twists on the toric code, and achieve Clifford gates on its state through pair-wise braidings, our system will be composed of four copies of mixed boundary-punctures. However, despite the ability of these punctures to hold both toric code anyons, their braiding remains Abelian. Hence, we introduce nonlocality in the encoding of Abelian anyons in order to generate the non-Abelian character. This is done by taking superpositions of anyons populating the punctures, which translates into superpositions of strings between each pair of punctures.

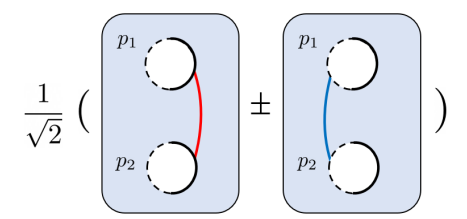


Figure 3.4: A state of a pair of mixed-boundary punctures. This state is defined in Eq. 3.1 and describes a superposition of red and blue string configurations, respectively describing p_1 and p_2 each one absorbing an e or an m anyon.

3.3.2 Logical encoding

We consider a pair of punctures with mixed boundaries created from vacuum, denoted by p_1 and p_2 , and allow strings between their matching boundaries. We denote the state of a pair of punctures by its anyon population such that the state of a pair enclosing an e anyon in each puncture is $|ee\rangle$; this corresponds to a red string with endpoints at each puncture, and likewise blue for $|mm\rangle$. Since the anyons are *inside* the punctures, we remain in the ground state of the code as opposed to an open string which has excitations at its endpoints. We now let the pair (p_1,p_2) be in the superposition of states given by

$$|p_1, p_2; \pm\rangle = \frac{|e_1 e_2\rangle \pm |m_1 m_2\rangle}{\sqrt{2}},$$
 (3.1)

where this notation translates to the two-puncture system being in a superposition of red and blue string configurations, as shown in Fig. 3.4, and the states given by Eq. 3.1 are degenerate. In fact, this choice of superposition is motivated by the fusion rules of Ising anyons in Eq. 2.76.

We will consider two such pairs of punctures (p_1,p_2) and (p_3,p_4) , and using Eq. 3.1 we

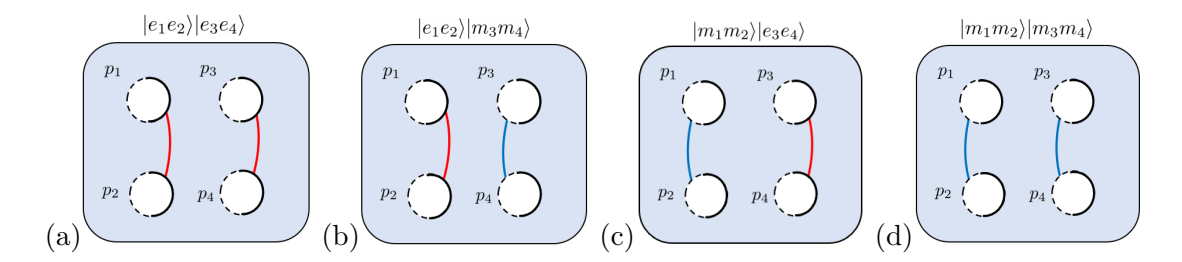


Figure 3.5: Logical encoding of four mixed-boundary punctures. The system is separated into two pairs each in a state described in Fig. 3.4. The string configurations and their corresponding quantum states are based on puncture populations, and each quadrant represents a term in the joint state in Eq. 3.2.

can write their joint states concisely as

$$|(p_1, p_2; \pm)(p_3, p_4; \pm)\rangle =$$

$$\frac{1}{2}(|e_1e_2\rangle |e_3e_4\rangle \pm |e_1e_2\rangle |m_3m_4\rangle$$

$$\pm |m_1m_2\rangle |e_3e_4\rangle + |m_1m_2\rangle |m_3m_4\rangle). \tag{3.2}$$

Note that these configurations are constructed from local lattice defects where nonlocal quantum operations can be encoded. The terms in Eq. 3.2 correspond to the string configurations indicated in Fig. 3.5.

3.3.3 Fusion action

We can verify that this system of punctures reproduces the fusion properties characteristic of Ising anyons by respectively fusing the charge contents of the pairs (p_1, p_3) and (p_2, p_4) . Indeed, the fusion takes the joint state in Eq. 3.2 to the state

$$|p_{13}, p_{24}; \pm\rangle = \frac{1}{\sqrt{2}}(|1_{13}, 1_{24}\rangle \pm |\psi_{13}, \psi_{24}\rangle)$$
 (3.3)

where we define

$$|1_{13}, 1_{24}\rangle = \frac{1}{\sqrt{2}}(|e_1 e_2\rangle |e_3 e_4\rangle + |m_1 m_2\rangle |m_3 m_4\rangle)$$
 (3.4)

and

$$|\psi_{13}, \psi_{24}\rangle = \frac{1}{\sqrt{2}}(|e_1 e_2\rangle |m_3 m_4\rangle + |m_1 m_2\rangle |e_3 e_4\rangle)$$
 (3.5)

analogously to the scheme in Ref. [HFP20]. We can understand this as the punctures from the terms in Eq. 3.4 behaving as the vacuum charge since each composite object is made up of either two e or two m anyons, while the terms in Eq. 3.5 each behave as a fermion string (i.e. both red and blue strings). If we identify the states $|1_{13}, 1_{24}\rangle$ and $|\psi_{13}, \psi_{24}\rangle$ respectively with the vacuum and ψ fermion sectors as described by the basis states in Eq. 2.78, then they are related to the fusion outcomes in Eq. 3.3 by a fusion matrix

$$F_{punct} = \frac{1}{\sqrt{2}} \begin{pmatrix} 1 & 1\\ 1 & -1 \end{pmatrix} \tag{3.6}$$

which matches the Ising model fusion properties in Eq. 2.79.

3.3.4 Braiding action

We are now interested in how the state in Eq. 3.2 is affected by braiding individual punctures. For this purpose, we can encode a logical qubit using the configuration described in Eq. 3.2, in the logical basis $\{|++\rangle, |--\rangle\}$ where

$$|++\rangle = |p_1, p_2; +\rangle |p_3, p_4; +\rangle$$
 (3.7)

$$|--\rangle = |p_1, p_2; -\rangle |p_3, p_4; -\rangle \tag{3.8}$$

which corresponds to the even parity sector. The basis in the odd parity sector is $\{|+-\rangle, |-+\rangle\}$ but we will not require it here.

Braiding p_1 around p_3 affects the states shown in Fig. 3.5 differently. The case for $|e_1e_2\rangle|m_3m_4\rangle$ is detailed in Fig. 3.6, where the step between panels (c) and (d) consists of respectively multiplying the red and blue strings by a Z-type stabilizer (i.e. a red loop) and X-type stabilizer (i.e. a blue loop) operator, which are trivial operations on the toric

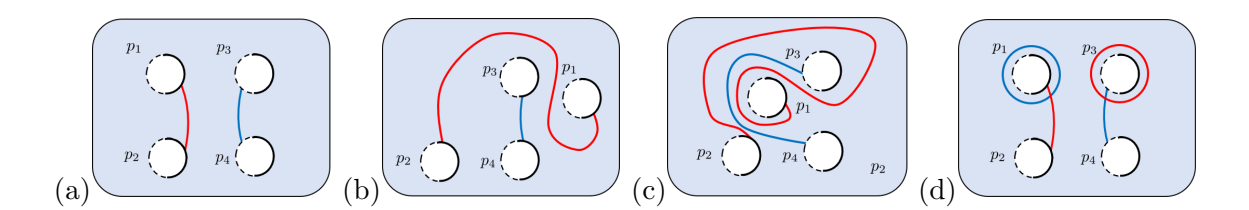


Figure 3.6: Braiding operation shown for state $|e_1e_2\rangle |m_3m_4\rangle$. The steps are shown in (a) - (d), taking p_1 around p_3 for the string configuration in Fig. 3.5(c), and illustrate the full exchange of the e anyon in p_1 around m in p_3 . The braiding has to be carried out without performing a self-twist of p_1 in order to recover (d).

code. We notice that in addition to the initial string configuration, punctures p_1 and p_3 are now enclosed by X (blue) and Z (red) loop operators after the braiding, crossing the original strings which are of opposite type. This evolution is a result of braiding the e anyon in p_1 around the m anyon in p_3 . This is particularly interesting when considering how each term in Eq. 3.2 evolves under the braiding. Indeed, we show the final configurations in Fig. 3.7, where only panels (b) and (c) have X and Z strings crossing and hence anti-commuting, while the braiding in (a) and (d) results in string crossings of the same type, i.e. Abelian. In fact, the braiding in (a) and (b) panels is equivalent to full self-rotations of p_1 and p_3 . The combined effect from this exchange acts on an encoded qubit non-trivially. Indeed, braiding p_1 around p_3 flips the sign in the second and third terms of Eq. 3.2 due to the mutual statistics of the toric code e and m anyons, resulting in the state in Eq. 3.10

$$|(p_1, p_2; \mp)(p_3, p_4; \mp)\rangle = \frac{1}{2}(|e_1e_2\rangle |e_3e_4\rangle \mp |e_1e_2\rangle |m_3m_4\rangle$$
 (3.9)

$$\mp |m_1 m_2\rangle |e_3 e_4\rangle + |m_1 m_2\rangle |m_3 m_4\rangle. \tag{3.10}$$

Upon rewriting Eq. 3.10 as a product of the states of pairs (p_1, p_2) and (p_3, p_4) , one can see that the braiding changes the relative phase in the superpositions of both states. This

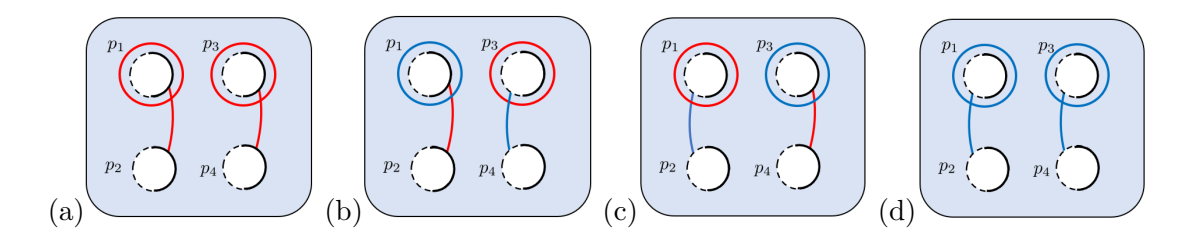


Figure 3.7: Logical gate by braiding operation in the four-puncture system. In all panels p_1 and p_3 were exchanged. The evolution in (a) and (d) is trivial, but combined with (b) and (c) affects the nonlocal superposition state in Eq. 3.2 (as shown in Fig. 3.5) non-trivially. This results in this final string configuration describing the state in Eq. 3.10.

transforms the logical encoding basis following

$$B_{13}^2 |++\rangle = |--\rangle,$$
 (3.11)

$$B_{13}^2 \left| -- \right\rangle = \left| ++ \right\rangle,\tag{3.12}$$

where B_{23}^2 denotes the full braid of p_1 around p_3 . This is identified with the logical Pauli-X operation on the qubit encoded in the four-puncture system, which is the signature of non-Abelian statistics of Ising anyon exchange given in Eq. 2.81. We also observe from Eq. 3.2 that braiding p_1 and p_4 or alternatively p_2 and p_3 or p_2 and p_4 changes the state in an equivalent fashion. However, braiding p_1 and p_2 or p_3 and p_4 (i.e. punctures from the same pair) acts trivially on Eq. 3.2 and likewise on our logical basis. Therefore, it appears that we cannot recreate the full set of operations achievable with Ising anyons (and twists by association). Indeed, obtaining a Pauli-Z operation in the same basis starting from the state in Eq. 3.2 requires an operation that transforms states according to: $|e_1e_2\rangle \rightarrow |m_1m_2\rangle$ and $|m_1m_2\rangle \rightarrow |e_1e_2\rangle$, which cannot be done exclusively by braiding operations in our system. We identify this Z logical operator with the string combination in Fig. 3.8. In consequence, the above encoding does not benefit from the simplicity of the logical operators available with twists since the logical X, which corresponds to applying the loop superposition in Fig. 3.7, and Z cannot be interchanged by puncture braiding only.

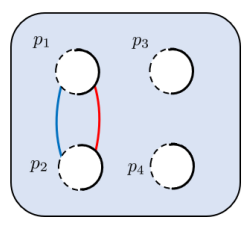


Figure 3.8: Logical \overline{Z} operator for the logical encoding described in Eq. 3.2 using the four mixed-boundary punctures.

3.4 Discussion

We studied an unusual defect on the toric code referred to as mixed-boundary puncture, which is introduced by two types of stabilizer measurements creating a hybrid boundary. This opened interesting possibilities of anyon configurations combined with the punctures. It was recently shown that twists in the non-Abelian phase of the KHLM not only localise Majorana zero-modes but are also equivalent to vortices via an adiabatic lattice transformation [HFP20]. Motivated by this we explored such an equivalence between twists and punctures using code deformations, in an attempt to find a local defect on the toric code that localises MZMs. However, we found no such adiabatic transformation. Indeed, in the Abelian phase of the KHM twists and punctures behave differently in that only twists have the ability to act as sources and sinks for ψ fermions and recreate the Ising anyon fusion space. In contrast, while punctures ensure fault-tolerance, regardless of their boundary composition they cannot provide the mechanical nonlocality offered by twists. In fact, mixed-boundary punctures inherently support a pair of twists on their boundary, and we find that any adiabatic mechanism that would promote them to an object that behaves as an Ising anyon requires moving the twists from the puncture boundary to the bulk of the code, which undermines the integrity of the puncture. Therefore, in order to recover the non-Abelian statistics on the toric code, we introduced a scheme that embraces the nonlocality of twists by simulating their domain wall using our logical encoding. Indeed, we considered a logical basis for computation formulated on a superposition of the anyonic population of four mixed-boundary punctures,

and found that braiding punctures from distinct pairs created from vacuum induces a Pauli-X operation on the encoded qubit, thus reproducing the non-Abelian exchange statistics characteristic of the Ising model. This type of structure appears to be the way around using twist defects in order to recreate Majorana statistics on the toric code.

The existing schemes such as those presented in Refs. [BM09a; DIP16] also utilise punctures to realise fault-tolerant gates by braiding, using combinations of X and Z boundary configurations, and can achieve Clifford and entangling gates. In contrast, further braiding operations with our chosen encoding do not expand our gate set to the full scope of logical operations accessible with twist and MZM exchange, and therefore does not recover the full set of Clifford gates topologically. However, we emphasize that the aforementioned operations are produced by the Abelian braiding of toric code anyons, while we exploit similar defects, with a different encoding combined with braiding to give rise to non-Abelian statistics.

Chapter 4

Universality of \mathbb{Z}_3 parafermions via edge mode interaction

4.1 Introduction

Fault-tolerant quantum computing schemes were shown to exist using error-correcting techniques [Kit03a; Kni05; 96] aimed at diminishing logical error rates by minimising the error rate on individual gates. In this context, physical systems that provide access to a set of exact elementary gates are advantageous. Topological quantum computation was introduced as a way to provide a computational framework for fault-tolerant quantum computation by Kitaev, Freedman and Preskill [WP99; Fre+03], which directly addresses the very low error rate requirement. The proposal is based on the use of anyons i.e. localised two-dimensional many-body quantum systems that display exotic exchange statistics. While the braiding of Abelian anyons is characterised by an arbitrary phase factor, the statistics of non-Abelian anyon exchange are described by representations of the braid group. The non-Abelian character renders these objects useful for computation, which is carried out by creating pairs of anyons from the vacuum, inducing operations by adiabatically moving them around each other and fusing them, with the classical outcome defined by the resulting charge types and

a very low estimated error rate. Quasi-particle modes emerging in condensed matter systems have been shown to carry (projective) non-Abelian statistics which can be identified with known anyon models. The most prominent example of such objects are Majorana zero-modes (MZMs) whose exchange is described by statistics of the Ising model [Kit01; Kit06], and which were found to appear in a two-dimensional electron gas in the Fractional Quantum Hall (FQH) regime [MR91], as one candidate for an experimental realisation.

Majorana fermions constitute the \mathbb{Z}_2 case of the more general \mathbb{Z}_d parafermion model. The latter can be used to encode qudits, and provides a wider set of braiding evolutions, making it a more computationally powerful and attractive counterpart [Fen12]. Indeed, in contrast with Majorana sparse encoding where additional measurements are required [SFN15b], parafermions can provide a scalable entangling gate by braiding alone [CAS13; HL16]. Much like MZMs, proposals to realise non-Abelian anyons typically consist of exploiting the edge states of FQH systems. In the following, we consider parafermionic zero-energy modes proposed to appear at the edges of suitably defined one-dimensional fractional topological superconductors [Lin+12; CAS13], arising in Hamiltonians described by Ref. [Fen12].

The braid group representation describing Ising and parafermionic statistics provides a reliable implementation of Clifford gates, but does not extend to a universal quantum gate set and can therefore be efficiently simulated classically [Got98b; Got98a]. Proposals exist to remedy this drawback for Majorana qubits, by allowing for additional noisy non-topological operations which take the form of direct short-range edge mode interaction, i.e. a tunnelling process. Such operations can give rise to the π /8-rotation that together with Clifford operations constitute a universal gate set [Bra06; BK05]. Parafermions generalise the Majorana encoding to topological qudits. For prime-d Clifford unitaries complemented by any arbitrary non-Clifford gate are sufficient for universal quantum computing (UQC) [ACB12]. Hence, the parafermion edge mode (PEM) interaction is expected to provide a noisy non-Clifford gate to be made fault-tolerant using magic state distillation (MSD) protocols. Such schemes have been extensively studied in particular for qudits of prime d.

Recent research has focused on quantum simulation with Rydberg atoms due to their

versatility [MW21]. They offer strong and controllable long-range interactions realised by selecting different Rydberg states and applying a wide range of optical fields [APS19]. With the development of experimental techniques improving the controllability of individual Rydberg atoms, such as optical tweezers, these systems represent an effective tool for simulating many-body physics of both coherent or dissipative, in- or out-of-equilibrium systems. This can be achieved by engineering the system Hamiltonian in order to simulate various spin systems and quantum phases of matter [BL20; Wei+10; Eba+21]. Lienhard et al. and Verresen et al. [VLV21; Lie+20] also suggested that geometric phases and topological effects can be probed with Rydberg atom-based quantum simulations. Additionally, Rydberg systems provide a way of encoding a qutrit by driving the Rydberg atom around three levels, using microwave lasers as described in Refs. [Bar+15; Spo+21], which is of interest in the light of works such as Ref. [Gok+19].

In this study, we investigate which family of gates the interaction between the PEMs of a \mathbb{Z}_3 parafermion chain gives rise to. Our main result concerns the adequacy of such gates for universal quantum computing with parafermions. We have chosen to focus on the three-dimensional qutrit space in this study since it has the benefit of prime dimension and computational tractability, though many of the features that we uncover are likely to be generic. In addition to this work, we suggest a scheme using a four-Rydberg level atomic system interacting with four microwave lasers, in order to simulate the topological evolution of the ground state of the parafermion chain Hamiltonian under parafermion interaction and two-parafermion braiding which we include in Appendix A1.

This chapter contains work published in Ref. [Ben+23c], and is structured as follows. In Sec. 4.2, we describe the \mathbb{Z}_3 parafermion chain and its edge modes, and how computation is carried out using parafermions. In Sec. 4.3 we investigate the parafermion edge mode interaction and its action on the ground state space. In Sec. 4.4 we show that the addition of the dynamical gate available using the parafermion edge-mode interaction to the Clifford group, accessible through braiding operations, generates a gate-set dense in SU(3). Finally, our results are discussed in Sec. 4.5.

4.2 Parafermion edge-modes and computation

The study of fractionalisation in quantum phases offers valuable insights into the nature of long-range entanglement, and plays a crucial role in identifying candidates for topological quantum computing. Fractionalisation refers to the phenomenon where collective excitations in a system behave as independent particles with fractional quantum numbers, leading to novel topological properties. In this context, parafermions are exotic emergent excitations that generalise Majorana fermions [AF16]. In the context of clock models with \mathbb{Z}_n symmetry, parafermions arise as excitations that are intrinsically linked to the topological nature of the system [FK80; Fen12], highlighting the connection between spin systems and their generalisation to topological phases of matter. The edge states associated with such topological phases are distinct from conventional boundary states in non-topological systems. Such quasi-particle modes, present in both 1D and 2D systems, can exhibit (projective) non-Abelian statistics, described by non-Abelian anyon models. This is similar to the case of Majorana edge modes, which are known to behave as Ising anyons. As a generalisation, the algebraic properties of anyon models based on parafermions offer a richer set of gates via fusion and braiding. Beyond lattice models, parafermions have also been proposed as localised zero-modes in fractional topological insulators, i.e. counter-propagating edge states with opposite spin using proximity with a superconductor or via backscattering between the counter-propagating states to generate the necessary topological gap [Lin+12; CAS13; Sni+18; SEG18]. Parafermions have also been proposed in 2D topological insulators and fractional topological superconductors [FK09: LLK19] amongst other proposals. In the following, we will explore the properties of a chain of \mathbb{Z}_3 parafermions.

4.2.1 The parafermion chain

The concept of parafermion chains extends the Kitaev chain to parafermion operators. This generalisation, introduced by Fendley in Ref. [Fen12], offers a new platform for exploring non-Abelian statistics and topological quantum computing. The Hamiltonian of a parafermion

chain takes the general form

$$H = -\sum_{j=1}^{L-1} J_j(\psi_j^{\dagger} \chi_{j+1} \alpha \bar{\omega} + \text{h.c}) - \sum_{j=1}^{L} f_j(\chi_j^{\dagger} \psi_j \hat{\alpha} \bar{\omega} + \text{h.c})$$
(4.1)

where L is the length of the chain, and at each site j lie two parafermions χ_j and ψ_j . The parameters α and $\hat{\alpha}$ are complex coefficients. The $\omega = e^{\frac{2\pi i}{3}}$ factors ensure Hermiticity, and the couplings f_j and J_j are real and non-negative. The above Hamiltonian can be rewritten in terms of the chiral clock model, by re-expressing the parafermion operators as

$$\chi_j = \left(\prod_{k=1}^{j-1} \tau_k\right) \sigma_j \quad \text{and} \quad \psi_j = \omega \left(\prod_{k=1}^{j-1} \tau_k\right) \sigma_j \tau_j, \tag{4.2}$$

where σ and τ generalise the usual Pauli σ^z and σ^x matrices to a three-dimensional space, as defined in Eqs. 2.30. These respectively characterise the flip and shift Hamiltonian terms in Eq. 4.1. For j < k, these operators follow the commutation relations

$$\chi_j \psi_j = \omega \psi_j \chi_j,$$

$$\chi_j \chi_k = \omega \chi_k \chi_j, \quad \psi_j \psi_k = \omega \psi_k \psi_j, \quad \chi_j \psi_k = \omega \psi_k \chi_j \tag{4.3}$$

and one can verify that $\chi_j^3 = \psi_j^3 = 1$ while each operator individually squares to its Hermitian conjugate. The three physical parameters of significance are the relative strengths of couplings in Eq. 4.1, and two angles ϕ , $\hat{\phi}$ which determine the parameters α and $\hat{\alpha}$. In the following, we consider the symmetric case of $\alpha = \hat{\alpha} = e^{-i\frac{\pi}{6}}$, which lies at the mid-section between the ferromagnetic and anti-ferromagnetic phases of the model in order to ensure chiral interactions and robust edge modes. Recent investigations of the parameter space of the system using DMRG tools offer detailed insight into the phases of this model [Zhu+15; MWS20].

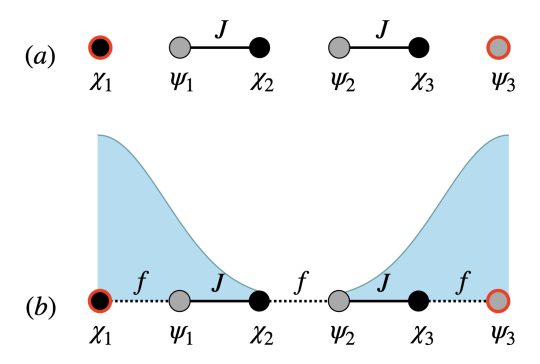


Figure 4.1: Schematic of the localised (a) and delocalised (b) edge modes, such that the latter are described by extended operators as introduced in Eq. (4.5), where the χ_i and ψ_i operators represent left and right parafermions occupying each site of the chain, as per Eq. 4.1. The shaded curves indicate their support on the bulk parafermions.

4.2.2 Parafermion edge modes

When both time-reversal and spatial-parity symmetries are broken, parafermion zero-energy modes can emerge in the parafermion chain, localised at its edges. These are characteristic of topological order, and described by the left and right edge mode operators Ψ_L and Ψ_R , which obey the relations

$$[H, \Psi_L] = [H, \Psi_R] = 0, \quad \omega^P \Psi = \omega \Psi \omega^P \tag{4.4}$$

where $\omega^P = \prod_{j=1}^L \tau_j^{\dagger}$ is the \mathbb{Z}_3 symmetry generator. These properties respectively describe that these are zero energy modes, which map between \mathbb{Z}_3 parity sectors, giving rise to the three-fold degeneracy of the energy spectrum of H. From Eq. (4.1) it is clear that exact PEMs exist when $f_i = 0 \ \forall \ i$ such that $[H, \chi_1]_{f_i=0} = [H, \psi_L]_{f_i=0} = 0$ for a chain of length L.

Since the system exhibits an energy gap, one expects its PEMs to remain approximate zero-modes for small enough f/J, with their support on the bulk of the chain exponentially suppressed in their distance to the bulk parafermions, as shown in Fig. 4.1 (b). The left edge mode operator of a chiral parafermion was constructed in Ref. [Fen12] up to order f/J (where the couplings were taken to be uniform across the chain) using an iterative procedure, and takes the form

$$\Psi_L = \chi_1 - 2ife^{-i\hat{\phi}}X + 2ife^{i\hat{\phi}}\chi_1^{\dagger}Y + \dots \tag{4.5}$$

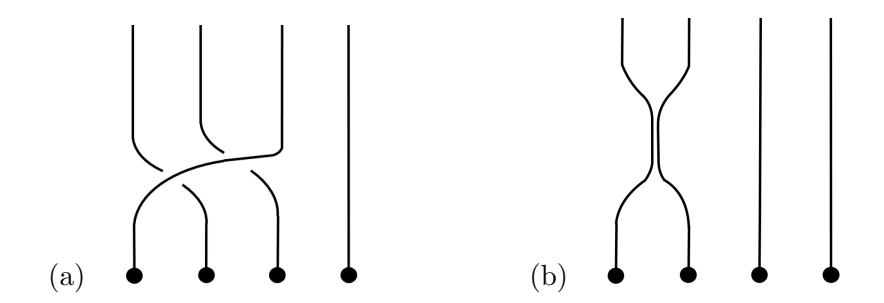


Figure 4.2: Schematic of single qutrit gates on a logical qutrit encoded in four parafermions denoted by the black dots. Their world-lines are depicted as time flows upwards. Sub-figure (a) represents a topological S gate produced by parafermion braiding [HL16]. In sub-figure (b) the closing distance between the world-lines of the first two parafermions represents the non-topological dynamical gate accessible by parafermion edge mode interaction.

where

$$X = \frac{1}{4J} \frac{1}{\sin(3\phi)} (\psi_1 + e^{2i\phi} \chi_2 + e^{-2i\phi} \omega \psi_1^{\dagger} \chi_2^{\dagger})$$
 (4.6)

and $Y=-X^{\dagger}$. It is straightforward to show that the right edge mode can be derived in a similar fashion. This procedure can be iterated, with the dimensionless expansion parameter $f/(2J\sin(3\hat{\phi}))$, but does not work at the approach of the parity-invariant ferromagnetic and anti-ferromagnetic points. One can see that the symmetric points $\phi=\frac{\pi}{6} \pmod{\frac{\pi}{3}}$ are the most robust for the existence of edge modes. We note that such edge modes have a strong character, necessary for such an analysis to hold [Mor+17].

4.2.3 Computing with parafermions

Regardless of the underlying physical system which gives rise to parafermionic excitations, computation relies on the ability to adiabatically braid and fuse parafermions and distinguish between their fusion outcomes. Combining these capabilities realises a set of exact unitary operators and measurements. In Ref. [HL16], Hutter and Loss derived the braiding operators acting on a logical qudit encoded using four \mathbb{Z}_n parafermions. In the qutrit case, one can

write the most general unitary representation of such gates as

$$U_i = \frac{1}{\sqrt{3}} \sum_{m \in \mathbb{Z}_3} c_m(\Lambda_i)^m, \tag{4.7}$$

where $\Lambda_i = \omega p_i p_{i+1}^{\dagger}$ are local parity operators for parafermions p_i and p_{i+1} , and c_m are coefficients derived by satisfying far-commutativity and the Yang-Baxter equation [Jim89]. The parity operators can be identified with

$$\Lambda_{2i-1} = X_i^{\dagger}, \qquad \Lambda_{2i} = Z_i Z_{i+1}^{\dagger} \tag{4.8}$$

which admit the same spectrum as that of the generalised qutrit Pauli operators, namely $\{1, \omega, \bar{\omega}\}$. Hence, an eigenbasis $\{|0\rangle, |1\rangle, |2\rangle\}$ can be defined for each parity operator such that $\Lambda_i |m_i\rangle = \omega^m |m\rangle_i$, for $m \in \mathbb{Z}_3$. These states form a basis of the fusion space of the pair of parafermions p_i and p_{i+1} . The form of the ansatz in Eq. 4.7 expresses the most general way of combining local phase shifts, introduced by powers of the parity operators Λ_i , into a unitary braid operation. Summing over these powers allows the braid operation to involve different levels or excitations of the parafermions. The coefficients c_m represent the amplitude of each phase shift, enabling a general unitary transformation that captures all possible braiding operations.

More generally, a three-dimensional Hilbert space is associated with each pair of parafermions. A qutrit can also be encoded into the fusion space of four parafermions $\{p_1, p_2, p_3, p_4\}$. The corresponding Hilbert space can be restricted under a global parity constraint $\Lambda_1\Lambda_3 = 1$. The group of unitaries generated by U_1, U_2 and U_3 as defined in Eq. 4.7 acts on this computational subspace, spanned by the states $\{|0\rangle_1 |3\rangle_3, |1\rangle_1 |2\rangle_3, |2\rangle_1 |1\rangle_3\}$. The authors showed that the braids U_1 and $U_1U_2U_1$ (up to global phases) respectively act on the logical space following

$$X \to X Z^\dagger, \ Z \to Z \ \text{ and } \ X \to Z, \ Z \to X^\dagger.$$

These gates have been proven to generate the single qutrit Clifford group [Far14]. In Fig. 4.2(a)

we show the $U_1U_2U_1$ braid which realises the topological S gate. However, Clifford unitary operators alone do not allow for universal quantum computing. In our study, we consider a similar approach to that in Ref. [BK05], namely allowing the parafermion modes to interact by bringing them close together so as to generate a dynamical non-Clifford unitary on the logical space.

4.3 A dynamical gate from parafermion interaction

The main objective of this section is to understand how parafermion edge modes interact when the f_i couplings in Eq. (4.1) are non-zero. This interaction ensures that one can induce a tunnelling process by transporting such PEMs within a sufficient distance of each other, running the interaction for a desired time interval and returning the anyons to their initial positions, whereby a dynamical gate is applied on a qutrit encoded in the degenerate ground subspace of the system [BK05; SFN15b].

4.3.1 Decimation of the highest-energy term

The strongly interacting nature of parafermion systems makes their analytical study challenging, particularly the computation of their spectrum.

A common approach for studying complex systems with strong interactions is to employ numerical techniques such as Density Matrix Renormalisation Group (DMRG) methods. This provides a powerful method for solving one-dimensional systems by truncating the Hilbert space efficiently, in order to compute the ground states and low-energy excitations. However, such techniques are not analytically tractable for the purpose of deriving the full spectrum of a system, or other critical properties. Real-space renormalisation group (RG) methods offer an alternative approach, particularly effective in strongly interacting disordered systems. In Ref. [Fis95], Fisher introduced a real-space RG method for the random transverse-field Ising model, which proceeds by decimating, i.e., removing, the largest local energy scale in the Hamiltonian. By iteratively applying this decimation, the system is simplified to an effective

description that retains the dominant physics at large length scales. Fisher's method involves two types of terms: transverse fields h_i , and nearest-neighbour couplings J_i . At each RG step, the largest energy scale is identified:

$$\Omega = \max\{J_i, h_i\},\,$$

and the term associated with Ω is treated exactly, while neighbouring terms are treated perturbatively to generate effective couplings. If the largest term is a transverse field h_i , the dominant Hamiltonian term is $H_0 = -h_i \sigma_i^x$, with eigenstates $|+\rangle_i$ and $|-\rangle_i$, with energy splitting $2h_i$. The spin at site i is thus 'frozen' in the ground state, which effectively eliminates it from the chain. Then, the perturbation includes the neighbouring bonds:

$$V = -J_{i-1}\sigma_{i-1}^z\sigma_i^z - J_i\sigma_i^z\sigma_{i+1}^z.$$

To second order in perturbation theory, this generates an effective interaction between sites i-1 and i+1, i.e.

$$\tilde{J} = \frac{J_{i-1}J_i}{h_i}.$$

The resulting effective Hamiltonian is $\tilde{H} = -\tilde{J}\sigma_{i-1}^z\sigma_{i+1}^z$. Hence, the original two bonds are replaced by a single effective bond, and one spin is eliminated from the chain. Alternatively, if the largest coupling is a bond J_i , the dominant Hamiltonian term is $H_0 = -J_i\sigma_i^z\sigma_{i+1}^z$, with two degenerate ground states, and an energy gap of $2J_i$ to excited states. The cluster of sites (i, i+1) is therefore treated as an effective spin. The perturbation now comes from transverse fields:

$$V = -h_i \sigma_i^x - h_{i+1} \sigma_{i+1}^x,$$

which induces tunnelling between the two degenerate ground states. To second order, this results in an effective transverse field acting on the cluster:

$$\tilde{h} = \frac{h_i h_{i+1}}{J_i}.$$

Hence, after decimating bond J_i , spins i and i+1 are replaced by one effective spin with renormalised transverse field \tilde{h} . These RG steps can be repeated recursively, and exhibit a duality between bond and field decimation. An important result in Ref. [Fis95] is that in a disordered system, as the energy scale of the system decreases, the randomness in couplings and fields increases without bound. This leads to infinite-randomness fixed points at criticality, where the system becomes asymptotically dominated by large fluctuations in couplings. In contrast, a clean system has translational invariance, with uniform couplings. If there exists a clear hierarchy between energy scales, i.e. $h \ll J$ or $h \gg J$, the RG method can still yield reliable approximations. In these regimes, the dominant coupling is well-defined, allowing controlled perturbative decimation. However, near the zero-temperature phase transition at h/J = 1, where $h \sim J$, there is no natural hierarchy. In this case, higher-order corrections become significant, and real-space RG loses its predictive power.

We utilise this method for the treatment of a \mathbb{Z}_3 -parafermion chain where the f_i onsite couplings are weak, such that the largest energy is the bond between chain sites as shown in Fig. 4.3 (a) for a three-site chain. This process freezes the clock states at neighbouring sites together in a ferromagnetic cluster with an effective field $f' = \frac{f_i f_{i+1}}{2J_{i,i+1}}$. This coupling is weaker than the individual f_i and f_{i+1} since the new interaction is a next-to-nearest neighbour one, which decimates the interaction between sites i and (i+1) (i.e. a parafermion pair). This process is illustrated in Fig. 4.3 (a-c). Hence, the form of the Hamiltonian remains the same, apart from an overall constant shift in the spectrum that can be neglected.

4.3.2 Effective Hamiltonian from PEM interaction

We first consider a two-site \mathbb{Z}_3 -parafermion chain with a Hamiltonian H_2 describing the two-site version of Fig. 4.3(a), such that $H_2 = F_2 + V_2$ where

$$F_{2} = -\frac{2}{\sqrt{3}}e^{-i\phi}\bar{\omega}(J_{1}\psi_{1}^{\dagger}\chi_{2}) + \text{h.c.}$$

$$V_{2} = -\frac{2}{\sqrt{3}}e^{-i\hat{\phi}}\bar{\omega}(f_{1}\chi_{1}^{\dagger}\psi_{1} + f_{2}\chi_{2}^{\dagger}\psi_{2}) + \text{h.c.}$$
(4.9)

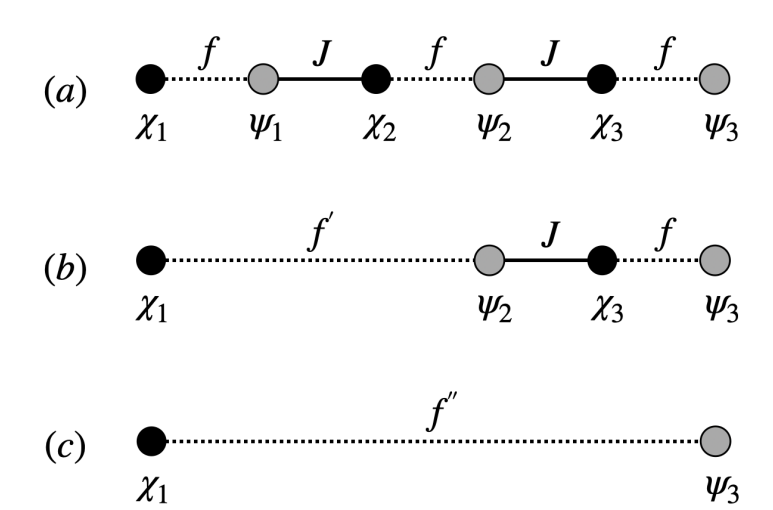


Figure 4.3: Schematic of a three-site parafermion chain with weak f and strong J couplings defined as per Eq. (4.1), where the χ_i and ψ_i represent the left and right parafermion operators at each site of the chain (a). The chains in (b) and (c) represent the decimation of the terms connecting parafermions in the bulk upon applying the RG method, with a final weaker effective coupling f''.

and we set the phase parameters to $\phi = \hat{\phi} = \frac{\pi}{6}$. To define the Hamiltonian we chose the representation

$$\sigma = \begin{pmatrix} 1 & 0 & 0 \\ 0 & \omega & 0 \\ 0 & 0 & \omega^2 \end{pmatrix} \quad \text{and} \quad \tau = \begin{pmatrix} 0 & 0 & 1 \\ 1 & 0 & 0 \\ 0 & 1 & 0 \end{pmatrix}, \tag{4.10}$$

to express the parafermion operators in Eq. (4.2). The eigenspectrum of F_2 is three-fold degenerate, with eigenvalues $\{-2J_1, 0, 2J_1\}$ and three degenerate ground states $\{|e_0\rangle, |e_1\rangle, |e_2\rangle\}$. When f_1 and f_2 are non-zero, the edge modes of the parafermion chain are no longer exactly localised, as described by Eq. (4.5). A perturbative treatment of the effect of F_2 on the ground state manifold, in terms of f_1/J_1 and f_2/J_1 , produces the effective coupling induced by an interaction between the edge parafermions χ_1 and ψ_2 up to arbitrary order. The first order perturbation vanishes for our system, while the second order terms contribute to an effective

Hamiltonian given by

$$H_2^{(2)} = -\frac{f_1^2 + f_2^2}{J_1} + \frac{f_1 f_2}{J_1} (\omega \chi_1 \psi_2^{\dagger} + \bar{\omega} \psi_2 \chi_1^{\dagger}). \tag{4.11}$$

where we can see that the first term is a global energy shift which we neglect, and the second term characterises the interaction of the PZMs, which happens with a coupling $f' = \frac{f_1 f_2}{J_1}$, and acts on the ground energy subspace with the following Hamiltonian

$$H_2^{(2)} = \begin{pmatrix} 0 & \omega & \bar{\omega} \\ \bar{\omega} & 0 & \omega \\ \omega & \bar{\omega} & 0 \end{pmatrix}. \tag{4.12}$$

Following the prescription described in 4.3.1, the form of the second term in Eq. (4.11) indicates that the decimation of the parafermion pair (ψ_1, χ_2) induces an f' interaction between the edge parafermions. This result is similar to the Majorana case explicitly shown in Ref. [Shi11] where the coupling between Majorana zero-modes takes an similar form for L=2. We iterate the above decimation procedure for a chain of arbitrary length L by decimating bonds from left to right to derive the interaction between the edge modes of a chain of arbitrary size, as shown in Fig. 4.3. We find that the effective Hamiltonian up to second order in the energy perturbation is given by

$$H_L^{(2)} = -\frac{1}{J_{L-1}} \begin{pmatrix} \prod_{i=1}^{L-1} f_i^2 \\ \prod_{i=1}^{L-2} J_i^2 \end{pmatrix} + \int_L^L + \frac{\prod_{i=1}^{L} f_i}{\prod_{i=1}^{L-1} J_i} (\omega \chi_1 \psi_L^{\dagger} + \bar{\omega} \psi_L \chi_1^{\dagger})$$
(4.13)

The PEM interaction term remains exactly $H_2^{(2)}$ in Eq. (4.12), and has an eigenspectrum of

$$E_0 = 2A$$

$$E_1 = -A$$

$$E_2 = -A$$

$$(4.14)$$

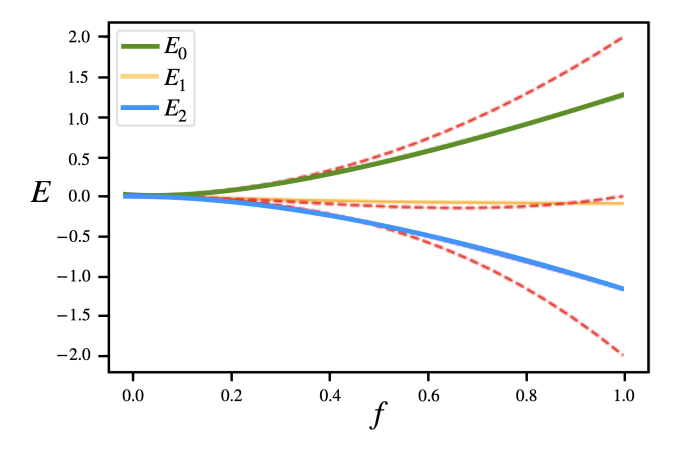


Figure 4.4: The three lowest energy eigenvalues for H_2 with $J_i = 1 \,\forall i$ and varying f. The numerical values are indicated by the continuous lines. The perturbative approximations up to third order are indicated with red dotted lines, which are in agreement with the exact results for a wide range of f values.

which now discriminates between the basis states up to a global \mathbb{Z}_3 rotation), where the energy scale is given by

$$A = \frac{\prod_{i=1}^{L} f_i}{\prod_{i=1}^{L-1} J_i}.$$
 (4.15)

The exact eigenvalues of the three lowest energy states of H_2 (for numerical convenience) are numerically plotted in Fig. 4.4 for $f_i = f \,\forall i$ and $J_i = 1 \,\forall i$, where the global energy shift was deducted. The degeneracy is lifted by the splitting of the eigenstates when $f \neq 0$. The energy shifts obtained using the decimation prescription to study the effect of edge mode interaction are plotted up to third order in f/J, and agree with the exact spectrum in the perturbative, i.e. low f/J regime.

4.3.3 Asymmetric \mathbb{Z}_3 parafermion chain

In this subsection we report the same procedure as in 4.3.2 while allowing the parafermion chain to deviate from the super-integrable point of the chiral phase by setting $\phi = \pi/6$ and leaving $\hat{\phi}$ as a free parameter. In this case, the effective Hamiltonian for the two-site chain

up to second order in f/J is given by

$$H_2^{(2)}(\hat{\phi}) = -\frac{f_1^2 + f_2^2}{J_1} - \frac{f_1 f_2}{J_1} (\bar{\omega} e^{2i\hat{\phi}} \chi_1 \psi_2^{\dagger} + \omega e^{-2i\hat{\phi}} \psi_2 \chi_1^{\dagger})$$
(4.16)

such that the parafermion interaction takes the form

$$H_2^{(2)}(\hat{\phi}) = \begin{pmatrix} 0 & e^{-2i\hat{\phi}} & e^{2i\hat{\phi}} \\ e^{2i\hat{\phi}} & 0 & e^{-2i\hat{\phi}} \\ e^{-2i\hat{\phi}} & e^{2i\hat{\phi}} & 0 \end{pmatrix}$$
(4.17)

up to a global energy shift, which maintains the structure of $H_2^{(2)}$ in Eq. (4.11), with an extra phase factor in the interaction term. The eigenvalues of $H_2^{(2)}(\hat{\phi})$ are given by:

$$E_{0} = 2\cos(2\hat{\phi})$$

$$E_{1} = -\cos(2\hat{\phi}) + \sqrt{3}\sin(2\hat{\phi})$$

$$E_{2} = -\cos(2\hat{\phi}) - \sqrt{3}\sin(2\hat{\phi}),$$
(4.18)

where setting $\hat{\phi} = \frac{\pi}{6}$ recovers the result in Eq. (4.13). This suggests that by allowing a margin of deviation closer to the ferromagnetic or anti-ferromagnetic phases of the system, one can modify the form of the interaction in Eq. (4.17). We note that while the following will focus on the dynamical gate from the symmetric point, setting the parameter $\hat{\phi} = \frac{\pi}{4}$, which still exists in the chiral phase of the chain, gives rise to an interesting eigenspectrum for the purpose of quantum computation.

4.4 A Non-Clifford gate \mathcal{U} from parafermion edge-mode interaction

4.4.1 Dynamical gate

The results in section 4.3.2 show that the interaction between the parafermions edge modes is described by a Hamiltonian which acts non-trivially on the encoded ground space, for which the leading term is shown in Eq. (4.12). Moreover, one can verify that this interaction (i.e. $H_{\rm int} = \omega \chi_1 \psi_L^{\dagger} + {\rm h.c.}$) commutes with the parity operator Λ_1 defined in subsection 4.2.3 and therefore preserves the computational subspace [HL16]. Hence, bringing the parafermion edge modes closer together allows for a dynamical unitary operation given by the evolution of the interaction Hamiltonian

$$\mathcal{U} \approx e^{-i\beta H_{\rm int}t},$$
 (4.19)

where β is a constant which depends on the effective coupling between the edge modes, namely up to second order

$$\prod_{i=1}^{L} f_i / \prod_{i=1}^{L-1} J_i. \tag{4.20}$$

4.4.2 \mathcal{U} in the Clifford hierarchy

The Clifford hierarchy introduced in Eq. 2.28 is useful to categorise the accessible non-Clifford gates using the dynamical gate \mathcal{U} , and probe geometrically significant gates and eigenstates for fault-tolerant universal quantum computation. In particular, defining gates such as the qudit equivalent of the $\pi/8$ -gate is useful to design magic state distillation protocols. It was shown in Ref. [CGK17] that a diagonal gate in any level of the Clifford hierarchy for qudits of dimension d can be written in a diagonal form. The qutrit case is given by

$$U_v = U(v_0, v_1, ...) = \sum_{j \in \mathbb{Z}_2} \zeta^{v_k} |k\rangle \langle k| \quad (v_k \in \mathbb{Z}_9),$$
 (4.21)

where $\zeta = e^{\frac{2\pi i}{9}}$, the indices v_k are given by: $v_0 = 0 \mod 9$, $v_1 = 6z' + 2\gamma' + 3\epsilon' \mod 9$, $v_2 = 6z' + \gamma' + 6\epsilon' \mod 9$ and $z', \gamma', \epsilon' \in \mathbb{Z}_3$. Following this insight, one can see that the dynamical gate \mathcal{U} generated by the parafermion interaction on a logical qutrit state can be decomposed as

$$\mathcal{U} = H \, \mathcal{U}_D H^{\dagger} \tag{4.22}$$

where \mathcal{U} if the gate in eq. 4.19, H is the qutrit Hadamard operator, and \mathcal{U}_D the diagonal matrix (up to a global phase) respectively given by the following matrix representations

$$H = \frac{1}{\sqrt{3}} \begin{pmatrix} 1 & 1 & 1\\ 1 & \omega & \bar{\omega}\\ 1 & \bar{\omega} & \omega \end{pmatrix}, \quad \mathcal{U}_D \sim \begin{pmatrix} 1 & 0 & 0\\ 0 & 1 & 0\\ 0 & 0 & e^{i\theta} \end{pmatrix}$$
(4.23)

where θ is specified by the interaction strength and duration in Eq. (4.19).

Furthermore, it was shown that analogously to the qubit case, the qutrit T-gate is required to be in $C_3^{(3)}/C_3^{(2)}$, i.e. belong in the third level of the Clifford hierarchy but not be a Clifford gate. For that, one requires that $TXT^{\dagger} \in C^{(2)}$, where $X = \sum_{j \in \mathbb{Z}_3} |j+1 \mod 3\rangle \langle j|$ is the qutrit Pauli-X operator. Since we are interested in which gates we can access with \mathcal{U} , we similarly verify its action on X and find that

$$\mathcal{U}_D X \mathcal{U}_D^{\dagger} = X M(\theta) \tag{4.24}$$

where $M(\theta) = \text{diag}\{1, e^{i\theta}, e^{-i\theta}\}$. In particular, $M(\frac{2\pi}{3}) = Z$ and $M(\frac{2\pi}{9}) = T$ where

$$Z = \sum_{j \in \mathbb{Z}_3} \omega^j |j\rangle\langle j| \quad \text{and} \quad T = \sum_{j \in \mathbb{Z}_3} \zeta^{j^3} |j\rangle\langle j|$$
 (4.25)

are matrix representations of the qutrit Z and T (analogous to a qubit $\frac{\pi}{8}$ -phase gate) gates. Hence, for $\theta = \frac{2\pi}{9}$, $\mathcal{U}_D \in \mathcal{C}^{(4)}$, i.e. in the fourth level of the Clifford hierarchy.

In general, for a phase $\theta = \frac{2\pi}{3^m}$, we can write M in the following diagonal form [CGK17]

where p = 3 is the qudit dimension:

$$M\left(\frac{2\pi}{3^m}\right) = P_m(k) = \sum_{j=0, k \neq j}^p \left(|j\rangle\langle j| + e^{\frac{2\pi i}{3^m}}|k\rangle\langle k|\right)$$
(4.26)

where $P_m(k) \in \mathcal{D}_{m,p-1}$, the set of diagonal qutrit unitary operators with precision m and degree a is defined recursively as

$$\mathcal{D}_{m,a} = \langle U_{m,b} \rangle_{b=1}^{a} \{ e^{i\phi} \} \mathcal{D}_{m-1,p-1}$$
(4.27)

where

$$U_{m,b} := \sum_{j \in \mathbb{Z}_p} \exp(\frac{2\pi i}{p^m} j^b) |j\rangle\langle j|,$$

where $\langle U_{m,b}\rangle_{b=1}^a$ is the group generated by the set of diagonal unitary gates $U_{m,b}$ where $b \in \{1, ..., a\}$, and $\{e^{i\phi}\}$ accounts for all global phase factors. This definition implies that $\mathcal{U}_D \in \mathcal{D}_{m,2}$. Cui et. al. also showed that for $m \in \mathbb{N}$ and $1 \le a \le p-1$, $\mathcal{D}_{m,a} = \mathcal{C}_d^{((p-1)(m-1)+a)}$. According to this result $\mathcal{D}_{m,2} = C_d^{(2m)}$, which signifies that for $\theta = \frac{2\pi}{3^m}$, the corresponding \mathcal{U}_D belong to the 2m-th levels of the Clifford hierarchy, i.e.

$$\mathcal{U}_D \in \mathcal{C}^{(2m)},\tag{4.28}$$

so that for $m \geq 2$, U_D is a non-Clifford operator. As stated in Eq. (4.22), \mathcal{U} is related to \mathcal{U}_D by a Hadamard operator, which belongs to $\mathcal{C}^{(2)}$. It is useful here to introduce Lemma 1 below which follows from Eq. (2.28), along with the observation that $H^3 = H^{\dagger}$.

Lemma 4.1. Let $U \in \mathcal{C}^{(k)}$ and $P \in \mathcal{C}^{(1)}$. Then,

$$(HUH^{\dagger})P(HU^{\dagger}H^{\dagger}) = H\tilde{U}H^{\dagger} \tag{4.29}$$

for some $\tilde{U} \in \mathcal{C}^{(k-1)}$.

Theorem 4.1. Let $U = HVH^{\dagger}$ where $H \in \mathcal{C}^{(2)}$, $V \in \mathcal{C}^{(n)}$ and $\mathcal{C}^{(k)}$ is k-th level of the Clifford

CHAPTER 4. UNIVERSALITY OF \mathbb{Z}_3 PARAFERMIONS VIA EDGE MODE INTERACTION92

hierarchy, it then follows that $U \in \mathcal{C}^{(n)}$.

Proof. Let $V \in \mathcal{C}^{(n)}$ and P be an arbitrary Pauli operator such that $VPV^{\dagger} \in \mathcal{C}^{(n-1)}$. We define the unitary operator $U = HVH^{\dagger}$. By Lemma 1, it follows that

$$UPU^{\dagger} \sim H\beta_{n-1}H^{\dagger} \tag{4.30}$$

where β_i is a unitary operator in the i^{th} level of the Clifford hierarchy, i.e. $\beta_i \in \mathcal{C}^{(i)}$. The case n=2 is straightforward, since $VPV^{\dagger} \in \mathcal{C}^{(1)}$, from which we obtain

$$(HVH^{\dagger})P(HV^{\dagger}H^{\dagger}) \in \mathcal{C}^{(1)}. \tag{4.31}$$

For general $n \geq 3$, starting from Eq. (4.30) and again acting on an arbitrary Pauli operator with $H\beta_{n-1}H^{\dagger}$, the following holds:

$$(H\beta_{n-1}H^{\dagger})P(H\beta_{n-1}^{\dagger}H^{\dagger}) \sim H\beta_{n-2}H^{\dagger}, \tag{4.32}$$

where $P \in \mathcal{C}^{(1)}$. This procedure can be iterated m times such that for m = 0:

$$(H\beta_n H^{\dagger}) P(H\beta_n^{\dagger} H^{\dagger}) \sim H\beta_{n-1} H^{\dagger}. \tag{4.33}$$

Then, for general m, it follows that

$$(H\beta_{n-m}H^{\dagger})P(H\beta_{n-m}^{\dagger}H^{\dagger}) \sim H\beta_{n-m-1}H^{\dagger}. \tag{4.34}$$

Finally, when m = n - 3:

$$(H\beta_3 H^{\dagger}) P(H\beta_3^{\dagger} H^{\dagger}) \sim H\beta_2 H^{\dagger} \tag{4.35}$$

where one identifies $H\beta_2H^{\dagger} \in \mathcal{C}^{(2)}$. Using equation 4.33 recursively, we conclude that $H\beta_nH^{\dagger} \in \mathcal{C}^{(n)}$, and therefore that $U \in \mathcal{C}^{(n)}$.

Moreover, using Theorem 1, we show that parametrising $\theta = \frac{2\pi}{3^m}$ gives rise to the gates in

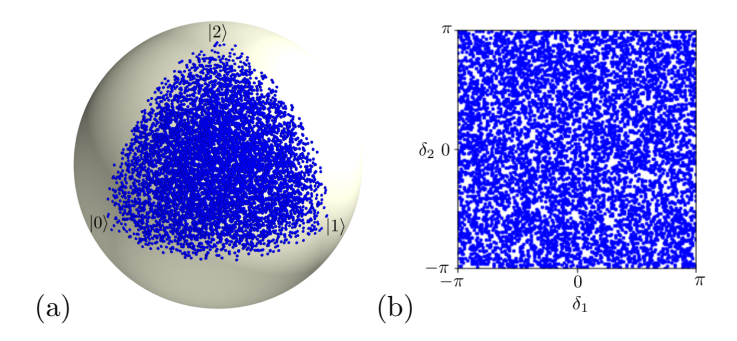


Figure 4.5: Magnitude (a) and phase (b) plots for 5000 sampled states computed by creating random words of length 50 using \mathcal{U} and Clifford operations, and applying them on the initial state $|\psi\rangle = |0\rangle$.

even levels of the Clifford hierarchy, i.e. that

$$\mathcal{U} \in \mathcal{C}^{(2m)}.\tag{4.36}$$

Setting m=2 gives rise to the gate \mathcal{U} in $\mathcal{C}^{(4)}$ directly, from which implementing the qutrit T-gate is done with the combination

$$T = X^{\dagger} \mathcal{U}_D X \mathcal{U}_D^{\dagger}. \tag{4.37}$$

In order to obtain a set dense in SU(d), one requires at least one non-Clifford element in the operational gate-set as shown in Ref. [CAB12] for prime d by combining results from Nebe, Rains and Sloane [NRA10]. The above illustrates how the parafermion interaction provides such gates, by choosing a parametrisation which creates a gate from low levels of the Clifford hierarchy, namely third and fourth. Additionally, we note that the form of the qutrit T-gate arises naturally from the eigenspectrum of the interaction Hamiltonian in Eq. (4.17) for $\hat{\phi} = \frac{\pi}{4}$.

4.4.3 Universality with \mathcal{U}

In the following, we consider a generic logical qutrit state encoded in a set of parafermions, as described in 4.2.3. In order to study the universality of the parafermion computing scheme

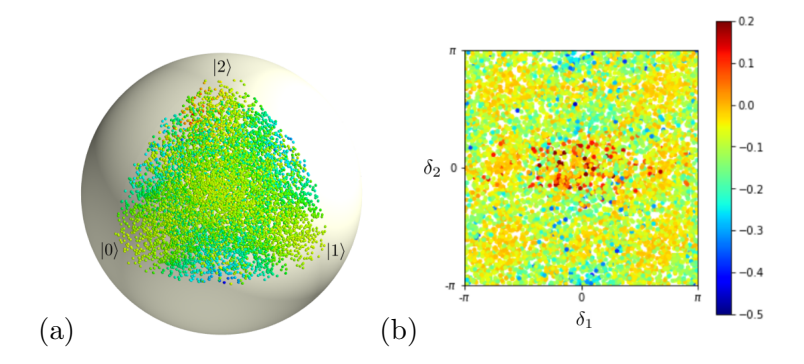


Figure 4.6: Magnitude (a) and phase (b) plots of a dense set of 10000 sampled qutrit states using random words of length 50 composed of the \mathcal{U} and Clifford operations. The colour plot indicates the values of \mathcal{M} .

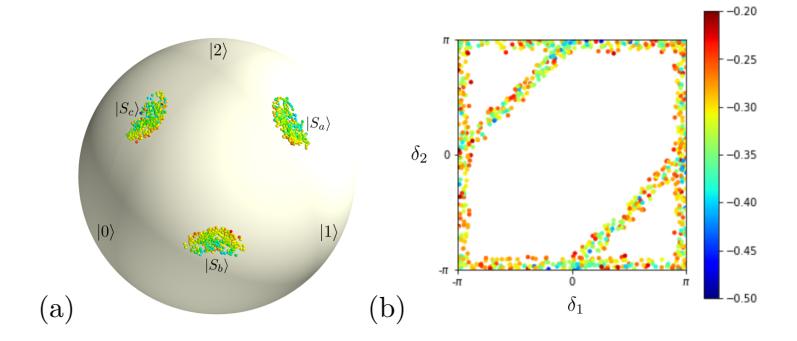


Figure 4.7: Magnitude (a) and phase (b) plots of states close to the strange states $|S_a\rangle$, $|S_b\rangle$ and $|S_c\rangle$, within a trace distance of 0.2. The states were sampled using random words of length 50 composed of the \mathcal{U} and Clifford operations. The colour plot indicates the values of \mathcal{M} .

that encompasses parafermion zero-mode braiding as well as interaction, we created a series of words $W := U_1U_2...U_n$ such that U_i is chosen randomly from the set $\{X, S, H, \mathcal{U}\}$ where the first three elements are Clifford operators. In this representation S takes the form

$$S = \begin{pmatrix} 1 & 0 & 0 \\ 0 & \omega & 0 \\ 0 & 0 & 1 \end{pmatrix},\tag{4.38}$$

generalising the qubit \sqrt{Z} , and H is the qutrit Hadamard defined in Eq. (4.23). The non-Clifford \mathcal{U} of the set is given by Eq. (4.19) with $\theta = 1$ for simplicity. We apply words W

to an initial logical qutrit state $|\psi_{\rm ini}\rangle = |0\rangle$, and write the final states $|\psi_{\rm fin}\rangle = W |\psi_{\rm ini}\rangle$ as $|\psi_{\rm fin}\rangle = \alpha |0\rangle + e^{i\delta_1}\beta |1\rangle + e^{i\delta_2}\gamma |2\rangle$ where $\alpha, \beta, \gamma \in \mathbb{R}$. We plot the resulting phases (δ_1, δ_2) and magnitudes (α, β, γ) from the final states in Fig. 4.5 (a) and (c) by sampling 5000 words of length 50 and applying them to $|\psi_{\rm ini}\rangle$. The resulting parameter spaces are densely populated, which indicates the universality of the braiding Clifford operations supplemented with \mathcal{U} .

4.4.4 Contextual qutrit states using \mathcal{U}

With the consideration that the set $\{X, S, H, \mathcal{U}\}$ is dense in SU(3), and can be used to generate arbitrary elements in the qutrit state space using four parafermions, one can characterise such accessible states by their resourcefulness in the context of magic state distillation protocols (MSD). Indeed, MSD represents a powerful method to distil reliable quantum states from multiple noisy counterparts, which proves useful in our context since contrary to the Clifford operations, the dynamical gate \mathcal{U} is non-topological. Moreover, MSD can also be used to obtain useful non-stabiliser states granted one accesses a state in the appropriate distillable region to the former. In Ref. [Vei+12], Veitch et. al. showed that all qutrit states with positive Wigner function are undistillable, and the positive region was charted out in Ref. [ACB12]. In particular, Howard et. al. argued in Ref. [How+14] that contextuality supplies the magic for quantum computation, and introduced the following contextuality inequality

$$\mathcal{M} \equiv \max_{\mathbf{r}} \operatorname{Tr}[A^{\mathbf{r}}\rho] \overset{\text{NCHV}}{\leq} 0 \tag{4.39}$$

where ρ is an arbitrary qutrit state and the $A^{\mathbf{r}}$ are projectors onto eigenstates of the qutrit stabilizer operators given by $A^{x,z} = D^{x,z}A^{0,0}D^{x,z^{\dagger}}$ where $x,z \in \mathbb{Z}_3$ and $A^{0,0} = \frac{1}{3}\sum_{x,z}D^{x,z}$ using $D^{x,z} = \omega^{2xz}X^xZ^z$, where X and Z are the qutrit Pauli operators. The inequality sets the threshold for a non-contextual hidden variable (NCHV) model reproducing such quantum tests. We sampled a large set of qutrit states starting from a random choice of basis states, and plot the negative Wigner states, i.e. violating Eq. (4.39) indicating their contextuality measure in Fig. 4.6. In Fig. 4.6, we see an overlap of points with different \mathcal{M} . This is clearly

CHAPTER 4. UNIVERSALITY OF \mathbb{Z}_3 PARAFERMIONS VIA EDGE MODE INTERACTION96

due to the fact that the phase and magnitude projections introduced in the figures above do not constitute a direct map of the state space, though are useful to witness the coverage density of the Hilbert space accessible with our parafermion universal gate set. Indeed, we use this representation as a witness that our gate set provides access to a dense set of negative, and therefore potentially distillable states. In fact states which considerably violate Eq. (4.39) can be obtained from short gate combinations (eg. $\mathcal{U}(t_1)H\mathcal{U}(t_2)|0\rangle$ given optimal evolution times t_1 and t_2). We note from Fig. 4.6 that the majority of the 10000 sample states created using the full gate-set fulfill the condition $\mathcal{M} < 0$.

There exists a class of states which maximally violates Eq. (4.39), namely the "strange" states defined by having one negative Wigner function entry of value -1/3 [Vei+14] such as $|S_a\rangle = \frac{|1\rangle - |2\rangle}{\sqrt{2}}$ [JP20]. These are the eigenstates of the qutrit Fourier transform, and are located at the mid-sections between basis states on the magnitude plot as indicated in Fig. 4.7, with $\mathcal{M} = -0.5$. Finding a combination of gates to generate $|S\rangle$ exactly is a non-trivial problem. However, we show in Fig. 4.5 that using \mathcal{U} and Clifford gate combinations one can access states close to the strange states. We indicate in Fig. 4.7 the points of maximal \mathcal{M} by labels $|S_{a,b,c}\rangle$, and characterise this using the trace distance, i.e. $\mathcal{D} = \text{Tr}(\rho,\sigma) = \frac{1}{2}||\rho - \sigma||_1$ where ρ and σ are the density matrices of the sampled states and $|S_{a,b,c}\rangle$ respectively. In Fig. 4.7 states with $\text{Tr}(\rho,\sigma) < 0.2$ are plotted to indicate the regions of interest, and Table. 4.1 summarises the trace distances and \mathcal{M} for the three points closest to the strange states in Fig. 4.7. We note that both points admit a close to maximal violation of Eq. (4.39).

	$ S_a\rangle$	$ S_b\rangle$	$ S_c\rangle$
\mathcal{D}	0.059	0.057	0.035
\mathcal{M}	-0.436	-0.422	-0.469

Table 4.1: Trace distances \mathcal{D} and non-contextuality inequality \mathcal{M} of the three sampled states in Fig. 4.7 closest to $|S_a\rangle$, $|S_b\rangle$ and $|S_c\rangle$.

Hence, using the Clifford gates supplemented with \mathcal{U} one can possibly reach states arbitrarily close to the strange states, allowing for large enough gate sequences, and time evolutions in

Eq. (4.19). Recent results in Ref. [Pra20] show how one can distil strange states using an MSD protocol (Ternary Golay Code [Ple68]), with particularly high threshold. This showcases the advantage of accessing such states.

4.5 Discussion

Motivated by the use of direct short-range interaction between Majorana quasi-particles to achieve the $\frac{\pi}{8}$ -phase gate on a topologically encoded qubit [BK05], we investigated a similar prescription in the case of \mathbb{Z}_3 parafermions. We studied the interaction between the edge modes of a parafermion chain using exact perturbation for low orders, in order to find its effect on the degenerate ground space of the system, which is used to encode one qutrit. We find that allowing the edge modes a degree of delocalisation facilitates the generation of a nontopological dynamical gate. In particular, the structure of this gate can directly be exploited to realise interesting non-Clifford operations such as the qutrit equivalent of the (qubit) $\frac{\pi}{8}$ phase gate (provided access to extra Clifford operations), as well as unitaries in higher levels of the Clifford hierarchy. This is a crucial complement to the topological operations since the addition of any non-Clifford gate to the Clifford group generates a set of unitaries that is dense in SU(d) [CAB12]. We illustrated this universality by sampling states obtained with Clifford operations (as provided by braiding parafermions [HL16]), complemented with the dynamical non-Clifford gate \mathcal{U} , visualised using two parameter spaces which we defined to characterise qutrit states. While such representations served their purpose within our study, we refer the reader to the recent Ref. [Elt+21] by Eltschka et al. for a three-dimensional model of the qutrit state space that captures its prominent and essential geometric features. We additionally adopted recent results on the universality of one-qudit gates [SK17] in order to test our gate set supplemented with the non-topological \mathcal{U} with success, which was completed as a sanity check and left outside the scope of our presented results.

The non-Clifford gate accessible through PEM interaction is not topologically protected. However, fault-tolerance can be reinstated using stabilizer operations in a magic state distillation protocol [BK05; CAB12; ACB12]. Contextuality represents a critical resource for MSD and can be characterised by a state-independent measure \mathcal{M} [How+14]. Using this result, we showed that our gate set provides states with contextuality under stabilizer measurements, which can be exploited in appropriate distillation routines. While we studied the \mathbb{Z}_3 case for convenience, one could generalise the above analysis to \mathbb{Z}_d parafermion edge-mode interaction, particularly for prime odd d as the emergent gates are of interest in the context of quantum information processing.

Finally, in additional related work presented in Appendix A1, we demonstrate how the interaction and braiding of two parafermion edge modes can be simulated using a four-level Rydberg system. This provides an experimental platform for probing simulated topological qudits. Alternatively, it has been suggested to use ultra-cold molecules to realize qudits with different four vibrational levels as shown in [Saw+20] which benefits from its longer coherence time [Gre+21]. However, the strength of dipole-dipole interactions between molecules remains less significant than in the case of Rydberg atoms, making them more favourable to implement a qutrit. Finally, it is worth mentioning that quantum simulations with qutrits might yield a novel tool for studying quantum many-body physics such as quantum phase transitions and out-of-equilibrium phenomena. It is of interest that the Hamiltonian of many qutrit systems with dipole-dipole interactions can show quantum phase transitions or topological effects, which might yield exotic results in condensed matter physics. As an example, in recent work from Blok et al. [Blo+21] quantum information scrambling was witnessed on a superconducting processor which can provide insight into quantum chaos and black hole dynamics.

Chapter 5

Minimising surface-code failures using a colour-code decoder

5.1 Introduction

We envisage that a large-scale quantum computer will operate by performing fault-tolerant logic gates on qubits encoded using quantum error-correcting codes (QEC) [Sho95; Sho96; CS96; Ter15; Bro+16; CTV17]. As quantum information is processed, a classical decoding algorithm [Den+02; DP10; WL12; Anw+14; HWL14; TM17; PK21; DN21] will be used to interpret syndrome information that is collected by making parity measurements over the physical qubits of a code, to determine the errors it experiences. It is important to design high-performance and practical decoding algorithms to minimise the number of failure mechanisms that lead to a logical qubit error in real quantum systems. Such algorithms will reduce the high resource cost of encoding logical qubits, as better decoding algorithms will allow us to achieve a target rate of logical failures using fewer physical qubits.

Topological codes, such as the surface code [Kit03a; BK98; Den+02; Fow+12b] and colour code [BM06; BM07; Bom15; KB15], are among the most promising quantum error-correcting codes to be realised with quantum technology that is now under development [Ega+21;

Rya+21; Kri+22; Sun+23; AI23; Gup+23]. This is due to their layout which can be realised with a planar array of qubits with only nearest-neighbour interactions, and their demonstrated high threshold error rates, such that they can function under significant laboratory noise. A well-established class of decoders for the surface code [Den+02; WHP03; RH07; Fow+12b] is based on the minimum-weight perfect-matching algorithm (MWPM) [Edm65; HG23].

We colloquially refer to these decoders as matching decoders. Matching decoders give rise to high thresholds for topological codes, and have been demonstrated to be highly versatile in that they can be adapted to correct for different noise models [Fow13a; FM14; HL14; NB19; Tuc+20; Bon+21; SBB21; Sie+22; Lin+23], as well as different codes [BW20; NB21; MWB23], including the colour code [Wan+10; DT14; Cha+20; BKS21; SB22; KD23] and surface code variants [RBH05; HB21; GNM22; Pae+23; Kes+22]. See the perspective article, Ref. [Bro22] for a discussion.

A matching decoder exploits the structure of the code to identify errors which likely caused the error syndrome. Specifically, we take subsets of the syndrome data and represent them on a lattice, such that this syndrome data respects certain symmetries of the code [Kit03a; BW20; Bro22]. These symmetries are characterised by the fact that errors produce syndrome violations, commonly known as defects, in spatially local pairs over the lattice. Given such a lattice, the MWPM algorithm can be used to pair spatially local defects. In turn, this pairing can be interpreted to identify an error that is likely to have given rise to the syndrome, such that a correction that recovers the encoded state can be determined.

The performance of a matching decoder is determined by the choice of syndrome lattice. The surface code has consistently demonstrated high thresholds by concentrating on syndrome lattices which correct for bit-flip errors and dephasing errors separately. However, without additional decoding steps [Fow13b; DT14; Hig+23], such decoders cannot identify correlations between these two error types that occur in common error models such as depolarising noise. See for example Refs. [DP10; Fow13b] where candid discussions are presented on the limitations of matching decoder variations correcting for depolarising noise. In this work, we introduce a syndrome lattice for the surface code that accounts for correlations between

bit-flip and dephasing errors, which we obtain by exploiting a correspondence between the surface code and the colour code, commonly known as an unfolding map [BDP12; KYP15; BS15; CT16]. Through this mapping, we can adopt colour-code decoding algorithms to correct noise on the surface code. Indeed, a syndrome lattice for our decoder naturally ensues by adapting the decoding methods introduced in Ref. [SB22].

We find that our unified decoder determines a least-weight correction for all weight d/2depolarising noise errors for surface codes with even distance d. As such, in the limit of low error rate, we obtain optimal logical failure rates. In contrast, conventional matching decoders that do not account for spatially-correlated multi-qubit errors have a logical failure rate $O(2^{d/2})$ higher than the decoder we present. We adopt a number of methods to analyse the performance of our decoder at low error rates. We first evaluate the number of weight d/2 errors that should lead to a logical failure for both our matching decoder, as well as a conventional matching decoder. We verify our expressions with exhaustive searching of weight d/2 errors. In addition, we measure the logical failure rate of our decoder using the splitting method [Ben76; BV13]. We find the numerical results we obtain to be consistent with our analytic results in the limit of vanishing physical error rate, thereby verifying the performance of our decoder in comparison to conventional decoders. We also show that the threshold of our decoder is comparable to more conventional decoding methods. Finally, we investigate the performance of our scheme to decode the colour code undergoing bit-flip noise. We find our analysis sheds light on the role of entropy in quantum error correction with the matching decoders that are central to our study [SB10; CA18; Bev+19].

This chapter reports the work in Ref. [Ben+23a], and is structured as follows. The quantum error-correcting codes of relevance in this study, namely the surface code and colour code, were introduced in Sec. 2.3. In Sec. 5.2, we define the concept of symmetries of QEC codes, apply it to the colour code, then explain how it can be used to obtain matching decoders. We also explain why the unified decoder is capable of decoding high-weight errors. In Sec. 5.3, we describe the mapping from surface to colour code, and introduce a noise mapping from depolarising errors on the surface code to bit flips on the colour code. We present analytical

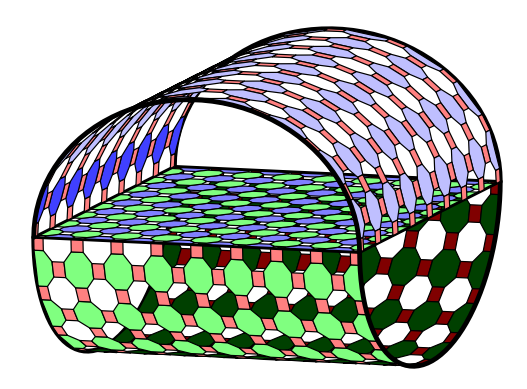


Figure 5.1: The manifold which preserves the global symmetry of the square-octagonal colour code is a punctured torus.

and numerical results supporting the out-performance of the unified decoder over its restricted counterpart under depolarising noise on the surface code in Sec. 5.4, and we present results using the same decoder to correct bit-flip noise on the colour code in Sec. 5.5. We finally offer concluding remarks in Sec. 3.4.

5.2 Materialised symmetries and decoding

We start by reviewing the concept of materialised symmetries for topological quantum codes introduced in Refs. [Kit03a; BW20; SB22; Bro22]. These symmetries give rise to a parity conservation law among syndrome defects, that is, any error creates an even number of defects on the symmetry. We exploit this parity conservation law to make a matching decoder for the square-boundary colour code. In Ref. [SB22], a global symmetry termed the *unified lattice* was derived for the triangular colour code with a single red, blue and green boundary. Notably, the unified lattice presented in Ref. [SB22] had the topology of a Möbius strip. Due to the unified lattice's improved capacity to handle correctable errors at the boundary [GJ23], Ref. [SB22] reported improvements in both the threshold and logical failure rates for the triangular colour code using decoding on the unified lattice. Motivated by this, we introduce a unified decoder for the colour code presented in Sec. 2.3.5.2. In addition to introducing the unified lattice decoder, we will also review the matching decoder on the restricted lattice [Wan+10; DT14;

Cha+20; BKS21; KD23]. In later sections, we will compare the restricted-lattice decoder to the unified-lattice decoder.

5.2.1 Symmetries of the colour code

In this work, we use symmetries of the colour code to devise a matching decoder. We define a symmetry as a subset of stabilizers Σ such that

$$\prod_{s \in \Sigma} s = \mathbf{1}.\tag{5.1}$$

This definition is such that the elements of the symmetry Σ necessarily give rise to an even number of syndrome defects under any error. Given an appropriate choice of Σ we can thus design a matching decoder, demonstrated with a number of examples [Den+02; Wan+10; DT14; NB19; Tuc+20; Bon+21; NB21; SFG22; SB22; KD23; MWB23; Hua+22] which are summarised in Ref. [Bro22].

The colour code is a CSS code defined in Sec. 2.3.5.2. We find the symmetries of the colour code by considering subsets of its stabilizer generators with specific colours [DT14; SB22]. These subsets are known as restricted lattices, as we will define below. Our goal is to derive a single 'unifying' symmetry for the colour code with boundaries. We also investigate other colour code decoders based on restricted lattices. Interestingly, we find that the square-boundary colour code has a unified lattice with a topology that is distinct from that in Ref. [SB22], and is given by the manifold in Fig. 5.1. In this subsection, we show how to derive this unified lattice for the square boundary colour code, which we will adopt in our matching decoder implementation. In the following, we restrict our interest to the Pauli-Z stabilizer generators of the colour code, and as such, we omit the superscript label indicating the stabilizer type, such that $S_f = S_f^Z$. Moreover, we henceforth refer to the instance of the square-octagon colour code shown in Fig. 2.4 merely as the colour code, and alternatively as the square-boundary colour code when paying specific attention to its boundary conditions. Prior work has established a specific set of bulk symmetries, referred to as restricted lattices

on the colour code [DT14]. A **uv**-restricted lattice, denoted by $\mathcal{R}_{\mathbf{w}}$ (where $\mathbf{u} \neq \mathbf{v} \neq \mathbf{w} \neq \mathbf{u}$), is defined as

$$\mathcal{R}_{\mathbf{w}} = \{ \{ S_f \}_{\mathbf{col}(f) \neq \mathbf{w}} \}. \tag{5.2}$$

We show the restricted lattices $\mathcal{R}_{\mathbf{b}}$, $\mathcal{R}_{\mathbf{r}}$, and $\mathcal{R}_{\mathbf{g}}$ in Fig. 5.2(a). Errors in the bulk of the colour code preserve defect parity on any single restricted lattice. We show examples of bulk errors on the restricted lattices in Fig. 5.2(a), where the bottom left error on the lattice flips a single qubit and creates a single defect of each colour, and the top right error flips two qubits, and creates two green defects.

Note that the restricted lattices are not symmetries for the colour code with boundaries. Errors at the boundary may give rise to a single defect on the restricted lattice, see the error in Fig. 5.2(a) (bottom right). We must therefore introduce a boundary operator to complete the restricted lattice symmetry; see Refs. [SB22; Bro22] for discussions on boundary operators.

We introduce a boundary operator for each restricted lattice, defined as

$$b'u = \prod_{\mathbf{col}(f) \neq \mathbf{u}} S_f$$
(5.3)

where we take the product over all faces of the restricted lattice, i.e. those not coloured \mathbf{u} . This operator is highlighted for each restricted lattice in Fig. 5.2(b). We note that the boundary operator $b_{\mathbf{u}}$ is supported on all boundaries and corners that are not \mathbf{u} -coloured.

We find that the inclusion of the boundary operator with its restricted lattice gives rise to a materialised symmetry [SB22]. A set that includes this boundary operator, $b_{\mathbf{u}}$, together with the face operators of its respective restricted lattice, $\mathcal{R}_{\mathbf{u}}$, completes a symmetry and thereby allows us to match lone defects on the restricted lattice to the boundary. Explicitly,

we write this symmetry as follows

$$\Sigma_{\mathbf{u}} = \{b_{\mathbf{u}}, \mathcal{R}_{\mathbf{u}}\}, \quad \prod_{s \in \Sigma_{\mathbf{u}}} s = \mathbf{1}.$$
 (5.4)

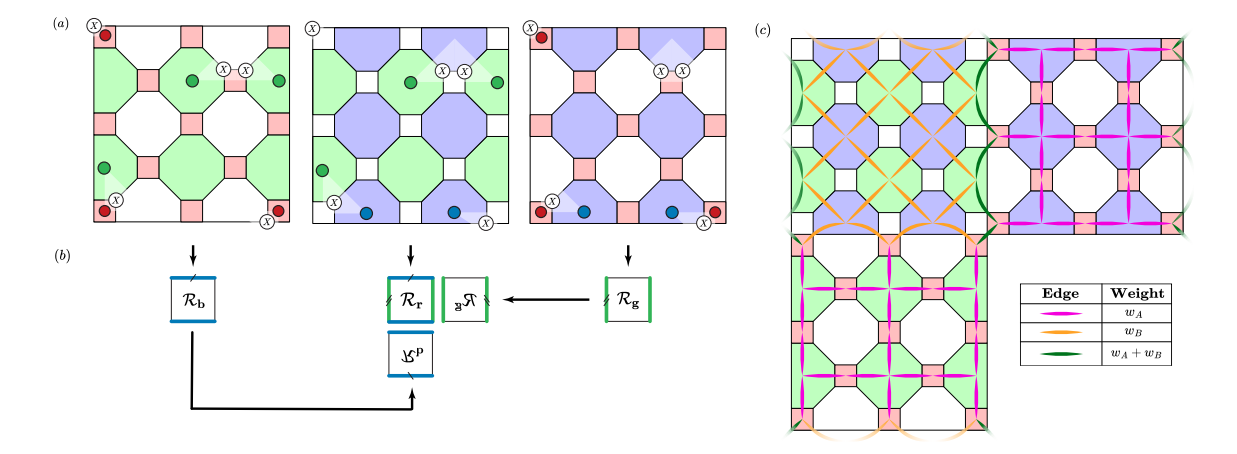


Figure 5.2: (a) One and two-qubit errors with the corresponding syndromes on the three restricted lattices of the d=6 colour code. (b) Stitching the lattices together along the boundary operators. (c) Edge weights for the matching graph. This configuration is empirically chosen to correct for all expected minimum-weight uncorrectable errors, but is non-unique.

We now derive a global symmetry by taking products of smaller symmetries. Relationships among the boundary operators reveal that restricted lattices can be unified by their boundaries, $b_{\mathbf{r}}b_{\mathbf{g}}b_{\mathbf{b}}=\mathbf{1}$. This is discussed in generality in Ref. [SB22]. Let us describe this unification procedure in steps. We start by examining the subproduct $b_{\mathbf{r}}b_{\mathbf{g}}$ of this equation; this is essentially the combination of the \mathbf{gb} and \mathbf{rb} restricted lattices, as in Fig. 5.2(b) (centre right). Because the qubits at the right (left) of $\mathcal{R}_{\mathbf{r}}$ are the same as those on the left (right) of a horizontally flipped $\mathcal{R}_{\mathbf{g}}$, this product stitches the symmetries together, thus forming a cylinder. We now add $b_{\mathbf{b}}$, the product of all faces on \mathcal{R}_{b} to this subproduct. Analogously, the qubits at the top (bottom) of $\mathcal{R}_{\mathbf{r}}$ are the same as that on the bottom (top) of a vertically flipped $\mathcal{R}_{\mathbf{b}}$, and we join them accordingly, as in Fig. 5.2(b) (left). This creates the manifold seen in Fig. 5.1.

We now provide an alternate explanation of the stitching procedure adopted to produce the unified lattice. To do so, we consider the syndromes created by errors at the lattice boundary. Let us specifically consider a single qubit error at the lattice boundary, such as the single error shown at the green boundary in Fig. 5.2(a) (bottom right). We concentrate our attention on the two single defects created by this error on both the $\mathcal{R}_{\mathbf{r}}$ and $\mathcal{R}_{\mathbf{b}}$ lattices. Ideally, these defects should be paired by a single low-weight edge. As such, we can consider stitching these two restricted lattices together along the green boundary, such that these two defects are adjacent on the unified lattice. Next, by analogy, we join $\mathcal{R}_{\mathbf{r}}$ with $\mathcal{R}_{\mathbf{g}}$ along the **b** boundaries. The system takes on the topology of a torus with a disk-shaped puncture, again resulting in the manifold of Fig. 5.1.

Let us additionally examine a single qubit error at the corner of the lattice to show how we stitch the corners of the unified lattice. See for example the top left error in Fig. 5.2(a). This error produces syndromes only on $\mathcal{R}_{\mathbf{b}}$ and $\mathcal{R}_{\mathbf{g}}$, not on $\mathcal{R}_{\mathbf{r}}$. Consequently, we would like our matching decoder to pair defects across any corner of $\mathcal{R}_{\mathbf{b}}$ to the equivalent corner of $\mathcal{R}_{\mathbf{g}}$. This manifests on the unified lattice as a string stretching from the top of the cylinder diagonally across to the sheet-like handle.

5.2.2 Matching decoders code symmetries

We can use symmetries to design decoders based on minimum-weight perfect matching. See Ref. [Bro22] for a discussion. Here, let us briefly review the restricted-lattice decoder and the unified lattice decoder that we use throughout this work.

Prior work has proposed using the individual restricted lattices for error correction [KD23]. In the restriction-lattice decoder, defects on each of the $\mathcal{R}_{\mathbf{g}}$ and $\mathcal{R}_{\mathbf{b}}$ lattices are matched within the lattice or to the boundary operator that completes the symmetry to produce local correction operators $\{\mathcal{C}_{\mathbf{g}}, \mathcal{C}_{\mathbf{b}}\}$. In Fig.5.3(a), for instance, these consist of Pauli corrections on the qubits lying along the highlighted paths. In order to apply a global correction, the union of the local correction operators $\mathcal{C}_{\mathbf{g}} \cup \mathcal{C}_{\mathbf{b}}$ is applied to the underlying physical qubits.

The unified-lattice decoder is obtained from the global symmetry of the colour code de-

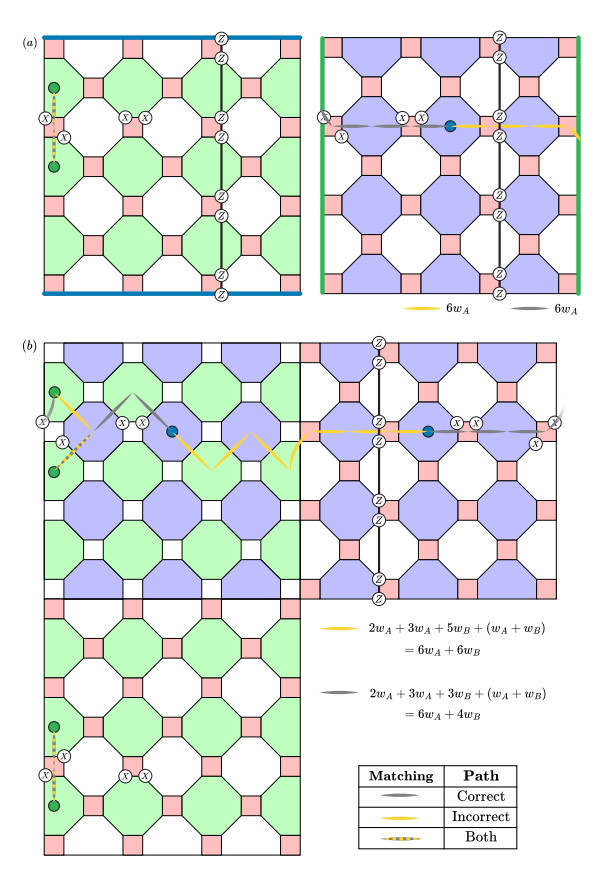


Figure 5.3: Here we consider a weight-4 error on a d=8 colour code lattice, which can be interpreted as a weight-2 error on the d=4 surface code as per Sec. 5.3, further shown in Fig. 5.5. We examine correction operators found by matching using (a) the restricted decoder, and (b) the unified decoder. A correct (incorrect) pairing of defects that returns the encoded qubit to the correct (incorrect) state in the logical subspace is depicted in grey (yellow). Matching on the restricted lattice is unable to reliably determine the correct defect pairing. Matching on the unified lattice correctly pairs the syndrome defects when the error string contains a Pauli-Y error, by having a demonstrably lower weight.

scribed in the previous subsection, on which errors give rise to pairs of defects. Given a collection of defects on the unified lattice, the matching-based decoding problem reduces to finding a pairing between these defects that is created by an underlying error with maximal probability. Towards this goal, a matching between a pair of defects is assigned a weight inversely dependent on the probability of errors on all the qubits along the shortest path connecting the two. As a result, decoding is equivalent to finding the perfect matching of

minimum weight on this weighted graph.

It was seen in Ref. [SB22] that the choice of edge weights on this graph can be determined by examining simple error patterns at the bulk, boundary and corners of the unified lattice. We apply the same basic concept in this work, but we set the edge weights as free parameters w_A to bulk edges on $\mathcal{R}_{\mathbf{g}}$ and $\mathcal{R}_{\mathbf{b}}$, and w_B on $\mathcal{R}_{\mathbf{r}}$, as shown in Fig 5.2(c), where we adopt a matching graph which allows for the correction of all expected errors when the global symmetry is respected. In the following sections, specific weights were found by numerical tests depending on the noise model.

Given a matching on a particular lattice – unified or restricted –, we now lay out the procedure to obtain the relevant correction to the logical qubit subjected to X errors on the underlying physical qubits. Note that the following procedure is valid for both the restricted and unified lattices. We first apply the Pauli-Z corrections to qubits along the shortest paths between the pairs of defects determined by the matching algorithm. This returns the logical qubit to the code space. During this process, we track the parity of a logical operator, here the vertical Z logical depicted in Fig. 5.3. We successfully return the encoded qubit to the correct logical state if the decoding algorithm has determined that the parity of matched paths across this logical operator path is the same as the parity of the number of physical Pauli errors on the qubits along the logical, a method discussed in more detail in Ref. [Bro22; SB22]. In Fig. 5.3, if the decoder finds the yellow matching, the corresponding correction, together with the initial error, applies \overline{X} to the encoded qubit; the grey matching returns the lattice to the correct state. Henceforth, we will refer to the MWPM-based decoder applied to syndrome data on the restricted (unified) lattice as the restricted (unified) decoder.

5.3 Mapping surface code errors to colour code errors

We have introduced the surface code and the colour code in Sec. 2.3.5, and proposed a decoding procedure for bit-flip errors acting on the colour code by matching on either the restricted lattice or the unified lattice. We now describe the local mapping from the surface code onto

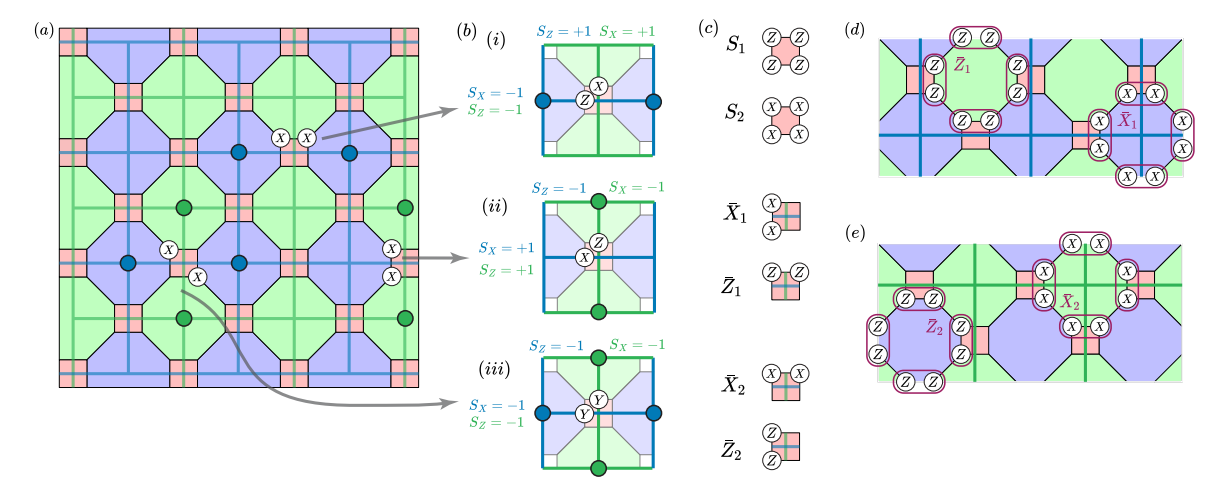


Figure 5.4: The surface-colour code mapping. (a) The colour code with an overlay of two surface codes - blue and green - to indicate their positioning with respect to the colour code stabilizers, along with weight-2 bit-flip errors and their syndromes on the colour code. (b) Correspondence of the indicated weight-2 bit-flip errors on the colour code to singlequbit depolarising noise on the surface codes. For a given error on the colour code in (a), the corresponding error for the blue (green) surface code is shown on the blue (green) edge across the red squares in (i-iii), with the surface code stabilizer measurements to its left and top displayed in the same colour. (c) Stabilizers and logical operators of the [4, 2, 2]code defined on a single square with qubits on its vertices. The displayed orientation is used for a red square traversed by a horizontal (vertical) edge of the blue (green) surface code. In the alternate case, an orientation rotated by 90° applies. (d,e) Stabilizers of the (d) blue and (e) green surface codes obtained from the mapping in Sec. 5.3. The star operators of the blue (green) surface code are Pauli-X stabilizers, where each X operator is encoded as the logical $\overline{X}_1(\overline{X}_2)$ operator of the [4,2,2] codes shown in (c). The face operators are Pauli-Z stabilizers where each Z operator is encoded as the logical $\overline{Z}_1(\overline{Z}_2)$ operator of the [4, 2, 2] codes.

the square-octagonal colour code, inspired by the unfolding of the colour code [KYP15], and introduce a mapping from depolarising errors on the former to spatially-correlated pairs of bit-flip errors on the latter. We exploit this mapping to adopt the restricted-lattice and unified-lattice colour code decoder for the surface code undergoing depolarising noise.

The two-dimensional colour code is locally equivalent to two copies of the surface code [Yos11; BDP12; BS15; KYP15; CT16], as mentioned Sec. 2.3.5. We first describe this equivalence via operators, before providing a formalism to reconstruct it. As a guide for the mapping, we show the surface code in blue overlaid with the colour code in Fig. 5.4(a). The figure addi-

tionally depicts a second copy of the surface code in green, laid out on the dual lattice, that duplicates the syndrome of the blue copy. Considering two copies of the duplicate syndrome facilitates the unfolding map between two copies of the surface code and the colour code.

Let us begin by stating the equivalence between the different lattice elements under this mapping, by considering the surface code displayed with a blue lattice in Fig. 5.4(a). First, we map the vertex and face operators of this blue surface code onto octagonal face operators of the colour code. Specifically, each surface code star operator corresponds to a blue octagon S_f of the colour code and, likewise, each face operator of the surface code corresponds to a green octagonal face operator in the colour-code picture S_f . This is shown in Fig. 5.4(a), where the star and face operators of the blue surface code align with their corresponding colour code stabilizers exactly, thereby illustrating this mapping. We also show the surface code displayed with a green lattice, which represents a rotation of the blue counterpart, and where a similar argument holds.

Now that we have identified stars and plaquettes of each surface code with octagonal face operators of the colour code, we must choose errors in the colour-code picture that give rise to equivalent syndromes in the surface code picture. A Pauli-Z error on the surface code will violate its two adjacent vertex operators, as shown in Fig. 2.3. In the colour code picture, this error will violate the corresponding blue octagonal operators as shown in Fig. 5.4(b)(i) where we indicate this Z-flip on the blue surface code edge. To obtain this violation in the colour code picture, we add two horizontal bit-flip errors onto the single red face of the colour code on which the edge lies such that its two adjacent blue octagons support a syndrome, see Fig. 5.4(a). Similarly, a Pauli-X error in the surface code picture will violate two adjacent face operators, which correspond to green octagons in the colour code picture in Fig. 5.4(b)(ii). We find that the error in the colour code picture that violates these appropriate colour code octagons is a pair of bit-flip errors lying vertically on a single red square-shaped face operator shown in the corresponding diagram in Fig. 5.4(a).

We can obtain a Pauli-Y error by adding a Pauli-Z error and a Pauli-X error to the same red face of the colour code, which results in a diagonal bit-flip pair on the latter. Since the surface code defined using the green lattice is rotated, so is the orientation of the errors it detects, namely a horizontal (vertical) pair of bit-flips on such a red plaquette in the colour code picture corresponds to a Pauli-X(Z) error, also shown in Fig. 5.4(a) and (b).

We have now proposed an error model that violates pairs of either blue or green face operators according to the mapping from the surface code undergoing a depolarising noise model. As we have alluded, single qubit errors in the surface code picture correspond to two-qubit errors supported on individual red faces of the colour code. Indeed, we see that the edges in the surface code picture each have an underlying red face operator in the colour-code picture, where the red square inherits an orientation from the underlying edge. We therefore identify qubits in the surface code picture with red faces in the colour code picture. In what follows, it will be helpful to keep this identification in mind as we describe the mapping more rigorously. We note that this mapping is non-trivial in the sense that the commutation relations of the errors are not preserved. Nevertheless, we find a valid decoder for the surface code with the equivalence we have proposed.

Let us make this mapping more concrete using the more rigorous language of the unfolding map [BDP12; BS15; KYP15]. Specifically, we duplicate the surface code supporting the syndrome, where the second copy differs from the first by a transversal Hadamard rotation. We show the duplicate surface code syndrome on the dual lattice in green in Fig. 5.4. We then put the two duplicate copies through a folding map, see e.g. Refs. [BDP12; KYP15; CT16]. Specifically, we will consider the unfolding map of Ref. [CT16] where pairs of surface code qubits are encoded with the [4, 2, 2]-code. See also Ref. [Bre+11] on this equivalence. This four-qubit code can be regarded as an inner code for a concatenated model with the surface code as the outer code. All together, this concatenated model gives the square-octagon colour code we have studied throughout this work.

Under this mapping, the inner [4, 2, 2] code can be regarded as a red face of the colour code. Indeed each disjoint red face supports the four qubits of the [4, 2, 2] code lying on its vertices as shown in Fig. 5.4(c). Furthermore, the stabilizer group of the inner code is generated by $S^X = XXXX$ and $S^Z = ZZZZ$, which coincide with the red face operators of the squareoctagon colour code. Moreover, the inner code encodes two logical qubits represented by the operators $\overline{X}_1 = XIXI$, $\overline{Z}_1 = ZZII$, $\overline{X}_2 = XXII$ and $\overline{Z}_2 = ZIZI$ visualised per the convention in Fig. 5.4(c).

We then express the stabilizers of the blue and green surface codes respectively, using the two logical operators of the inner code $\{\overline{X}_1, \overline{Z}_1\}$ and $\{\overline{X}_2, \overline{Z}_2\}$, where the first(second) qubit encodes the blue(green) copy of the surface code, as shown in Fig. 5.4(d) (Fig. 5.4(e)). We emphasize that that the orientation of the edge qubit of the surface code dictates the orientation of the encoding of the [4, 2, 2] code. See Fig. 5.4(c). Indeed, a red square associated with a horizontal (vertical) edge of the blue (green) surface code is encoded as per Fig. 5.4(c), but when traversed by a vertical edge, this encoding must be rotated by 90° to preserve our mapping.

Hence, in this mapping, a Pauli operator on a surface code qubit corresponds to a pair of Pauli operators on the red stabilizer lying on the associated edge, where this pair defines the appropriate logical operator of the [4,2,2] code. This is summarised in the following equivalences between stabilizers of the surface codes, colour codes, and product of logical operators of the inner code

$$S_{\mathrm{SC},\mathbf{b}}^X \equiv S_{f,\mathbf{b}}^X \equiv \prod_{r \in \partial f} \overline{X}_1^r$$
 (5.5)

$$S_{\mathrm{SC},\mathbf{b}}^{Z} \equiv S_{f,\mathbf{g}}^{Z} \equiv \prod_{r \in \partial f} \overline{Z}_{1}^{r}$$
 (5.6)

$$S_{\mathrm{SC},\mathbf{g}}^X \equiv S_{f,\mathbf{g}}^X \equiv \prod_{r \in \partial f} \overline{X}_2^r$$
 (5.7)

$$S_{\mathrm{SC},\mathbf{g}}^{Z} \equiv S_{f,\mathbf{b}}^{Z} \equiv \prod_{r \in \partial f} \overline{Z}_{2}^{r}$$
 (5.8)

where the product over $r \in \partial f$ indicates that the logical operator is applied to all four red square operators on the boundary of the appropriate colour code stabilizer.

Finally, since the surface code on the green lattice is a duplicate of its blue counterpart up to a Hadamard rotation, we identify certain logical operators of the inner code to complete our

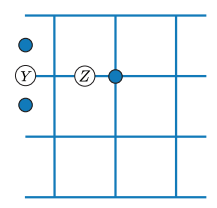


Figure 5.5: The d=4 surface code, with depolarising errors giving rise to the corresponding set of syndrome defects seen in Fig. 5.3 on the colour code.

mapping. Indeed, under the duplication, with the Hadamard rotation, we have the following relations between pairs of logical operators of the inner code, namely $\overline{X}_1 \equiv \overline{Z}_2$ and $\overline{Z}_1 \equiv \overline{X}_2$. This ensures the syndrome correspondence in Fig. 5.4(a) such that all depolarising errors on the surface code now have a one-to-one correspondence with a commuting two-qubit bit-flip error model. Most importantly, this enables us to use a decoder for a CSS code [CS96] to correct after depolarising noise on the surface code, represented in the colour code picture.

5.4 Surface code performance under depolarising noise

In this section, we study the surface code under depolarising Pauli noise on data qubits and perfect measurements. We compare the performance of the surface-code decoder we have introduced to the conventional matching decoder. Under the mapping, these correspond to the unified decoder and the restricted decoder, respectively.

Our analysis begins by counting the number of minimum-weight uncorrectable errors on the lattice for each decoder. The unified decoder provides an advantage that results in a logical error rate suppression in the low physical error-rate regime. We interrogate our analytical estimates numerically using the splitting method [BV13]. Additionally, we investigate the threshold performance of the code numerically using PyMatching [HG23].

5.4.1 Correcting Pauli-Y errors on the surface code

Under the depolarising noise channel, introduced in Sec. 2.3.3.1, the probability of each singlequbit Pauli error is uniform. Since Y = XZ, breaking Ys down into X and Z creates correlated X and Z errors and corresponding correlated syndromes among the star and plaquette stabilizers. However, these correlations generally elude decoders which treat X and Z errors independently. As we will argue, the unified decoder identifies these correlations.

We use the unified decoder on the syndrome of the surface code mapped onto the colour code lattice to correct for a depolarising noise model. This is motivated by the ability of such a decoder to identify Pauli-Y errors on the surface code, since each one gives rise to a distinct syndrome pattern on the unified lattice. Indeed, a Pauli-X error on the blue surface code introduces a syndrome defect on $\mathcal{R}_{\mathbf{r}}$ and $\mathcal{R}_{\mathbf{b}}$ as shown in Fig. 5.4. Similarly, a Pauli-Z error leads to a syndrome on $\mathcal{R}_{\mathbf{r}}$ and $\mathcal{R}_{\mathbf{g}}$, and finally a Pauli-Y error is distinguished by its syndrome featuring on all three restricted lattices. Hence, we find that in the presence of at least one Y error, decoding on the unified lattice captures correlations that any one or pair of restricted lattices remain oblivious to.

To illustrate our argument, we provide an example of a minimum-weight uncorrectable error on the surface code with one Pauli-Y that corresponds to a weight d/2 bit-flip error on the colour code in Fig. 5.3. Note that due to the presence of a diagonal bit-flip pair on a red stabilizer of the colour code, the syndrome on the unified decoder spans all three sublattices and a lower-weight matching path emerges for the successful correction (Fig. 5.3(a)). We numerically find that this improvement from the unified decoder is valid for a range of values of weights w_A and w_B in the matching graph depicted in Fig. 5.2(c). For example, $w_A = w_B = 1$ achieves an optimal number of successful corrections.

5.4.2 Path-counting of failure mechanisms

The advantages of using the unified-lattice decoder are very apparent in the limit where physical error rates p are low. In the regime of asymptotically low p, the logical failure rate is dominated by minimum-weight failure mechanisms, such that the following holds

$$\overline{P}_{0,n} := \lim_{p \to 0} \overline{P}(p,n) \sim N_{\text{fail}} p^{d/2}$$
(5.9)

where N_{fail} is the entropic term that denotes the number of least-weight errors leading to a logical failure.

In what follows we evaluate the entropic term for both the restricted-lattice decoder and the unified lattice decoder, $N_{\text{fail}}^{\text{res}}$ and $N_{\text{fail}}^{\text{uni}}$ respectively. We find the restricted-lattice decoder has an exponentially larger number of failure mechanisms in the low error rate regime than the unified-lattice decoder as a function of the code distance:

$$N_{\text{fail}}^{\text{res}}/N_{\text{fail}}^{\text{uni}} = 2^{d/2}.$$
 (5.10)

We attribute this factor to the ability of the unified-lattice decoder to identify the occurrence of Pauli-Y errors. First, we count $N_{\rm fail}^{\rm res}$ and $N_{\rm fail}^{\rm uni}$ exactly. In the following section we interrogate the relative performance of the two decoders numerically, and verify our expressions with exhaustive testing.

We now evaluate the number of least-weight errors that lead the surface code to failure using the restricted-lattice decoder. This decoder cannot distinguish between Pauli-Z or Pauli-Y errors. As such we count the number of weight d/2 configurations of errors along a major row of the colour-code lattice, where we say a major row is a row of d red plaquettes. In contrast, a minor row of the lattice is a row of d-1 red colour-code plaquettes. Since the lattice is square, it supports d major rows and d-1 minor rows.

The probability of d/2 Pauli-Z or Pauli-Y errors occurring is $(1-p)^{n-d/2}(2p/3)^{d/2}$. There are d major rows on which one of these error configurations can occur, and on each of these rows, there are $d! \times (d/2)!^{-2}$ distinct configurations the d/2 errors can find on the d plaquettes of the major row. We therefore find that

$$\overline{P}_{0,n}^{\text{res}} = (1-p)^n \frac{d}{2} \binom{d}{\frac{d}{2}} \left(\frac{2p}{3(1-p)}\right)^{\frac{d}{2}}$$
(5.11)

$$\approx \frac{d}{2} \binom{d}{\frac{d}{2}} \left(\frac{2}{3}\right)^{\frac{d}{2}} p^{\frac{d}{2}}.\tag{5.12}$$

where we include an additional prefactor of one half due to the matching decoder correctly

guessing a correction that successfully corrected the error with probability 1/2 and, on the right hand side, we assume that $1-p \approx 1$ in the limit of very small p. Expressing the equation this way allows us to read off the entropic term,

$$N_{\text{fail}}^{\text{res}} = \frac{d}{2} \binom{d}{\frac{d}{2}} (2/3)^{d/2}.$$
 (5.13)

We verify Eq. 5.13 by exhaustively testing the restricted-lattice decoder for all configurations of weight d/2 across the lattice of distances d = 4, 6 and 8.

Let us next evaluate the entropic term for the unified-lattice decoder. As discussed in Sec. 5.4.1, unlike the restricted-lattice decoder, the unified-lattice decoder allows us to identify correlations between the syndromes caused by Pauli-Y errors to distinguish Pauli-Y errors from Pauli-Z errors. The unified-lattice decoder fails when d/2 Pauli-Z errors are configured along a major row of the lattice. This occurs with probability $(1-p)^{n-d/2}(p/3)^{d/2}$. These errors may be configured along the d sites of one of the d major rows. We therefore obtain a logical failure rate in the low error rate limit,

$$\overline{P}_{0,n}^{\text{uni}} = (1-p)^n \frac{d}{2} \binom{d}{\frac{d}{2}} \left(\frac{2p}{3(1-p)}\right)^{\frac{d}{2}}$$
(5.14)

$$\approx \frac{d}{2} \binom{d}{\frac{d}{2}} \left(\frac{1}{3}\right)^{\frac{d}{2}} p^{\frac{d}{2}}.\tag{5.15}$$

where, as in the restricted-lattice decoder case, a factor 1/2 is included to account for error configurations where the decoder guesses the correct solution. We can therefore identify the entropic term for the unified-lattice decoder

$$N_{\text{fail}}^{\text{uni}} = \frac{d}{2} \binom{d}{\frac{d}{2}} (1/3)^{d/2}.$$
 (5.16)

We again verify this numerically by exhaustively generating all errors of weight d/2 on the lattice, and decoding each error using the unified lattice for surface code distances d = 4,6 and 8, using different values of w_A and w_B . We find that a range of weight configurations

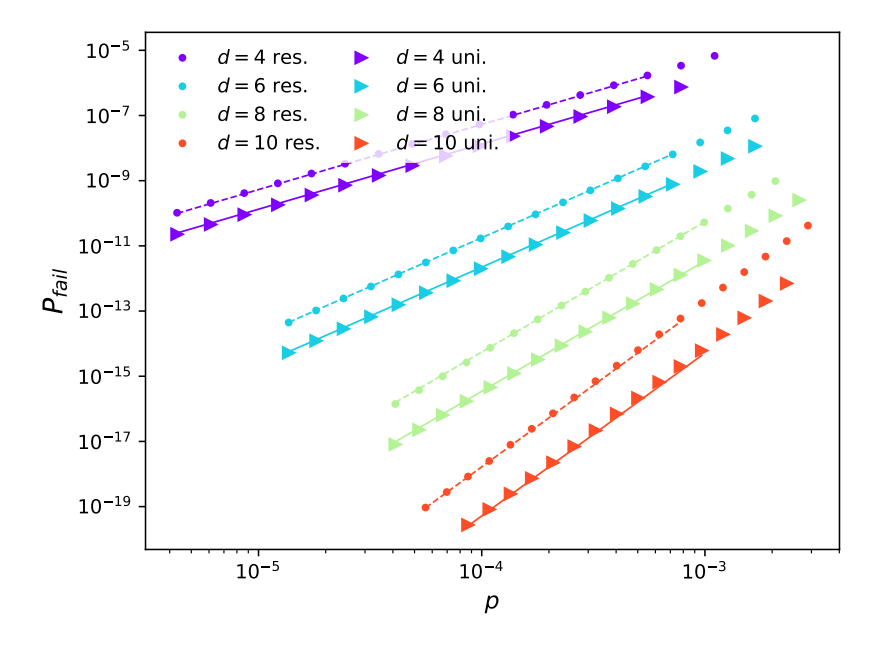


Figure 5.6: The logical failure rate data (in logarithmic scale) for the surface code under low physical error rates computed using the splitting method [BV13] to test the restricted and unified decoders for even surface code distances. The dashed and solid lines respectively indicate the fits obtained using Eqs. 5.13 and 5.16 for the restricted and unified decoders.

minimises the entropic term by achieving Eq. 5.16, with the constraint that $0 < w_B < \delta$, where δ is a constant changing with code distance. We numerically find that when $w_A \approx w_B$, the entropic term is recovered. With Eq. 5.13 and Eq. 5.16 evaluated, the ratio stated at the beginning of this subsection, Eq. 5.10 is readily checked.

5.4.3 Low error-rate performance

We adopt the splitting method [BV13] for the simulation of rare events, in order to numerically investigate logical failure rates at low physical error rates p. These estimates are used to numerically verify the analytical expressions derived from path-counting in Sec. 5.4.2.

As discussed in Refs. [BV13; Bev+19], the splitting method is used to evaluate ratios of logical failure rates $R_j = \overline{P}(p_j, n)/\overline{P}(p_{j+1}, n)$ evaluated at physical error rates p_j and p_{j+1} that are similar. The product of many such ratios can be used to interpolate between the high error rate regime where logical failure rates can be obtained using Monte Carlo sampling, and

the path-counting regime discussed in the previous subsection where logical error rates are very small. Each term in a given ratio is evaluated by averaging over a sample of failure paths drawn from the appropriate error distribution. We note that when sampling these errors, we heuristically chose a number of steps such that statistical fluctuations are smaller than the desired logical error rate precision, and discard 50% of the total generated Metropolis samples to ensure that the mixing time of the Markov process was surpassed. We adopt the heuristic sequence of ratios R_j with physical error rates $p_{j+1} = p_j 2^{\pm 1/\sqrt{w_j}}$, as proposed in Ref. [BV13] to minimise statistical error, where $w_j = \max(d/2, p_j n)$ for a code distance d.

We use this splitting method to numerically interpolate between initial estimates obtained using Monte Carlo sampling at p = 5%, and the analytical path counting results in the low error rate regime derived in Sec. 5.4.2. Our numerical results show good agreement with our analytical estimates for the logical error rates for both the restricted and unified decoders. In Fig. 5.6 we compare logical failure rates obtained with the splitting method to our analytical expressions.

5.4.4 Thresholds

The threshold is a critical physical error rate $p_{\rm th}$ below which a topological code is protected such that error correction succeeds with an probability exponentially suppressed as the code distance increases. Decoding becomes ineffective above this threshold, and the logical failure rate increases with the size of the code. We fit the logical failure rate data from Monte Carlo sampling near the threshold to a second order Taylor function given by

$$f = Ax^2 + Bx + C (5.17)$$

where x is the re-scaled error rate $x=(p-p_{\rm th})^{1/\nu}$ [WHP03]. We find a fitted threshold of $p_{\rm th} \sim 15.4(7)\%$ for the restricted decoder under depolarising errors using the data shown in Fig. 5.7, where we obtain a fitted critical exponent $\nu \approx 0.611$, and Taylor fit constants A=0.471, B=0.540 and C=0.153. For the unified decoder, we find that the threshold

estimate varies slightly with the chosen values of w_A and w_B . We considered multiple weights w_B with fixed $w_A = 1$ for edges of the matching graph in Fig. 5.2(c), and find a threshold of $p_{\rm th} \sim 15.2(1)\%$ using $w_A = 1$ for $w_B = 0.5$, as shown in Fig. 5.7 where $\nu = 0.664$, A = 0.606, B = 0.452 and C = 0.127. We provide the data for different weight configurations in Appendix A3, where the threshold is still comparable to that of the standard surface code, with a minor discrepancy.

5.5 Colour code performance under bit-flip noise

In this section, we compare the performance of the restricted and unified decoders used to decode the colour code undergoing independent and identically distributed bit-flip noise and perfect measurements, where a bit flip occurs on each qubit with probability p. We begin by counting the number of minimum-weight uncorrectable errors on the lattice for each decoder. We show that using the unified decoder achieves a higher success rate, providing an advantage in the low physical error-rate regime. We verify the estimates numerically using the splitting method as was done in Sec. 5.4.3 [BV13], as well as direct Monte Carlo sampling. We investigate the threshold performance of the code numerically assuming perfect measurements.

5.5.1 Path-counting

We start by counting the number of minimum-weight uncorrectable error configurations on each row of the colour code $n_{\rm fail}^{\rm res}$ of distance D supporting $M=\frac{D}{2}$ square plaquettes. We define these new parameters to avoid confusion with the surface code parameters used in earlier sections. Since the lattice is square, there are M such rows. Using the restricted decoder, the number of errors that cannot be corrected is given by counting configurations consisting of errors lying on such rows. The possible paths an error can take depend on the configuration of X errors in an error string lying on each red square of a row, where each square can support a single-qubit X error, or a two-qubit error lying either on the two vertex

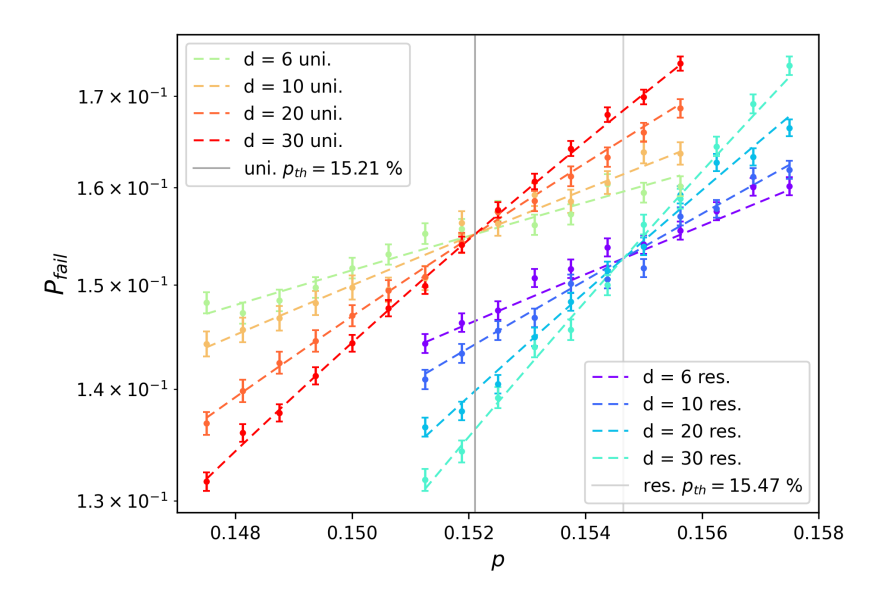


Figure 5.7: The logical failure rate $P_{\rm fail}$ (in logarithmic scale) as a function of physical error rate p for the restricted and unified surface codes of even distance d, under an i.i.d depolarising noise channel. The threshold $p_{\rm th}$ is indicated by the intersection. Edge weights were set to $w_A = 1$ and $w_B = 0.5$ in Fig. 5.2(c). Each dashed line indicates the fit to a Taylor expansion for a given system size, and the error bars show the standard deviation of the mean logical failure rate where each data point is collected using $> 6 \times 10^4$ Monte Carlo samples.

qubits of a horizontal edge, or on diagonal vertices of the square. Placing any of these four combinations on |M/2| locations on a row accounts for a number of strings

$$n_{\text{fail}}^{\text{res}} = \sum_{k=0}^{\left\lfloor \frac{M}{2} \right\rfloor} \begin{pmatrix} M \\ k \end{pmatrix} \begin{pmatrix} M-k \\ M-2k \end{pmatrix} 4^k 4^{M-2k}, \tag{5.18}$$

where k is the number of red plaquettes that support a weight-2 error, and M-2k the number of weight-1 errors. Hence, the total number of logical failures on the restricted lattice

corresponds to the number of equivalent configurations supported on all M rows, namely

$$N_{\text{fail}}^{\text{res}} = \frac{1}{2} n_{\text{fail}}^{\text{res}} M$$

$$= \frac{M}{2} \sum_{k=0}^{\left\lfloor \frac{M}{2} \right\rfloor} {M \choose k} {M-k \choose k} 4^{M-k}$$
(5.19)

where the prefactor of one half is due to the classical decoder misidentifying the right correction with a 50% probability.

We consider the MWPM problem on the unified lattice shown in Fig. 5.2(c). Unlike decoding on the restricted lattice, a diagonal error gives rise to a syndrome mapped onto all sub-lattices of the unified lattice, as depicted in Fig. 5.3. On each row supporting M square plaquettes, the number of weight-M error configurations that cannot be corrected is given by

$$n_{\text{fail}}^{\text{uni}} = \sum_{k=0}^{\left\lfloor \frac{M}{2} \right\rfloor} \binom{M}{k} \binom{M-k}{M-2k} 2^k 4^{M-2k}, \tag{5.20}$$

where k is the number of weight-2 errors that can reside on each square plaquette. As for the restricted lattice, the total number of logical failures when decoding on the unified lattice is

$$N_{\text{fail}}^{\text{uni}} = \frac{1}{2} n_{\text{fail}}^{\text{uni}} M$$

$$= \frac{M}{2} \sum_{k=0}^{\lfloor \frac{M}{2} \rfloor} \binom{M}{k} \binom{M-k}{k} 4^{M-\frac{3}{2}k}.$$
(5.21)

We numerically verified these estimate by exhaustively generating all error strings of weight M on each M-square row of the colour code, mapping the error configuration respectively to a restricted and unified lattice, and running the MWPM decoder.

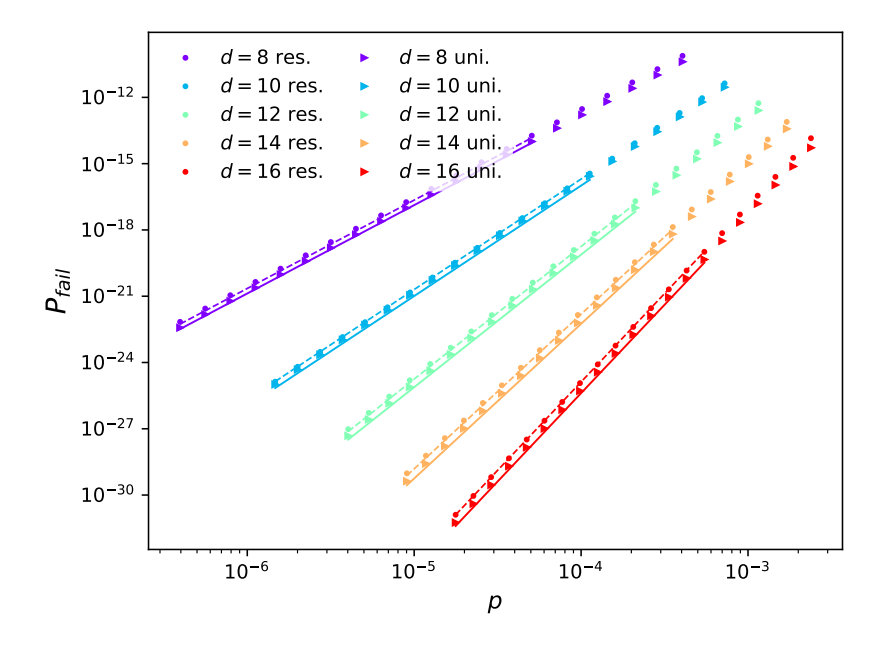


Figure 5.8: The logical failure rates at low physical error rates (in logarithmic scale) computed using the splitting method [BV13] for the restricted and unified decoders on the colour code under i.i.d bit-flip noise. For the latter, edge weights were set to $w_A = 1.1, w_B = 1$. The dashed and solid lines respectively indicate the fits using Eq. 5.19 and 5.21.

5.5.2 Low error-rate performance

We implement the splitting method under the assumption of errors drawn from an i.i.d bit-flip noise on the colour code, which can be written as

$$\pi_j(E) = p_j^{|E|} (1 - p_j)^{n - |E|}$$
(5.22)

where n is the number of physical qubits in the colour code, |E| the weight of an error operator E. Once again, we adopt the sequence $p_{j+1} = p_j 2^{\pm 1/\sqrt{w_j}}$ to split ratios [BV13] to minimise statistical error, where $w_j = \max(d/2, p_j n)$ for a code distance d. We numerically interpolate between initial estimates obtained using Monte Carlo sampling at physical error rate p = 5%, and the analytical path counting results in the low error rate regime shown in Sec. 5.5.1. The results are shown in Fig. 5.8 where a MWPM decoder was executed on the colour code restricted and unified lattices respectively, under bit-flip noise and perfect measurements. For

the distances considered, the analytic estimates in Eqs. 5.19 and 5.21 accurately predict the dominant behaviour of the error chains in the low error rate regime, as indicated by the solid line fits. We note that in order to correct for all expected minimum-weight configurations for bit-flip errors on the colour code there is a constraint on the edge weights, namely that $w_A > w_B$, which does not exist is the case of depolarising errors on the even-distance surface code. The source code and data used in the figures in this manuscript can be accessed at https://github.com/abenhemou/unimatch.

5.5.3 Thresholds

The restricted decoder recovers the threshold $p_{\rm th} \sim 10.2\%$ under independent and identically distributed bit-flip noise, see Fig. 5.9, where we obtain a fitted critical exponent $\nu = 0.628$, and Taylor fit constants A = -0.0419, B = 1.136 and C = 0.165 for Eq. 5.17. This is consistent with that of the surface code on a square lattice [WHP03; DT14]. In the case of the unified decoder, we considered multiple weights w_A with $w_B = 1$ for edges of the matching graph in Fig. 5.2(c), and find a peak in threshold at $p_{\rm th} \sim 10.1(3)\%$ around $w_A = 2.1$ (Fig. 5.9). Surprisingly, the unified decoder demonstrates a marginally lower threshold than the restricted decoder. This pattern is consistent with the threshold comparison applied to the surface code in Sec. 5.4.4. We hypothesize that in the near-threshold regime, the presence of additional defects on the unified lattice contributes to an increased number of incorrect minimum-weight paths that the decoder may choose, leading to this reduction.

5.6 Discussion

In conclusion, we demonstrated a method to reduce the logical error rate of the surface code under depolarising errors. This was done by first outlining a mapping from the surface to the colour code. We then showed that this noise model on the surface code can be mapped onto a set of two-qubit bit-flip errors on the colour code. Subsequently, we constructed a unified lattice in the form of a punctured torus, for use under a minimum-weight perfect

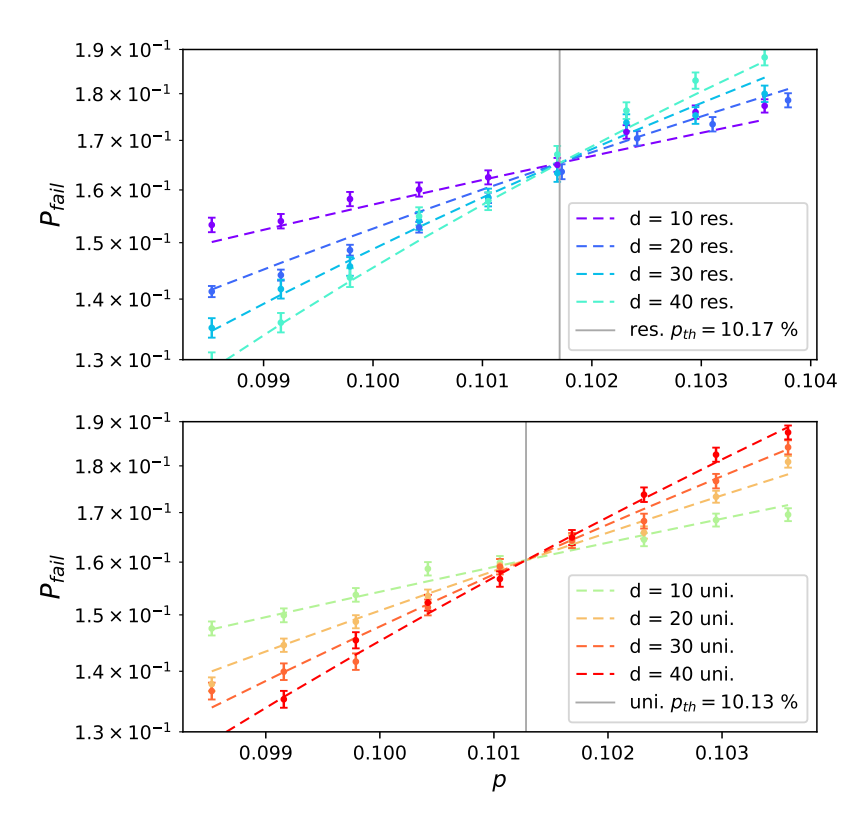


Figure 5.9: The logical failure rate $P_{\rm fail}$ (in logarithmic scale) as a function of physical error rate p for codes of different distance d, under an i.i.d bit-flip noise model. The threshold indicated by the intersection is found to be $p_{\rm th} \sim 10.2\%$ for the restricted decoder (top). The unified decoder threshold (bottom) is $p_{\rm th} \sim 10.1(3)\%$, using edge weights $w_A = 2.1$ and $w_B = 1$ with the matching graph in Fig. 5.2(c). Each dashed line indicates this fitting for a given system size, and the error bars show the standard deviation of the mean logical failure rate where each data point is collected using $> 6 \times 10^4$ Monte Carlo samples.

matching decoder to correct high-weight errors. To evaluate the performance of our decoder we analytically and numerically investigated the logical failure rates at low physical error rates and verified their agreement. For even code distances, our unified decoder achieves a least-weight correction for all weight d/2 depolarising errors on the surface code. We also demonstrated an exponential suppression in the logical error rate for the colour code under independent and identically distributed bit-flip noise, extending the work in Ref. [SB22] to the square-octagonal colour code with boundaries.

It will be interesting to determine how the performance of our decoder compares to other

practical decoders that are designed to account for depolarising noise, both in terms of errorcorrection performance and runtime. For instance, both iterative [DT14; Fow13b] and beliefmatching decoders [Hig+23] have been proposed to augment matching decoders with the ability to take advantage of correlations between the syndromes measured by the star and plaquette operators. To complete such a comparison, it will first be necessary to determine the performance of other decoding algorithms in the limit of low error rate. Of course, the matching decoder we have presented here is compatible with other decoding techniques such as belief-matching and two-stage decoding [CA18; Rof+23], at the cost of added computational complexity, and it may be interesting to design versatile decoders for other codes by adapting these techniques. However, it is important to note that our decoder only requires a single invocation of an MWPM decoder to address Pauli correlations. As a result, it benefits from the expected linear time complexity of MWPM [HG23], with only a constant factor increase of 4 in the size of the matching graph. One could also readily combine our decoder with fast decoders such as union-find [DN21; CB23; GB23] or weighted union-find [HNB20] to improve its runtime. We note that we can also generalise our versatile matching decoder to deal with non-trivial syndrome correlations that occur in fault-tolerant error correction [WHP03; RBH05; Fow+12b], and may be adapted for use in other variations of the surface code with boundaries such as Floquet codes [HH22; Kes+22]. One might also explore generalising our decoding method to surface codes with alternative topologies, or perhaps using other colour code symmetries. Both of these directions are discussed in Appendix F of Ref. [SB22].

Broadly speaking, we have shown that we can obtain a matching decoder for the surface code capable of correcting depolarising noise by mapping its syndrome onto an enlarged state space, namely, the syndrome of the colour code. It will be interesting to explore this method further to determine the extent to which it generalises. For instance, it is compelling to investigate whether we obtain near-optimal performance using our mapped decoder for different lattice geometries [Bev+19]. It is also crucial to incorporate circuit-level noise, where decoding is conducted on a (2+1)-dimensional syndrome history. Trivially, we can adapt the matching graph obtained from the unified lattice for this setting by extending it

along the time direction in the standard way [Den+02; BW20; Bro22]. Nevertheless, the novel decoding methods we have proposed have the potential to be generalised to offer an advantage in correcting the types of correlated errors at the circuit level. For instance, the edge weights on the unified lattice can be chosen appropriately to account for correlated errors such as hook errors. Perhaps there exists an alternative lattice that can be found to offer an advantage in dealing with this more complicated noise model. More generally, it is exciting to consider other decoding problems on extended Hilbert spaces. This may lead to practical, high-performance decoders for more sophisticated codes and noise. We leave this exploration to future work.

Part II

Simulation of black hole properties using a quantum system

Chapter 6

Preliminaries

This chapter introduces the preliminary background and context for the work presented in Chapter 7. It is also intended to provide the necessary definitions to understand the physics of the quantum platform chosen for our quantum simulation proposal in [Ben+23b], namely optical lattices. Lattice systems displaying quantum many-body physics provide a platform to explore continuum phenomena. A prominent example is graphene, whose low-energy behaviour in the continuum limit is governed by the Dirac equation in Minkowski spacetime [KNG06]. In Part II of the thesis, we apply this to simulate quantum properties of black holes. Indeed, black holes are among the most enigmatic objects in the universe, described by seemingly simple solutions to the Einstein equations of general relativity, yet displaying quantum mechanical properties. The ability to probe black hole phenomena in the semiclassical regime and beyond, using quantum many-body systems, is a powerful tool to test theories of quantum gravity and push the limits of quantum simulation platforms, both in theory and experiment.

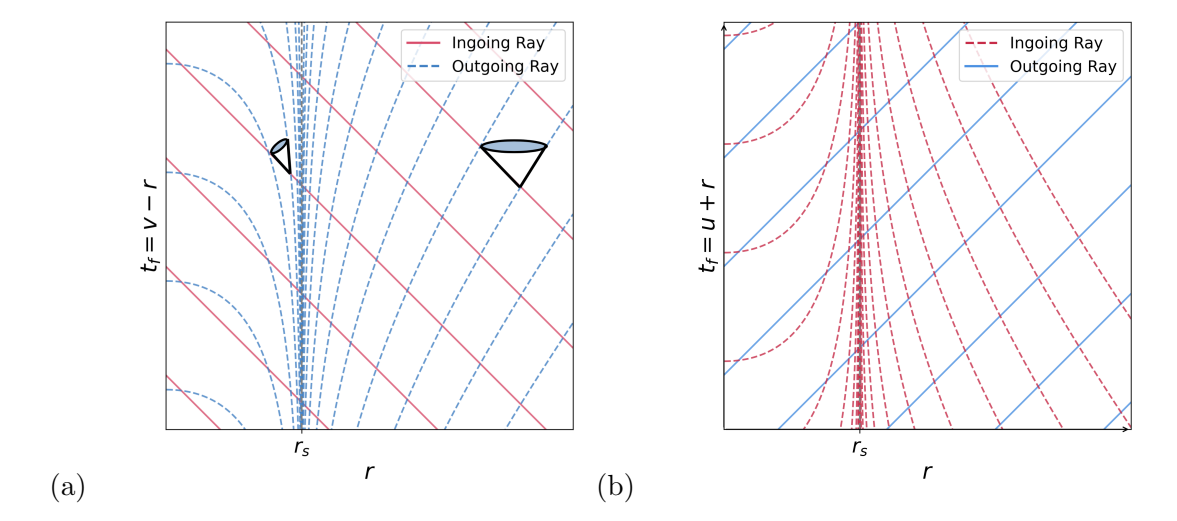


Figure 6.1: The Finkelstein spacetime diagram in ingoing (a) and outgoing (b) Eddington-Finkelstein coordinates. Ingoing null geodesics are shown in red and outgoing one in blue, with the event horizon located at $r_S = 2GM$ in. In panel (a), outgoing geodesics do not leave the black hole interior, while in panel (b) ingoing geodesics do not cross the horizon to enter the black hole. The light cones in (a) indicate regions of spacetime that can be influenced by signals or events at the origin of the cone, while the region outside the light cone is causally disconnected from the event. Notice that the light cone tilts inwards inside the horizon.

6.1 Black hole phenomena and quantum systems in curved spacetime

6.1.1 Black holes and thermodynamics

General relativity predicts that a massive hot star will undergo a complete gravitational collapse and form a black hole. A black hole is an asymptotically flat spacetime that contains a region in spacetime delimited by a surface, the *event horizon*, behind which no causal signal can reach an observer located infinitely far away. The simplest model is a black hole in a Schwarzschild metric, i.e. the solution to the Einstein equations in Schwarzschild coordinates (t, r, θ, ϕ) ,

$$ds^{2} = -\left(1 - \frac{2GM}{r}\right)dt^{2} + \left(1 - \frac{2GM}{r}\right)^{-1}dr^{2} + r^{2}d\Omega^{2},\tag{6.1}$$

where G is Newton's constant. This equation solves the vacuum Einstein equation $R_{\mu\nu}=0$ and represents a static and spherically symmetric black hole with mass M and no charge, discovered by Karl Schwarzschild in 1916 [Sch16]. Note that this coordinate system presents an "unphysical" singularity at the Schwarzschild radius $r_S=2GM$ where a component of the metric diverges, which can be remedied by a coordinate transformation, unlike the singularity at the centre r=0 which indicates that the theory breaks down. In the region near the event horizon r_S , the singularity can be removed by introducing a radial coordinate defined by

$$dr_f^2 = \left(1 - \frac{2GM}{r}\right)^{-2} dr^2 \tag{6.2}$$

such that $r \to r_f = r + 2GM\log\left(\frac{r-2GM}{2GM}\right)$, which maps the region $r \in (2GM, \infty)$ to $r_f \in (-\infty, +\infty)$ [Edd24; Fin58]. Note that r increases slowly with r_f , which led to the name tortoise coordinate. In these coordinates, null radial geodesics are given by $t \pm r_f = C$ where C is a constant, and the \pm sign designates ingoing and outgoing geodesics respectively. Using the change of coordinates to $v = t + r_f$, and substituting in Eq.6.1, returns a new metric

$$d^{2} = -\left(1 - \frac{2GM}{r}\right)dv^{2} + 2dvdr + r^{2}d\Omega_{2}^{2},\tag{6.3}$$

describing a Schwarzschild black hole in *ingoing* Eddington-Finkelstein metric which avoids the unphysical singularity at the horizon. However, in that limit, the dv^2 term disappears at $r = r_S$ and changes sign when $r < r_S$. This behaviour can be understood by examining the structure of the metric. Outside the event horizon, the term g_{vv} is negative, indicating the timelike nature of the coordinate v. Inside the horizon, the g_{vv} term becomes positive, indicating that v behaves as a spacelike coordinate. This change reflects the fact that the roles of time and space are effectively reversed across the event horizon. Next, we consider Eq. 6.1 under the change of coordinates $u = t - r_f$ which results in,

$$ds^{2} = -\left(1 - \frac{2GM}{r}\right)du^{2} - 2dudr + r^{2}d\Omega^{2},\tag{6.4}$$

where the sign of the dudr differs from Eq. 6.4. In fact, these two formulae describe different black hole interiors, which can be seen using the diagram in Fig. 6.1.

Under the metric in Eq. 6.3, which defines the outgoing Eddington-Finkelstein coordinates, light rays travelling into the black hole follow constant trajectories $v = t + r_f$ unimpeded by the event horizon at a 45° angle towards r=0, as shown in red in Fig. 6.1(a). In contrast, outward-travelling light rays starting outside at $r \gg r_S$ appear at a 45° angle, while the strong curvature near r_S causes them to bend near the horizon, as shown in blue in Fig. 6.1(a) for $r > r_S$. If initially located at $r < r_S$, outgoing null geodesics initially directed outward turn inward towards r=0 as they are dragged by the black hole's gravity. The light cones in this figure represent all possible paths that light or causal signals can take through spacetime from an event at the origin of the cone. They respectively illustrate that the causal structure is such that outside the horizon, outgoing light rays can escape to infinity, yet in the black hole interior all light cones are tilted inwards, indicating that no signal can escape. The spacetime diagram in outgoing Finkelstein diagram is shown in Fig. 6.1(b), where outgoing light rays correspond to surfaces of constant $(r, u + r_f)$ as shown in blue at a 45° angle. Contrastingly, ingoing null geodesics (in red) pass through the event horizon, and eventually converging at the singularity r=0, while bending sharply at $r\to r_S$ under the curvature. This illustrates how in Eddington-Finkelstein coordinates all paths ultimately converge inwards once inside the horizon.

As we have seen, black holes are classical objects with a boundary such that anything that falls into the black hole is causally disconnected from the exterior. Therefore, one would expect that an outside observer cannot know the microscopic composition of the black hole interior, which leads to the assumption that the entropy of a black hole vanishes. However, notions of thermodynamics are still encountered in the study of black holes, which proves otherwise. Indeed, an analogy was formulated by Hawking in Ref. [Haw71] through his derivation of the area theorem for a black hole, which states that the total surface area of an event horizon can only increase or stagnate over time, even if the black hole is interacting with other systems (e.g. accreting matter or mergers). This observation was key in establishing the

laws of thermodynamics of black hole physics, since it is reminiscent of the behaviour of entropy. Note that the Penrose process [PF71] provides an interesting exception for rotating black holes, allowing energy to be extracted through the emission of particles. This process decreases the black hole mass, angular momentum, and size, while still respecting the area theorem, as it does not violate the general principle that horizon area cannot decrease.

Bekenstein proposed in Ref. [Bek73] that black holes should have entropy proportional to the area of their event horizon rather than volume. Loosely, his argument was that the entropy of infalling matter into a black hole must be accounted for in order for the entire joint system to respect the second law of thermodynamics, which requires that a black hole must have entropy. Since in general relativity nothing escapes from the horizon, information in the interior becomes inaccessible to an outside observer, which leads to the interpretation of the event as a membrane that captures the maximum amount of information about infalling systems. In this sense, the complete thermodynamic state of the black hole is determined entirely by the properties of the event horizon, as described by the relationship

$$S \propto A$$
. (6.5)

Nevertheless, the dimensions of these quantities do differ. Subsequently, Hawking derived the proportionality constant using first principles in Ref. [Haw75]. By applying the thermodynamic law dU = TdS to a Schwarzschild black hole (where $U = Mc^2$ comes from its mass M), the entropy emerges for the black hole given by the Bekenstein-Hawking formula,

$$S = \frac{A}{4l_P^2} = \frac{c^3 A}{4\hbar G},\tag{6.6}$$

where $l_P = \sqrt{\hbar G/c^3}$ is the Planck length. While in general relativity black holes do not emit any radiation, and are therefore zero-temperature stellar bodies, that is no longer true when incorporating this thermodynamic treatment. Their temperature is referred to as the

Hawking temperature, defined as

$$T_H = \frac{\hbar c^3}{8\pi G M k_B}. (6.7)$$

A remarkable feature of Eq. 6.6 is that the presence of the Planck constant hints at the existence of an ensemble of microscopic states contributing to the black hole entropy, which requires a quantum mechanical framework even though the black hole itself arises as a solution to classical equations. This highlights the need for a full theory of quantum gravity. Additionally, the scaling of the black hole entropy with area rather than volume indicates that the degrees of freedom of the black hole are stored in one less dimension than in ordinary systems—this fact inspired the development of the holographic principle, which stipulates that a theory of gravity could be holographic. This in turn led to the formulation of the AdS/CFT correspondence [Mal99], a duality suggesting that a theory of gravity in a bulk Anti-de-Sitter space (a maximally symmetric solution to Einstein's field equations exhibiting a hyperbolic geometry) is equivalent to a Conformal Field Theory (a quantum field theory that is invariant under conformal transformations) living on the boundary of this space. This area of research is outside the scope of this thesis, but we hope that the work we propose in Chapter 7 could offer a platform to test features of such theories.

6.1.2 Hawking radiation and black hole evaporation

A blackbody at temperature T emits an average photon per mode given by the Bose-Einstein distribution with energy $E = \hbar \omega$, i.e. $\langle n_{\omega} \rangle = (e^{\frac{\hbar \omega}{k_B T_H}} - 1)^{-1}$. Since a black hole is characterised by an effective temperature T_H , Hawking expected that it must radiate, and derived the distribution of its radiation, namely a black body spectrum at temperature T_H [Haw74]. His approach considers an initially stationary star collapsing into a black hole, which becomes stationary in the asymptotic future. This assumption allows for time-translation symmetry in the spacetime, which permits a notion of energy both in the distant past and future, using Noether's theorem. However, this symmetry typically breaks down at finite times leading to different energies in causally distinct regions of spacetime.

The problem can then be framed in multiple ways, which converge to the same blackbody solution. For instance, consider quantised Klein-Gordon fields which satisfy the wave equation in Schwarzschild spacetime, with its modes decomposed differently for different observers. The first is an inertial observer in the asymptotic future, and observes Fourier modes that vary with time as $e^{i\omega t}$, where t is the Schwarzschild coordinate time. The second is an infalling observer crossing the horizon, using the advanced time coordinate $u=t-r_f$ as defined in the previous section, observing Fourier modes $e^{i\nu t}$. To the first observer we assign the creation (annihilation) operators a_{ω}^{\dagger} (a_{ω}) which are well-defined only in the region outside the event horizon due to the time translation symmetry, and to the second, the creation (annihilation) operators b_{ν}^{\dagger} (b_{ν}) well-defined because the infalling observer's experience is regular as they cross the horizon. Using the adiabatic principle [BD84], the modes crossing the horizon approach the vacuum state of the black hole such that $b_{\nu} = |\Psi\rangle$. The Bogoliubov transformations connect these two sets of operators and encode how different observers perceive particle creation. To the asymptotic observer, the vacuum observed by the infalling observer appears to be filled with a number of particles $\langle \Psi | a_{\omega}^{\dagger} a_{\omega} | \Psi \rangle$, given by the spectrum

$$\langle N_{\omega} \rangle = \langle \Psi | \, a_{\omega}^{\dagger} a_{\omega} \, | \Psi \rangle \propto \frac{\Gamma}{e^{\frac{\hbar \omega}{k_B T_H}} - 1},$$
 (6.8)

which describes the thermal radiation emanating from the black hole perceived by a far observer, known as the Hawking radiation, and where the proportionality constant encodes the lower intensity of the emitted radiation in comparison to that of an ideal black body at temperature T_H , referred to as the greybody factor. A distant observer perceives particles with a non-zero energy coming out of the black hole. This process carries energy from the black hole which in turn loses mass and is said to evaporate. This process is typically considered slow, even for small astrophysical black holes. For instance, a black hole of mass 10^{12} kg has temperature $T_H \sim 10^1$ K, and therefore completely evaporates in several trillion years, and even longer for stellar-mass and supermassive black holes for which $T_H \ll 1$ making them effectively undetectable. For completeness, we also mention other paradigms which provide

insights into Hawking radiation in Appendix A4.

Much like the relationship between entropy and the area of the black hole, the Hawking temperature of the blackbody spectrum in Eq. 6.8 finds its analogue in the surface gravity of the black hole. This is defined as the gravitational acceleration near its event horizon,

$$\kappa = \frac{1}{2} \frac{\partial g_{tt}}{\partial r} \bigg|_{r=r_S} \tag{6.9}$$

i.e. force per unit mass, to keep a particle at rest near the event horizon as seen from infinity. From the time component of the Schwarzschild metric in Eq. 6.1 it is easy to see that the surface gravity in Schwarzschild coordinates is given by

$$\kappa_S = \frac{GM}{r_S} = \frac{c^2}{4GM},\tag{6.10}$$

which is also valid in Eddington-Finkelstein coordinates since the surface gravity is a geometric property of the spacetime in which the black hole is defined, and is therefore not dependent on the coordinate system. Using the definition in Eq. 6.7, the relationship

$$T_H = \frac{\hbar c\kappa}{2\pi k_B} \tag{6.11}$$

emerges, which indicates that the Hawking temperature is a property of the curvature at the horizon, and is exactly what we probe in Chapter 7. In fact, this expression can be derived using quantum field theory in curved spacetime [BD84]. This expression also reveals that the Hawking temperature is directly proportional to the surface gravity, which characterises the acceleration experienced by particles at the event horizon. This mirrors the Unruh effect [Unr76], whereby an observer undergoing uniform acceleration perceives a thermal bath in what is perceived as vacuum by an inertial observer.

The evaporation of black holes raised a concern put forward by Hawking in the 1970s, known as the *black hole information paradox* [Haw76b]. This problem suggests that information of the infalling matter into a black hole seems to be permanently lost, thereby violating

the principle of unitarity in quantum mechanics, which asserts that the evolution of quantum states is deterministic and reversible. Several proposals exist to resolve this issue [t H95; Haw15], as well as protocols framing the retrieval of infalling quantum information as a decoding experiment [HP07; YK17].

6.2 Introduction to relevant quantum many-body systems

6.2.1 The XY model

We start by introducing the one-dimensional spin-1/2 XY model, an infamous cornerstone in the study of condensed matter physics and quantum magnetism. The XY model emerged as a simpler variant of the more general Heisenberg spin chain, obtained by turning off the z components of neighbouring spins [LSM61]. The system is defined using an L-spin chain, with Hilbert space given by $\mathcal{H} = \mathcal{H}_{1/2}^{\otimes L}$, where $\mathcal{H}_{1/2}$ is the Hilbert space of a spin-1/2 particle, and dim($\mathcal{H}_{1/2}$) = 2. The Hamiltonian of the XY model is expressed as

$$H = -\frac{u}{2} \sum_{l=0}^{L-1} \left[\sigma_l^x \sigma_{l+1}^x + \sigma_l^y \sigma_{l+1}^y \right]$$
 (6.12)

where $u \in \mathbb{R}$, and σ_l^x, σ_l^y are the Pauli matrices acting on the l^{th} spin (cf. Eq. 2.15) on the chain such that $\sigma_l^p = \mathbb{1}^{\otimes l-1} \otimes \sigma_l^p \otimes \mathbb{1}^{\otimes L-l}$, where $p \in \{x, y, z\}$. This Hamiltonian simplifies to a free theory of spinless fermions under the Jordan-Wigner transformation [JW28]. This mapping arises from the similarity of half-spin raising(lowering) operators $\sigma_l^{\pm} = (\sigma_l^x + i\sigma_l^y)/2$ and fermion creation(annihilation) operators $c_l^{\dagger}(c_l)$, with the following transformations

$$\sigma_l^+ = \exp\left(-i\pi \sum_{m=0}^{l-1} c_m^{\dagger} c_m\right) c_l^{\dagger}, \qquad \sigma_l^- = \exp\left(i\pi \sum_{m=0}^{l-1} c_m^{\dagger} c_m\right) c_l \tag{6.13}$$

where $\sigma_l^z = 1 - 2c_l^{\dagger}c_l$. The fermionic operators respect the commutation relations

$$\{c_l, c_m^{\dagger}\} = \delta_{lm}, \qquad \{c_l, c_m\} = 0, \qquad \{c_l^{\dagger}, c_m^{\dagger}\} = 0.$$
 (6.14)

Using Eq. 6.14 and Eq. 6.13, Eq. 6.12 takes the simple form

$$H = -u \sum_{l=0}^{L-1} c_l^{\dagger} c_{l+1} + c_{l+1}^{\dagger} c_l$$
 (6.15)

which describes a chain with nearest-neighbour hopping that is quadratic in the fermionic operators. Since this Hamiltonian is non-interacting, it can be exactly diagonalised, as shown in Appendix A5.

Despite its simplicity, the XY model shares key physical features with the Heisenberg model, such as gapless excitations and the absence of long-range magnetic order in its ground state. Moreover, it provides a versatile framework to explore rich physics through variations such as anisotropy and inhomogeneous couplings. This allows for the study of phenomena such as phase transitions, localisation of spin excitations, modified spin correlation behaviour, and more. In particular, inhomogeneous couplings —where the interaction strengths vary across the lattice—introduce spatial disorder or structure to the system, significantly altering its physical properties, which can be leveraged to simulate tunnelling effects across a barrier.

6.2.2 The Bose-Hubbard model

The Bose-Hubbard model describes the dynamics of bosons on a lattice with onsite repulsion. Consider the bosonic creation and annihilator operators acting on a boson at site i, b_i^{\dagger} and b_i respectively, and the number operator which counts the number of bosons at a given site i,

$$n_i = b_i^{\dagger} b_i. \tag{6.16}$$

In a 1D system, the Hamiltonian for this model is given by

$$H_{BH} = J \sum_{i} \left(b_i^{\dagger} b_{i+1} + b_{i+1}^{\dagger} b_i \right) - \mu \sum_{i} n_i + \frac{U}{2} \sum_{i} n_i (n_i - 1).$$
 (6.17)

The three terms in H_{BH} respectively account for the boson hopping between nearest-neighbouring sites with an energy coupling J, a chemical potential term with coefficient μ , which couples to the total number of bosons, and an onsite pairwise repulsive interaction of magnitude U between bosons. This model can also describe higher-dimensional systems where the nearest-neighbouring term accounts for nearest-neighbour pairings $\langle i, j \rangle$ on the lattice.

In the limit where the onsite interaction becomes large, $U \to \infty$, the system is restricted to at most one boson per site, i.e. $n_i = 0$ or 1. This constraint plays a critical role in shaping the effective interactions between particles. Indeed, this constraint effectively enforces a Pauli-like exclusion principle for bosons, mimicking the behaviour of spin-1/2 particles. This regime is known as the hardcore boson limit, and is equivalent to the XY Hamiltonian in Eq. 6.12, where b_i^{\dagger} and b_i act as the spin-half raising and lowering operators σ_i^+ and σ_i^- . The hopping in terms in Eq 6.12 now represent boson hopping between nearest-neighbour sites $\langle i,j \rangle$. Interestingly, the forbidden double-site occupation induces correlations in the spatial arrangement and dynamics of the bosons, such that if a boson occupies a site, neighbouring sites become less favourable for occupation, which effectively creates a repulsive interaction between bosons.

The Bose-Hubbard model is a faithful approximation for spinless bosonic atoms in an optical lattice with repulsive interaction between atoms [Jak+98]. In general, the Bose-Hubbard model can be realised in laboratory using various quantum simulation platforms, such as optical lattices [BDZ08], superconducting qubits [HTK12], and trapped ions [PC04].

6.2.3 Optical lattices and Floquet driving

Optical lattices are periodic potential landscapes created by the interference of laser beams, which can trap ultracold atoms. Ultracold atoms in optical lattices provide an excellent platform for probing many-body phenomena in translationally invariant systems, since they allow for high control over the system parameters, long coherence times, scalability and advanced measurement schemes [Blo05; GB17b; Sch+20b]. This allows for the quantum simulation of condensed matter [Zha+22], high energy physics [ZCR15], statistical physics [Yu+23], quan-

tum chemistry [Arg+19] and more. Furthermore, advances in the control and manipulation of single lattice sites allows for the use of optical lattices beyond the translationally invariant regime, which is necessary to probe inhomogeneous systems where individual tunnelling links must be tuned independently.

It has been shown in Ref. [NUS23] that this full local control over tunnelling elements can be realised by periodically modulating the onsite energy of individual lattice sites, such that two nearest-neighbour tunnelling elements can be addressed by controlling the relative modulation between the two connected lattice sites. This method relies on Floquet driving, which consists of applying a periodic time-dependent perturbation to a system, which involves modulating its parameters such as lattice depth, position, and trapped atom interactions. These modulations enable experimental control over the system properties, so that an effective time-independent Hamiltonian emerges that exhibits properties not present in the non-driven system. This powerful technique can be employed to induce gauge fields, spin-orbit couplings, introduce topological bands and edge states, control the tunnelling rate between lattice sites, and stabilise exotic phases of matter such as time crystals [Tah+22] and Floquet topological insulators [Cav+13]. Experimentally, this is realised by a combination of lattice shaking, amplitude modulation, and periodically driven interactions between atoms. In Chapter 7, we proposed a scheme using such a full local control in one and two dimensions to simulate quantum properties of a black hole in the semiclassical regime and potentially beyond, and provide a description of the Floquet engineering in Appendix A6.

Chapter 7

Probing quantum properties of black holes with a Floquet-driven optical lattice simulator

7.1 Introduction

A classical particle in the gravitational pull of a black hole cannot escape once it crosses the event horizon. However, quantum fluctuations from the interior of a black hole can tunnel across the horizon and radiate outwards, a phenomenon known as Hawking radiation which we reviewed in Sec. 6.1.2 [Bek73; Haw74; Haw75; DR76; AMV05; PW00]. The emitted thermal radiation carries no information about the quantum state inside the black hole and its temperature only depends on the gravitational curvature around the horizon. Hawking radiation can be fully analysed in the semiclassical limit (\hbar small), which describes a non-interacting theory of free fields in a static background geometry [Haw80; BD84]. In addition, any quantum state entering the black hole is expected to scramble (thermalise) with the highest possible rate. This optimal ergodicity property is caused by quantum gravity interactions that are present beyond the semiclassical description of black holes, and is the subject of intense ongoing

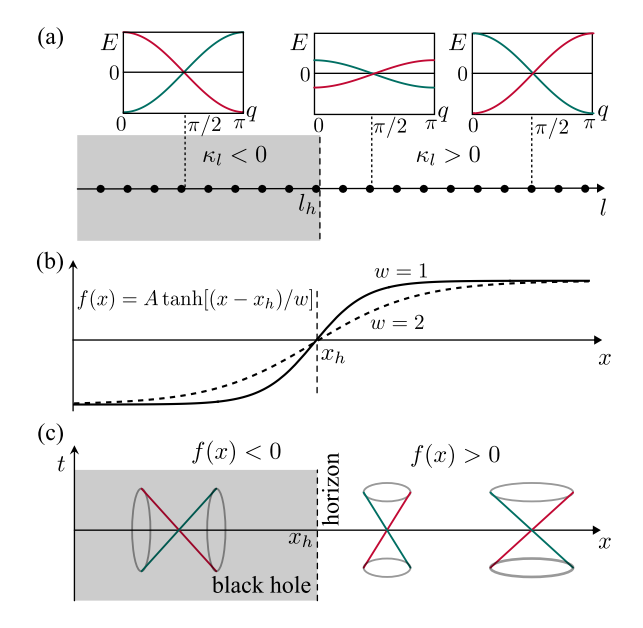


Figure 7.1: Schematic of the black hole simulator. (a) The black hole geometry is encoded in the position-dependent tunnelling amplitudes $\kappa_{l\,l+1}$ of a fermionic tight-binding chain, and change sign across the horizon. The tunnelling elements $\kappa_{l\,l+1} = [f(ld) + f((l+1)d)]/(8d)$, where d is the discretisation length, follow the behaviour of the black hole curvature f(x), an example of which is given in (b). Insets show the local dispersion relation E(q) at different positions. The left-moving branch is shifted in momentum by π to highlight the analogy with light cones. At low energies $|E| \ll J_0$, E(q) is linear and describes massless Dirac fermions in a curved background. (c) The light-cones collapse on each other at the horizon, $x_h = 0$, signalling that it is impossible for classical particles to cross.

investigations [SS08; Kit15; MS16; BD84].

There are several classical and quantum analogues that can simulate the geometric properties of a black hole, e.g. by studying sound waves propagating in a supersonic fluid [Unr81; Unr95; Wei+11a; MP14; Ngu+15; CW16; BRN18; JWK20; Jac+20; Jac+22; RBF22], using ultracold atoms in the continuum [Lah+10; Ste16; Muñ+19; Vie+22; FS04; FF04], ion trapping [Tia+22] or quantum circuits [Jaf+22]. However, an open question remains as to how to devise a system that can produce the geometrical features of the black hole's horizon, while also exhibiting the scrambling behaviour expected to be present in its interior [SY93; Swi+16; Has+21]. As an alternative, theoretical proposals have demonstrated how lattice Hamiltonians can simulate quantum field theories in curved space-time geometry [Mal+19; Yan+20;

Shi+23; She+21; Lap+20] and ultracold atoms in optical lattices have emerged as highly flexible and effective analogue quantum simulators of lattice Hamiltonians [GB17a; Sch+20a; Cho23]. Indeed, optical lattices already allow us to probe intriguing quantum many-body phenomena such as entanglement entropy [Isl+15; Kau+16], many-body localisation [Sch+15; Kon+15; Cho+16; Bor+16; Ris+19] and quantum scars [Zha+20; Hud+20].

In this Chapter, we propose to simulate both (1+1)D and (2+1)D black holes using an optical lattice, and investigate the resulting behaviour. We employ local Floquet driving to realise position-dependent tunnelling [WÜE18; NUS23] in order to encode massless Dirac fermions in the gravitational curvature of a black hole, as shown in Fig. 7.1 and explained in Sec. 7.2 and Sec. 7.3. We show that wave packets of single atoms initialised inside the black hole in 1D eventually tunnel across the horizon and can be witnessed from outside the black hole as thermal Hawking radiation. Based on the effect local curvature has on the quantum evolution of the system, we propose a straightforward scheme to measure the Hawking temperature from onsite population measurements of atoms in Sec. 7.4. In Sec. 7.5, we demonstrate the resilience of our 1D optical lattice simulator under a range of experimental imperfections. The simplicity of our scheme paves the way for various extensions. We show how our simulator is generalised to (2+1)D black holes in Sec. 7.6, by using readily available higher-dimensional optical lattices. Introducing tuneable interactions between the atoms in an optical lattice quantum simulator can be achieved using Feshbach resonances [Chi+10]. Numerical simulations of an interacting 2D black hole in Sec. 7.7 across a 7×7 site lattice show level statistics of a diffusive phase. Our simulator provides an opportunity to study the many-body physics of black holes beyond the semiclassical regime, where information scrambling can be witnessed.

7.2 The tight-binding model and the Dirac Equation

In this section we present a brief derivation of the dynamics of non-interacting atoms moving in an optical lattice can simulate the dynamics of a relativistic particle described by the Dirac equation. We start with the Heisenberg equation of motion for the fermionic annihilation operator c_l at a specific site l, i.e.

$$i\partial_t c_l = [c_l, \mathcal{H}],\tag{7.1}$$

where fermionic anti-commutation relations $\{c_l, c_{l'}^{\dagger}\} = \delta_{l,l'}$ apply. The tight-binding Hamiltonian describing atoms moving in an optical lattice is given as

$$\mathcal{H} = -\sum_{l} \left[\kappa_l (\hat{c}_l^{\dagger} \hat{c}_{l+1} + \hat{c}_{l+1}^{\dagger} \hat{c}_l) \right], \tag{7.2}$$

where we set the global energy scale to $J_0 = c = \hbar = 1$. It can be shown that $[c_l, \mathcal{H}] = -\kappa_l c_{l+1} - \kappa_{l-1} c_{l-1}$. After substituting $c_l = i^l \phi_l$ where the fermionic operator is transformed to the field operator ϕ , we arrive at the following equation of motion for the (discrete) field ϕ_l :

$$\partial_t \phi_l = -\kappa_l \phi_{(l+1)} + \kappa_{l-1} \phi_{(l-1)} \tag{7.3}$$

We next discuss the solution of the (1+1)D Dirac equation in the massless limit

$$i\gamma^a e^\mu_a (\partial_\mu + \omega_\mu) \psi = 0, \tag{7.4}$$

which takes a similar form, allowing us to identify the relationship between the tunnelling elements κ_l of the lattice model and a curved background with the metric $ds^2 = f(x)dt^2 - \frac{1}{f(x)}dx^2$. To be concrete, we consider a black hole with a horizon at $x = x_h$ and transform the Schwarzschild metric to Eddington-Finkelstein coordinates [Edd24; Fin58]. In this metric the time coordinate remains constant along the radial null geodesics, resulting in non-singular metric components. The metric can be expressed as $ds^2 = f(x)dt^2 - 2dtdx$. Next, we select vierbeins as $e_t^0 = [-f(x) - 1]/2$, $e_t^1 = [-f(x) + 1]/2$, while the remaining vierbein components are equal to 1 and gamma matrices as $\gamma^0 = \sigma^z$, $\gamma^1 = i\sigma^y$ [Yan+20]. The vierbeins are linking the curved metric $g_{\mu\nu} = \eta_{ab}e_{\mu}^a e_{\nu}^b$ to the flat metric $\eta_{ab} = \text{diag}(1, -1)$, while ω_{μ} represents the spin connection. We select the following spinor $\psi = (\phi, -\phi)/\sqrt{2}$, where the two components

are interdependent. Upon incorporating all these elements into the Dirac equation [Yan+20], we arrive at the formula

$$\partial_t \phi_x = -\frac{1}{4} \{ \partial_x \left[f(x)\phi_x \right] + f(x)\partial_x \phi_x \}. \tag{7.5}$$

We now discretise Eq. (7.5) by replacing the continuous coordinate x with a discretised version ld, where l is an integer and d denotes the discretisation length (lattice constant). Together with the central difference formula for functions

$$\partial_x(f(x)\phi_x) = \frac{f_{(l+1)}\phi_{(l+1)} - f_{(l-1)}\phi_{(l-1)}}{2d},\tag{7.6}$$

we obtain the following form

$$\partial_t \phi_l = -\left[\frac{f_{l+1} + f_l}{8d} \right] \phi_{(l+1)} + \left[\frac{f_{l-1} + f_l}{8d} \right] \phi_{(l-1)}. \tag{7.7}$$

Now, by comparing Eq. (7.3) with Eq. (7.7), we obtain the following relationship

$$\kappa_l = \frac{f_{l+1} + f_l}{8d}.\tag{7.8}$$

7.3 An optical lattice simulator of Dirac fermions in a black hole background

We now present the fermionic lattice Hamiltonian that in the low energy limit is mathematically equivalent to the Dirac equation in the curved space around a black hole [BD84; Yan+20; Shi+23; Mer+22; Mor+22; Hor22; DHP23; HHP23]. Our optical lattice simulator is described by a fermionic tunnelling Hamiltonian given by

$$H = -J_0 \sum_{\langle i,j \rangle} \kappa_{ij} (\hat{c}_i^{\dagger} \hat{c}_j + \hat{c}_j^{\dagger} \hat{c}_i)$$
 (7.9)

where the $\hat{c}_{j}^{\dagger}(\hat{c}_{j})$ denote the fermionic creation (annihilation) operators on site j, J_{0} defines a global energy scale, and the κ_{ij} 's are position-dependent dimensionless tunnelling amplitudes that encode the metric of the curved space. When varying the amplitudes $\kappa_{l\,l+1}$ in a 1D model [Fig. 7.1(a)] according to a possible metric describing a 1D black hole [Fig. 7.1(b)], the (local) dispersion relation of the lattice near zero energy mirrors the behaviour of the relativistic light cones, see Fig. 7.1(c). In the continuum limit and at half filling, the behaviour of the fermionic chain can be faithfully described by the massless Dirac equation $i\gamma^{a}e^{\mu}_{a}(\partial/\partial x^{\mu}+\omega_{\mu})\psi=0$. Here the coordinates are $(x^{0},x^{1})=(ct,x)$ with c the speed of light, γ^{a} are the two-dimensional Dirac matrices, e^{a}_{μ} are the vierbeins connecting the curved metric $g_{\mu\nu}=\eta_{ab}e^{a}_{\mu}e^{b}_{\nu}$, to the flat metric $\eta_{ab}={\rm diag}(1,-1)$, where ω_{μ} is the spin connection and ψ is the two-component spinor as previously defined –see Refs. [Bor61; Yep11] for an introduction to this formalism. The time evolution under the lattice Hamiltonian Eq. (7.9) is equivalent to that of a Dirac field in a curved background under the metric

$$ds^{2} = f(x)c^{2}dt^{2} - \frac{1}{f(x)}dx^{2},$$
(7.10)

when $\gamma^0 = \sigma^z$, $\gamma^1 = i\sigma^y$, $\hbar c = J_0$ [CMP10], where the spacetime curvature f(x) is encoded in the lattice tunnelling amplitudes via $\kappa_{l\,l+1} = [f(ld) + f((l+1)d)]/(8d)$ and d is a chosen discretisation length [Yan+20]. A typical Schwarzschild-like metric f(x) in Eq. (7.10) possesses a horizon at a distance x_h where $f(x_h) = 0$, while f(x) < 0 describes the black hole interior $(x < x_h)$ and f(x) > 0 the exterior $(x > x_h)$, as shown in Fig. 7.1(b). In this metric, that corresponds to the free-falling frame, the light cones compress radially near the event horizon due to the strong gravitational pull as depicted in Fig. 7.1(c). At the horizon, the light cone collapses to a vertical line, signalling the impossibility for classical particles to cross. Nevertheless, quantum particles can tunnel across the horizon resulting in Hawking radiation. The change of sign in f(x) across the event horizon reflects the interchange of the role of the temporal and radial coordinates inside the black hole. While there is no singularity at the horizon, this means that within the black hole interior the radial coordinate becomes timelike, and all future-directed paths inevitably lead toward the singularity at x=0. This reversal is encoded in the sign change of the tunnelling amplitudes $\kappa_{l\,l+1}$, which capture the shift in causal structure across the horizon. A typical profile for (1+1)-dimensional black holes is $f(x) = A \tanh(x/w)$ [Yan+20; HHP23], where w is positive and controls the steepness of the curve around the horizon and A is a scaling factor, see Fig. 7.1(b). For simplicity, in our proposed simulator we approximate this profile around the horizon with a linear function where the dimensionless slope $\alpha = Ad/w$ is controlled by the width w. This corresponds to tunnelling coefficients of the form

$$\kappa_{l\,l+1} = \alpha(l - l_h + 0.5)/4,$$
(7.11)

such that $\kappa_{l\,l+1} \neq 0$ at the horizon despite the required $f(x_h) = 0$.

The discrete lattice representation of a black hole with curvature encoded into the local tunnelling coefficients $\kappa_{l\,l+1}$ in Eq. (7.9) can be implemented using a locally-driven, one-dimensional optical lattice, where tightly-focused far off-resonant optical tweezers [Ber+17; Bar+18; MBV24; Tri+22; You+22] independently drive the onsite potentials of individual lattice sites in an optical lattice [NUS23], as illustrated in Fig. 7.2. In the following, we utilise Floquet-Bloch theory to capture the long-term evolution of the periodically driven system and demonstrate that it corresponds to a time-independent effective Hamiltonian [GD14; BDP15; Eck17; WS21] that matches the desired position-dependent tunnelling profile given by Eq. (7.11). The full time-dependent Hamiltonian of the driven system is given by

$$H(t) = -J_0 \kappa \sum_{\langle i,j \rangle} (\hat{c}_i^{\dagger} \hat{c}_j + \hat{c}_j^{\dagger} \hat{c}_i) + \cos(\omega t) \sum_j A_j \hat{c}_j^{\dagger} \hat{c}_j.$$
 (7.12)

where κ is a dimensionless value such that κJ_0 is the bare tunnelling between neighbouring lattice sites, A_j is the driving amplitude of site j, and ω is the global driving frequency ensuring H(t) = H(t+T) with period $T = 2\pi/\omega$. Given a fixed global energy scale J_0 , the constant κ is required to encode a larger range of Hawking temperatures in our simulator, as

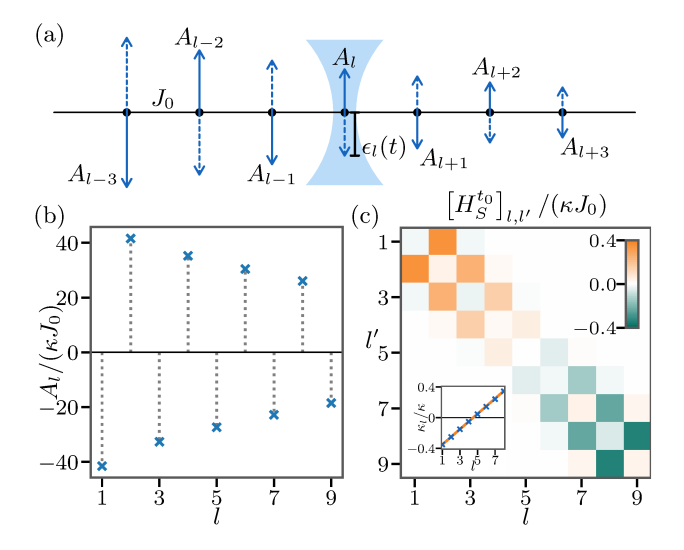


Figure 7.2: A black hole simulator implemented using local Floquet driving of a 1D optical lattice. (a) The onsite potential of each site l is modulated according to $\epsilon_l(t) = A_l \cos(\omega t)$ with an independent amplitude A_l using individual tweezer beams indicated by the light-blue shading. (b) Driving amplitudes A_l for a nine-site lattice that generate renormalised dimensionless tunnelling elements $\kappa_{l\,l+1}$ following the linear profile given by Eq. (7.11). The inverted sign of neighbouring driving amplitudes indicates the modulations are π out of phase. (c) The numerically calculated stroboscopic Hamiltonian $H_S^{t_0}$ for $t_0 = 0$, $\hbar \omega / \kappa J_0 = 25$, and the A_l shown in (b). The inset shows that the stroboscopic tunnelling elements perfectly follow the target linear profile in Eq. (7.11) (red line). Here we took $\alpha / \kappa = 0.4$ and $l_h = 5$.

seen in Sec. 7.2. The T-periodic nature of Eq. (7.12) ensures that the resulting stroboscopic evolution during multiples of the global driving period T can be captured by

$$U(t_0 + nT, t_0) = e^{-\frac{i}{\hbar}nTH_S^{t_0}}, (7.13)$$

where $n \in \mathbb{N}$, and $H_S^{t_0}$ is the time-independent, "stroboscopic Hamiltonian" [Eck17; BDP15]. The stroboscopic Hamiltonian is analytically difficult to calculate, but can be accessed numerically as mentioned in Appendix A6. A convenient analytical approximation of $H_S^{t_0}$ can be obtained in the high-frequency regime, resulting in Hamiltonian Eq. (7.9) with

$$\kappa_{ij} = \kappa \mathcal{J}_0 \left(\frac{|A_i - A_j|}{\hbar \omega} \right), \tag{7.14}$$

where \mathcal{J}_0 is the Bessel function of the 0th kind. Crucially, Eq. (7.14) illustrates that local tunnelling elements depend only on the relative modulation between neighbouring lattice sites [NUS23]. We can now reverse-engineer Eq. (7.14) to generate a sequence of A_l and a global κ that result in the desired tunnelling profile given in Eq. (7.11), and hence encode the black-hole geometry. For example, Figure 7.2(b) shows a series of driving amplitudes A_l that generate $\kappa_{l\,l+1}$ following the linear profile of Eq. (7.11) with $\alpha/\kappa = 0.4$ and $l_h = 5$. In order to minimise the absolute size of the required A_l , and thereby the resulting Floquet heating [Wei+15; Rei+17; Eck17], we alternate their signs.

Figure 7.2(c) shows the numerically generated stroboscopic Hamiltonian obtained from the driving amplitudes of Fig. 7.2(b) - cf. Appendix A6. This operator matches the analytic approximation in Eq. (7.14) up to small higher-order corrections such as next-to-nearest neighbour tunnelling elements, and new onsite energies that are invisible on this scale [NUS23]. As we demonstrate later, our analogue black hole simulator is resilient to these corrections and the resulting stroboscopic Hamiltonian can faithfully reproduce the expected Hawking radiation.

7.4 Hawking temperature from radiation population

To demonstrate the reliability of our simulator in reproducing the quantum features of a black hole, we first investigate the behaviour of the Hawking temperature

$$T_H = \frac{\hbar c}{4\pi k_B} \left. \frac{df(x)}{dx} \right|_{x=x_b},\tag{7.15}$$

which depends on the curvature of the black hole at the horizon [GH77]. Then we propose a simple method to measure T_H in an optical lattice experiment by utilising easily accessible insitu density measurements to analyse the quantum walk of an initially localised atom [Dür+02; Wei+11b; Fuk+13]. In the following, we take for simplicity $\hbar = 1$, $k_B = 1$ and $c = J_0 = 1$ unless stated otherwise. This leads to $\alpha = 4\pi T_H$ in our linearised simulator given in (7.11).

To study the physics close to the simulated event horizon we consider the evolution of a single quantum particle, termed the walker, initially positioned inside the black hole, and its potential tunnelling across the horizon. In Fig. 7.3(a) we show the density evolution of such a walker under the linearised tunnelling profile of Eq. (7.11) with $l_h = 50$, $\alpha = 1$ on a chain of 100 sites where the walker is initially at site l = 45, i.e. inside the black hole. The walker noticeably remains mostly confined inside the black hole but with a non-zero probability of escaping, i.e. evaporating [Sab+22; Hor22]. This forms the outgoing Hawking radiation. We explore walker dynamics for a range of Hawking temperatures by evolving the initially localised state $|\Psi_i\rangle$ numerically using $|\Psi(t)\rangle = e^{-i\mathcal{H}t} |\Psi_i\rangle$.

An observer outside the horizon only has access to the visible (outside) part of the system and will therefore see the emergence of an incoherent state expected to correspond to a black-body spectrum at temperature T_H [GH77]. We compute the probability $P_n = \langle E_n | \rho_{\text{out}} | E_n \rangle$ of a particle with energy E_n being detected outside the horizon, where $\rho_{\text{out}} = \text{Tr}_{\text{in}} (\rho_t)$ is the reduced density matrix of the evolved state $\rho_t = |\psi(t)\rangle\langle\psi(t)|$ at time t in the exterior of the black hole, and $|E_n\rangle$ are the energy eigenstates of the Hamiltonian H_{out} taken to be acting only on the sites outside the horizon. In analogy with the particle-type solutions of the Dirac equation, we focus our analysis on positive energies, and indeed find that this spectrum decays exponentially as $P_n \propto e^{-E_n/\tilde{T}_H}$, as shown in Fig. 7.3(b). In fitting the slopes in Fig. 7.3(b) we ignored the exponentially suppressed contributions from very large energies as our Dirac simulation is valid in the low energy regime, and also from very small energies where discretisation effects become dominant.

Experimentally, directly monitoring the populations of all eigenstates $|E_n\rangle$ necessitates full state tomography in the black hole exterior, which is a difficult task. Using the full tanh profile sketched in Fig. 7.1(b), it would also be possible to extract the spectrum from the experimentally accessible momentum distribution of the walker in the flat region of space. However, this would require large systems that might be challenging to realise experimentally. Hence, in the following we propose an alternative means to extract the Hawking temperature, and hence the curvature at the horizon, purely from in-situ population measurements routinely

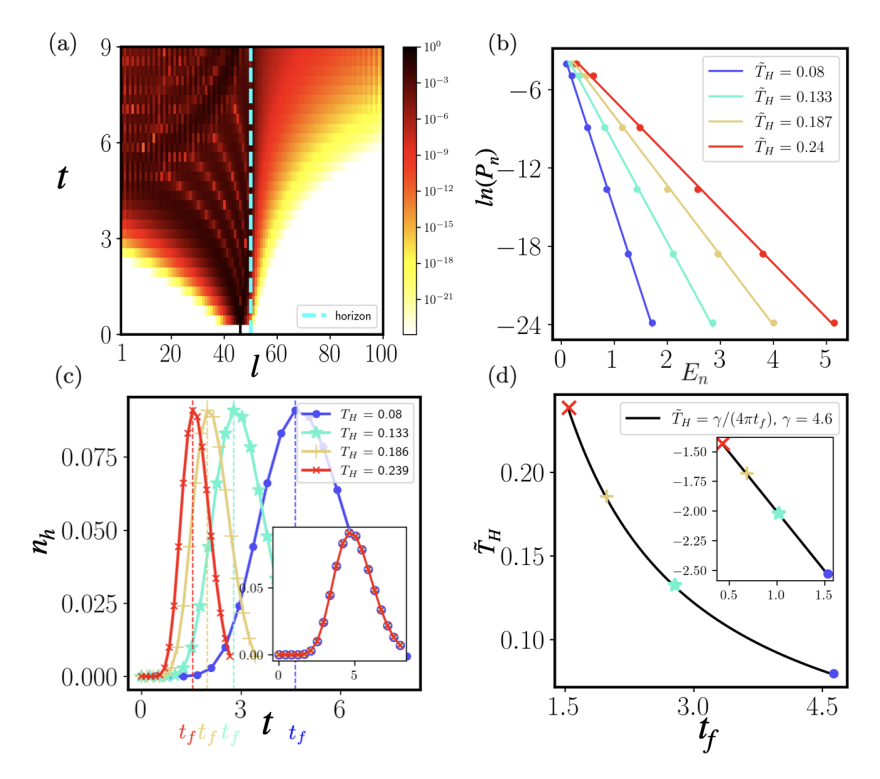


Figure 7.3: (a) Density evolution (log-scale) of a single particle initialised at l=45 under the Hamiltonian in Eq. (7.9) for a Hawking temperature $T_H=\alpha/(4\pi)\approx 0.08$. (b) Probability (log scale) of finding a particle with energy E_n outside the event horizon satisfying a blackbody spectrum $P_n \propto e^{-E_n/\tilde{T}_H}$, evaluated at time $t=6/\alpha$, for varying α . Extracted temperatures \tilde{T}_H from the thermal distribution agree with the expected Hawking temperature T_H encoded in the Hamiltonian. (c) Time evolution of the density n_h at the horizon site $l_h=50$ for several α (or T_H). Same colours in (b) and (c) corresponds to the same α . t_f denotes the time at which peak density is reached at the horizon. (Inset) Collapsed curves with time rescaled by $1/\alpha$. (d) Hawking temperature \tilde{T}_H extracted from spectrum in (b) against the measured time t_f of the peak of the density at the event horizon. The solid line fits the data to the ansatz $\tilde{T}_H \propto t_f^{-1}$ (inset in log-log scale). This relationship allows for the extraction of \tilde{T}_H from an experimentally measured peak time t_f .

available in quantum gas microscopes [Bak+09; She+10; Pre+15; GB21]. Intuitively, due to the decreasing tunnelling amplitudes close to the horizon, the walker will slow down in this region, before either being reflected back into the black hole or tunnelling through to the exterior, resulting in a pronounced maximum in density that depends on α , i.e. on the local curvature at the horizon.

To demonstrate this, we plot in Fig. 7.3(c) the time evolution of the population density $n_h = \langle c_{l_h}^{\dagger} c_{l_h} \rangle$ at the event horizon site l_h . The density n_h is initially zero until the wave packet has reached the horizon, after which it reaches a maximum at a time t_f before decreasing again. In Fig. 7.3(d) we plot t_f against the temperature \tilde{T}_H extracted from the thermalised spectrum and find the simple inverse relationship

$$t_f = \gamma (4\pi \tilde{T}_H)^{-1} \tag{7.16}$$

with a proportionality constant γ , directly linking Hawking temperature and time dynamics. This effect also transpires in the inset of Fig. 7.3(c), where the density evolutions at the event horizon are collapsed by a linear rescaling of the time axis. Note that γ depends on the particular experimental conditions, in particular the initial position of the walker. We highlight that monitoring density at a single site is sufficient since the Hawking temperature is controlled by the local curvature at the horizon [Haw75; DR76; PW00; AMV05; LTT20]. Alternatively, one can measure the total probability density outside the horizon, i.e. $P_{\text{out}} = \sum_{l=l_h+1}^{l=L} n_l$, where $n_l = \langle c_l^{\dagger} c_l \rangle$, which provides a direct measure for the total intensity of the Hawking radiation. Within the linear profile of Eq. (7.11), scaling the encoded Hawking temperature T_H amounts to an equivalent global scaling of the tunnelling coefficients $\kappa_{l\,l+1}$, which is directly equivalently to an inverse scaling of time and hence explains the behaviour observed in (7.16).

Our simulator is described by a single-particle Hamiltonian, hence we do not anticipate thermalisation or scrambling. However, due to the specific tunnelling profile that simulates the black hole horizon, components of quantum states that tunnel through the horizon appear thermal for the degrees of freedom outside the black hole even for a pure initial quantum state. This corresponds to the notion that the Hawking radiation loses memory of the initial state of the black hole when observed from the outside. This is manifested in our simulator by obtaining a thermal spectrum outside the black hole with the same Hawking temperature regardless of the initial position of the walker inside the black hole.

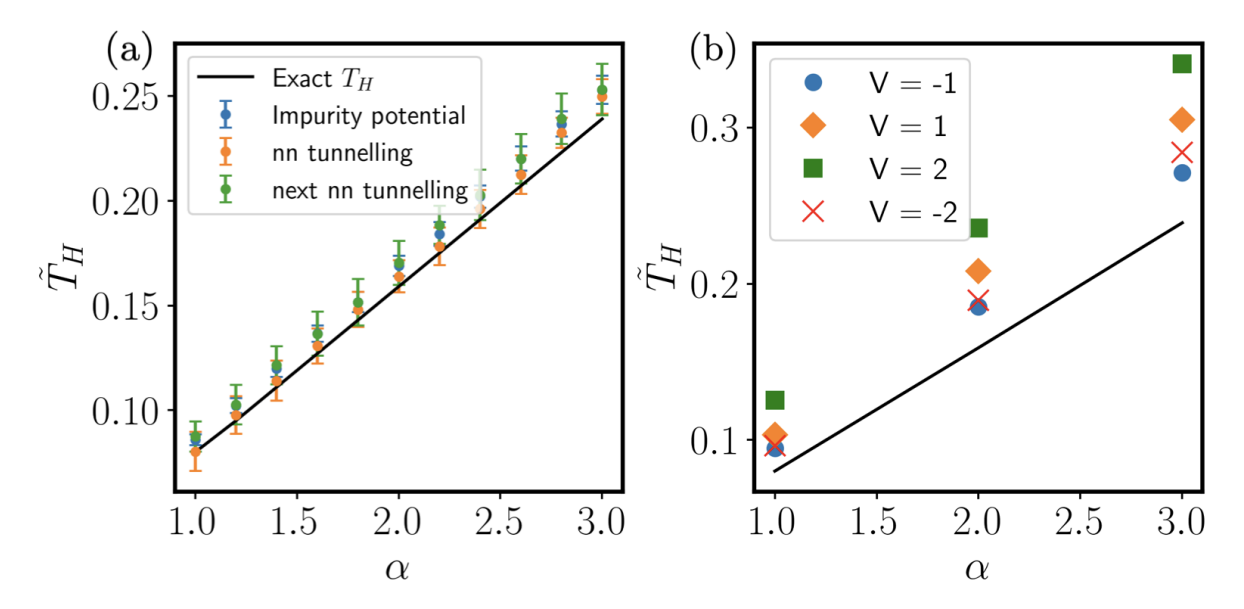


Figure 7.4: (a) Error resilience to random onsite potentials (blue) with $\varepsilon = 0.1$, additive random nearest-neighbour (nn) tunnelling error (orange) ($\varepsilon = 0.1$) and random next-nearest neighbour (nnn) tunnelling with $\varepsilon = 0.01$ (green). These results are averaged over time, initialised sites and 100 realisations for a system with size L = 100 and horizon $l_h = 50$. The error bar indicates the standard deviation across different realisations. The theoretical Hawking temperature value is represented by the black lines. (b) Density-density interaction of strength V for a system size of L = 30 and $l_h = 15$.

7.5 Resilience to errors

We now investigate the sensitivity of the extracted Hawking temperature to errors pertinent to Floquet-driven optical lattice experiments. Specifically, we extract the Hawking temperature \tilde{T}_H as per the method used in Fig. 7.3(b), after introducing noise to the system Hamiltonian in Eq. (7.9). We model random onsite potentials as an additional term of the form $J_0 \sum_{l=1}^N \varepsilon_l n_l$ in the Hamiltonian with the coefficients ε_l drawn randomly from a standard normal distribution with mean zero and variance ε . Despite the existence of random potentials, the essential features of the extracted T_H persist even with an impurity strength of $\varepsilon = 0.1$ for a wide range of α 's, as shown in Fig. 7.4(a). We next evaluate nearest-neighbour (k = 1), and next-nearest neighbour (k = 2) tunnelling errors, represented by $J_0 \sum_{l=1}^N \varepsilon_l(\hat{c}_l^{\dagger}\hat{c}_{l+k} + \hat{c}_{l+k}^{\dagger}\hat{c}_l)$. These errors can reflect higher-order corrections beyond Eq. (7.14). Fig. 7.4(a) shows that

the extracted Hawking temperature remains stable for error strength $\varepsilon = 0.1$ for k = 1 and $\varepsilon = 0.01$ for k = 2. The observed robustness against all these errors stems from the independence of Hawking temperature on various details of the black hole.

Finally, we extend our analysis to include two-particle dynamics. Fig. 7.4(b) depicts the outcome of introducing an interaction term $J_0V\sum_{l=1}^N n_l n_{l+1}$ between two particles. Our results underscore the resilience of our method against attractive interactions, i.e. negative values of V, which encourage particle clustering, causing them to act as a single entity, effectively replicating the single-particle behaviour. In contrast, for repulsive interactions (V=1,2), the Hawking temperature is consistently higher than the theoretical values across various ranges of α .

7.6 2D Implementation of the black hole simulator

The Floquet simulator can directly be extended to a two-dimensional configuration. This opens the door to the probing of non-trivial quantum features that are not present in the one-dimensional case. This includes hallmarks such as the area law for the Bekenstein-Hawking entropy, namely that the black hole entropy scales with the size of its boundary according to thermodynamic arguments [Bom+86; Sre93; Car86; Str98; Emp06]. This property also arises in the Ryu–Takayanagi formula conjectured to describe the relationship between the entanglement entropy of a conformal field theory, and the geometry of an Anti-de-Sitter spacetime, i.e. the AdS-CFT correspondence [RT06b; RT06a; Ran+17; Mal99; CCW22].

We can generate an analogue 2D black-hole simulator using a Floquet-driven 2D lattice as given by Eq. (7.12). As an example, Figure 7.5 illustrates driving amplitudes A_l on a square 2D lattice for a black hole centred at the origin. The resulting effective Hamiltonian is given by Eq. (7.9) and encodes the behaviour of free Dirac fermions in a curved space-time background [DHP23]. The event horizon r_h is indicated by the dashed line and the chosen amplitudes approximately encode a linear curvature profile $f(r) = \alpha(r - r_h)$ where r denotes the Euclidean distance from the centre of the black hole.

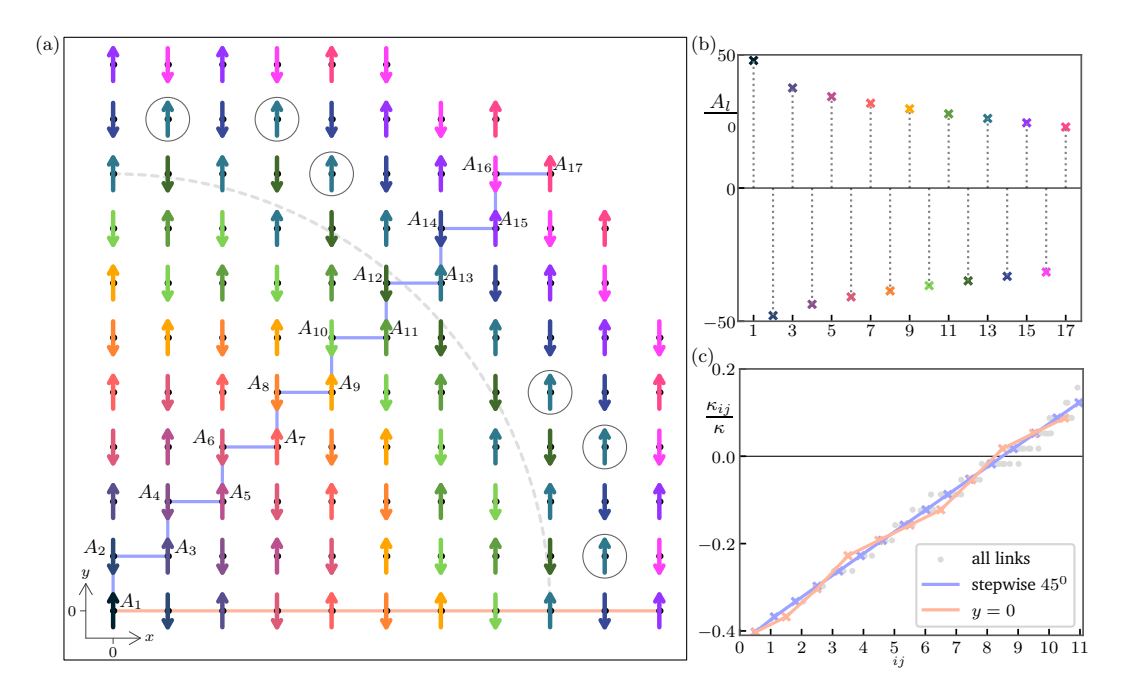


Figure 7.5: (a) Analogue quantum simulation of a 2D black hole using a Floquet-driven square optical lattice. Sites are driven with amplitudes A_l as labelled and arrows of the same colour indicate the same amplitude. Neighbouring sites are driven π out of phase as depicted by opposite arrow directions. The simulated event horizon is at the dashed grey line and the centre of the black hole (x,y)=0 is at the site driven by the red arrow with amplitude A_1 . Pictured is the top right quarter of the simulator; the simulation is symmetric under 90° rotations around the centre. (b) The driving amplitudes indexed by l are chosen such that the tunnelling amplitudes along the 45° path (blue line in (a)) follow a linear gradient. The alternating sign of A_l shown in (b) indicates that neighbouring sites are driven π out of phase. (c) The resulting tunnelling coefficients κ_{ij} according to Eq. (7.14) vs. the Euclidean distance $r_{ij} = \sqrt{(x_i/2 + x_j/2)^2 + (y_i/2 + y_j/2)^2}$ of each tunnelling link to the black hole centre. The tunnelling coefficients for the blue line give a perfectly linear profile. Tunnelling coefficients following the x axis (orange line) are also approximately linear. Sites marked by a black circle in (a) have been changed to ensure that all plaquettes have an even number of negative tunnelling links and hence zero flux.

In a 2D tight-binding scheme, one needs to ensure that for any given plaquette, the number of links with negative tunnelling amplitudes is always even, i.e. 0, 2, or 4, in order to not create unwanted artificial gauge fields [NUS23]. To achieve this and to minimize the total number of amplitudes required, in the given example we first set the tunnelling elements κ_{ij} along the diagonal (blue path) to match the desired linear gradient. Eq. (7.14) then

provides a set of corresponding amplitudes A_l that are shown in Fig 7.5(b). Similarly to the 1D case, neighbouring sites are driven out of phase to each other to minimize the required driving amplitudes. Next, all other amplitudes are chosen from the above set such that they match the site on the diagonal blue path with the closest matching Euclidean distance to the centre, while also requiring that neighbouring sites are driven out of phase. As a last step, certain sites just outside of the event horizon (marked by black circles in Figure 7.5(a)) are changed to ensure the condition of even numbers of negative tunnelling amplitudes for all plaquettes. Figure 7.5(c) shows the resulting tunnelling amplitudes for all links and highlights the approximate linear relationship between κ_{ij} and the Euclidean distance from the link to the centre of the black hole.

The Hawking temperature T_H is encoded in the 2D tunnelling profile analogously to the 1D case, i.e. by the prefactor $\alpha = 2\pi T_H$. In a square lattice, we do not expect to preserve the perfect rotational symmetry of the black hole. However, in the limit of large r_h or small d, the small distortions visible in Figure 7.5(c) will disappear. An analytical and numerical investigation of similarly encoded linear tunnelling profiles and the robust validity of the resulting encoded Hawking temperature is given in Ref. [DHP23].

7.7 Chaotic behaviour

A central but conjectured property of real black holes is that they are the fastest scrambling—and hence most chaotic—systems in nature [SS08; SS14; MSS16], a property stemming from the interactions between the particles in the black hole. Crucially, the simulation platform described above can be extended to interacting quantum particles in the curved spacetime of a black hole by making use of the widely tunable contact interactions natural for fermionic and bosonic cold atoms [Chi+10]. This leads to a Hubbard model with an onsite interaction term in addition to the spatially-dependent hopping term from Eq. 7.9 [BDZ08]. Interacting 2D Hubbard models are non-integrable and generally show thermalising, ergodic dynamics [RDO08; Sch+12; Ron+13; Kar+24].

While the experimental implementation can directly use fermionic or bosonic atoms with tunable interactions, we now consider hard-core bosons, i.e. bosonic atoms in the strongly-interacting limit where the interactions suppress site occupations higher than one, for numerical convenience. In this limit, the Bose-Hubbard Hamiltonian is reduced back to the form of Eq. 7.9, but with the ladder operators \hat{c}_i^{\dagger} , \hat{c}_j now describing hard-core bosons with the commutation relations

$$[c_i, c_i^{\dagger}] = [c_i, c_j] = [c_i^{\dagger}, c_j^{\dagger}] = 0, \quad \forall i \neq j$$

$$(7.17)$$

$$\{c_i, c_i^{\dagger}\} = 1, \quad (c_i)^2 = (c_i^{\dagger})^2 \quad \forall i.$$
 (7.18)

This model is expected to be ergodic in the homogeneous case where all tunnellings are equal, corresponding to flat space [RDO08; Ron+13; Kar+24]. To demonstrate the ergodicity of this model also in the black-hole setting, we turn to its level statistics and analyse the ratio between energetically adjacent energy gaps as introduced in Ref. [OH07]. Namely we calculate

$$r_n = \frac{\min(g_n, g_{n-1})}{\max(g_n, g_{n-1})},\tag{7.19}$$

where $g_n = E_{n+1} - E_n \ge 0$ is the gap between two adjacent eigenvalues of the Hamiltonian at a given fixed number of particles, giving $r_n \in [0, 1]$. In an ergodic system in the thermodynamic limit, the distribution of r_n will show level repulsion and follow the Wigner-Dyson statistics characteristic of the Gaussian Orthogonal Ensemble (GOE) of random matrix theory [BT77; BGS84; GMW98; OH07]. However, in an integrable system where one would not expect scrambling, there is no level repulsion and the resulting distribution is Poissonian. Figure 7.7 compares the mean adjacent energy gap ratios

$$\langle r \rangle = \frac{1}{s-2} \sum_{n=1}^{s-1} r_n,$$
 (7.20)

where s is the Hilbert space dimension, between multiple 2D systems for varying particle number N. The orange data corresponds to a system with homogeneous tunnelling, i.e.

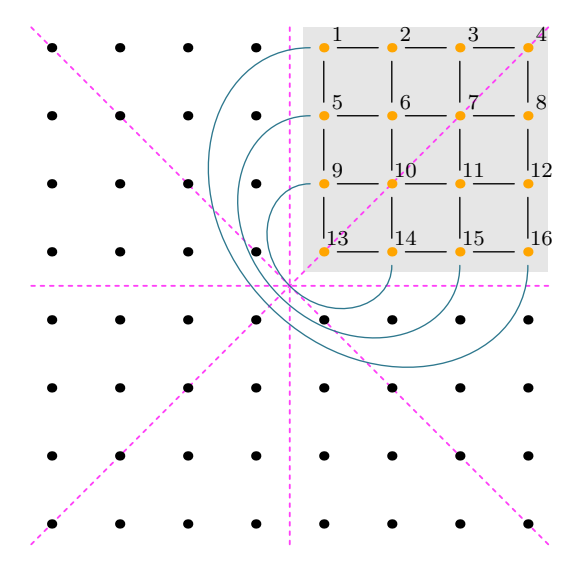


Figure 7.6: An 8×8 lattice with 90° rotational symmetry can be simulated using 16 sites. The black and yellow dots show the full 8×8 lattice, only the yellow dots in the shaded region are needed for the 16 site simulation described in Sec. 7.7. Black lines indicate tunnelling between neighbouring sites common to both the full system and the 16 site simulation. To the simulation, we add three additional tunnelling terms indicated by blue curves, connecting sites $1 \to 16$, $5 \to 15$, $9 \to 14$.

encoding a flat spacetime, while blue data shows the black hole case with site-dependent tunnellings following Eq. (7.9). Both the curved and flat systems effectively simulate an 8×8 lattice using cone-like boundary conditions, as shown in Fig. 7.6. In a finite-sized system, Hamiltonian symmetries cause degeneracies in the spectrum, perturbing the level statistics. To circumvent this, we introduce a local potential of size ε on a single site of the lattice.

The flat system is expected to be ergodic in the thermodynamic limit [Ron+13; Kar+24]. The data in Figure 7.7 shows that our black-hole simulator gives level statistics that are consistently closer to an ergodic distribution compared to the flat system for the same parameter values, thereby demonstrating the potential to study chaotic and scrambling dynamics in this platform.

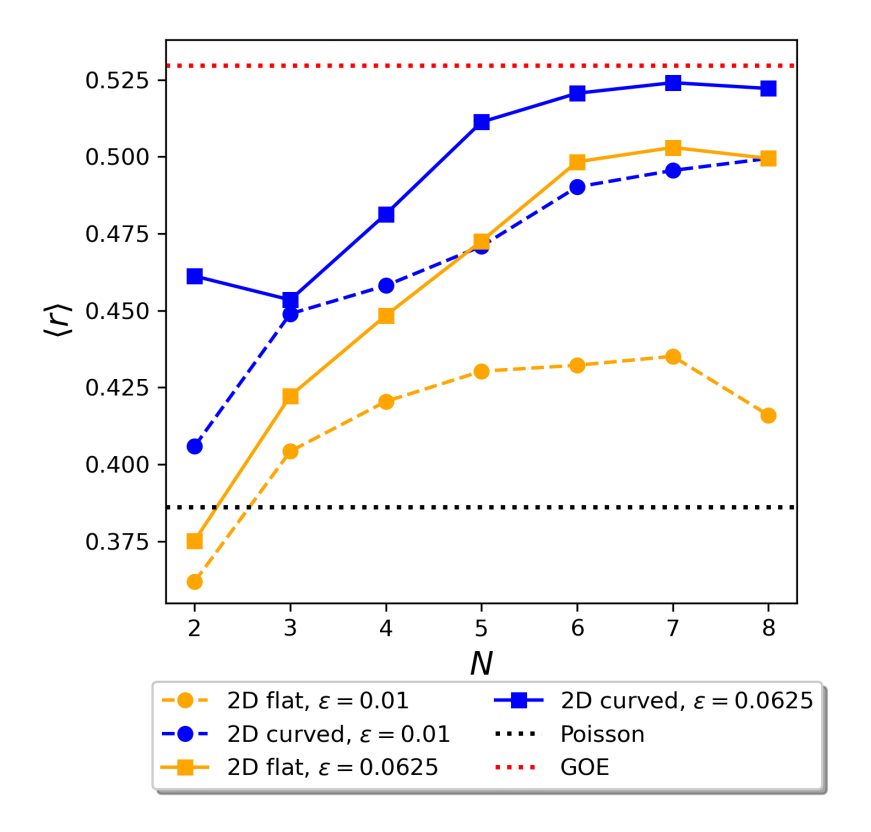


Figure 7.7: Comparing level statistics between finite 2D square lattices encoding flat (orange) and curved (blue) space-time backgrounds. The mean gap ratio $\langle r \rangle$ is computed using Eq. 7.19 for varying particle number N. For the blue data, $\alpha=0.46$, $J_0=1$ and we add a perturbation of strength $\epsilon=0.01$ (dashed lines) or $\epsilon=0.0625$ (solid lines) to lift degeneracies. For the flat system, homogeneous tunnelling is set to $\kappa J_0=0.28$. The expected mean gap ratios $\langle r_{\rm GOE} \rangle = 0.5295 \pm 0.0006$ and $\langle r_{\rm Poiss} \rangle \approx 0.386$ [OH07] for a GOE and Poissonian ensemble in the thermodynamic limit are indicated by red-dotted and black-dotted lines. The curved spacetime encoded in the blue data gives rise to higher values of $\langle r \rangle$ and hence does not break the ergodicity expected for the flat system.

7.8 Discussion

Our study utilises the power of locally driving the sites of an optical lattice to generate an efficient analogue quantum simulator for the intricate physics of Dirac particles in a black hole. We introduced a direct approach for determining the Hawking temperature of the simulated black hole from readily accessible onsite atom population measurements at the horizon. The resulting Hawking temperatures exhibit a remarkable resilience against the common sources of errors inherent in Floquet-driven optical lattices, as corroborated by our numerical findings. Additionally, we have unveiled that the presence of weak interatomic interactions introduces a minor, albeit systematic, deviation in the measured value of T_H .

Our approach can furthermore be directly extended to higher dimensions. We give an example of a (2+1)D geometry, capitalising on the experimental accessibility of higher-dimensional optical lattices. Furthermore, optical lattices offer a natural platform for implementing tuneable (non-gravitational) interactions [Chi+10]. Our simulator can therefore probe thermalising (scrambling) quantum behaviour with the background curvature of a black hole. By analysing level statistics, we show that the background curvature in a 2D system results in a more ergodic phase relative to flat space. Together with the realisation of Hawking radiation, being able to implement such chaotic behaviour could enable us to realise the Hayden-Preskill quantum teleportation protocol responsible for the information retrieval from evaporating black holes [HP07; Lan+22; ALX23].

Finally, combined with quantum gas microscopes, optical lattices naturally provide access to multi-particle correlations, thus offering an ideal system to monitor the behaviour of quantum information during the evaporation of black holes encoded in our simulator by changing the tunnelling coefficients in a time-dependent fashion.

Moving forward, we aim to experimentally realise our simulation in 1D to validate our methodology, then realise the 2D counterpart to explore more complex phenomena.

Chapter 8

Conclusion

The fields of quantum error correction (QEC) and topological quantum computing (TQC) are both aimed at achieving reliable quantum computation using an underlying physical system, that is prone to decoherence and various intrinsic noise processes. The former aims to redundantly encode information using entangling operations on a set of physical qubits. The latter, however, considers information storage in the ground state of a many-body Hamiltonian described by a topological quantum field theory at zero temperature. As we have seen, these two frameworks share certain aspects and mathematical formalism. Beyond a quantum memory, building a quantum processor requires addressing the encoded logical information to enact non-trivial quantum logic gates. Developing encoding mechanisms, as well as logical gates are fundamental for both quantum error correction and topological quantum computing.

In Chapter 3, we investigated the logical operations accessible on the toric code using a collection of hybrid defects, namely mixed-boundary punctures. We found that while the computational power of these defects is limited in that it does not recover the full Clifford group, our defects reproduce the exotic behaviour of Majorana anyons, much like vortices and twists, while providing a different physical realisation which does not require lattice dislocations. Moreover, our approach adds understanding of the similarities and divergence between local and nonlocal defects in the different coupling strength configurations of the Kitaev Hon-

eycomb model. Moving forward, we would like to turn our attention to the computational power of defects beyond topological codes. Indeed, a specific instance thereof has been studied, namely punctures on hypergraph product codes [KP20; KP21], but further explorations lack in the literature since the nonlocal nature of general candidates for quantum codes renders the study of these defects quite involved. However, these graphical structures could see a new description in light of the emerging understanding of the physics of quantum low-density parity check codes [RK23a; RK23b].

In Chapter 4, we considered a logical encoding scheme based on a generalisation of the Majorana chain, known as the parafermion chain. Parafermions enable the encoding of topological qudits and fault-tolerant Clifford operations through braiding. We analytically derived the quantum gate induced by the short-range interaction of parafermion edge modes in a \mathbb{Z}_3 parafermion chain. Our results demonstrate that this (tunable) interaction produces a non-Clifford phase gate, which can be configured to reside in even levels of the Clifford hierarchy, enabling a universal qutrit gate set. We also proposed an experimental simulation of the braiding and dynamical evolutions of the \mathbb{Z}_3 topological states, using Rydberg atom technology. We showed that this gate allows access to highly non-contextual, albeit noisy, quantum states. To address this limitation, this work can be extended by devising a magic state distillation protocol to increase the fidelity of these states.

In Chapter 5, we proposed a novel decoder for the surface code tailored to the depolarising noise model. By mapping the surface code syndrome onto that of the colour code, we leveraged sophisticated matching decoders originally designed for the colour code to achieve an exponential improvement in the logical error rate, compared to traditional decoders. In future work, the methods included in this work could be extended to other types of correlated noise, as well as other codes exhibiting materialised symmetries.

Quantum simulation is a technique that consists of manipulating an accessible and highly controlled quantum system, to infer knowledge of another quantum system, that is not directly accessible. In this work, we propose using optical lattices, which trap ultracold atoms near absolute zero temperature in a grid-like potential.

In Chapter 7, we proposed a novel simulation of black hole physics using a one and twodimensional optical lattice, with position-dependent tunnelling achieved through local Floquet driving. This simulation encodes massless Dirac fermions under gravitational curvature, reproducing Hawking radiation as atom populations tunnelling across the event horizon. The Hawking temperature can be extracted via onsite atomic population measurements, and the setup demonstrates robustness to experimental imperfections. Our aim is to realise this proposal in the laboratory, and extend its scope to explore additional aspects of black hole physics both in the semiclassical regime and beyond. For instance, our platform could enable experimental verification of the entanglement entropy of (2+1)D and (3+1)D black holes, which involves more subtleties [DHP23]. Moreover, black holes are expected to optimally scramble quantum information due to quantum gravity interactions. Hence, a platform to simulate models of their spacetime curvature could allow simulating their scrambling behaviour.

Appendices

A1 Simulating parafermions with Rydberg atoms

Rydberg systems offer an attractive potential candidate for quantum simulation, since they possess several advantageous properties [MW21]. For instance, their strong interactions, long lifetimes, greater than about 50 µs at room temperature, allow high-fidelity state-resolved readout [Mad+20; Cov+19], high-fidelity entangling operations [Mad+20], and high-control native multi-qubit gates [Lev+19]. Various experimental techniques to suppress the error and enhance the fidelity of Rydberg operations also exist in the literature [Lev+18; Shi18]. Rydberg systems hold great promise for simulating topologically protected quantum systems. In light of these facts, Rydberg atoms offer alternative ways to effectively simulate the Hamiltonian, such as that in Eq. (4.12). In practice, it is preferable to use ground state hyperfine levels for the qutrit basis states, and Rydberg states only for entangling operations.

Here, we propose a setting for the quantum simulation of PEM interaction by engineering the interaction Hamiltonian in the three-fold ground subspace with four atomic levels coupled by four classical light fields as shown in Fig. A.1(a). In order to use a Rydberg atom to simulate the Hamiltonian as in Eq. (4.12), we need a three-dimensional Rydberg atom which can be realised by many-photon excitations to 3 different Rydberg states, denoted $|0\rangle$, $|1\rangle$ and $|2\rangle$. In general, this process is not trivial, since some transitions may be dipole-forbidden due to the selection rule of dipole interaction. However, this can be overcome by introducing an intermediate state $|3\rangle$, which can later be removed via adiabatic elimination (see Fig. A.1(a)

for the setting). This experimental technique is analogous to the one used in stimulated Raman transitions. In the following procedure, we first derive the Hamiltonian for a general four-level system and then perform an adiabatic elimination to the intermediate state $|3\rangle$ to obtain the desired effective three-level Hamiltonian. We then choose the specific parameters to imitate the Hamiltonian in Eq. (4.12). All classical light fields are monochromatic microwave

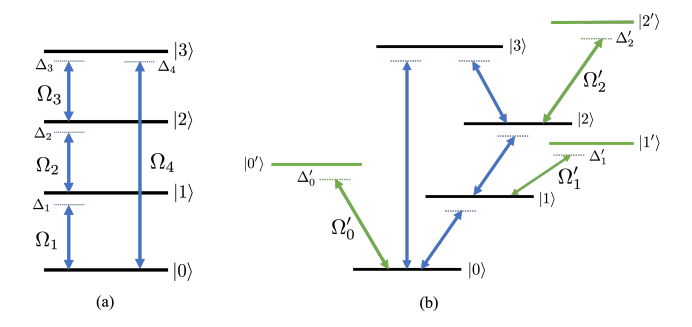


Figure A.1: (a) The four-level atomic system coupled by four monochromatic classical microwave fields, where we indicate the respective Rabi frequencies and detunings between our levels by Ω_i and Δ_i for $i \in \{1, 2, 3, 4\}$ (b) The additional states $|0'\rangle$, $|1'\rangle$ and $|2'\rangle$ coupled to states $|0\rangle$, $|1\rangle$ and $|2\rangle$ with Rabi frequencies Ω'_0 , Ω'_1 , Ω'_2 and detunings Δ'_0 , Δ'_1 , Δ'_2 , respectively. These additional couplings are to induce the light-shifts that could compensate out the diagonal terms.

lasers, described by the overall field

$$\mathbf{E} = \hat{\epsilon}_1 E_1 \cos(\omega_1 t + \phi_1) + \hat{\epsilon}_2 E_2 \cos(\omega_2 t + \phi_2) + \\
\hat{\epsilon}_3 E_3 \cos(\omega_3 t + \phi_3) + \hat{\epsilon}_4 E_4 \cos(\omega_4 t + \phi_4)$$
(A.1)

where $\hat{\boldsymbol{\epsilon}}_{\alpha}$ and ϕ_{α} are a unit polarization vector and relative phase of each field, respectively. The electric fields can then be decomposed into two exponential terms $\boldsymbol{E} = \boldsymbol{E}^{(+)} + \boldsymbol{E}^{(-)}$, where $\boldsymbol{E}^{(+)} = \sum_{j=1}^4 \frac{1}{2} \hat{\boldsymbol{\epsilon}}_j E_j \mathrm{e}^{-i(\omega_j t + \phi_j)}$ is the positive-rotating component and $\boldsymbol{E}^{(-)} = \sum_{j=1}^4 \frac{1}{2} \hat{\boldsymbol{\epsilon}}_j E_j \mathrm{e}^{i(\omega_j t + \phi_j)}$ negative-rotating. Additionally, we assume that the wavelength of the field is much longer than the size of the atom. Hence, the spatial dependence of the field can be ignored over the size of the atom as per the dipole approximation.

Since the dipole operator $\mathbf{d} = -\mathbf{e}\mathbf{r}_e$ is an odd parity operator, its diagonal elements vanish,

and the (real) dipole matrix elements of each coupling pair are given by

$$\mathbf{d} = \langle 0 | \mathbf{d} | 1 \rangle (\sigma_1 + \sigma_1^{\dagger}) + \langle 0 | \mathbf{d} | 2 \rangle (\sigma_2 + \sigma_2^{\dagger}) + \langle 2 | \mathbf{d} | 3 \rangle (\sigma_3 + \sigma_3^{\dagger}) + \langle 0 | \mathbf{d} | 3 \rangle (\sigma_4 + \sigma_4^{\dagger}),$$
(A.2)

where $\sigma_1 = |0\rangle\langle 1|$, $\sigma_2 = |1\rangle\langle 2|$, $\sigma_3 = |2\rangle\langle 3|$ and $\sigma_4 = |0\rangle\langle 3|$. Under free atomic evolution, the expectation values of $\sigma_{1,2,3,4}$ have unperturbed time-dependence terms of $e^{-i\omega_{01}t}$, $e^{-i(\omega_{02}-\omega_{01})t}$, $e^{-i(\omega_{03}-\omega_{02})t}$, $e^{-i\omega_{03}t}$ which are all positive-rotating. These terms can be considered as $\mathbf{d}^{(+)}$. Similarly, the expectation values of $\sigma_{1,2,3,4}^{\dagger}$ have unperturbed time dependence of opposite sign, which therefore can be considered as $\mathbf{d}^{(-)}$, such that the dipole operator can be decomposed as $\mathbf{d} = \mathbf{d}^{(+)} + \mathbf{d}^{(-)}$. The interaction Hamiltonian caused by dipole interaction is given by $\hat{H}_{\text{int}} = -\mathbf{d} \cdot \mathbf{E}$. After applying the rotating-wave approximation, which focuses on slow dynamics rather than fast, thereby ignoring interaction terms $\mathbf{d}^{(+)} \cdot \mathbf{E}^{(+)}$ and $\mathbf{d}^{(-)} \cdot \mathbf{E}^{(-)}$. The interaction Hamiltonian becomes

$$\hat{H}_{\text{int}} = -(\mathbf{d}^{(+)} \cdot \mathbf{E}^{(-)} + \mathbf{d}^{(-)} \cdot \mathbf{E}^{(+)})$$
(A.3)

$$= \frac{\Omega_1}{2} (\sigma_1 e^{i(\omega_1 t + \phi_1)} + \sigma_1^{\dagger} e^{-i(\omega_1 t + \phi_1)})$$
(A.4)

$$+ \frac{\Omega_2}{2} (\sigma_2 e^{i(\omega_2 t + \phi_2)} + \sigma_2^{\dagger} e^{-i(\omega_2 t + \phi_2)})$$
 (A.5)

$$+\frac{\Omega_3}{2}(\sigma_3 e^{i(\omega_3 t + \phi_3)} + \sigma_3^{\dagger} e^{-i(\omega_3 t + \phi_3)}) \tag{A.6}$$

$$+ \frac{\Omega_4}{2} (\sigma_4 e^{i(\omega_4 t + \phi_4)} + \sigma_4^{\dagger} e^{-i(\omega_4 t + \phi_4)}), \tag{A.7}$$

where the Rabi frequencies for each coupling pair are $\Omega_1 = -\langle 0|\hat{\epsilon}_1 \cdot \mathbf{d}|1\rangle E_1$, $\Omega_2 = -\langle 1|\hat{\epsilon}_2 \cdot \mathbf{d}|2\rangle E_2$, $\Omega_3 = -\langle 0|\hat{\epsilon}_3 \cdot \mathbf{d}|3\rangle E_3$ and $\Omega_4 = -\langle 0|\hat{\epsilon}_4 \cdot \mathbf{d}|3\rangle E_4$. The free atomic Hamiltonian is defined as

$$\hat{H}_A = \omega_{01} |1\rangle\langle 1| + \omega_{02} |2\rangle\langle 2| + \omega_{03} |3\rangle\langle 3|, \qquad (A.8)$$

where $|0\rangle$ is the zero energy ground state. The evolution of the system is calculated by solving

the Schrödinger equation

$$i\partial_t |\tilde{\psi}\rangle = (\hat{H}_A + \hat{H}_{int}) |\tilde{\psi}\rangle$$
 (A.9)

The state $|\tilde{\psi}\rangle$ is defined as the quantum state in the rotating-frame. In this frame, we assume that the state $|3\rangle$ maintains the same velocity of its dynamics in the original frame, while other states are sped up with different velocities, such that $|\tilde{\psi}\rangle = \tilde{c_0} |0\rangle + \tilde{c_1} |1\rangle + \tilde{c_2} |2\rangle + c_3 |3\rangle$ where $\tilde{c_0} = \mathrm{e}^{-i(\omega_1 + \omega_2 + \omega_3)t} c_0$, $\tilde{c_1} = \mathrm{e}^{-i(\omega_2 + \omega_3)t} c_1$ and $\tilde{c_2} = \mathrm{e}^{-i\omega_3 t} c_2$. The multiplied exponential factors are inserted to fasten the dynamics of states $|0\rangle$, $|1\rangle$ and $|2\rangle$. It can be shown that the resulting Hamiltonian under which the state $|\tilde{\psi}\rangle$ evolves, is explicitly time-independent when the condition $\Delta_4 = \Delta_1 + \Delta_2 + \Delta_3$ is satisfied, also known as the four-photon resonance condition. The time-independent Schrödinger equation is given by

$$i\partial_{t} \begin{pmatrix} \tilde{c_{0}} \\ \tilde{c_{1}} \\ \tilde{c_{2}} \\ c_{3} \end{pmatrix} = \begin{pmatrix} -(\Delta_{1} + \Delta_{2} + \Delta_{3}) & \frac{\Omega_{1}}{2} e^{i\phi_{1}} & 0 & \frac{\Omega_{4}}{2} e^{i\phi_{4}} \\ \frac{\Omega_{1}}{2} e^{-i\phi_{1}} & -(\Delta_{2} + \Delta_{3}) & \frac{\Omega_{2}}{2} e^{i\phi_{2}} & 0 \\ 0 & \frac{\Omega_{2}}{2} e^{-i\phi_{2}} & -\Delta_{3} & \frac{\Omega_{3}}{2} e^{i\phi_{3}} \\ \frac{\Omega_{4}}{2} e^{-i\phi_{4}} & 0 & \frac{\Omega_{3}}{2} e^{-i\phi_{3}} & 0 \end{pmatrix} \begin{pmatrix} \tilde{c_{0}} \\ \tilde{c_{1}} \\ \tilde{c_{2}} \\ c_{3} \end{pmatrix}, \tag{A.10}$$

where for convenience the energy reference is adjusted such that the state $|3\rangle$ is the zero-energy level.

Since the ground subspace of the parafermion chain is three-dimensional, we will perform an adiabatic elimination to the system's equations of motion in Eq. (A.10), which yields the effective three-level Hamiltonian that can simulate the desired subspace. Firstly, we multiply the system's four-state vector by an overall phase factor $e^{i\Delta t}$, to shift all the energy level by Δ . However, to satisfy the condition of an adiabatic elimination, the Δ , which is the fast oscillation term of c_3 from the Schrödinger equation, needs to be much larger compared to other oscillation terms for $\tilde{c_0}$, $\tilde{c_1}$ and $\tilde{c_2}$, i.e., $|\Delta| \gg |\Delta - \Delta_3|$, $|\Delta - (\Delta_2 + \Delta_3)|$, $|\Delta - (\Delta_1 + \Delta_2 + \Delta_3)|$. The last three terms here are respectively the oscillation terms for $\tilde{c_2}$, $\tilde{c_1}$ and $\tilde{c_0}$ after multiplying $e^{i\Delta t}$. To make sure that the state $|3\rangle$ is never populated, the condition $\Delta_3 \gg \Omega_3$ and $\Delta_4 \gg \Omega_4$ are required. Besides, the condition $|\Delta_{3,4}| \gg \Gamma$, where Γ is natural

decay rate of the state $|3\rangle$, is also needed to make sure that the spontaneous emission can be negligible. For convenience, we can set $\Delta = \Delta_3 = \Delta_4$, and overall constraints on Δ by the above conditions due to adiabatic elimination are : (1) $|\Delta| \gg |\Delta_1| + |\Delta_2|$, (2) $|\Delta| \gg |\Omega_{3,4}|$, (3) $|\Delta| \gg \Gamma$. Considering the equation of motion for c_3 , when Δ is satisfied all above conditions, it is obvious that c_3 carries the fast oscillation at frequencies of order $|\Delta| \gg \Gamma$ so that c_3 is damped by coupling to the vacuum on timescales of $1/\Gamma$. Here, we only consider the motions on timescales slow compared to $1/\Gamma$, i.e., \tilde{c}_2 , \tilde{c}_1 and \tilde{c}_0 , and thus can make the approximation that c_3 damps to equilibrium instantaneously, i.e. $\partial_t c_3 = 0$. Therefore, we can obtain the substitution for c_3 by \tilde{c}_0 , \tilde{c}_1 , \tilde{c}_2 from the last equation of Eq. (A.10) such that $c_3 = -\left(\frac{\Omega_4}{2\Delta}e^{-i\phi_4}\tilde{c}_0 + \frac{\Omega_3}{2\Delta}e^{-i\phi_3}\tilde{c}_2\right)$. Substituting this into the equation for \tilde{c}_0 , \tilde{c}_1 , \tilde{c}_2 in Eq. (A.10), we finally obtain the effective three-level Hamiltonian in which the state $|3\rangle$ is eliminated.

$$i\partial_{t} \begin{pmatrix} \tilde{c}_{0} \\ \tilde{c}_{1} \\ \tilde{c}_{2} \end{pmatrix} = \begin{pmatrix} -\left(\Delta_{1} + \Delta_{2} + \Delta_{3} + \frac{\Omega_{4}^{2}}{4\Delta}\right) & \frac{\Omega_{1}}{2} e^{i\phi_{1}} & \frac{-\Omega_{4}\Omega_{3}}{4\Delta} e^{i(\phi_{4} - \phi_{3})} \\ \frac{\Omega_{1}}{2} e^{-i\phi_{1}} & -(\Delta_{2} + \Delta_{3}) & \frac{\Omega_{2}}{2} e^{i\phi_{2}} \\ \frac{-\Omega_{4}\Omega_{3}}{4\Delta} e^{-i(\phi_{4} - \phi_{3})} & \frac{\Omega_{2}}{2} e^{-i\phi_{2}} & -\left(\Delta_{3} + \frac{\Omega_{3}^{2}}{4\Delta}\right) \end{pmatrix} \begin{pmatrix} \tilde{c}_{0} \\ \tilde{c}_{1} \\ \tilde{c}_{2} \end{pmatrix}. \tag{A.11}$$

Since the state $|0\rangle$ and $|2\rangle$ initially interact directly with the state $|3\rangle$, the adiabatic elimination of the state $|3\rangle$ gives rise to an effective Rabi coupling between the state $|0\rangle$ and $|2\rangle$, which is $\Omega_R = \frac{-\Omega_4 \Omega_3}{2\Delta} e^{i(\phi_4 - \phi_3)}$. Additionally, the energy terms are also shifted due to AC Stark shifts, amounting to $\Omega_4^2/(4\Delta)$ and $\Omega_3^2/(4\Delta)$ for the state $|0\rangle$ and $|2\rangle$, respectively.

In order to recover the parafermion interaction Hamiltonian given in Eq. 4.12, we first need the all diagonal terms to be zero. This can be realised by coupling the states $|0\rangle$, $|1\rangle$ and $|2\rangle$ to complemented states $|0'\rangle$, $|1'\rangle$ and $|2'\rangle$ respectively as shown in Fig. A.1(b). This is to allow the additional light shifts, i.e., $\Omega_0'^2/4\Delta_0'$, $\Omega_1'^2/4\Delta_1'$ and $\Omega_2'^2/4\Delta_2'$, for each diagonal term to be cancelled. Experimentally, one can choose the complemented states and parameters such that the diagonal terms disappear. Additionally, the non-diagonal terms can also be set to simulate the Hamiltonian as in Eq. (4.12) by choosing the states and

parameters such that $|\Omega_1| = |\frac{\Omega_3\Omega_4}{2\Delta}| = |\Omega_2| = g$, and relative phases of the laser fields following $\phi_1 = \phi_2 = -(\phi_4 - \phi_3) = \frac{2\pi}{3}$, where g is a controllable factor depending on laser detuning.

By fixing the external field parameters according to these identities, we can implement the braiding of parafermions, by realising a Berry phase evolution on states $|2\rangle$ and $|3\rangle$. This entails turning on solely the interaction between the latter states, and allowing for an adiabatic evolution in order for a geometric phase to accumulate, as described in Ref. [AMT09], where it was shown that the adiabatic evolution of a two-level model in the presence of an external classical electric field yields the Berry phase

$$\gamma_l = \frac{l}{2} \oint_0^T dt \frac{|D(t)|^2}{F_l(t)} \dot{\phi}_3(t), \tag{A.12}$$

where l indicates the instantaneous eigenstates of the model,

$$D(t) = \langle 2| \mathbf{d} | 3 \rangle \cdot \hat{\epsilon}_3 E_3(t), \tag{A.13}$$

$$F_l(t) = \left(\frac{\omega_{23}}{2}\right)^2 + |D(t)|^2 - l \cdot \left(\frac{\omega_{23}}{2}\right) \sqrt{\left(\frac{\omega_{23}}{2}\right)^2 + |D(t)|^2},\tag{A.14}$$

and $\phi_3(t)$ is the time-dependent relative phase of the coupling laser between state $|2\rangle$ and $|3\rangle$. While dynamical phases arise in this procedure, leading to unwanted dephasing in the time evolution, these can be closely monitored and compensated for. Indeed, to cancel out the accumulated dynamical phase, the other coupling channels are turned on, as shown in Fig. A.1. This allows us to apply adiabatic elimination to state $|3\rangle$, which yields the additional AC Stark shift to state $|2\rangle$, that destructively compensates for the unwanted dephasing, leaving only the geometric phase. This corresponds to the Berry phase required to simulate the braiding of parafermion as derived in Eq. (A6) in Ref. [HL16].

A2 Pseudocode for unified decoding on the surface code

Here, we outline the Unified decoder presented in Chapter 5. The procedure requires a set of syndrome measurements of the colour code stabilizers $\sigma_{\text{c.c.}}$, a subroutine which restricts $\sigma_{\text{c.c.}}$ to syndromes on restricted lattices, and one which builds the unified lattice as prescribed in Fig. 5.2. A minimum-weight perfect matching decoder, mwpmdecoder, is then used to decode the syndrome and provide a correction \bar{C} . The correction operator returns the code to the codespace, and its success is given by the following condition. Namely, that the decoding algorithm has determined that the parity of the edges in the matching solution crossing a chosen logical representative \bar{Z} , is equal to the parity of Pauli errors which occurred on qubits $q \in \bar{Z}$, as mentioned in Sec. 5.2.2.

Algorithm 1: Unified Decoder

```
1 Require:
       Restricted lattices \mathcal{R}_{\mathbf{u}} = \{\{S_f\}_{\mathbf{col}(f) \neq \mathbf{u}}\} on a manifold G_{\mathcal{R}_{\mathbf{u}}}
       Unified lattice constructor \mathcal{U}(.)
       A MWPM decoder mwpmdecoder
  2 Input: A colour code syndrome \sigma_{c.c.} on the colour code manifold G_{c.c.}
  3 Output: A correction operator \bar{C}
     /* Map syndromes to restricted lattices
                                                                                                                                          */
 4 foreach u \in \{r, g, b\} do
           foreach \sigma_i \in \sigma_{\text{c.c.}} do
  5
                if colour(\sigma_i) = u then
  6
                     \mathcal{R}_{\mathbf{u}}(\sigma_i) on G_{\mathcal{R}_{\mathbf{u}}} \leftarrow \sigma_i on G_{\text{c.c.}}
  7
  8
                end
          end
  9
10 end
     /* Construct unified lattice, and map syndrome on the unified lattice
11 (G_{\mathcal{U}}, \sigma_{i,\mathcal{U}}) \leftarrow \mathcal{U}(G_{\mathcal{R}_{\mathbf{r}}}, G_{\mathcal{R}_{\mathbf{g}}}, G_{\mathcal{R}_{\mathbf{b}}}, \mathcal{R}_{\mathbf{r}}(\sigma_{i}), \mathcal{R}_{\mathbf{g}}(\sigma_{i}), \mathcal{R}_{\mathbf{b}}(\sigma_{i}))
     /* Decode
                                                                                                                                          */
12 \bar{C} = \text{mwpmdecoder}(G_{\mathcal{U}}, \sigma_{i,\mathcal{U}})
     /* Apply Pauli-Z corrections to qubits along the shortest paths
           determined by the decoder
                                                                                                                                          */
13 Apply \prod_{q \in \bar{C}} Z_q
```

A3 Thresholds for the even-distance surface code using varied weights

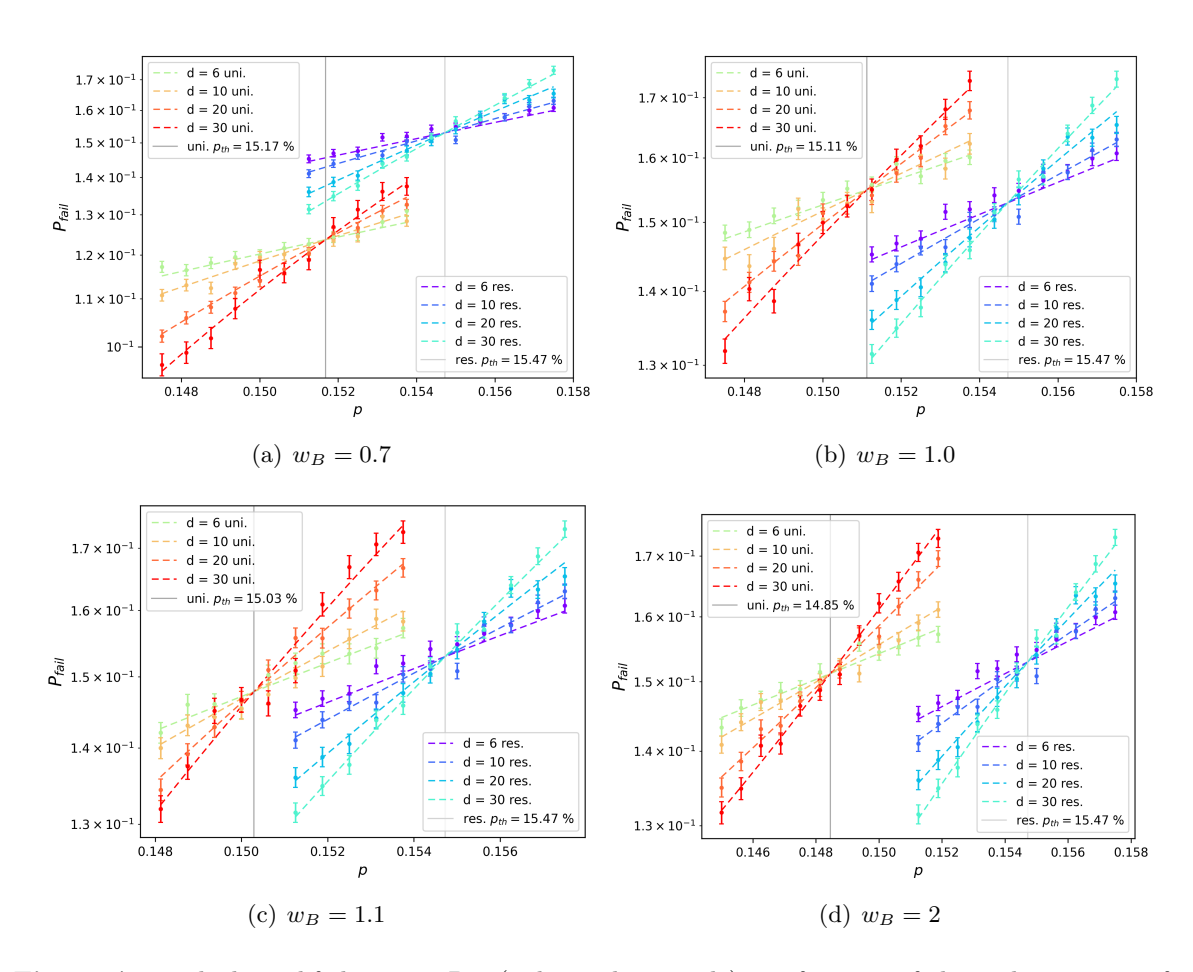


Figure A.2: The logical failure rate $P_{\rm fail}$ (in logarithmic scale) as a function of physical error rate p for surface codes of different even distance d, under i.i.d depolarising noise. The restricted decoder threshold is shown against the unified decoder configured with weights $w_A = 1$, and (a) $w_B = 0.7$, (b) $w_B = 1$ and (c) $w_B = 1.1$, (d) $w_B = 2$ using the matching graph in Fig. 5.2(c). Each dashed line indicates the fit to a Taylor expansion for each system size, and the error bars show the standard deviation of the mean logical failure rate where each data point is collected using $> 6 \times 10^4$ Monte Carlo samples.

A4 A note on other derivations of Hawking radiation

The spectrum in Eq. 6.8 can also be derived by considering the creation of particle-antiparticle pairs near the black hole horizon, as first proposed by Hawking in [Haw74]. In this picture, quantum fluctuations near the event horizon give rise to pairs of particles, with one falling into the black hole and the other escaping to infinity, forming the thermal spectrum characteristic of Hawking radiation. A second approach was introduced by Hawking in Ref. [Haw76a], which recovers the Hawking radiation spectrum by analytically continuing the Schwarzschild (Lorentzian) black hole metric into a Riemannian (Euclidean) metric using the introduction of an imaginary time $t \to i\tau$. In this framework, quantum fields are analysed in the Euclidean Schwarzschild background, and the periodicity of the imaginary time coordinate implies that the quantum field is in a thermal equilibrium state at the Hawking temperature, with this state responsible for the Hawking radiation observed in the Lorentzian picture.

Moreover, Unruh's seminal work in [Unr76] reinforces the importance of the causal structure on Hawking radiation. This argument draws on the Unruh effect, where an accelerating observer in flat spacetime perceives the vacuum as populated by a thermal bath of particles due to the observer's acceleration and the frame-dependent nature of the vacuum state. Similarly, near the event horizon of a black hole, an infalling observer detects no particles, whereas an observer in a distant stationary frame perceives the region near the horizon as a hot thermal bath. Hence, this reasoning shows that the black hole emits Hawking radiation due to the relative acceleration between the event horizon and the distant observer, but overlooks the quantum mechanical treatment of the state of the field near the horizon.

Finally, Parikh and Wilczek offered a semiclassical approximation whereby particles escape the black hole via quantum tunnelling through the potential barrier formed by the event horizon. The spectrum of outgoing particles reflects the emission of Hawking radiation [PW00] at a temperature T_H , but their approach also accounts for non-thermal corrections due to the effect of back-reaction from the emitted particle on the black hole. As the black hole radiates, these corrections accumulate, eventually leading to its complete evaporation as predicted by Hawking. Moreover, this slight deviation from thermality implies that Hawking radiation carries information about the black hole's microstates. This is significant in discussions of the black hole information paradox.

A5 Diagonalising the XY model

Let us rewrite the Hamiltonian in Eq. 6.15 as

$$H = \sum_{l,m} h_{lm} c_l^{\dagger} c_m \tag{A.15}$$

where the matrix h with entries $[h]_{lm}$ is Hermitian. Hence, there exists a unitary operator U satisfying $h = UDU^{\dagger}$, for a diagonal matrix D containing the corresponding energy eigenvalues $D_{ij} = \delta_{ij}E_j$. Upon substitution, we can rewrite the Hamiltonian in Eq. A.15 as

$$H = \sum_{j} E_{j} c_{j}^{\dagger} c_{j} \tag{A.16}$$

where the new fermionic modes follow from the above transformation such that

$$c_j = \sum_k U_{kj}^* c_j \ , \ c_j^{\dagger} = \sum_k U_{kj} c_j$$
 (A.17)

which obey the canonical fermionic commutation relations. In this basis, H is diagonalised, and represents a sum of harmonic oscillators. The ground state of this Hamiltonian corresponds to the configuration where all modes with negative energy are occupied, i.e.

$$|GS\rangle = \Pi_{i:E_i < 0} c_i^{\dagger} |0\rangle.$$
 (A.18)

A6 Floquet Engineering

The full time-dependent Hamiltonian describing a Floquet-driven 2D lattice system is given by

$$H(t) = -J_0 \kappa \sum_{\langle i,j \rangle} (\hat{c}_i^{\dagger} \hat{c}_j + \hat{c}_j^{\dagger} \hat{c}_i) + \cos(\omega t) \sum_j A_j \hat{c}_j^{\dagger} \hat{c}_j. \tag{A.19}$$

The equivalent of Eq. (A.19) in 1D is shown in Eq. (4) in the main text. The stroboscopic Hamiltonian $H_S^{t_0}$ generates the evolution over one driving cycle from t_0 to $t_0 + T$. The choice of t_0 is a gauge choice, named the "Floquet gauge". There exists a family of stroboscopic Hamiltonians $H_S^{t_0}$ for each $t_0 \in \{0, T\}$ and they are all related by a unitary transformation.

We can numerically calculate the stroboscopic Hamiltonian by simulating the evolution of time-independent basis elements under the Schrödinger equation using the time-dependent Hamiltonian Eq. (A.19). After one period, we diagonalise the time evolution operator $U(t_0 + T, t_0)|\psi_n(t_0)\rangle = u_n|\psi_n(t_0)\rangle$. The quasienergy $\{\epsilon_n\}$ is given by the natural logarithm $\epsilon_n = \frac{i}{T}\log(u_n)$, defining the stroboscopic Hamiltonian via $H_S^{t_0} = \sum_n \epsilon_n |\psi_n(t_0)\rangle \langle \psi_n(t_0)|$.

We can change basis and work with a representation of the stroboscopic Hamiltonian which is expressly t_0 -independent. This Floquet-gauge invariant Hamiltonian is labelled the "effective Hamiltonian," H_{eff} [EA15]. To explore the analytical behaviour of the effective Hamiltonian and utilise the high-frequency expansion [BDP15; EA15], it is convenient to make a gauge transformation from Eq. (A.19) into the "lattice frame" given by

$$\tilde{H}(t) = -J_0 \kappa \sum_{\langle i,j \rangle} e^{i\frac{A_i - A_j}{\hbar \omega} \sin(\omega t)} \hat{c}_i^{\dagger} \hat{c}_j, \tag{A.20}$$

where the time dependence has been transferred to time-dependent Peierls phases [Eck17].

There exists an infinite series expansion, which describes the effective Hamiltonian involving terms of increasing order of the inverse frequency

$$H_{\text{eff}} = \sum_{n=0}^{\infty} \frac{1}{\omega^n} H_{\text{eff}}^{(n)}.$$
 (A.21)

For sufficiently large driving frequencies, the effective Hamiltonian can be well approximated by the first two terms [EA15; BDP15]

$$H_{\text{eff}}^{(0)} = \tilde{H}_0, \qquad H_{\text{eff}}^{(1)} = \frac{1}{\hbar} \sum_{l=1}^{\infty} \frac{1}{l} [\tilde{H}_l, \tilde{H}_{-l}]$$
 (A.22)

where $\tilde{H}_l = \frac{1}{T} \int_0^T e^{-il\omega t} \tilde{H}(t)$ are Fourier harmonics of the time-dependent Hamiltonian in the lattice frame given by Eq. (A.20). They are given by $\tilde{H}_m = -J_0 \kappa \sum_{\langle i,j \rangle} \hat{c}_i^{\dagger} \hat{c}_j \mathcal{J}_m \left(\frac{A_i - A_j}{\omega}\right)$ where \mathcal{J}_m is the Bessel function of the m^{th} kind. The first term (n=0) of the high-frequency expansion Eq. (A.21) is therefore the first Fourier harmonic which corresponds to a Hamiltonian

$$H = -J_0 \sum_{\langle i,j \rangle} \kappa_{ij} (\hat{c}_i^{\dagger} \hat{c}_j + \hat{c}_j^{\dagger} \hat{c}_i)$$
(A.23)

with tunnelling elements given by

$$\kappa_{ij} = \kappa \mathcal{J}_0 \left(\frac{|A_i - A_j|}{\hbar \omega} \right), \tag{A.24}$$

see also the main text. We utilise this approximation to generate a sequence of local driving amplitudes that generate the desired tunnelling profile encoding the black hole geometry. The dimensionless constant κ relates the chosen energy scale J_0 to the bare tunnelling in the non-driven optical lattice, i.e. the first term of Eq. (A.19). We make an explicit distinction between these energy scales to enable a wider variety of Hawking temperatures in our simulator. The Bessel function in Eq. A.24 is limited to values between 1 and ~ -0.4 ; the constant κ acts as essential leverage to achieve larger effective tunnelling elements and therefore larger simulated α and encoded Hawking temperatures [see Eq. (3) in the main text]. For instance, the analysis on error resilience in the main text simulates α values between 1 and 3 which would require $\kappa \gg 1$ for large lattices.

Since $[H_m, H_{-m}] = 0$, the second-order term of the high-frequency expansion vanishes and the leading-order corrections to the effective Hamiltonian scale as $1/\omega^2$ as discussed in the

main text.

Finally, we note that the complex phase of the tunnelling elements in a one-dimensional lattice constitutes a gauge freedom. Hence, a system with a purely real and positive "V-shaped" tunnelling profile would deliver the same dynamics given in Fig. 7.2 and provide an equally valid simulation of Hawking radiation. In contrast, tunnelling phases cannot be gauged away in 2D.

Bibliography

- [t H95] G't Hooft. "Black holes, hawking radiation, and the information paradox". In: Nuclear Physics B (Proceedings Supplements) 43.1-3 (1995), pp. 1–11. DOI: 10. 1016/0920-5632(95)00444-E.
- [ABK21] David Aasen, Parsa Bonderson, and Christina Knapp. "Characterization and classification of fermionic symmetry enriched topological phases". In: arXiv preprint arXiv:2109.10911 (2021). DOI: https://doi.org/10.48550/arXiv.2109. 10911.
- [Ach+24] Rajeev Acharya et al. "Quantum error correction below the surface code threshold". In: Nature (Dec. 2024). ISSN: 1476-4687. DOI: 10.1038/s41586-024-08449-y. URL: https://doi.org/10.1038/s41586-024-08449-y.
- [APS19] C S Adams, J D Pritchard, and J P Shaffer. "Rydberg atom quantum technologies". In: Journal of Physics B: Atomic, Molecular and Optical Physics 53.1 (Dec. 2019), p. 012002. DOI: 10.1088/1361-6455/ab52ef. URL: https://doi.org/10.1088/1361-6455/ab52ef.
- [ALX23] Lakshya Agarwal, Christopher M Langlett, and Shenglong Xu. "Long-range bell states from local measurements and many-body teleportation without time reversal". In: *Physical Review Letters* 130.2 (2023), p. 020801. DOI: https://doi.org/10.1103/PhysRevLett.130.020801.

[AMT09] A.C. Aguiar Pinto, M. Moutinho, and M.T. Thomaz. "Berry's phase in the two-level model". In: *Brazilian Journal of Physics* 39.2 (June 2009), pp. 326–330. ISSN: 0103-9733. DOI: 10.1590/s0103-97332009000300016. URL: http://dx.doi.org/10.1590/S0103-97332009000300016.

- [AB97] Dorit Aharonov and Michael Ben-Or. "Fault-tolerant quantum computation with constant error". In: (1997), pp. 176–188. DOI: https://doi.org/10.1145/258533.258579.
- [AI23] Google Quantum AI. "Suppressing quantum errors by scaling a surface code logical qubit". In: Nature 614.7949 (2023), pp. 676-681. DOI: https://doi.org/10.48550/arXiv.2207.06431.
- [Ali12] Jason Alicea. "New directions in the pursuit of Majorana fermions in solid state systems". In: Reports on progress in physics 75.7 (2012), p. 076501. DOI: https://doi.org/10.1088/0034-4885/75/7/076501.
- [AF16] Jason Alicea and Paul Fendley. "Topological phases with parafermions: theory and blueprints". In: *Annual Review of Condensed Matter Physics* 7.1 (2016), pp. 119–139. DOI: https://doi.org/10.1146/annurev-conmatphys-031115-011336.
- [AGP05] Panos Aliferis, Daniel Gottesman, and John Preskill. "Quantum accuracy threshold for concatenated distance-3 codes". In: arXiv preprint quant-ph/0504218 (2005). DOI: https://doi.org/10.48550/arXiv.quant-ph/0504218.
- [ACB12] Hussain Anwar, Earl T Campbell, and Dan E Browne. "Qutrit magic state distillation". In: New Journal of Physics 14.6 (June 2012), p. 063006. DOI: 10. 1088/1367-2630/14/6/063006. URL: https://doi.org/10.1088/1367-2630/14/6/063006.
- [Anw+14] Hussain Anwar et al. "Fast decoders for qudit topological codes". In: New J. Phys. 16 (2014), p. 063038. DOI: https://doi.org/10.1088/1367-2630/16/6/ 063038.

[Arg+19] Javier Argüello-Luengo et al. "Analogue quantum chemistry simulation". In: Nature 574.7777 (2019), pp. 215–218. DOI: https://doi.org/10.1038/s41586-019-1614-4.

- [AMV05] Michele Arzano, A Joseph M Medved, and Elias C Vagenas. "Hawking radiation as tunneling through the quantum horizon". In: *Journal of High Energy Physics* 2005.09 (2005), p. 037. DOI: 10.1088/1126-6708/2005/09/037.
- [Bai+19] Paul Baireuther et al. "Neural network decoder for topological color codes with circuit level noise". In: New Journal of Physics 21.1 (2019), p. 013003. DOI: https://doi.org/10.1088/1367-2630/aaf29e.
- [Bak+09] Waseem S. Bakr et al. "A Quantum Gas Microscope for Detecting Single Atoms in a Hubbard-regime Optical Lattice". In: Nature 462.7269 (Nov. 2009), pp. 74–77. ISSN: 0028-0836, 1476-4687. DOI: 10.1038/nature08482. (Visited on 04/21/2023).
- [Ban+16] A Banerjee et al. "Proximate Kitaev quantum spin liquid behaviour in a honeycomb magnet". In: *Nature materials* 15.7 (2016), pp. 733-740. DOI: https://doi.org/10.1038/nmat4604.
- [BJQ13a] Maissam Barkeshli, Chao-Ming Jian, and Xiao-Liang Qi. "Twist defects and projective non-Abelian braiding statistics". In: *Physical Review B* 87.4 (Jan. 2013). ISSN: 1550-235X. DOI: 10.1103/physrevb.87.045130. URL: http://dx.doi.org/10.1103/PhysRevB.87.045130.
- [BJQ13b] Maissam Barkeshli, Chao-Ming Jian, and Xiao-Liang Qi. "Twist defects and projective non-Abelian braiding statistics". In: *Physical Review B—Condensed Matter and Materials Physics* 87.4 (2013), p. 045130. DOI: https://doi.org/10.1103/PhysRevB.87.045130.
- [BQ12] Maissam Barkeshli and Xiao-Liang Qi. "Topological nematic states and non-abelian lattice dislocations". In: *Physical Review X* 2.3 (2012), p. 031013. DOI: https://doi.org/10.1103/PhysRevX.2.031013.

[Bar+19] Maissam Barkeshli et al. "Symmetry fractionalization, defects, and gauging of topological phases". In: *Physical Review B* 100.11 (2019), p. 115147. DOI: https://doi.org/10.1103/PhysRevB.100.115147.

- [Bar+15] Daniel Barredo et al. "Coherent Excitation Transfer in a Spin Chain of Three Rydberg Atoms". In: *Physical Review Letters* 114.11 (Mar. 2015). ISSN: 1079-7114. DOI: 10.1103/physrevlett.114.113002. URL: http://dx.doi.org/10.1103/PhysRevLett.114.113002.
- [Bar+18] Daniel Barredo et al. "Synthetic Three-Dimensional Atomic Structures Assembled Atom by Atom". In: *Nature* 561.7721 (Sept. 2018), pp. 79–82. ISSN: 1476-4687. DOI: 10.1038/s41586-018-0450-2. (Visited on 09/21/2023).
- [Bar+23] Sara Bartolucci et al. "Fusion-based quantum computation". In: Nature Communications 14.1 (2023), p. 912. DOI: https://doi.org/10.1038/s41467-023-36493-1.
- [Bau+23a] Nora M Bauer et al. "Non-Abelian anyons with Rydberg atoms". In: *Physical Review A* 107.6 (2023), p. 062407. DOI: https://doi.org/10.1103/PhysRevA. 107.062407.
- [Bau+23b] Johannes Bausch et al. "Learning to decode the surface code with a recurrent, transformer-based neural network". In: arXiv preprint arXiv:2310.05900 (2023).

 DOI: https://doi.org/10.48550/arXiv.2310.05900.
- [Bek73] Jacob D. Bekenstein. "Black Holes and Entropy". In: Phys. Rev. D 7 (8 Apr. 1973), pp. 2333-2346. DOI: 10.1103/PhysRevD.7.2333. URL: https://link.aps.org/doi/10.1103/PhysRevD.7.2333.
- [BRN18] F Bemani, R Roknizadeh, and MH Naderi. "Quantum simulation of discrete curved spacetime by the Bose-Hubbard model: From analog acoustic black hole to quantum phase transition". In: *Annals of Physics* 388 (2018), pp. 186–196. DOI: https://doi.org/10.1016/j.aop.2017.11.010.

[BPB22] Asmae Benhemou, Jiannis K Pachos, and Dan E Browne. "Non-Abelian statistics with mixed-boundary punctures on the toric code". In: *Physical Review A* 105.4 (2022), p. 042417. DOI: https://doi.org/10.1103/PhysRevA.105.042417.

- [Ben+23a] Asmae Benhemou et al. "Minimising surface-code failures using a color-code decoder". In: arXiv preprint arXiv:2306.16476 (2023). DOI: https://doi.org/10.48550/arXiv.2306.16476.
- [Ben+23b] Asmae Benhemou et al. "Probing quantum properties of black holes with a Floquet-driven optical lattice simulator". In: arXiv preprint arXiv:2312.14058 (2023). DOI: https://doi.org/10.48550/arXiv.2312.14058.
- [Ben+23c] Asmae Benhemou et al. "Universality of Z₃ parafermions via edge-mode interaction and quantum simulation of topological space evolution with Rydberg atoms". In: *Physical Review Research* 5.2 (2023), p. 023076. DOI: https://doi.org/10.1103/PhysRevResearch.5.023076.
- [Ben76] Charles H Bennett. "Efficient estimation of free energy differences from Monte Carlo data". In: Journal of Computational Physics 22.2 (1976), pp. 245-268.

 ISSN: 0021-9991. DOI: https://doi.org/10.1016/0021-9991(76)90078-4.

 URL: https://www.sciencedirect.com/science/article/pii/0021999176900784.
- [Ber+17] Hannes Bernien et al. "Probing Many-Body Dynamics on a 51-Atom Quantum Simulator". In: Nature 551.7682 (Nov. 2017), pp. 579–584. ISSN: 0028-0836, 1476-4687. DOI: 10.1038/nature24622. (Visited on 05/07/2023).
- [BV93] Ethan Bernstein and Umesh Vazirani. "Quantum complexity theory". In: Proceedings of the twenty-fifth annual ACM symposium on Theory of computing. 1993, pp. 11–20. DOI: https://doi.org/10.1137/S0097539796300921.
- [BT77] M. V. Berry and M. Tabor. "Level Clustering in the Regular Spectrum". In: Proceedings of the Royal Society A 356.1686 (Sept. 1977), pp. 375–394. DOI: 10.1098/rspa.1977.0140. URL: https://doi.org/10.1098/rspa.1977.0140.

[Bev+19] Michael E Beverland et al. "The role of entropy in topological quantum error correction". In: Journal of Statistical Mechanics: Theory and Experiment 2019.7 (2019), p. 073404. DOI: https://doi.org/10.1088/1742-5468/ab25de.

- [BKS21] Michael E. Beverland, Aleksander Kubica, and Krysta M. Svore. "Cost of Universality: A Comparative Study of the Overhead of State Distillation and Code Switching with Color Codes". In: *PRX Quantum* 2 (2 June 2021), p. 020341.

 DOI: 10.1103/PRXQuantum.2.020341. URL: https://link.aps.org/doi/10.1103/PRXQuantum.2.020341.
- [BS15] Arjun Bhagoji and Pradeep Sarvepalli. "Equivalence of 2D color codes (without translational symmetry) to surface codes". In: 2015 IEEE International Symposium on Information Theory (ISIT). 2015, p. 1109. DOI: 10.1109/ISIT.2015. 7282627.
- [BD84] Nicholas David Birrell and Paul Charles William Davies. *Quantum fields in curved space*. Cambridge university press, 1984. DOI: Quantumfieldsincurvedspace.
- [Blo05] Immanuel Bloch. "Ultracold quantum gases in optical lattices". In: *Nature physics* 1.1 (2005), pp. 23–30. DOI: https://doi.org/10.1038/nphys138.
- [BDZ08] Immanuel Bloch, Jean Dalibard, and Wilhelm Zwerger. "Many-body physics with ultracold gases". In: *Reviews of modern physics* 80.3 (2008), pp. 885–964.

 DOI: https://doi.org/10.1103/RevModPhys.80.885.
- [Blo+21] M.S. Blok et al. "Quantum Information Scrambling on a Superconducting Qutrit Processor". In: *Physical Review X* 11.2 (Apr. 2021). ISSN: 2160-3308. DOI: 10. 1103/physrevx.11.021010. URL: http://dx.doi.org/10.1103/PhysRevX. 11.021010.
- [Blu+23] Dolev Bluvstein et al. "Logical quantum processor based on reconfigurable atom arrays". In: Nature 626.7997 (Dec. 2023), pp. 58-65. ISSN: 1476-4687. DOI: https://doi.org/10.1038/s41586-023-06927-3. URL: http://dx.doi.org/10.1038/s41586-023-06927-3.

[BGS84] O. Bohigas, M. J. Giannoni, and C. Schmit. "Characterization of Chaotic Quantum Spectra and Universality of Level Fluctuation Laws". In: *Physical Review Letters* 52.1 (Jan. 1984), pp. 1–4. DOI: 10.1103/PhysRevLett.52.1. URL: https://link.aps.org/doi/10.1103/PhysRevLett.52.1.

- [Bom+86] Luca Bombelli et al. "Quantum source of entropy for black holes". In: *Phys. Rev. D* 34 (2 July 1986), pp. 373-383. DOI: 10.1103/PhysRevD.34.373. URL: https://link.aps.org/doi/10.1103/PhysRevD.34.373.
- [BM09a] H Bombin and M A Martin-Delgado. "Quantum measurements and gates by code deformation". In: Journal of Physics A: Mathematical and Theoretical 42.9 (Feb. 2009), p. 095302. ISSN: 1751-8121. DOI: 10.1088/1751-8113/42/9/095302. URL: http://dx.doi.org/10.1088/1751-8113/42/9/095302.
- [Bom10] H. Bombin. "Topological Order with a Twist: Ising Anyons from an Abelian Model". In: *Physical Review Letters* 105.3 (July 2010). ISSN: 1079-7114. DOI: 10.1103/physrevlett.105.030403. URL: http://dx.doi.org/10.1103/PhysRevLett.105.030403.
- [BM06] H. Bombin and M. A. Martin-Delgado. "Topological Quantum Distillation". In: Phys. Rev. Lett. 97 (18 Oct. 2006), p. 180501. DOI: https://doi.org/10. 1103/PhysRevLett.97.180501. URL: https://link.aps.org/doi/10.1103/PhysRevLett.97.180501.
- [BDP12] Hector Bombin, Guillaume Duclos-Cianci, and David Poulin. "Universal topological phase of two-dimensional stabilizer codes". In: New Journal of Physics 14.7 (2012), p. 073048. DOI: https://doi.org/10.1088/1367-2630/14/7/073048.
- [BM07] Hector Bombin and Miguel-Angel Martin-Delgado. "Topological computation without braiding". In: *Physical review letters* 98.16 (2007), p. 160502. DOI: https://doi.org/10.1103/PhysRevLett.98.160502.

[Bom13] Héctor Bombín. "An introduction to topological quantum codes". In: arXiv preprint arXiv:1311.0277 (2013). DOI: https://doi.org/10.48550/arXiv. 1311.0277.

- [Bom15] Héctor Bombín. "Gauge color codes: optimal transversal gates and gauge fixing in topological stabilizer codes". In: New Journal of Physics 17.8 (Aug. 2015), p. 083002. DOI: 10.1088/1367-2630/17/8/083002. URL: https://dx.doi.org/10.1088/1367-2630/17/8/083002.
- [BM09b] Héctor Bombín and Miguel Angel Martin-Delgado. "Quantum measurements and gates by code deformation". In: Journal of Physics A: Mathematical and Theoretical 42.9 (2009), p. 095302. DOI: https://doi.org/10.1088/1751-8113/42/9/095302.
- [Bon+10] Parsa Bonderson et al. "A blueprint for a topologically fault-tolerant quantum computer". In: arXiv preprint arXiv:1003.2856 (2010). DOI: https://doi.org/10.48550/arXiv.1003.2856.
- [Bon+21] J Pablo Bonilla Ataides et al. "The XZZX surface code". In: *Nature communications* 12.1 (2021), p. 2172. DOI: https://doi.org/10.1038/s41467-021-22274-1.
- [Bor+16] Pranjal Bordia et al. "Coupling Identical One-Dimensional Many-Body Localized Systems". In: *Physical Review Letters* 116.14 (Apr. 2016), p. 140401. DOI: 10. 1103/PhysRevLett.116.140401. (Visited on 11/18/2023).
- [Bor61] M Born. The Born-Einstein letters 1916-1955. International series in pure and applied physics. 1961.
- [Bou+21] J. Eli Bourassa et al. "Blueprint for a Scalable Photonic Fault-Tolerant Quantum Computer". In: Quantum 5 (Feb. 2021), p. 392. ISSN: 2521-327X. DOI: 10.22331/q-2021-02-04-392. URL: http://dx.doi.org/10.22331/q-2021-02-04-392.

[Boy+00] P.Oscar Boykin et al. "A new universal and fault-tolerant quantum basis". In:

Information Processing Letters 75.3 (2000), pp. 101-107. ISSN: 0020-0190. DOI:

https://doi.org/10.1016/S0020-0190(00)00084-3. URL: https://www.sciencedirect.com/science/article/pii/S0020019000000843.

- [BK98] S. B. Bravyi and A. Yu. Kitaev. Quantum codes on a lattice with boundary. 1998. arXiv: quant-ph/9811052 [quant-ph].
- [Bra06] Sergey Bravyi. "Universal quantum computation with the $\nu = 5/2$ fractional quantum Hall state". In: *Physical Review A* 73.4 (2006), p. 042313.
- [BK05] Sergey Bravyi and Alexei Kitaev. "Universal quantum computation with ideal Clifford gates and noisy ancillas". In: *Physical Review A* 71.2 (Feb. 2005). ISSN: 1094-1622. DOI: 10.1103/physreva.71.022316. URL: http://dx.doi.org/10.1103/PhysRevA.71.022316.
- [BSV14] Sergey Bravyi, Martin Suchara, and Alexander Vargo. "Efficient algorithms for maximum likelihood decoding in the surface code". In: *Physical Review A* 90.3 (2014), p. 032326. DOI: https://doi.org/10.1103/PhysRevA.90.032326.
- [BV13] Sergey Bravyi and Alexander Vargo. "Simulation of rare events in quantum error correction". In: *Physical Review A* 88.6 (Dec. 2013). DOI: 10.1103/physreva. 88.062308. URL: https://doi.org/10.11032Fphysreva.88.062308.
- [Bre+11] Courtney G Brell et al. "Toric codes and quantum doubles from two-body Hamiltonians". In: New Journal of Physics 13.5 (May 2011), p. 053039. DOI: https://doi.org/10.1088/1367-2630/13/5/053039. URL: https://dx.doi.org/10.1088/1367-2630/13/5/053039.
- [Bre+17] Nikolas P Breuckmann et al. "Hyperbolic and semi-hyperbolic surface codes for quantum storage". In: Quantum Science and Technology 2.3 (2017), p. 035007.

 DOI: https://doi.org/10.1088/2058-9565/aa7d3b.

[BL20] Antoine Browaeys and Thierry Lahaye. "Many-body physics with individually controlled Rydberg atoms". In: *Nature Physics* 16.2 (Jan. 2020), pp. 132–142. ISSN: 1745-2481. DOI: 10.1038/s41567-019-0733-z. URL: http://dx.doi.org/10.1038/s41567-019-0733-z.

- [Bro22] Benjamin J Brown. "Conservation laws and quantum error correction: towards a generalised matching decoder". In: arXiv preprint arXiv:2207.06428 (2022).

 DOI: https://doi.org/10.1109/MBITS.2023.3246025.
- [BW20] Benjamin J Brown and Dominic J Williamson. "Parallelized quantum error correction with fracton topological codes". In: *Physical Review Research* 2.1 (2020), p. 013303. DOI: https://doi.org/10.1103/PhysRevResearch.2.013303.
- [Bro+16] Benjamin J Brown et al. "Quantum memories at finite temperature". In: Reviews of Modern Physics 88.4 (2016), p. 045005. DOI: https://doi.org/10.1103/RevModPhys.88.045005.
- [Bro+17] Benjamin J. Brown et al. "Poking Holes and Cutting Corners to Achieve Clifford Gates with the Surface Code". In: *Physical Review X* 7.2 (May 2017). ISSN: 2160-3308. DOI: 10.1103/physrevx.7.021029. URL: http://dx.doi.org/10.1103/PhysRevX.7.021029.
- [BB02] Jean-Luc Brylinski and Ranee Brylinski. "Universal quantum gates". In: Mathematics of quantum computation. Chapman and Hall/CRC, 2002, pp. 117–134.

 DOI: https://doi.org/10.48550/arXiv.quant-ph/0108062.
- [BDP15] Marin Bukov, Luca D'Alessio, and Anatoli Polkovnikov. "Universal High-Frequency Behavior of Periodically Driven Systems: From Dynamical Stabilization to Floquet Engineering". In: *Advances in Physics* 64.2 (Mar. 2015), pp. 139–226. ISSN: 0001-8732, 1460-6976. DOI: 10.1080/00018732.2015.1055918. eprint: 1407. 4803 (cond-mat).

[Cai+23] Zhenyu Cai et al. "Quantum error mitigation". In: Reviews of Modern Physics 95.4 (2023), p. 045005. DOI: https://doi.org/10.1103/RevModPhys.95.045005.

- [CS96] A Robert Calderbank and Peter W Shor. "Good quantum error-correcting codes exist". In: *Physical Review A* 54.2 (1996), p. 1098. DOI: https://doi.org/10.1103/PhysRevA.54.1098.
- [CTV17] Earl T Campbell, Barbara M Terhal, and Christophe Vuillot. "Roads towards fault-tolerant universal quantum computation". In: *Nature* 549.7671 (2017), pp. 172–179. DOI: https://doi.org/10.1038/nature23460.
- [CAB12] Earl T. Campbell, Hussain Anwar, and Dan E. Browne. "Magic-State Distillation in All Prime Dimensions Using Quantum Reed-Muller Codes". In: *Physical Review X* 2.4 (Dec. 2012). ISSN: 2160-3308. DOI: 10.1103/physrevx.2.041021. URL: http://dx.doi.org/10.1103/PhysRevX.2.041021.
- [Car86] John L. Cardy. "Operator content of two-dimensional conformally invariant theories". In: Nuclear Physics B 270 (1986), pp. 186-204. ISSN: 0550-3213. DOI: https://doi.org/10.1016/0550-3213(86)90552-3. URL: https://www.sciencedirect.com/science/article/pii/0550321386905523.
- [Cay+13] Jérôme Cayssol et al. "Floquet topological insulators". In: physica status solidi (RRL)-Rapid Research Letters 7.1-2 (2013), pp. 101-108. DOI: https://doi.org/10.1002/pssr.201206451.
- [CJK10] Jiří Chaloupka, George Jackeli, and Giniyat Khaliullin. "Kitaev-Heisenberg Model on a Honeycomb Lattice: Possible Exotic Phases in Iridium Oxides A 2 IrO 3". In: *Physical review letters* 105.2 (2010), p. 027204. DOI: https://doi.org/10. 1103/PhysRevLett.105.027204.
- [CC19] Christopher Chamberland and Andrew W. Cross. "Fault-tolerant magic state preparation with flag qubits". In: *Quantum* 3 (May 2019), p. 143. ISSN: 2521-

327X. DOI: https://doi.org/10.22331/q-2019-05-20-143. URL: http://dx.doi.org/10.22331/q-2019-05-20-143.

- [CR18] Christopher Chamberland and Pooya Ronagh. "Deep neural decoders for near term fault-tolerant experiments". In: Quantum Science and Technology 3.4 (2018), p. 044002. DOI: https://doi.org/10.1103/PhysRevLett.119.030501.
- [Cha+20] Christopher Chamberland et al. "Triangular color codes on trivalent graphs with flag qubits". In: New Journal of Physics 22.2 (Feb. 2020), p. 023019. DOI: 10. 1088/1367-2630/ab68fd. URL: https://dx.doi.org/10.1088/1367-2630/ab68fd.
- [CB23] Tim Chan and Simon C. Benjamin. "Strictly local Union-Find". In: arXiv:2305.18534 (2023). DOI: https://doi.org/10.22331/q-2023-11-14-1183.
- [CCW22] Bowen Chen, Bartlomiej Czech, and Zi-Zhi Wang. "Quantum information in holographic duality". In: Reports on Progress in Physics 85.4 (2022), p. 046001. DOI: https://doi.org/10.48550/arXiv.2108.09188.
- [CN08] Han-Dong Chen and Zohar Nussinov. "Exact results of the Kitaev model on a hexagonal lattice: spin states, string and brane correlators, and anyonic excitations". In: Journal of Physics A: Mathematical and Theoretical 41.7 (2008), p. 075001. DOI: https://doi.org/10.1088/1751-8113/41/7/075001.
- [CGW10] Xie Chen, Zheng-Cheng Gu, and Xiao-Gang Wen. "Local unitary transformation, long-range quantum entanglement, wave function renormalization, and topological order". In: Physical Review B—Condensed Matter and Materials Physics 82.15 (2010), p. 155138. DOI: https://doi.org/10.1103/PhysRevB.82.155138.
- [Chi+10] Cheng Chin et al. "Feshbach Resonances in Ultracold Gases". In: Reviews of Modern Physics 82.2 (Apr. 2010), pp. 1225–1286. ISSN: 0034-6861, 1539-0756.
 DOI: 10.1103/RevModPhys.82.1225. (Visited on 10/05/2023).

[Cho23] Jae-yoon Choi. "Quantum Simulations with Ultracold Atoms in Optical Lattices: Past, Present and Future". In: Journal of the Korean Physical Society 82.9 (May 2023), pp. 875–881. ISSN: 1976-8524. DOI: 10.1007/s40042-023-00777-y. (Visited on 06/26/2023).

- [Cho+16] Jae-yoon Choi et al. "Exploring the Many-Body Localization Transition in Two Dimensions". In: *Science* 352.6293 (June 2016), pp. 1547–1552. DOI: 10.1126/science.aaf8834.
- [CF21] Christopher T. Chubb and Steven T. Flammia. "Statistical mechanical models for quantum codes with correlated noise". In: Annales de l'Institut Henri Poincaré D, Combinatorics, Physics and their Interactions 8.2 (May 2021), pp. 269–321. ISSN: 2308-5835. DOI: https://doi.org/10.4171/AIHPD/105. URL: http://dx.doi.org/10.4171/AIHPD/105.
- [CMP10] J. Ignacio Cirac, Paolo Maraner, and Jiannis K. Pachos. "Cold Atom Simulation of Interacting Relativistic Quantum Field Theories". In: Phys. Rev. Lett. 105 (19 Nov. 2010), p. 190403. DOI: 10.1103/PhysRevLett.105.190403. URL: https://link.aps.org/doi/10.1103/PhysRevLett.105.190403.
- [Cir+21] Virginia N Ciriano-Tejel et al. "Spin readout of a CMOS quantum dot by gate reflectometry and spin-dependent tunneling". In: PRX Quantum 2.1 (2021), p. 010353. DOI: https://doi.org/10.1103/PRXQuantum.2.010353.
- [CAS13] David J Clarke, Jason Alicea, and Kirill Shtengel. "Exotic non-Abelian anyons from conventional fractional quantum Hall states". In: *Nature communications* 4.1 (2013), pp. 1–9.
- [CW16] Antonin Coutant and Silke Weinfurtner. "The imprint of the analogue Hawking effect in subcritical flows". In: *Physical Review D* 94.6 (2016), p. 064026. DOI: https://doi.org/10.1103/PhysRevD.94.064026.
- [Cov+19] Jacob P Covey et al. "2000-times repeated imaging of strontium atoms in clock-magic tweezer arrays". In: *Physical review letters* 122.17 (2019), p. 173201.

[CA18] Ben Criger and Imran Ashraf. "Multi-path summation for decoding 2D topological codes". In: Quantum 2 (2018), p. 102. DOI: https://doi.org/10.22331/q-2018-10-19-102.

- [CT16] Ben Criger and Barbara Terhal. "Noise thresholds for the [[4, 2, 2]]-concatenated toric code". In: arXiv preprint arXiv:1604.04062 (2016). DOI: https://doi.org/10.26421/QIC16.15-16.
- [CGK17] Shawn X. Cui, Daniel Gottesman, and Anirudh Krishna. "Diagonal gates in the Clifford hierarchy". In: *Physical Review A* 95.1 (Jan. 2017). ISSN: 2469-9934. DOI: 10.1103/physreva.95.012329. URL: http://dx.doi.org/10.1103/PhysRevA. 95.012329.
- [Dal23] Andrew J Daley. "Twenty-five years of analogue quantum simulation". In: *Nature Reviews Physics* 5.12 (2023), pp. 702–703. DOI: https://doi.org/10.1038/s42254-023-00666-0.
- [DR76] Thibaut Damour and Remo Ruffini. "Black-hole evaporation in the Klein-Sauter-Heisenberg-Euler formalism". In: *Physical Review D* 14.2 (1976), p. 332. DOI: https://doi.org/10.1103/PhysRevD.14.332.
- [DHP23] Aydin Deger, Matthew D. Horner, and Jiannis K. Pachos. "AdS/CFT correspondence with a three-dimensional black hole simulator". In: *Phys. Rev. B* 108 (15 Oct. 2023), p. 155124. DOI: 10.1103/PhysRevB.108.155124. URL: https://link.aps.org/doi/10.1103/PhysRevB.108.155124.
- [DIP16] Nicolas Delfosse, Pavithran Iyer, and David Poulin. Generalized surface codes and packing of logical qubits. 2016. arXiv: 1606.07116 [quant-ph].
- [DN21] Nicolas Delfosse and Naomi H. Nickerson. "Almost-linear time decoding algorithm for topological codes". In: Quantum 5 (Dec. 2021), p. 595. ISSN: 2521-327X. DOI: https://doi.org/10.22331/q-2021-12-02-595. URL: https://doi.org/10.22331/q-2021-12-02-595.

[DT14] Nicolas Delfosse and Jean-Pierre Tillich. "A decoding algorithm for CSS codes using the X/Z correlations". In: 2014 IEEE International Symposium on Information Theory. IEEE. 2014, pp. 1071–1075. DOI: https://doi.org/10.48550/arXiv.1401.6975.

- [Den+02] Eric Dennis et al. "Topological quantum memory". In: Journal of Mathematical Physics 43.9 (2002), pp. 4452–4505. DOI: https://doi.org/10.1063/1.1499754.
- [DJ92] David Deutsch and Richard Jozsa. "Rapid solution of problems by quantum computation". In: Proceedings of the Royal Society of London. Series A: Mathematical and Physical Sciences 439.1907 (1992), pp. 553–558. DOI: https://doi.org/10.1098/rspa.1992.0167.
- [DP10] Guillaume Duclos-Cianci and David Poulin. "Fast decoders for topological quantum codes". In: *Physical review letters* 104.5 (2010), p. 050504. DOI: https://doi.org/10.1103/PhysRevLett.104.050504.
- [Dür+02] W. Dür et al. "Quantum Walks in Optical Lattices". In: *Physical Review A* 66.5 (Nov. 2002), p. 052319. DOI: 10.1103/PhysRevA.66.052319. (Visited on 10/06/2023).
- [EK09] Bryan Eastin and Emanuel Knill. "Restrictions on transversal encoded quantum gate sets". In: *Physical review letters* 102.11 (2009), p. 110502. DOI: https://doi.org/10.1103/PhysRevLett.102.110502.
- [Eba+21] Sepehr Ebadi et al. "Quantum phases of matter on a 256-atom programmable quantum simulator". In: Nature 595.7866 (July 2021), pp. 227-232. ISSN: 1476-4687. DOI: 10.1038/s41586-021-03582-4. URL: http://dx.doi.org/10.1038/s41586-021-03582-4.
- [Eck17] André Eckardt. "Colloquium: Atomic Quantum Gases in Periodically Driven Optical Lattices". In: *Reviews of Modern Physics* 89.1 (Mar. 2017), p. 011004. DOI: 10.1103/RevModPhys.89.011004. (Visited on 06/26/2023).

[EA15] André Eckardt and Egidijus Anisimovas. "High-Frequency Approximation for Periodically Driven Quantum Systems from a Floquet-space Perspective". In: New Journal of Physics 17.9 (Sept. 2015), p. 093039. ISSN: 1367-2630. DOI: 10. 1088/1367-2630/17/9/093039. (Visited on 05/08/2023).

- [Edd24] A. S. Eddington. "A Comparison of Whitehead's and Einstein's Formulæ". In: 113.2832 (Feb. 1924), p. 192. DOI: 10.1038/113192a0.
- [Edm65] Jack Edmonds. "Paths, trees, and flowers". In: Canadian Journal of mathematics 17 (1965), pp. 449–467. DOI: https://doi.org/10.4153/CJM-1965-045-4.
- [Ega+21] Laird Egan et al. "Fault-tolerant control of an error-corrected qubit". In: *Nature* 598.7880 (2021), pp. 281–286. DOI: https://doi.org/10.1038/s41586-021-03928-y. URL: https://doi.org/10.1038/s41586-021-03928-y.
- [Elt+21] Christopher Eltschka et al. "The shape of higher-dimensional state space: Blochball analog for a qutrit". In: *Quantum* 5 (June 2021), p. 485. ISSN: 2521-327X. DOI: 10.22331/q-2021-06-29-485. URL: http://dx.doi.org/10.22331/q-2021-06-29-485.
- [Emp06] Roberto Emparan. "Black hole entropy as entanglement entropy: a holographic derivation". In: Journal of High Energy Physics 2006.06 (June 2006), p. 012. DOI: 10.1088/1126-6708/2006/06/012. URL: https://dx.doi.org/10.1088/1126-6708/2006/06/012.
- [FGG14] Edward Farhi, Jeffrey Goldstone, and Sam Gutmann. "A quantum approximate optimization algorithm". In: arXiv preprint arXiv:1411.4028 (2014). DOI: https://doi.org/10.48550/arXiv.1411.4028.
- [Far14] J M Farinholt. "An ideal characterization of the Clifford operators". In: Journal of Physics A: Mathematical and Theoretical 47.30 (July 2014), p. 305303. DOI: 10.1088/1751-8113/47/30/305303. URL: https://doi.org/10.1088%2F1751-8113%2F47%2F30%2F305303.

[FF04] Petr O Fedichev and Uwe R Fischer. ""Cosmological" quasiparticle production in harmonically trapped superfluid gases". In: *Physical Review A* 69.3 (2004), p. 033602. DOI: https://doi.org/10.1103/PhysRevA.69.033602.

- [Fei+07] Adrian Feiguin et al. "Interacting anyons in topological quantum liquids: The golden chain". In: *Physical review letters* 98.16 (2007), p. 160409. DOI: https://doi.org/10.1103/PhysRevLett.98.160409.
- [Fen12] Paul Fendley. "Parafermionic edge zero modes in Z_n -invariant spin chains". In: Journal of Statistical Mechanics: Theory and Experiment 2012.11 (Nov. 2012), P11020. ISSN: 1742-5468. DOI: 10.1088/1742-5468/2012/11/p11020. URL: http://dx.doi.org/10.1088/1742-5468/2012/11/P11020.
- [FS18] Bernard Field and Tapio Simula. "Introduction to topological quantum computation with non-Abelian anyons". In: Quantum Science and Technology 3.4 (2018), p. 045004. DOI: https://doi.org/10.1088/2058-9565/aacad2.
- [Fin58] David Finkelstein. "Past-future asymmetry of the gravitational field of a point particle". In: *Physical Review* 110.4 (1958), p. 965. DOI: https://doi.org/10.1103/PhysRev.110.965.
- [FS04] Uwe R Fischer and Ralf Schützhold. "Quantum simulation of cosmic inflation in two-component Bose-Einstein condensates". In: *Physical Review A* 70.6 (2004), p. 063615. DOI: https://doi.org/10.1103/PhysRevA.70.063615.
- [Fis95] Daniel S. Fisher. "Critical behavior of random transverse-field Ising spin chains". In: *Phys. Rev. B* 51 (10 Mar. 1995), pp. 6411–6461. DOI: 10.1103/PhysRevB. 51.6411. URL: https://link.aps.org/doi/10.1103/PhysRevB.51.6411.
- [96] FOCS '96: Proceedings of the 37th Annual Symposium on Foundations of Computer Science. USA: IEEE Computer Society, 1996.
- [FL97] M.P.C. Fossorier and Shu Lin. "Soft Decision Decoding of Linear Block Codes Based on Ordered Statistics for the Rayleigh Fading Channel with Coherent

- Detection". In: *IEEE Transactions on Communications* 45.1 (Jan. 1997), pp. 12–14. ISSN: 1558-0857. DOI: 10.1109/26.554278. (Visited on 04/18/2024).
- [Fow13a] Austin G. Fowler. "Coping with qubit leakage in topological codes". In: *Phys. Rev. A* 88 (4 Oct. 2013), p. 042308. DOI: 10.1103/PhysRevA.88.042308. URL: https://link.aps.org/doi/10.1103/PhysRevA.88.042308.
- [Fow13b] Austin G. Fowler. "Optimal complexity correction of correlated errors in the surface code". In: arXiv:1310.0863 (2013). DOI: https://doi.org/10.48550/arXiv.1310.0863.
- [FM14] Austin G. Fowler and John M. Martinis. "Quantifying the effects of local many-qubit errors and nonlocal two-qubit errors on the surface code". In: *Phys. Rev.* A 89 (3 Mar. 2014), p. 032316. DOI: 10.1103/PhysRevA.89.032316. URL: https://link.aps.org/doi/10.1103/PhysRevA.89.032316.
- [Fow+12a] Austin G. Fowler et al. "Surface codes: Towards practical large-scale quantum computation". In: *Physical Review A* 86.3 (Sept. 2012). ISSN: 1094-1622. DOI: 10.1103/physreva.86.032324. URL: http://dx.doi.org/10.1103/PhysRevA. 86.032324.
- [Fow+12b] Austin G. Fowler et al. "Surface codes: Towards practical large-scale quantum computation". In: *Phys. Rev. A* 86 (3 Sept. 2012), p. 032324. DOI: 10.1103/PhysRevA.86.032324. URL: https://link.aps.org/doi/10.1103/PhysRevA.86.032324.
- [FK80] Eduardo Fradkin and Leo P Kadanoff. "Disorder variables and para-fermions in two-dimensional statistical mechanics". In: *Nuclear Physics B* 170.1 (1980), pp. 1–15. DOI: https://doi.org/10.1016/0550-3213(80)90472-1.
- [Fre+03] Michael H. Freedman et al. "Topological Quantum Computation". In: Bull. Amer. Math. Soc. 40.10S (Oct. 2003). ISSN: 31-38. DOI: doi.org/10.1090/S0273-0979-02-00964-3. URL: https://www.ams.org/journals/bull/2003-40-01/S0273-0979-02-00964-3/.

[FK09] Liang Fu and Charles L Kane. "Josephson current and noise at a superconductor/quantum-spin-Hall-insulator/superconductor junction". In: *Physical Review B—Condensed Matter and Materials Physics* 79.16 (2009), p. 161408. DOI: https://doi.org/10.1103/PhysRevB.79.161408.

- [Fuk+13] Takeshi Fukuhara et al. "Microscopic Observation of Magnon Bound States and Their Dynamics". In: *Nature* 502.7469 (Oct. 2013), pp. 76–79. ISSN: 1476-4687. DOI: 10.1038/nature12541.
- [Gal63] Robert G Gallager. Low density parity check codes, monograph. 1963. DOI: https://doi.org/10.7551/mitpress/4347.001.0001. URL: https://direct.mit.edu/books/monograph/3867/Low-Density-Parity-Check-Codes.
- [GH77] Gary W Gibbons and Stephen W Hawking. "Action integrals and partition functions in quantum gravity". In: *Physical Review D* 15.10 (1977), p. 2752. DOI: https://doi.org/10.1103/PhysRevD.15.2752.
- [GE21] Craig Gidney and Martin Ekerå. "How to factor 2048 bit RSA integers in 8 hours using 20 million noisy qubits". In: Quantum 5 (2021), p. 433. DOI: https://doi.org/10.22331/q-2021-04-15-433.
- [GJ23] Craig Gidney and Cody Jones. New circuits and an open source decoder for the color code. 2023. arXiv: 2312.08813 [quant-ph]. URL: https://arxiv.org/abs/2312.08813.
- [GNM22] Craig Gidney, Michael Newman, and Matt McEwen. "Benchmarking the Planar Honeycomb Code". In: Quantum 6 (Sept. 2022), p. 813. ISSN: 2521-327X. DOI: 10.22331/q-2022-09-21-813. URL: https://doi.org/10.22331/q-2022-09-21-813.
- [GSJ24] Craig Gidney, Noah Shutty, and Cody Jones. "Magic state cultivation: growing T states as cheap as CNOT gates". In: arXiv preprint arXiv:2409.17595 (2024). DOI: https://doi.org/10.48550/arXiv.2409.17595.

[Gok+19] Pranav Gokhale et al. "Asymptotic improvements to quantum circuits via qutrits". In: Proceedings of the 46th International Symposium on Computer Architecture (June 2019). DOI: 10.1145/3307650.3322253. URL: http://dx.doi.org/10.1145/3307650.3322253.

- [GD14] N. Goldman and J. Dalibard. "Periodically Driven Quantum Systems: Effective Hamiltonians and Engineered Gauge Fields". In: *Physical Review X* 4.3 (Aug. 2014), p. 031027. ISSN: 2160-3308. DOI: 10.1103/PhysRevX.4.031027. (Visited on 05/08/2023).
- [Got96] Daniel Gottesman. "Class of quantum error-correcting codes saturating the quantum Hamming bound". In: *Physical Review A* 54.3 (1996), p. 1862. DOI: https://doi.org/10.1103/PhysRevA.54.1862.
- [Got97] Daniel Gottesman. "Stabilizer Codes and Quantum Error Correction". PhD thesis. California Institute of Technology, 1997.
- [Got98a] Daniel Gottesman. "The Heisenberg representation of quantum computers". In: $arXiv\ preprint\ quant-ph/9807006\ (1998).$
- [Got98b] Daniel Gottesman. "Theory of fault-tolerant quantum computation". In: *Physical Review A* 57.1 (Jan. 1998), pp. 127–137. DOI: 10.1103/physreva.57.127. URL: https://journals.aps.org/pra/abstract/10.1103/PhysRevA.57.127.
- [Got13] Daniel Gottesman. "Fault-tolerant quantum computation with constant overhead". In: arXiv preprint arXiv:1310.2984 (2013). DOI: https://doi.org/10.48550/arXiv.1310.2984.
- [GC99] Daniel Gottesman and Isaac L. Chuang. "Demonstrating the viability of universal quantum computation using teleportation and single-qubit operations". In: 402.6760 (Nov. 1999), pp. 390–393. DOI: 10.1038/46503. arXiv: quant-ph/9908010 [quant-ph].

[Gre+21] Philip D. Gregory et al. "Robust storage qubits in ultracold polar molecules".
In: Nature Physics 17.10 (Sept. 2021), pp. 1149–1153. ISSN: 1745-2481. DOI: 10.
1038/s41567-021-01328-7. URL: http://dx.doi.org/10.1038/s41567-021-01328-7.

- [GB23] Sam J. Griffiths and Dan E. Browne. "Union-find quantum decoding without union-find". In: arXiv:2306.09767 (2023). DOI: https://doi.org/10.48550/arXiv.2306.09767.
- [GB21] Christian Gross and Waseem S. Bakr. "Quantum Gas Microscopy for Single Atom and Spin Detection". In: Nature Physics 17.12 (Dec. 2021), pp. 1316– 1323. ISSN: 1745-2473, 1745-2481. DOI: 10.1038/s41567-021-01370-5. (Visited on 05/07/2023).
- [GB17a] Christian Gross and Immanuel Bloch. "Quantum Simulations with Ultracold Atoms in Optical Lattices". In: *Science* 357.6355 (Sept. 2017), pp. 995–1001. DOI: 10.1126/science.aal3837. (Visited on 05/07/2023).
- [GB17b] Christian Gross and Immanuel Bloch. "Quantum simulations with ultracold atoms in optical lattices". In: Science 357.6355 (2017), pp. 995–1001. DOI: https://doi.org/10.1126/science.aal3837.
- [Gro96] Lov K Grover. "A fast quantum mechanical algorithm for database search". In: Proceedings of the twenty-eighth annual ACM symposium on Theory of computing. 1996, pp. 212–219. DOI: https://doi.org/10.48550/arXiv.quantph/9605043.
- [GMW98] Thomas Guhr, Axel Müller-Groeling, and Hans A. Weidenmüller. "Random-Matrix Theories in Quantum Physics: Common Concepts". In: *Physics Reports* 299.4 (June 1998), pp. 189–425. ISSN: 0370-1573. DOI: 10.1016/S0370-1573(97) 00088-4. URL: https://www.sciencedirect.com/science/article/pii/S0370157397000884.

[Gup+23] Riddhi S. Gupta et al. "Encoding a magic state with beyond break-even fidelity". In: arXiv:2305.13581 (2023). DOI: https://doi.org/10.1038/s41586-023-06846-3.

- [HH22] Jeongwan Haah and Matthew B. Hastings. "Boundaries for the Honeycomb Code". In: Quantum 6 (Apr. 2022), p. 693. ISSN: 2521-327X. DOI: 10.22331/q-2022-04-21-693. URL: https://doi.org/10.22331/q-2022-04-21-693.
- [Ham50] Richard W. Hamming. "Error Detecting and Error Correcting Codes". In: *The Bell System Technical Journal* 29.2 (1950), pp. 147–160. DOI: DOI: 10.1002/j. 1538-7305.1950.tb00463.x.
- [Han+24] Connor T Hann et al. "Hybrid cat-transmon architecture for scalable, hardware-efficient quantum error correction". In: arXiv preprint arXiv:2410.23363 (2024).

 DOI: https://doi.org/10.48550/arXiv.2410.23363.
- [HK10] M Zahid Hasan and Charles L Kane. "Colloquium: topological insulators". In: Reviews of modern physics 82.4 (2010), pp. 3045-3067. DOI: https://doi.org/10.1103/RevModPhys.82.3045.
- [Has+21] Tomohiro Hashizume et al. "Deterministic fast scrambling with neutral atom arrays". In: *Physical Review Letters* 126.20 (2021), p. 200603. DOI: https://doi.org/10.1103/PhysRevLett.126.200603.
- [Haw74] S. W. Hawking. "Black Hole Explosions?" In: *Nature* 248.5443 (Mar. 1974), pp. 30–31. ISSN: 0028-0836, 1476-4687.
- [Haw80] S. W. Hawking. THE PATH INTEGRAL APPROACH TO QUANTUM GRAV-ITY. Cambridge University Press, 1980, pp. 746–789.
- [Haw71] Stephen W Hawking. "Gravitational radiation from colliding black holes". In: Physical Review Letters 26.21 (1971), p. 1344. DOI: https://doi.org/10.1103/ PhysRevLett.26.1344.

[Haw75] Stephen W Hawking. "Particle creation by black holes". In: Communications in mathematical physics 43.3 (1975), pp. 199–220. DOI: https://doi.org/10.1007/BF02345020.

- [Haw76a] Stephen W Hawking. "Black holes and thermodynamics". In: *Physical Review D* 13.2 (1976), p. 191. DOI: https://doi.org/10.1103/PhysRevD.13.191.
- [Haw76b] Stephen W Hawking. "Breakdown of predictability in gravitational collapse".
 In: Physical Review D 14.10 (1976), p. 2460. DOI: https://doi.org/10.1103/PhysRevD.14.2460.
- [Haw15] Stephen W Hawking. "The information paradox for black holes". In: arXiv preprint arXiv:1509.01147 (2015). DOI: https://doi.org/10.48550/arXiv. 1509.01147.
- [HP07] Patrick Hayden and John Preskill. "Black holes as mirrors: quantum information in random subsystems". In: Journal of high energy physics 2007.09 (2007), p. 120.

 DOI: https://doi.org/10.1088/1126-6708/2007/09/120.
- [HB21] Oscar Higgott and Nikolas P. Breuckmann. "Subsystem Codes with High Thresholds by Gauge Fixing and Reduced Qubit Overhead". In: *Phys. Rev. X* 11 (3 Aug. 2021), p. 031039. DOI: 10.1103/PhysRevX.11.031039. URL: https://link.aps.org/doi/10.1103/PhysRevX.11.031039.
- [HG23] Oscar Higgott and Craig Gidney. "Sparse blossom: correcting a million errors per core second with minimum-weight matching". In: arXiv preprint arXiv:2303.15933 (2023). DOI: https://doi.org/10.48550/arXiv.2303.15933.
- [Hig+23] Oscar Higgott et al. "Improved decoding of circuit noise and fragile boundaries of tailored surface codes". In: *Physical Review X* 13.3 (2023), p. 031007. DOI: https://doi.org/10.48550/arXiv.2203.04948.
- [HPP01] Andreas Honecker, Marco Picco, and Pierre Pujol. "Universality class of the Nishimori point in the 2D±J random-bond Ising model". In: *Physical review*

- letters 87.4 (2001), p. 047201. DOI: https://doi.org/10.1103/PhysRevLett. 87.047201.
- [Hor+07] Layla Hormozi et al. "Topological quantum compiling". In: *Physical Review B—Condensed Matter and Materials Physics* 75.16 (2007), p. 165310. DOI: https://doi.org/10.1103/PhysRevB.75.165310.
- [Hor22] Matthew D Horner. "Emergent Spacetime in Quantum Lattice Models". In: arXiv preprint arXiv:2212.12548 (2022).
- [HHP23] Matthew D Horner, Andrew Hallam, and Jiannis K Pachos. "Chiral Spin-Chain Interfaces Exhibiting Event-Horizon Physics". In: *Physical Review Letters* 130.1 (2023), p. 016701. DOI: https://doi.org/10.1103/PhysRevLett.130.016701.
- [HFP20] Matthew D. Horner, Ashk Farjami, and Jiannis K. Pachos. "Equivalence between vortices, twists, and chiral gauge fields in the Kitaev honeycomb lattice model".
 In: Phys. Rev. B 102 (12 Sept. 2020), p. 125152. DOI: 10.1103/PhysRevB.102. 125152. URL: https://link.aps.org/doi/10.1103/PhysRevB.102.125152.
- [HTK12] Andrew A Houck, Hakan E Türeci, and Jens Koch. "On-chip quantum simulation with superconducting circuits". In: *Nature Physics* 8.4 (2012), pp. 292–299. DOI: https://doi.org/10.1038/nphys2251.
- [HV12] Mark Howard and Jiri Vala. "Qudit versions of the qubit π/8 gate". In: Physical Review A 86.2 (Aug. 2012). ISSN: 1094-1622. DOI: 10.1103/physreva.86.
 022316. URL: http://dx.doi.org/10.1103/PhysRevA.86.022316.
- [How+14] Mark Howard et al. "Contextuality supplies the "magic" for quantum computation". In: Nature 510.7505 (June 2014), pp. 351-355. ISSN: 1476-4687. DOI: 10.1038/nature13460. URL: http://dx.doi.org/10.1038/nature13460.
- [Hua+22] Eric Huang et al. Tailoring three-dimensional topological codes for biased noise. 2022. arXiv: 2211.02116 [quant-ph].

[HNB20] Shilin Huang, Michael Newman, and Kenneth R. Brown. "Fault-tolerant weighted union-find decoding on the toric code". In: *Phys. Rev. A* 102 (1 July 2020), p. 012419. DOI: 10.1103/PhysRevA.102.012419. URL: https://link.aps.org/doi/10.1103/PhysRevA.102.012419.

- [Hud+20] Ana Hudomal et al. "Quantum Scars of Bosons with Correlated Hopping". In: Communications Physics 3.1 (June 2020), pp. 1–12. ISSN: 2399-3650. DOI: 10.1038/s42005-020-0364-9.
- [HL14] Adrian Hutter and Daniel Loss. "Breakdown of surface-code error correction due to coupling to a bosonic bath". In: *Phys. Rev. A* 89 (4 Apr. 2014), p. 042334. DOI: 10.1103/PhysRevA.89.042334. URL: https://link.aps.org/doi/10.1103/PhysRevA.89.042334.
- [HL16] Adrian Hutter and Daniel Loss. "Quantum computing with parafermions". In: Physical Review B 93.12 (Mar. 2016). ISSN: 2469-9969. DOI: 10.1103/physrevb. 93.125105. URL: http://dx.doi.org/10.1103/PhysRevB.93.125105.
- [HWL14] Adrian Hutter, James R Wootton, and Daniel Loss. "Efficient Markov chain Monte Carlo algorithm for the surface code". In: *Physical Review A* 89.2 (2014), p. 022326. DOI: https://doi.org/10.1103/PhysRevA.89.022326.
- [Iqb+24] Mohsin Iqbal et al. "Non-Abelian topological order and anyons on a trapped-ion processor". In: *Nature* 626.7999 (2024), pp. 505–511. DOI: https://doi.org/10.1038/s41586-023-06934-4.
- [Isl+15] Rajibul Islam et al. "Measuring Entanglement Entropy in a Quantum Many-Body System". In: Nature 528.7580 (Dec. 2015), pp. 77–83. ISSN: 1476-4687.
 DOI: 10.1038/nature15750. (Visited on 11/18/2023).
- [Iva01] D. A. Ivanov. "Non-Abelian Statistics of Half-Quantum Vortices in p-Wave Superconductors". In: Phys. Rev. Lett. 86 (2 Jan. 2001), pp. 268-271. DOI: 10. 1103/PhysRevLett.86.268. URL: https://link.aps.org/doi/10.1103/PhysRevLett.86.268.

[Jac+22] Maxime Jacquet et al. "Analogue quantum simulation of the Hawking effect in a polariton superfluid". In: *The European Physical Journal D* 76.8 (2022), p. 152. DOI: https://doi.org/10.1140/epjd/s10053-022-00477-5.

- [JWK20] Maxime J Jacquet, Silke Weinfurtner, and Friedrich König. "The next generation of analogue gravity experiments". In: *Philosophical Transactions of the Royal Society A* 378.2177 (2020), p. 20190239. DOI: https://doi.org/10.1098/rsta. 2019.0239.
- [Jac+20] MJ Jacquet et al. "Polariton fluids for analogue gravity physics". In: *Philosophical Transactions of the Royal Society A* 378.2177 (2020), p. 20190225. DOI: https://doi.org/10.1098/rsta.2019.0225.
- [Jaf+22] Daniel Jafferis et al. "Traversable wormhole dynamics on a quantum processor". In: *Nature* 612.7938 (2022), pp. 51–55. DOI: https://doi.org/10.1038/s41586-022-05424-3.
- [JP20] Akalank Jain and Shiroman Prakash. "Qutrit and ququint magic states". In: Physical Review A 102.4 (Oct. 2020). ISSN: 2469-9934. DOI: 10.1103/physreva. 102.042409. URL: http://dx.doi.org/10.1103/PhysRevA.102.042409.
- [Jak+98] Dieter Jaksch et al. "Cold bosonic atoms in optical lattices". In: *Physical Review Letters* 81.15 (1998), p. 3108. DOI: https://doi.org/10.1103/PhysRevLett. 81.3108.
- [Jim89] Michio Jimbo. "Introduction to the Yang-Baxter equation". In: *International Journal of Modern Physics A* 4.15 (1989), pp. 3759–3777.
- [JW28] P. Jordan and E. Wigner. "Über das Paulische Äquivalenzverbot". In: Zeitschrift für Physik 47 (1928), pp. 631–651. DOI: https://doi.org/10.1007/BF01331938.
- [Jor+24] Stephen P Jordan et al. "Optimization by decoded quantum interferometry". In: arXiv preprint arXiv:2408.08292 (2024). DOI: https://doi.org/10.48550/ arXiv.2408.08292.

[KML23] Marcin Kalinowski, Nishad Maskara, and Mikhail D Lukin. "Non-Abelian Floquet spin liquids in a digital Rydberg simulator". In: Physical Review X 13.3 (2023), p. 031008. DOI: https://doi.org/10.1103/PhysRevX.13.031008.

- [Kar+24] Amir H. Karamlou et al. "Probing entanglement in a 2D hard-core Bose-Hubbard lattice". In: Nature 2024 629:8012 629 (8012 Apr. 2024), pp. 561-566. ISSN: 1476-4687. DOI: 10.1038/s41586-024-07325-z. URL: https://www.nature.com/articles/s41586-024-07325-z.
- [KNG06] M. I. Katsnelson, K. S. Novoselov, and A. K. Geim. "Chiral tunneling and the Klein paradox in graphene". In: Nature Physics 2 (2006), pp. 620–625. DOI: https://doi.org/10.1038/nphys384.
- [KBM09] Helmut G Katzgraber, Héctor Bombín, and Martin A Martin-Delgado. "Error threshold for color codes and random three-body Ising models". In: Physical review letters 103.9 (2009), p. 090501. DOI: https://doi.org/10.1103/PhysRevLett.103.090501.
- [Kat+10] Helmut G Katzgraber et al. "Topological color codes on Union Jack lattices: a stable implementation of the whole Clifford group". In: *Physical Review A—Atomic, Molecular, and Optical Physics* 81.1 (2010), p. 012319. DOI: https://doi.org/10.1103/PhysRevA.81.012319.
- [Kau90] Louis H Kauffman. "An invariant of regular isotopy". In: Transactions of the American Mathematical Society 318.2 (1990), pp. 417–471. DOI: https://doi. org/10.2307/2001315.
- [KB93] Louis H Kauffman and Randy A Baadhio. Quantum topology. Vol. 3. World Scientific, 1993.
- [Kau+16] Adam M. Kaufman et al. "Quantum Thermalization through Entanglement in an Isolated Many-Body System". In: Science 353.6301 (Aug. 2016), pp. 794–800. DOI: 10.1126/science.aaf6725.

[KSV09] G. Kells, J. K. Slingerland, and J. Vala. "Description of Kitaev's honeycomb model with toric-code stabilizers". In: *Physical Review B* 80.12 (Sept. 2009). ISSN: 1550-235X. DOI: 10.1103/physrevb.80.125415. URL: http://dx.doi.org/10.1103/PhysRevB.80.125415.

- [Kes+22] Markus S. Kesselring et al. "Anyon condensation and the color code". In: arXiv:2212.00042 (2022). DOI: https://doi.org/10.1103/PRXQuantum.5.010342.
- [KTH14] Mayukh Nilay Khan, Jeffrey CY Teo, and Taylor L Hughes. "Anyonic symmetries and topological defects in abelian topological phases: An application to the ade classification". In: *Physical Review B* 90.23 (2014), p. 235149. DOI: https://doi.org/10.1103/PhysRevB.90.235149.
- [Kit15] A Kitaev. A simple model of quantum holography, Talks at KITP, April 7 and May 27. 2015.
- [Kit97] A Yu Kitaev. "Quantum computations: algorithms and error correction". In: Russian Mathematical Surveys 52.6 (1997), p. 1191. DOI: doi.org/10.1070/ RM1997v052n06ABEH002155.
- [Kit01] A Yu Kitaev. "Unpaired Majorana fermions in quantum wires". In: Physics-Uspekhi 44.10S (Oct. 2001), pp. 131–136. ISSN: 1468-4780. DOI: 10.1070/1063-7869/44/10s/s29. URL: http://dx.doi.org/10.1070/1063-7869/44/10S/S29.
- [Kit03a] A Yu Kitaev. "Fault-tolerant quantum computation by anyons". In: Annals of physics 303.1 (2003), pp. 2–30. DOI: https://doi.org/10.1016/S0003-4916%2802%2900018-0.
- [Kit03b] A.Yu. Kitaev. "Fault-tolerant quantum computation by anyons". In: Annals of Physics 303.1 (Jan. 2003), pp. 2–30. ISSN: 0003-4916. DOI: 10.1016/s0003-4916(02)00018-0. URL: http://dx.doi.org/10.1016/S0003-4916(02) 00018-0.

[Kit95] Alexei Kitaev. "Quantum measurements and the Abelian stabilizer problem". In: arXiv:quant-ph/9511026 (1995). DOI: https://doi.org/10.48550/arXiv.quant-ph/9511026.

- [Kit06] Alexei Kitaev. "Anyons in an exactly solved model and beyond". In: Annals of Physics 321.1 (Jan. 2006), pp. 2-111. ISSN: 0003-4916. DOI: 10.1016/j.aop. 2005.10.005. URL: http://dx.doi.org/10.1016/j.aop.2005.10.005.
- [Kle03] Étienne Klein. Les atomes de l'Univers. Éditions Flammarion, 2003.
- [KMM12] Vadym Kliuchnikov, Dmitri Maslov, and Michele Mosca. "Fast and efficient exact synthesis of single qubit unitaries generated by Clifford and T gates". In: arXiv preprint arXiv:1206.5236 (2012). DOI: https://doi.org/10.48550/arXiv. 1206.5236.
- [Kni05] E. Knill. "Quantum computing with realistically noisy devices". In: Nature 434.7029 (Mar. 2005), pp. 39–44. ISSN: 1476-4687. DOI: 10.1038/nature03350. URL: http://dx.doi.org/10.1038/nature03350.
- [KL97] Emanuel Knill and Raymond Laflamme. "Theory of quantum error-correcting codes". In: *Physical Review A* 55.2 (1997), p. 900. DOI: https://doi.org/10.1103/PhysRevA.55.900.
- [KLZ96] Emanuel Knill, Raymond Laflamme, and Wojciech Zurek. "Threshold accuracy for quantum computation". In: arXiv preprint quant-ph/9610011 (1996). DOI: https://doi.org/10.48550/arXiv.quant-ph/9610011.
- [KLZ98a] Emanuel Knill, Raymond Laflamme, and Wojciech H Zurek. "Resilient quantum computation: error models and thresholds". In: Proceedings of the Royal Society of London. Series A: Mathematical, Physical and Engineering Sciences 454.1969 (1998), pp. 365–384. DOI: https://doi.org/10.1098/rspa.1998.0166.
- [KLZ98b] Emanuel Knill, Raymond Laflamme, and Wojciech H. Zurek. "Resilient Quantum Computation". In: Science 279.5349 (1998), pp. 342–345. ISSN: 0036-8075. DOI:

10.1126/science.279.5349.342. eprint: https://science.sciencemag.org/content/279/5349/342.full.pdf. URL: https://science.sciencemag.org/content/279/5349/342.

- [Kol09] Vladimir Kolmogorov. "Blossom V: a new implementation of a minimum cost perfect matching algorithm". In: *Mathematical Programming Computation* 1 (2009), pp. 43–67. DOI: https://doi.org/10.1007/s12532-009-0002-8.
- [Kon+15] S. S. Kondov et al. "Disorder-Induced Localization in a Strongly Correlated Atomic Hubbard Gas". In: *Physical Review Letters* 114.8 (Feb. 2015), p. 083002. DOI: 10.1103/PhysRevLett.114.083002.
- [Kri+22] Sebastian Krinner et al. "Realizing repeated quantum error correction in a distance-three surface code". In: *Nature* 605 (2022), pp. 669–674. DOI: https://doi.org/10.1038/s41586-022-04566-8. URL: https://doi.org/10.1038/s41586-022-04566-8.
- [KP20] Anirudh Krishna and David Poulin. "Topological wormholes: Nonlocal defects on the toric code". In: *Physical Review Research* 2.2 (May 2020). ISSN: 2643-1564. DOI: 10.1103/physrevresearch.2.023116. URL: http://dx.doi.org/10.1103/PhysRevResearch.2.023116.
- [KP21] Anirudh Krishna and David Poulin. "Fault-tolerant gates on hypergraph product codes". In: *Physical Review X* 11.1 (2021), p. 011023. DOI: https://doi.org/10.1103/PhysRevX.11.011023.
- [KB15] Aleksander Kubica and Michael E. Beverland. "Universal transversal gates with color codes: A simplified approach". In: *Phys. Rev. A* 91 (3 Mar. 2015), p. 032330.

 DOI: https://doi.org/10.1103/PhysRevA.91.032330. URL: https://link.aps.org/doi/10.1103/PhysRevA.91.032330.
- [KD23] Aleksander Kubica and Nicolas Delfosse. "https://doi.org/10.22331/q-2023-02-21-929". In: Quantum 7 (2023), p. 929. DOI: https://doi.org/10.22331/q-2023-02-21-929.

[KYP15] Aleksander Kubica, Beni Yoshida, and Fernando Pastawski. "Unfolding the color code". In: New Journal of Physics 17.8 (Aug. 2015), p. 083026. DOI: 10.1088/1367-2630/17/8/083026. URL: https://doi.org/10.10882F1367-26302F172F82F083026.

- [Lah+10] Oren Lahav et al. "Realization of a sonic black hole analog in a Bose-Einstein condensate". In: *Physical review letters* 105.24 (2010), p. 240401. DOI: https://doi.org/10.1103/PhysRevLett.105.240401.
- [Lah+08] Ville Lahtinen et al. "Spectrum of the non-abelian phase in Kitaev's honeycomb lattice model". In: Annals of Physics 323.9 (2008), pp. 2286–2310. DOI: https://doi.org/10.1016/j.aop.2007.12.009.
- [Lan+37] Lev Davidovich Landau et al. "On the theory of phase transitions". In: Zh. eksp. teor. Fiz 7.19-32 (1937), p. 926. DOI: https://doi.org/10.1016/B978-0-08-010586-4.50034-1.
- [Lan+22] Christopher M Langlett et al. "Rainbow scars: From area to volume law". In: Physical Review B 105.6 (2022), p. L060301. DOI: https://doi.org/10.1103/ PhysRevB.105.L060301.
- [Lap+20] Bastien Lapierre et al. "Emergent Black Hole Dynamics in Critical Floquet Systems". In: *Physical Review Research* 2.2 (Apr. 2020), p. 023085. ISSN: 2643-1564.

 DOI: 10.1103/PhysRevResearch.2.023085. (Visited on 02/09/2024).
- [LLK19] Katharina Laubscher, Daniel Loss, and Jelena Klinovaja. "Fractional topological superconductivity and parafermion corner states". In: *Physical Review Research* 1.3 (2019), p. 032017. DOI: https://doi.org/10.1103/PhysRevResearch.1. 032017.
- [Lev+18] Harry Levine et al. "High-fidelity control and entanglement of Rydberg-atom qubits". In: *Physical review letters* 121.12 (2018), p. 123603.
- [Lev+19] Harry Levine et al. "Parallel implementation of high-fidelity multiqubit gates with neutral atoms". In: *Physical review letters* 123.17 (2019), p. 170503.

[LTT20] Stefano Liberati, Giovanni Tricella, and Andrea Trombettoni. "Back-reaction in canonical analogue black holes". In: *Applied Sciences* 10.24 (2020), p. 8868. DOI: https://doi.org/10.3390/app10248868.

- [LSM61] Elliott Lieb, Theodore Schultz, and Daniel Mattis. "Two soluble models of an antiferromagnetic chain". In: *Annals of Physics* 16.3 (1961), pp. 407–466. DOI: https://doi.org/10.1016/0003-4916(61)90115-4.
- [Lie+20] Vincent Lienhard et al. "Realization of a Density-Dependent Peierls Phase in a Synthetic, Spin-Orbit Coupled Rydberg System". In: *Phys. Rev. X* 10 (2 May 2020), p. 021031. DOI: 10.1103/PhysRevX.10.021031. URL: https://link.aps.org/doi/10.1103/PhysRevX.10.021031.
- [Lin+23] Sophia Fuhui Lin et al. "Empirical overhead of the adapted surface code on defective qubit arrays". In: arXiv:2305.00138 (2023).
- [Lin+12] Netanel H. Lindner et al. "Fractionalizing Majorana Fermions: Non-Abelian Statistics on the Edges of Abelian Quantum Hall States". In: *Physical Review X* 2.4 (Oct. 2012). DOI: 10.1103/physrevx.2.041002. URL: https://doi.org/10.1103%2Fphysrevx.2.041002.
- [LO18] Daniel Litinski and Felix von Oppen. "Quantum computing with Majorana fermion codes". In: *Physical Review B* 97.20 (May 2018). ISSN: 2469-9969. DOI: 10.1103/physrevb.97.205404. URL: http://dx.doi.org/10.1103/PhysRevB. 97.205404.
- [Llo96] Seth Lloyd. "Universal quantum simulators". In: *Science* 273.5278 (1996), pp. 1073–1078.
- [LSD10] Roman M Lutchyn, Jay D Sau, and S Das Sarma. "Majorana Fermions and a Topological Phase Transition in Semiconductor-Superconductor Heterostructures". In: *Physical review letters* 105.7 (2010), p. 077001. DOI: https://doi.org/10.1103/PhysRevLett.105.077001.

[MS77] Florence Jessie MacWilliams and Neil James Alexander Sloane. The Theory of Error-Correcting Codes. Elsevier, 1977. ISBN: 978-0-444-85010-2. URL: https://books.google.com/books?id=nv6WCJgcjxcC.

- [Mad+20] Ivaylo S Madjarov et al. "High-fidelity entanglement and detection of alkaline-earth Rydberg atoms". In: *Nature Physics* 16.8 (2020), pp. 857–861.
- [MBV24] Daan Maertens, Nick Bultinck, and Karel Van Acoleyen. "Hawking radiation on the lattice from Floquet and local Hamiltonian quench dynamics". In: *Physical Review B* 109.1 (2024), p. 014309. DOI: https://doi.org/10.1103/PhysRevB. 109.014309.
- [MWS20] Iman Mahyaeh, Jurriaan Wouters, and Dirk Schuricht. "Phase diagram of the Z₃-Fock parafermion chain with pair hopping". In: SciPost Physics Core 3.2 (Nov. 2020). ISSN: 2666-9366. DOI: 10.21468/scipostphyscore.3.2.011. URL: http://dx.doi.org/10.21468/SciPostPhysCore.3.2.011.
- [Mal99] Juan Maldacena. "The large-N limit of superconformal field theories and supergravity". In: *International journal of theoretical physics* 38.4 (1999), pp. 1113–1133. DOI: https://doi.org/10.1023/A:1026654312961.
- [MSS16] Juan Maldacena, Stephen H. Shenker, and Douglas Stanford. "A Bound on Chaos". In: Journal of High Energy Physics 2016.8 (Aug. 2016), p. 106. ISSN: 1029-8479. DOI: 10.1007/JHEP08(2016)106. URL: https://doi.org/10.1007/ JHEP08(2016)106.
- [MS16] Juan Maldacena and Douglas Stanford. "Remarks on the sachdev-ye-kitaev model".
 In: Physical Review D 94.10 (2016), p. 106002. DOI: https://doi.org/10.1103/
 PhysRevD.94.106002.
- [Mal+19] Arindam Mallick et al. "Simulating Dirac Hamiltonian in curved space-time by split-step quantum walk". In: Journal of Physics Communications 3.1 (2019), p. 015012. DOI: 10.1088/2399-6528/aafe2f.

[Mar+23] Nicolas Maring et al. A general-purpose single-photon-based quantum computing platform. 2023. DOI: https://doi.org/10.48550/arXiv.2306.00874. arXiv: 2306.00874 [quant-ph]. URL: https://arxiv.org/abs/2306.00874.

- [MA08] Ken Matsumoto and Kazuyuki Amano. "Representation of quantum circuits with Clifford and $\pi/8$ gates". In: $arXiv\ preprint\ arXiv:0806.3834\ (2008)$. DOI: https://doi.org/10.48550/arXiv.0806.3834.
- [Mer+22] Lotte Mertens et al. "Thermalization by a synthetic horizon". In: *Phys. Rev. Res.* 4 (4 Nov. 2022), p. 043084. DOI: 10.1103/PhysRevResearch.4.043084. URL: https://link.aps.org/doi/10.1103/PhysRevResearch.4.043084.
- [MC02] F Merz and JT Chalker. "Two-dimensional random-bond Ising model, free fermions, and the network model". In: *Physical Review B* 65.5 (2002), p. 054425. DOI: https://doi.org/10.1103/PhysRevB.65.054425.
- [MP14] Florent Michel and Renaud Parentani. "Probing the thermal character of analogue Hawking radiation for shallow water waves?" In: *Physical Review D* 90.4 (2014), p. 044033. DOI: https://doi.org/10.1103/PhysRevD.90.044033.
- [MWB23] Jonathan F. San Miguel, Dominic J. Williamson, and Benjamin J. Brown. "A cellular automaton decoder for a noise-bias tailored color code". In: Quantum 7 (Mar. 2023), p. 940. ISSN: 2521-327X. DOI: 10.22331/q-2023-03-09-940. URL: https://doi.org/10.22331/q-2023-03-09-940.
- [MR91] Gregory Moore and Nicholas Read. "Nonabelions in the fractional quantum hall effect". In: Nuclear Physics B 360.2 (1991), pp. 362-396. ISSN: 0550-3213. DOI: https://doi.org/10.1016/0550-3213(91)90407-0. URL: https://www.sciencedirect.com/science/article/pii/0550321391904070.
- [Mor+17] Niall Moran et al. "Parafermionic clock models and quantum resonance". In: *Physical Review B* 95.23 (2017), p. 235127.

[MW21] M Morgado and S Whitlock. "Quantum simulation and computing with Rydberg-interacting qubits". In: AVS Quantum Science 3.2 (2021), p. 023501.

- [Mor+22] Corentin Morice et al. "Quantum dynamics in 1D lattice models with synthetic horizons". In: SciPost Physics Core 5.3 (Aug. 2022). DOI: 10.21468/scipostphyscore.5.3.042. URL: https://doi.org/10.21468%2Fscipostphyscore.5.3.042.
- [Mos+23] S. A. Moses et al. "A Race-Track Trapped-Ion Quantum Processor". In: Physical Review X 13.4 (Dec. 2023). ISSN: 2160-3308. DOI: https://doi.org/10.1103/ PhysRevX.13.041052. URL: http://dx.doi.org/10.1103/PhysRevX.13. 041052.
- [Muñ+19] Juan Ramón Muñoz de Nova et al. "Observation of thermal Hawking radiation and its temperature in an analogue black hole". In: *Nature* 569.7758 (2019), pp. 688-691. DOI: https://doi.org/10.1038/s41586-019-1241-0.
- [NRA10] G. Nebe, Eric M. Rains, and Sloane N J A. Self-dual codes and invariant theory. Springer, 2010.
- [Ngu+15] H. S. Nguyen et al. "Acoustic Black Hole in a Stationary Hydrodynamic Flow of Microcavity Polaritons". In: Phys. Rev. Lett. 114 (3 Jan. 2015), p. 036402. DOI: 10.1103/PhysRevLett.114.036402. URL: https://link.aps.org/doi/10. 1103/PhysRevLett.114.036402.
- [NB19] Naomi H. Nickerson and Benjamin J. Brown. "Analysing correlated noise on the surface code using adaptive decoding algorithms". In: Quantum 3 (Apr. 2019), p. 131. ISSN: 2521-327X. DOI: https://doi.org/10.22331/q-2019-04-08-131. URL: https://doi.org/10.22331/q-2019-04-08-131.
- [NC10] Michael A Nielsen and Isaac L Chuang. Quantum computation and quantum information. Cambridge university press, 2010.

[NB21] Georgia M Nixon and Benjamin J Brown. "Correcting spanning errors with a fractal code". In: *IEEE Transactions on Information Theory* 67.7 (2021), pp. 4504–4516. DOI: https://doi.org/10.1109/TIT.2021.3068359.

- [NUS23] Georgia M. Nixon, F. Nur Unal, and Ulrich Schneider. "Individually Tunable Tunnelling Coefficients in Optical Lattices Using Local Periodic Driving". In: arXiv preprint (Sept. 2023). DOI: 10.48550/arXiv:2309.12124.
- [23] "Non-Abelian braiding of graph vertices in a superconducting processor". In: Nature 618.7964 (2023), pp. 264–269. DOI: https://doi.org/10.1038/s41586-023-05954-4.
- [NO09] Zohar Nussinov and Gerardo Ortiz. "A symmetry principle for topological quantum order". In: Annals of Physics 324.5 (2009), pp. 977–1057. DOI: https://doi.org/10.1016/j.aop.2008.11.002.
- [OH07] Vadim Oganesyan and David A Huse. "Localization of interacting fermions at high temperature". In: *Physical Review B—Condensed Matter and Materials Physics* 75.15 (2007), p. 155111. DOI: https://doi.org/10.1103/PhysRevB. 75.155111.
- [Pac07] Jiannis K Pachos. "The wavefunction of an anyon". In: *Annals of Physics* 322.6 (2007), pp. 1254–1264. DOI: https://doi.org/10.1016/j.aop.2006.05.007.
- [Pac12] Jiannis K. Pachos. Introduction to Topological Quantum Computation. Cambridge University Press, 2012. DOI: 10.1017/CB09780511792908.
- [Pae+23] Adam Paetznick et al. "Performance of Planar Floquet Codes with Majorana-Based Qubits". In: *PRX Quantum* 4 (1 Jan. 2023), p. 010310. DOI: 10.1103/PRXQuantum.4.010310. URL: https://link.aps.org/doi/10.1103/PRXQuantum.4.010310.

[PK21] Pavel Panteleev and Gleb Kalachev. "Degenerate quantum LDPC codes with good finite length performance". In: Quantum 5 (2021), p. 585. DOI: https://doi.org/10.22331/q-2021-11-22-585.

- [PW00] Maulik K Parikh and Frank Wilczek. "Hawking radiation as tunneling". In: *Physical review letters* 85.24 (2000), p. 5042. DOI: https://doi.org/10.1103/PhysRevLett.85.5042.
- [PY15] Fernando Pastawski and Beni Yoshida. "Fault-tolerant logical gates in quantum error-correcting codes". In: *Physical Review A* 91.1 (2015), p. 012305. DOI: https://doi.org/10.1103/PhysRevA.91.012305.
- [PF71] Roger Penrose and Robert M Floyd. "Extraction of rotational energy from a black hole". In: Nature Physical Science 229.6 (1971), pp. 177–179. DOI: https://doi.org/10.1038/physci229177a0.
- [Ple68] Vera Pless. "On the uniqueness of the Golay codes". In: Journal of Combinatorial Theory 5.3 (1968), pp. 215-228. ISSN: 0021-9800. DOI: https://doi.org/10.1016/S0021-9800(68)80067-5. URL: https://www.sciencedirect.com/science/article/pii/S0021980068800675.
- [PC04] Diego Porras and J Ignacio Cirac. "Effective quantum spin systems with trapped ions". In: *Physical review letters* 92.20 (2004), p. 207901. DOI: https://doi.org/10.1103/PhysRevLett.92.207901.
- [Pra20] Shiroman Prakash. "Magic state distillation with the ternary Golay code". In: Proceedings of the Royal Society A: Mathematical, Physical and Engineering Sciences 476.2241 (Sept. 2020), p. 20200187. ISSN: 1471-2946. DOI: 10.1098/rspa. 2020.0187. URL: http://dx.doi.org/10.1098/rspa.2020.0187.
- [Pre+15] Philipp M. Preiss et al. "Strongly Correlated Quantum Walks in Optical Lattices". In: *Science* 347.6227 (Mar. 2015), pp. 1229–1233. DOI: 10.1126/science. 1260364. (Visited on 10/06/2023).

[Pre15] John Preskill. "Lecture notes for ph219/cs219: Quantum information". In: Accesible via http://www. theory. caltech. edu/people/preskill/ph229 1997 (2015).

- [RK23a] Tibor Rakovszky and Vedika Khemani. "The Physics of (good) LDPC Codes I. Gauging and dualities". In: arXiv preprint arXiv:2310.16032 (2023). DOI: https://doi.org/10.48550/arXiv.2402.16831.
- [RK23b] Tibor Rakovszky and Vedika Khemani. "The Physics of (good) LDPC Codes I. Gauging and dualities". In: arXiv preprint arXiv:2310.16032 (2023). DOI: https://doi.org/10.48550/arXiv.2310.16032.
- [Ran+17] Mukund Rangamani et al. *Holographic entanglement entropy*. Springer, 2017. DOI: https://doi.org/10.1007/978-3-319-52573-0.
- [RHG07] R Raussendorf, J Harrington, and K Goyal. "Topological fault-tolerance in cluster state quantum computation". In: New Journal of Physics 9.6 (June 2007), pp. 199–199. ISSN: 1367-2630. DOI: 10.1088/1367-2630/9/6/199. URL: http://dx.doi.org/10.1088/1367-2630/9/6/199.
- [RBH05] Robert Raussendorf, Sergey Bravyi, and Jim Harrington. "Long-range quantum entanglement in noisy cluster states". In: *Phys. Rev. A* 71 (6 June 2005), p. 062313. DOI: 10.1103/PhysRevA.71.062313. URL: https://link.aps.org/doi/10.1103/PhysRevA.71.062313.
- [RH07] Robert Raussendorf and Jim Harrington. "Fault-Tolerant Quantum Computation with High Threshold in Two Dimensions". In: *Phys. Rev. Lett.* 98 (19 May 2007), p. 190504. DOI: https://doi.org/10.1103/PhysRevLett.98.190504. URL: https://link.aps.org/doi/10.1103/PhysRevLett.98.190504.
- [RR99] N. Read and E. Rezayi. "Beyond paired quantum Hall states: Parafermions and incompressible states in the first excited Landau level". In: *Phys. Rev. B* 59 (12 Mar. 1999), pp. 8084–8092. DOI: 10.1103/PhysRevB.59.8084. URL: https://link.aps.org/doi/10.1103/PhysRevB.59.8084.

[Rei+17] Martin Reitter et al. "Interaction Dependent Heating and Atom Loss in a Periodically Driven Optical Lattice". In: Physical Review Letters 119.20 (Nov. 2017), p. 200402. DOI: 10.1103/PhysRevLett.119.200402. (Visited on 10/09/2023).

- [RBF22] Caio C Holanda Ribeiro, Sang-Shin Baak, and Uwe R Fischer. "Existence of steady-state black hole analogs in finite quasi-one-dimensional Bose-Einstein condensates". In: *Physical Review D* 105.12 (2022), p. 124066. DOI: https://doi.org/10.1103/PhysRevD.105.124066.
- [RDO08] Marcos Rigol, Vanja Dunjko, and Maxim Olshanii. "Thermalization and its mechanism for generic isolated quantum systems". In: Nature 452.7189 (2008), pp. 854–858. DOI: https://doi.org/10.1038/nature06838.
- [Ris+19] Matthew Rispoli et al. "Quantum Critical Behaviour at the Many-Body Localization Transition". In: *Nature* 573.7774 (Sept. 2019), pp. 385–389. ISSN: 1476-4687. DOI: 10.1038/s41586-019-1527-2. (Visited on 11/18/2023).
- [Rod+24] Pedro Sales Rodriguez et al. "Experimental demonstration of logical magic state distillation". In: arXiv preprint arXiv:2412.15165 (2024). DOI: https://doi.org/10.48550/arXiv.2412.15165.
- [Rof+20] Joschka Roffe et al. "Decoding across the quantum low-density parity-check code landscape". In: *Physical Review Research* 2.4 (Dec. 2020). ISSN: 2643-1564. DOI: https://doi.org/10.1103/PhysRevResearch.2.043423. URL: http://dx.doi.org/10.1103/PhysRevResearch.2.043423.
- [Rof+23] Joschka Roffe et al. "Bias-tailored quantum LDPC codes". In: Quantum 7 (2023),
 p. 1005. DOI: https://doi.org/10.22331/q-2023-05-15-1005.
- [Ron+13] J. P. Ronzheimer et al. "Expansion Dynamics of Interacting Bosons in Homogeneous Lattices in One and Two Dimensions". In: Phys. Rev. Lett. 110 (20 May 2013), p. 205301. DOI: 10.1103/PhysRevLett.110.205301. URL: https://link.aps.org/doi/10.1103/PhysRevLett.110.205301.

[Rya+21] C. Ryan-Anderson et al. "Realization of Real-Time Fault-Tolerant Quantum Error Correction". In: *Phys. Rev. X* 11 (4 Dec. 2021), p. 041058. DOI: https://doi.org/10.1103/PhysRevX.11.041058. URL: https://link.aps.org/doi/10.1103/PhysRevX.11.041058.

- [RT06a] Shinsei Ryu and Tadashi Takayanagi. "Aspects of holographic entanglement entropy". In: Journal of High Energy Physics 2006.08 (2006), p. 045. DOI: https://doi.org/10.1088/1126-6708/2006/08/045.
- [RT06b] Shinsei Ryu and Tadashi Takayanagi. "Holographic derivation of entanglement entropy from the anti-de sitter space/conformal field theory correspondence". In: *Physical review letters* 96.18 (2006), p. 181602. DOI: https://doi.org/10.1103/PhysRevLett.96.181602.
- [Sab+22] Daniel Sabsovich et al. "Hawking fragmentation and Hawking attenuation in Weyl semimetals". In: *Physical Review Research* 4.1 (2022), p. 013055. DOI: https://doi.org/10.1103/PhysRevResearch.4.013055.
- [Sac23] Subir Sachdev. Quantum phases of matter. Cambridge University Press, 2023.

 DOI: https://doi.org/10.1017/9781009212717.
- [SY93] Subir Sachdev and Jinwu Ye. "Gapless spin-fluid ground state in a random quantum Heisenberg magnet". In: *Physical review letters* 70.21 (1993), p. 3339. DOI: https://doi.org/10.1103/PhysRevLett.70.3339.
- [SB22] Kaavya Sahay and Benjamin J Brown. "Decoder for the Triangular Color Code by Matching on a Möbius Strip". In: *PRX Quantum* 3.1 (2022), p. 010310. DOI: https://doi.org/10.1103/PRXQuantum.3.010310.
- [SFN15a] Sankar Das Sarma, Michael Freedman, and Chetan Nayak. "Majorana zero modes and topological quantum computation". In: npj Quantum Information 1.1 (2015), pp. 1–13. DOI: https://doi.org/10.1038/npjqi.2015.1.

[SFN15b] Sankar Das Sarma, Michael Freedman, and Chetan Nayak. "Majorana zero modes and topological quantum computation". In: npj Quantum Information 1.1 (Oct. 2015). ISSN: 2056-6387. DOI: 10.1038/npjqi.2015.1. URL: http://dx.doi.org/10.1038/npjqi.2015.1.

- [Saw+20] Rahul Sawant et al. "Ultracold polar molecules as qudits". In: New Journal of Physics 22.1 (Jan. 2020), p. 013027. ISSN: 1367-2630. DOI: 10.1088/1367-2630/ab60f4. URL: http://dx.doi.org/10.1088/1367-2630/ab60f4.
- [SK17] Adam Sawicki and Katarzyna Karnas. "Universality of Single-Qudit Gates". In:

 Annales Henri Poincaré 18.11 (Aug. 2017), pp. 3515–3552. ISSN: 1424-0661. DOI:

 10.1007/s00023-017-0604-z. URL: http://dx.doi.org/10.1007/s00023017-0604-z.
- [Sch+20a] Florian Schäfer et al. "Tools for Quantum Simulation with Ultracold Atoms in Optical Lattices". In: Nature Reviews Physics 2.8 (July 2020), pp. 411–425. ISSN: 2522-5820. DOI: 10.1038/s42254-020-0195-3. (Visited on 05/07/2023).
- [Sch+20b] Florian Schäfer et al. "Tools for quantum simulation with ultracold atoms in optical lattices". In: *Nature Reviews Physics* 2.8 (2020), pp. 411–425. DOI: https://doi.org/10.1038/s42254-020-0195-3.
- [Sch19] Wolfgang Scherer. Mathematics of quantum computing. Vol. 11. Springer, 2019.

 DOI: https://doi.org/10.1201/9781420035377.
- [SDV08] Kai Phillip Schmidt, Sébastien Dusuel, and Julien Vidal. "Emergent fermions and anyons in the Kitaev model". In: *Physical review letters* 100.5 (2008), p. 057208.

 DOI: https://doi.org/10.1103/PhysRevLett.100.057208.
- [Sch+12] Ulrich Schneider et al. "Fermionic transport and out-of-equilibrium dynamics in a homogeneous Hubbard model with ultracold atoms". In: *Nature Physics* 8 (3 Jan. 2012), pp. 213–218. ISSN: 1745-2473. DOI: 10.1038/nphys2205. URL: http://dx.doi.org/10.1038/nphys2205.

[Sch+15] Michael Schreiber et al. "Observation of Many-Body Localization of Interacting Fermions in a Quasirandom Optical Lattice". In: *Science* 349.6250 (Aug. 2015), pp. 842–845. DOI: 10.1126/science.aaa7432. (Visited on 11/18/2023).

- [SML64] Theodore D Schultz, Daniel C Mattis, and Elliott H Lieb. "Two-dimensional Ising model as a soluble problem of many fermions". In: Reviews of Modern Physics 36.3 (1964), p. 856. DOI: https://doi.org/10.1103/RevModPhys.36.856.
- [Sch16] Karl Schwarzschild. "Über das gravitationsfeld eines massenpunktes nach der einsteinschen theorie". In: Sitzungsberichte der königlich preussischen Akademie der Wissenschaften (1916), pp. 189–196.
- [SS08] Yasuhiro Sekino and L. Susskind. "Fast scramblers". In: Journal of High Energy Physics 2008.10 (Oct. 2008), p. 065. DOI: 10.1088/1126-6708/2008/10/065. URL: https://dx.doi.org/10.1088/1126-6708/2008/10/065.
- [Sha48] Claude Elwood Shannon. "A mathematical theory of communication". In: *The Bell system technical journal* 27.3 (1948), pp. 379–423. DOI: 10.1002/j.1538-7305.1948.tb01338.x.
- [She+21] Chong Sheng et al. "Simulating the escape of entangled photons from the event horizon of black holes in nonuniform optical lattices". In: *Physical Review A* 103.3 (2021), p. 033703. DOI: https://doi.org/10.1103/PhysRevA.103.033703.
- [SS14] Stephen H. Shenker and Douglas Stanford. "Black Holes and the Butterfly Effect". In: Journal of High Energy Physics 2014.3 (Mar. 2014), p. 67. ISSN: 1029-8479. DOI: 10.1007/JHEP03(2014)067. URL: https://doi.org/10.1007/JHEP03(2014)067.
- [She+10] Jacob F. Sherson et al. "Single-Atom-Resolved Fluorescence Imaging of an Atomic Mott Insulator". In: *Nature* 467.7311 (Sept. 2010), pp. 68–72. ISSN: 0028-0836, 1476-4687. DOI: 10.1038/nature09378. (Visited on 05/07/2023).

[Shi18] Xiao-Feng Shi. "Accurate quantum logic gates by spin echo in Rydberg atoms". In: *Physical Review Applied* 10.3 (2018), p. 034006.

- [Shi+23] Yun-Hao Shi et al. "Quantum simulation of Hawking radiation and curved spacetime with a superconducting on-chip black hole". In: *Nature Communications* 14.1 (2023), p. 3263. DOI: https://doi.org/10.6084/m9.figshare.22802981.
- [Shi11] Vasudha Shivamoggi. "Majorana fermions and Dirac edge states in topological phases". PhD thesis. University of California, Berkeley, 2011.
- [Sho95] Peter W Shor. "Scheme for reducing decoherence in quantum computer memory". In: *Physical review A* 52.4 (1995), R2493. DOI: https://doi.org/10.1103/PhysRevA.52.R2493.
- [Sho96] Peter W Shor. "Fault-tolerant quantum computation". In: Proceedings of 37th conference on foundations of computer science. IEEE. 1996, pp. 56-65. DOI: https://doi.org/10.48550/arXiv.quant-ph/9605011.
- [Sho97] Peter W. Shor. "Polynomial-Time Algorithms for Prime Factorization and Discrete Logarithms on a Quantum Computer". In: SIAM Journal on Computing 26.5 (Oct. 1997), pp. 1484–1509. ISSN: 1095-7111. DOI: 10.1137/s0097539795293172. URL: http://dx.doi.org/10.1137/S0097539795293172.
- [Sie+22] Adam Siegel et al. "Adaptive surface code for quantum error correction in the presence of temporary or permanent defects". In: arXiv:2211.08468 (2022). DOI: https://doi.org/10.22331/q-2023-07-25-1065.
- [SEG18] Kyrylo Snizhko, Reinhold Egger, and Yuval Gefen. "Measurement and control of a Coulomb-blockaded parafermion box". In: Physical Review B 97.8 (2018), p. 081405. DOI: https://doi.org/10.1103/PhysRevB.97.081405.
- [Sni+18] Kyrylo Snizhko et al. "Parafermionic generalization of the topological Kondo effect". In: *Physical Review B* 97.23 (2018), p. 235139. DOI: https://doi.org/10.1103/PhysRevB.97.235139.

[Spo+21] Nicholas L. R. Spong et al. "Collectively Encoded Rydberg Qubit". In: Phys. Rev. Lett. 127 (6 Aug. 2021), p. 063604. DOI: 10.1103/PhysRevLett.127.063604. URL: https://link.aps.org/doi/10.1103/PhysRevLett.127.063604.

- [Sre93] Mark Srednicki. "Entropy and area". In: Phys. Rev. Lett. 71 (5 Aug. 1993), pp. 666-669. DOI: 10.1103/PhysRevLett.71.666. URL: https://link.aps. org/doi/10.1103/PhysRevLett.71.666.
- [SFG22] Basudha Srivastava, Anton Frisk Kockum, and Mats Granath. "The XYZ² hexagonal stabilizer code". In: *Quantum* 6 (Apr. 2022), p. 698. ISSN: 2521-327X. DOI: https://doi.org/10.22331/q-2022-04-27-698. URL: https://doi.org/10.22331/q-2022-04-27-698.
- [SB10] Thomas M Stace and Sean D Barrett. "Error correction and degeneracy in surface codes suffering loss". In: *Physical Review A* 81.2 (2010), p. 022317. DOI: https://doi.org/10.1103/PhysRevA.81.022317.
- [Ste96a] Andrew Steane. "Multiple-particle interference and quantum error correction". In: Proceedings of the Royal Society of London. Series A: Mathematical, Physical and Engineering Sciences 452.1954 (1996), pp. 2551–2577. DOI: https://doi.org/10.1098/rspa.1996.0136.
- [Ste96b] Andrew M Steane. "Error correcting codes in quantum theory". In: *Physical Review Letters* 77.5 (1996), p. 793. DOI: https://doi.org/10.1103/PhysRevLett. 77.793.
- [Ste16] Jeff Steinhauer. "Observation of quantum Hawking radiation and its entanglement in an analogue black hole". In: *Nature Physics* 12.10 (2016), pp. 959–965. DOI: https://doi.org/10.1038/nphys3863.
- [SBB21] Armands Strikis, Simon C. Benjamin, and Benjamin J. Brown. Quantum computing is scalable on a planar array of qubits with fabrication defects. 2021. DOI: https://doi.org/10.48550/arXiv.2111.06432. URL: https://arxiv.org/abs/2111.06432.

[Str98] Andrew Strominger. "Black hole entropy from near-horizon microstates". In: Journal of High Energy Physics 1998.02 (May 1998), p. 009. DOI: 10.1088/ 1126-6708/1998/02/009. URL: https://dx.doi.org/10.1088/1126-6708/1998/02/009.

- [Sun+23] Neereja Sundaresan et al. "Demonstrating multi-round subsystem quantum error correction using matching and maximum likelihood decoders". In: *Nature Communications* 14 (2023), p. 2852. DOI: 10.1038/s41467-023-38247-5. URL: https://doi.org/10.1038/s41467-023-38247-5.
- [Swi+16] Brian Swingle et al. "Measuring the scrambling of quantum information". In: Physical Review A 94.4 (2016), p. 040302. DOI: https://doi.org/10.1103/ PhysRevA.94.040302.
- [Tah+22] Hossein Taheri et al. "All-optical dissipative discrete time crystals". In: Nature communications 13.1 (2022), p. 848. DOI: https://doi.org/10.1038/s41467-022-28462-x.
- [Tan81] R Tanner. "A recursive approach to low complexity codes". In: *IEEE Transactions on information theory* 27.5 (1981), pp. 533–547. DOI: 10.1109/TIT.1981. 1056404.
- [Teo16] Jeffrey C Y Teo. "Globally symmetric topological phase: from anyonic symmetry to twist defect". In: Journal of Physics: Condensed Matter 28.14 (Mar. 2016), p. 143001. ISSN: 1361-648X. DOI: 10.1088/0953-8984/28/14/143001. URL: http://dx.doi.org/10.1088/0953-8984/28/14/143001.
- [TRC14] Jeffrey CY Teo, Abhishek Roy, and Xiao Chen. "Unconventional fusion and braiding of topological defects in a lattice model". In: *Physical Review B* 90.11 (2014), p. 115118. DOI: https://doi.org/10.1103/PhysRevB.90.115118.
- [Ter15] Barbara M Terhal. "Quantum error correction for quantum memories". In: Reviews of Modern Physics 87.2 (2015), p. 307. DOI: https://doi.org/10.1103/RevModPhys.87.307.

[Tho+82] David J Thouless et al. "Quantized Hall conductance in a two-dimensional periodic potential". In: *Physical review letters* 49.6 (1982), p. 405. DOI: https://doi.org/10.1103/PhysRevLett.49.405.

- [Tia+22] Zehua Tian et al. "Testing the upper bound on the speed of scrambling with an analogue of Hawking radiation using trapped ions". In: *The European Physical Journal C* 82.3 (2022), p. 212. DOI: https://doi.org/10.1140/epjc/s10052-022-10149-8.
- [TM17] Giacomo Torlai and Roger G. Melko. "Neural Decoder for Topological Codes". In: Phys. Rev. Lett. 119 (3 July 2017), p. 030501. DOI: https://doi.org/10.1103/PhysRevLett.119.030501. URL: https://link.aps.org/doi/10.1103/PhysRevLett.119.030501.
- [Tri+22] Jonathan Trisnadi et al. "Design and Construction of a Quantum Matter Synthesizer". In: Review of Scientific Instruments 93.8 (Aug. 2022), p. 083203. ISSN: 0034-6748, 1089-7623. DOI: 10.1063/5.0100088. (Visited on 05/07/2023).
- [Tuc+20] David K Tuckett et al. "Fault-tolerant thresholds for the surface code in excess of 5% under biased noise". In: *Physical review letters* 124.13 (2020), p. 130501.

 DOI: https://doi.org/10.1103/PhysRevLett.124.130501.
- [Unr76] William G Unruh. "Notes on black-hole evaporation". In: *Physical Review D* 14.4 (1976), p. 870. DOI: https://doi.org/10.1103/PhysRevD.14.870.
- [Unr95] William G Unruh. "Sonic analogue of black holes and the effects of high frequencies on black hole evaporation". In: *Physical Review D* 51.6 (1995), p. 2827. DOI: DOI:10.1103/physrevd.51.2827.
- [Unr81] William George Unruh. "Experimental black-hole evaporation?" In: *Physical Review Letters* 46.21 (1981), p. 1351. DOI: https://doi.org/10.1103/PhysRevLett.46.1351.

[Vei+12] Victor Veitch et al. Negative Quasi-Probability as a Resource for Quantum Computation. 2012. arXiv: 1201.1256 [quant-ph].

- [Vei+14] Victor Veitch et al. "The resource theory of stabilizer quantum computation".
 In: New Journal of Physics 16.1 (Jan. 2014), p. 013009. ISSN: 1367-2630. DOI:
 10.1088/1367-2630/16/1/013009. URL: http://dx.doi.org/10.1088/1367-2630/16/1/013009.
- [VLV21] Ruben Verresen, Mikhail D. Lukin, and Ashvin Vishwanath. "Prediction of Toric Code Topological Order from Rydberg Blockade". In: *Physical Review X* 11.3 (July 2021). ISSN: 2160-3308. DOI: 10.1103/physrevx.11.031005. URL: http://dx.doi.org/10.1103/PhysRevX.11.031005.
- [Vie+22] Celia Viermann et al. "Quantum field simulator for dynamics in curved spacetime". In: nature 611.7935 (2022), pp. 260-264. DOI: https://doi.org/10.1038/s41586-022-05313-9.
- [VKL99] Lorenza Viola, Emanuel Knill, and Seth Lloyd. "Dynamical decoupling of open quantum systems". In: *Physical Review Letters* 82.12 (1999), p. 2417. DOI: https://doi.org/10.1103/PhysRevLett.82.2417.
- [Vla02] Alexander Yu Vlasov. "Noncommutative tori and universal sets of nonbinary quantum gates". In: *Journal of Mathematical Physics* 43.6 (2002), pp. 2959–2964. DOI: https://doi.org/10.1063/1.1476391.
- [Vui+19] Christophe Vuillot et al. "Code deformation and lattice surgery are gauge fixing". In: New Journal of Physics 21.3 (2019), p. 033028. DOI: https://doi.org/10.1088/1367-2630/ab0199.
- [WP99] R. Walter Ogburn and John Preskill. "Topological Quantum Computation". In: Quantum Computing and Quantum Communications. Ed. by Colin P. Williams. Berlin, Heidelberg: Springer Berlin Heidelberg, 1999, pp. 341–356. ISBN: 978-3-540-49208-5.

[WÜE18] Botao Wang, F. Nur Ünal, and André Eckardt. "Floquet Engineering of Optical Solenoids and Quantized Charge Pumping along Tailored Paths in Two-Dimensional Chern Insulators". In: Physical Review Letters 120.24 (June 2018), p. 243602. ISSN: 0031-9007, 1079-7114. DOI: 10.1103/PhysRevLett.120.243602. (Visited on 06/26/2023).

- [WHP03] Chenyang Wang, Jim Harrington, and John Preskill. "Confinement-Higgs transition in a disordered gauge theory and the accuracy threshold for quantum memory". In: *Annals of Physics* 303.1 (2003), pp. 31–58. DOI: https://doi.org/10.1016/S0003-4916%2802%2900019-2.
- [Wan+09] David S Wang et al. "Threshold error rates for the toric and surface codes". In: arXiv preprint arXiv:0905.0531 (2009). DOI: https://doi.org/10.48550/arXiv.0905.0531.
- [Wan+10] David S. Wang et al. "Graphical Algorithms and Threshold Error Rates for the 2d Color Code". In: Quantum Info. Comput. 10.9 (2010), pp. 780–802. ISSN: 1533-7146. DOI: https://doi.org/10.48550/arXiv.0907.1708.
- [Wan+20] Yuchen Wang et al. "Qudits and high-dimensional quantum computing". In: Frontiers in Physics 8 (2020), p. 589504. DOI: https://doi.org/10.3389/fphy.2020.589504.
- [Wan10] Zhenghan Wang. Topological quantum computation. 112. American Mathematical Soc., 2010.
- [Wei+10] Hendrik Weimer et al. "A Rydberg quantum simulator". In: Nature Physics 6.5 (Mar. 2010), pp. 382–388. ISSN: 1745-2481. DOI: 10.1038/nphys1614. URL: http://dx.doi.org/10.1038/nphys1614.
- [Wei+15] M. Weinberg et al. "Multiphoton Interband Excitations of Quantum Gases in Driven Optical Lattices". In: *Physical Review A* 92.4 (Oct. 2015), p. 043621. DOI: 10.1103/PhysRevA.92.043621. (Visited on 10/09/2023).

[Wei+11a] Silke Weinfurtner et al. "Measurement of stimulated Hawking emission in an analogue system". In: *Physical Review Letters* 106.2 (2011), p. 021302. DOI: https://doi.org/10.1103/PhysRevLett.106.021302.

- [WS21] Christof Weitenberg and Juliette Simonet. "Tailoring Quantum Gases by Floquet Engineering". In: Nature Physics 17.12 (Dec. 2021), pp. 1342–1348. ISSN: 1745-2473, 1745-2481. DOI: 10.1038/s41567-021-01316-x. (Visited on 05/07/2023).
- [Wei+11b] Christof Weitenberg et al. "Single-Spin Addressing in an Atomic Mott Insulator".
 In: Nature 471.7338 (Mar. 2011), pp. 319–324. ISSN: 1476-4687. DOI: 10.1038/nature09827.
- [Wen03] Xiao-Gang Wen. "Quantum orders in an exact soluble model". In: *Physical review letters* 90.1 (2003), p. 016803. DOI: https://doi.org/10.1103/PhysRevLett. 90.016803.
- [Wen13] Xiao-Gang Wen. "Topological Order: From Long-Range Entangled Quantum Matter to a Unified Origin of Light and Electrons". In: International Scholarly Research Notices 2013.1 (2013), p. 198710. DOI: https://doi.org/10.1155/ 2013/198710.
- [WHY24] Adam Wills, Min-Hsiu Hsieh, and Hayata Yamasaki. Constant-Overhead Magic State Distillation. 2024. DOI: https://doi.org/10.48550/arXiv.2408.07764. arXiv: 2408.07764 [quant-ph]. URL: https://arxiv.org/abs/2408.07764.
- [Wit88] Edward Witten. "Topological quantum field theory". In: Communications in Mathematical Physics 117.3 (1988), pp. 353-386. DOI: https://doi.org/10.1007/BF01223371. URL: https://doi.org/10.1007/BF01223371.
- [WL12] James R Wootton and Daniel Loss. "High threshold error correction for the surface code". In: *Physical review letters* 109.16 (2012), p. 160503. DOI: https://doi.org/10.1103/PhysRevLett.109.160503.

[Woo+08] James R. Wootton et al. "Non-Abelian statistics from an Abelian model". In: Physical Review B 78.16 (Oct. 2008). ISSN: 1550-235X. DOI: 10.1103/physrevb. 78.161102. URL: http://dx.doi.org/10.1103/PhysRevB.78.161102.

- [XW08] Haitan Xu and Xin Wan. "Constructing functional braids for low-leakage topological quantum computing". In: *Physical Review A—Atomic, Molecular, and Optical Physics* 78.4 (2008), p. 042325. DOI: https://doi.org/10.1103/PhysRevA.78.042325.
- [Xu+23] Shibo Xu et al. "Digital simulation of projective non-abelian anyons with 68 superconducting qubits". In: *Chinese Physics Letters* 40.6 (2023), p. 060301.

 DOI: https://doi.org/10.1088/0256-307X/40/6/060301.
- [Xu+24] Shibo Xu et al. "Non-Abelian braiding of Fibonacci anyons with a superconducting processor". In: *Nature Physics* 20.9 (2024), pp. 1469–1475. DOI: https://doi.org/10.1038/s41567-024-02529-6.
- [Yan+20] Run-Qiu Yang et al. "Simulating quantum field theory in curved spacetime with quantum many-body systems". In: *Physical Review Research* 2.2 (2020), p. 023107. DOI: https://doi.org/10.1103/PhysRevResearch.2.023107.
- [Yep11] Jeffrey Yepez. "Einstein's vierbein field theory of curved space". In: $arXiv\ preprint$ $arXiv:1106.2037\ (2011)$.
- [Yos11] Beni Yoshida. "Classification of quantum phases and topology of logical operators in an exactly solved model of quantum codes". In: *Annals of Physics* 326.1 (2011), pp. 15–95. DOI: https://doi.org/10.1016/j.aop.2010.10.009.
- [YK17] Beni Yoshida and Alexei Kitaev. "Efficient decoding for the Hayden-Preskill protocol". In: arXiv preprint arXiv:1710.03363 (2017). DOI: https://doi.org/10.48550/arXiv.1710.03363.
- [YW12] Yi-Zhuang You and Xiao-Gang Wen. "Projective non-Abelian statistics of dislocation defects in a \mathbb{Z}_N rotor model". In: *Physical Review B* 86.16 (Oct. 2012).

- ISSN: 1550-235X. DOI: 10.1103/physrevb.86.161107. URL: http://dx.doi.org/10.1103/PhysRevB.86.161107.
- [You+22] Aaron W. Young et al. "Tweezer-Programmable 2D Quantum Walks in a Hubbard-regime Lattice". In: *Science* 377.6608 (Aug. 2022), pp. 885–889. DOI: 10.1126/science.abo0608. (Visited on 09/21/2023).
- [Yu+23] Jr-Chiun Yu et al. Observing the two-dimensional Bose glass in an optical quasicrystal. 2023. DOI: https://doi.org/10.48550/arXiv.2303.00737. arXiv: 2303.00737 [cond-mat.quant-gas]. URL: https://arxiv.org/abs/2303.00737.
- [Zha+20] Hongzheng Zhao et al. "Quantum Many-Body Scars in Optical Lattices". In: Physical Review Letters 124.16 (Apr. 2020), p. 160604. DOI: 10.1103/PhysRevLett. 124.160604. (Visited on 11/18/2023).
- [Zha+22] Wending Zhao et al. "Quantum simulation for topological Euler insulators". In: Communications Physics 5.1 (2022), p. 223. DOI: https://doi.org/10.1038/s42005-022-01001-2.
- [ZDJ15] Huaixiu Zheng, Arpit Dua, and Liang Jiang. "Demonstrating non-Abelian statistics of Majorana fermions using twist defects". In: *Physical Review B* 92.24 (Dec. 2015). ISSN: 1550-235X. DOI: 10.1103/physrevb.92.245139. URL: http://dx.doi.org/10.1103/PhysRevB.92.245139.
- [Zhu+15] Ye Zhuang et al. "Phase diagram of the Z₃ parafermionic chain with chiral interactions". In: *Physical Review B* 92.3 (July 2015). ISSN: 1550-235X. DOI: 10.1103/physrevb.92.035154. URL: http://dx.doi.org/10.1103/PhysRevB. 92.035154.
- [ZCR15] Erez Zohar, J Ignacio Cirac, and Benni Reznik. "Quantum simulations of lattice gauge theories using ultracold atoms in optical lattices". In: Reports on Progress in Physics 79.1 (Dec. 2015), p. 014401. ISSN: 1361-6633. DOI: https://doi.org/

10.1088/0034-4885/79/1/014401. URL: http://dx.doi.org/10.1088/0034-4885/79/1/014401.